

Development of the Nano-Aperture Ion Source (NAIS)

Proefschrift

ter verkrijging van de graad van doctor
aan de Technische Universiteit Delft,
op gezag van de Rector Magnificus Prof. dr. ir. K.C.A.M. Luyben,
voorzitter van het College voor Promoties
in het openbaar te verdedigen op
donderdag 6 november 2014 om 10.00 uur

door

David Sangbom JUN

Master of Science,
Portland State University, Portland, Oregon, USA

geboren te Seoul, Zuid-Korea

Dit proefschrift is goedgekeurd door de promotor:

Prof.dr.ir. P. Kruit

Samenstelling promotiecommissie:

Rector Magnificus,	voorzitter
Prof.dr.ir. P. Kruit,	Technische Universiteit Delft, promotor
Prof.dr.ir. O.J. Luiten,	Technische Universiteit Eindhoven
Prof.dr. U. Staufer,	Technische Universiteit Delft
Prof.dr. G.C.A.M. Janssen,	Technische Universiteit Delft
Prof.dr. H.W. Zandbergen,	Technische Universiteit Delft
Dr. C.W. Hagen,	Technische Universiteit Delft
Dr. A.F. de Jong,	FEI Company



ISBN 978-94-6186-384-3

Copyright © 2014 by David S. Jun

Table of Contents

1.	Introduction to focused ion beam (FIB) and ion sources.....	1
1.1	Fundamentals of FIB	2
1.1.1	FIB machines	2
1.1.2	Ion beam-matter interactions.....	3
1.1.3	FIB applications	7
1.1.4	Measure of FIB system performance.....	10
1.1.5	Effect of coulomb interactions in FIB columns	12
1.2	Existing ion sources for high resolution FIB applications.....	13
1.2.1	Liquid Metal Ion Source (LMIS)	13
1.2.2	Gas Field Ionization Source (GFIS)	14
1.3	About this thesis	15
	References	18
2.	The Concept of Nano-Aperture Ion Source (NAIS)	21
2.1	Introduction	22
2.2	Electron impact ionization	23
2.3	Nano-Aperture Ion Source (NAIS).....	25
2.3.1	The source concept.....	25
2.3.2	Electron impact gas ionization in a dilute gas.....	26
2.3.3	Theoretical source performance.....	27
2.4	Conclusions	32
	Acknowledgement	32
	References	32
3.	Simulated Performance of the Nano-Aperture Ion Source	35
3.1	Introduction	36
3.2	Simulation approach.....	36
3.3	Gas simulations	38
3.3.1	Steady state molecular flow gas simulation using the Monte Carlo method.....	38
3.3.2	Gas simulation results.....	40
3.4	Ion trajectory simulations	44
3.4.1	Ion transmission.....	45
3.4.2	Energy spread	48
3.4.3	Source reduced brightness	51

3.4.4	Virtual source size	58
3.5	Further work	59
3.6	Conclusions	60
	Acknowledgment	61
	References	61
4.	Miniaturized Gas Chamber Design and Fabrication	63
4.1	Introduction	64
4.2	The double-chip design	65
4.2.1	Fabrication process	65
4.2.2	Membrane buckling due to internal stress and oxidation	68
4.2.3	The double-chip gas chamber spacing issues	70
4.2.4	Prototype evaluation and future improvement	72
4.3	The single-chip design	74
4.3.1	Fabrication process	74
4.3.2	Prototype evaluation and future improvement	79
4.4	Conclusions	81
	Acknowledgements	82
	References	82
5.	Ion beams in SEM: the proof-of-concept experiments	83
5.1	Experimental setup	84
5.2	Ion beam pattern imaging	86
5.3	Ion beam current	87
5.3.1	Beam current measurement	87
5.3.2	Beam current stability	90
5.3.3	Current distribution and angular intensity	91
5.4	Energy spread	92
5.4.1	Retarding field energy analyzer	92
5.4.2	Results	96
5.5	FIB in a SEM: first ion imaging and milling using a NAIS	99
5.5.1	First FIB images	102
5.5.2	First FIB milling	103
5.6	Source reduced brightness	104
5.7	Conclusions	106
	Acknowledgement	107

References	107
6. Delft NAIS-FEI Sidewinder Integration: the concept and design	109
6.1 Introduction	110
6.2 Technical challenges	112
6.3 Prototype ion column design	114
6.3.1 Schottky electron focusing column.....	114
6.3.2 NAIS 'packaging'	116
6.3.3 Optics layout and electrical power configuration.....	126
6.4 Predicted prototype performance.....	127
6.5 Conclusions	132
Acknowledgement	132
References	133
Summary	135
Samenvatting	139
Acknowledgments.....	144
About the Author	145

1 ■ Introduction to focused ion beam (FIB) and ion sources

Although its introduction to the world dates back just over three decades, focused ion beam (FIB) tools have made tremendous impact in many research and engineering fields of nanotechnology and material science, particularly in the production and modification of semiconductor devices. FIB tools are already well-established micro- and nano-structure fabrication and characterization instruments but as long as the trend of miniaturization remains unchanged they will receive continued attention and strong demands for improvement. Further improvement and diversification of the FIB technology, however, depend greatly in the development of new ion sources as the ultimate machine performance and applications are dependent on the properties of the ion source. This is the underlying notion that motivated this PhD research and the challenge is undertaken by developing a novel ion source based on electron impact gas ionization that strives to meet simultaneously all of the critical ion source properties: high reduced beam brightness, low energy spread, ion species of a wide variety, beam stability, and operational reliability. Prior to detailing the development of the new technology, this introductory chapter provides a general overview on the current FIB and ion source technologies and other necessary background for establishing the relevance and importance of this research and defining the objectives and requirements for the new ion source.

1.1 Fundamentals of FIB

1.1.1 FIB machines

As its name unmistakably implies, a FIB machine (review articles/books^[1-7]) obviously deals with ions. It deals in a manner such that a large number of energetic ions are guided and focused onto a small area on the surface of a specimen. In many ways, particularly in the mechanical point of view, the look and feel of a FIB system resemble its more well-known counterpart SEM (Scanning Electron Microscope) as both are probe forming systems and both utilizing charged particles their optical behaviors are governed by the same electromagnetic principles.

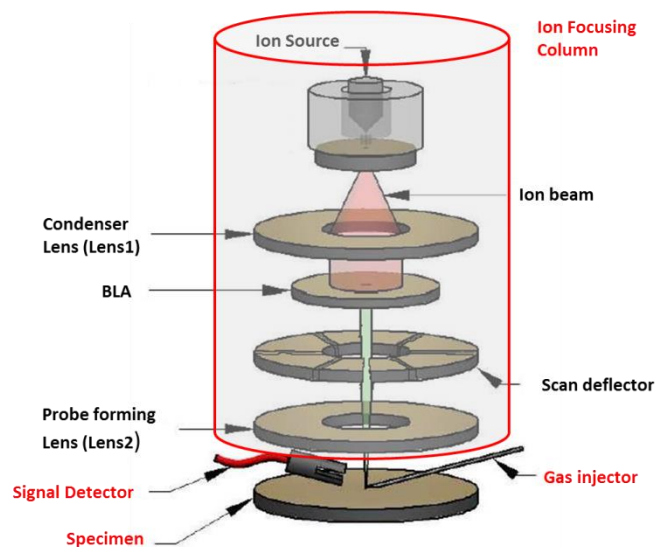


Fig. 1-1 A layout of the basic FIB machine. Re-drawn from Ref. [8]

Fig. 1-1 describes the inside of a typical FIB instrument. A FIB machine generally consists of an ion focusing column, a gas injection system, a detector and a sample stage, all operating in a vacuum chamber under computer control. For ensuring propagation of the ions through the focusing column and all the way down to the sample and discharge-free high voltage operation, an operating column pressure below 1×10^{-6} mbar is typical, but near the ion source, the pressure requirement can be much more stringent for the ion current stability and source longevity.

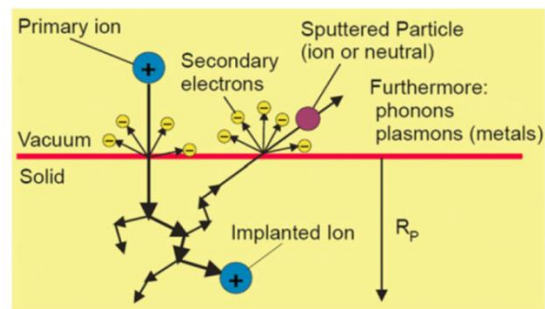
The basic FIB focusing column includes an ion source, beam limiting aperture (BLA), a set of scanning deflectors, and electrostatic focusing lenses. An ion beam originates from the ion source, however, typically only a fraction of the ion current reaches the specimen after being 'limited' by the BLA. A variable probe current can be realized by changing the size of the BLA as well as changing the condenser lens strength. A probe is the image of the ion 'source' projected on the specimen surface and its size determined by the overall (de)magnification of the source and the aberrations resulting from the combined strength of both the condenser (Lens 1) and final probe forming lens (Lens 2).

A set of deflectors allow 'scanning' of the focused ion beam over an area of interest on the specimen just like the electron beam raster-scanned over the phosphor screen in a cathode ray tube. The probe of an ion beam strikes on the surface of the specimen with a net landing energy determined by the potential difference between the source and the specimen. The commercial

systems typically operate with energies ranging from 1 keV to 50 keV with beam diameters ranging from a few nm to a few μm and currents from 1 pA to tens of nA.

1.1.2 Ion beam-matter interactions

When an energetic ion beam impinges on a target surface a number of physical processes arise as the ion encounters a series of collisions with atomic electrons and nuclei of the target material. Through inelastic and elastic interactions, ion kinetic energy and momentum are transferred to the solid. Specifically, the projectile ion can lose energy and slow down due to the inelastic collisions with bound electrons of the target atoms. This process is known as the ‘electronic energy loss’ and the outcomes are ionization of target atoms and the emissions of secondary electrons, X-rays, photons and phonons. The projectile ion can also lose energy via the ‘nuclear energy loss’ which involves elastic scattering between the screened nuclear charges of the incident ion and the target atoms. This results in displacement of target atoms from their initial positions and even removal (aka sputtering) from the target surface. The possible ion-matter interactions are schematically described in Fig. 1-2 and some details are also to follow.



(a)

Parameters	Typical value
Secondary electron yield	1 to 5
Secondary ion yield	10^{-1} to 10^{-5}
Photon yield	$\sim 10^{-2}$
Sputtering yield Y	2.4
Implantation depth R_p	~ 10 nm

(b)

Fig. 1-2 (a) Possible ion-matter interactions and (b) typical interaction parameters for a 30 keV Ga^+ ion bombardment on a Si target. Adapted from Ref. [7].

Sputtering

For the energy range in which a typical FIB operates, the nuclear energy loss dominates and the process of sputtering is sufficiently described by the linear collision cascade model (LCC) [9]. In this model, the penetrating ion shares its energy with stationary target atoms through a series of independent binary collisions. Upon the transfer of the translational energy to a target atom that exceeds the threshold displacement energy of the sample material (tens of eV or more), the atom will be displaced from its original lattice site, arising to ‘damage’ of creating an interstitial-vacancy pair in a crystalline sample and transforming the structure of crystalline to amorphous. The

displaced atom can in turn transfer energy with other stationary atoms with additional binary collisions, eventually creating a volume of large numbers of atoms having excess translational energy. Sputtering results when an atom near the sample surface is given enough energy to overcome the surface binding energy (3.8 eV for Au and 4.7 eV for Si). After a number of collisions, the incident ion can also by chance leave or eventually lose all of its kinetic energy and become implanted in the specimen.

Due to the fact that momentum transfer is the basis of all ion-matter interactions, ion penetration depth, the range and transverse straggle of target atoms, the sputtering yield (the number of atoms rejected per primary ion), ion backscattering, and the emission of electrons and electromagnetic radiation are all profoundly dependent on the energy of incident ion and the masses of both incoming ion and sample material. Additionally, because sputtering is near surface phenomenon, the angle of incidence is another important contributing factor. Figs. 1-3 through 1-5 are some results of TRIM (Trajectory of Ion in Matter, a Monte Carlo ion trajectory calculation software based on the LLC model) simulations ^[10, 11] that evidently illustrate some of the key dependences.

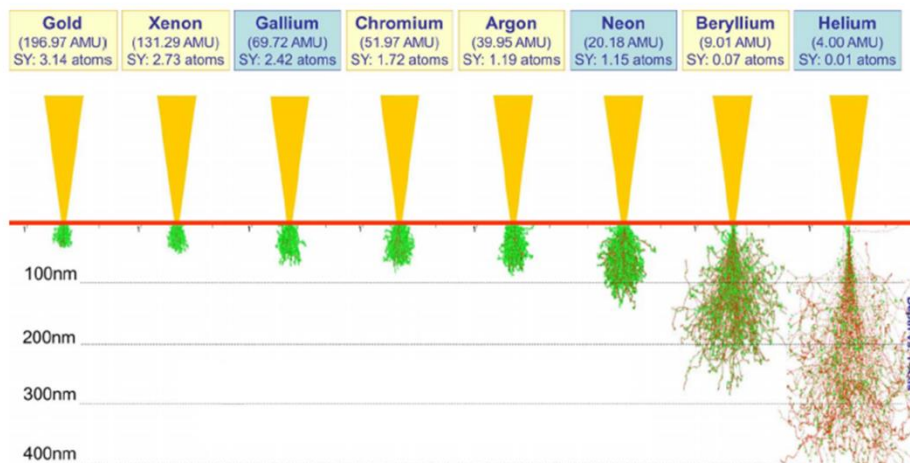


Fig. 1-3 Sputter yield (SY), interaction volume, implant depth of different ion beams at 30 keV in a silicon substrate simulated using TRIM. The trajectory of the incident ions are shown in red and the dislocated silicon atoms are represented in green. It is evident that the light ions penetrate much deeply into substrate. Adapted from Ref. [12].

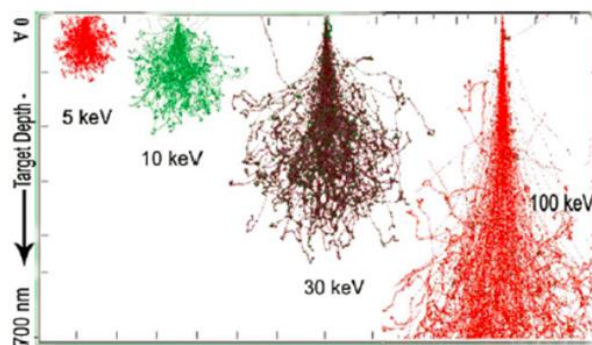


Fig. 1-4 TRIM simulation results showing the interaction volume of helium ions in aluminum at 5, 10, 30, and 100 keV beam energy. The target penetration depth increases with increasing energy. Adapted from Ref. [13].

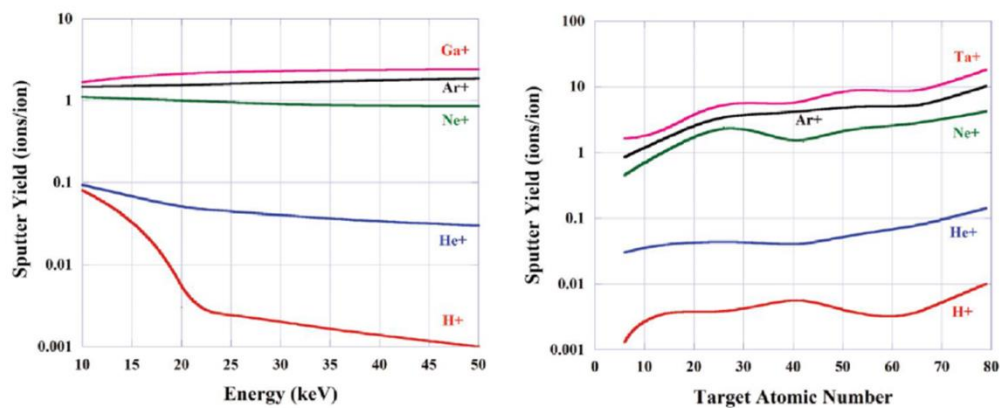


Fig. 1-5 (left) Sputter yield from a silicon substrate as a function of ion type and energy and (right) sputter yield as a function of the incident ion beam type and the target material atomic number given an incident ion energy of 40 keV. Adapted from Ref. [14].

Ion-matter interaction in the presence of a precursor gas

Yields resulting from the sputtering process described above are typically about 1 to 10 atoms per incident ion, for example, using a Ga^+ FIB. However, this yield can be either enhanced or retarded drastically by introducing a gas phase chemical precursor on the surface of target material, thus prompting FIB induced chemical reactions. This process, known as the ‘gas assisted etching’ or ‘chemical etching’, is regarded as quite different from the ‘physical etching’ which arises purely from the momentum transfer sputtering process of the linear collision cascade. The precursor gas is typically introduced and directed toward the vicinity of the desired etching site using a narrow delivery tube as shown in Fig. 1-6. The ion beam is then irradiated to decompose the precursor gas molecules that have been adsorbed, typically in the form of mono-layer on the sample surface. Enhancing the etching rate comes into effect by applying a precursor gas that will react with the sample to produce volatile products (Fig. 1-6 (a)). On the contrary, retarding the etching rate comes into effect by applying a precursor gas that will react with the sample to produce non-volatile products. In the case the ion beam decomposes the precursor gas more rapidly than being sputtered away, in fact, a material deposition occurs (Fig. 1-6 (b)). Typical gases used for etch enhancement / retardation for commonly used materials by the semiconductor industry and their effectiveness over the physical sputtering only are shown in Table 1-1. Some of the FIB chemical precursors frequently utilized for material deposition are also listed in Table 1-2.

Gas assisted ion beam processing obviously offers tremendous advantage and adds versatility of high speed etching (up to x10 speed compared to physical sputtering alone), material deposition capable of constructing 3D nano-structures, and even selective etching capability all in a same ion irradiation setup simply by applying a precursor of choice, however, for precise and accurate nanofabrication capabilities, sophisticated ion beam scanning strategy is needed to provide sufficient beam overlap with a sufficient precursor gas density in the area of interest. ^[15]

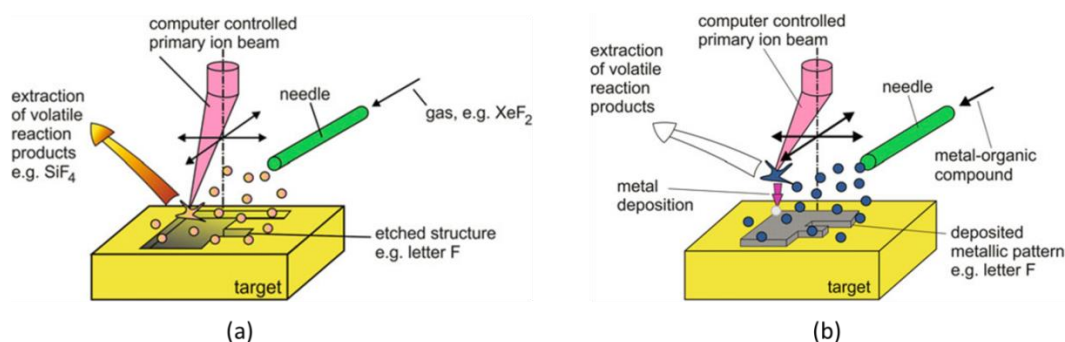


Fig. 1-6 Gas assisted FIB processing: enhanced etching (a) and deposition (b).

Table 1-1 Gas-assisted etch rate enhancement over physical sputtering only (Ga^+ beam)^[7]

		Substrate materials						
		Si	SiO ₂	Al	W	GaAs	InP	PMMA
Gases	Cl ₂	7-10	1	7-10	1	50	4	-
	Br ₂	5-6	1	8-16	1	-	-	-
	I ₂	5-10	1	5-15	-	-	11-13	2
	XeF ₂	7-12	7-10	1	7-10	-	-	4
	H ₂ O	0.05-0.1	0.1-0.15	0.02-0.05	-	-	-	18

Table 1-2 Common precursor gases used for ion beam induced material deposition^[7]

		Precursor gas
		Deposited material
	W	Tungsten Hexacarbonyl, W(CO) ₆
	Pt	Methylcyclopentadienyl platinum trimethyl, (CH ₃) ₃ (CH ₃ C ₅ H ₄)Pt
	Al	Trimethylamine alane (TMAA), (CH ₃) ₃ NAIH ₃
	SiO ₂	O ₂ + tetraethoxysilane (TEOS), O ₂ + tetramethoxysilane (TMOS), Si(OCH ₃) ₄
	C	Phenanthrene

Secondary electron generation

Ion bombardment induces generation of several different secondary species, but due to its dominance in terms of yield, secondary electron generation is an important aspect for FIB processing. Ion induced secondary electron (iSE) emission can occur through two distinct channels, namely potential electron emission and kinetic electron emission^[16, 17]. In the potential emission, an ion approaching the sample surface becomes neutralized by a target electron either by direct Auger neutralization or by resonance neutralization and the ejection of another electron from the target can occur following the subsequent Auger de-excitation of the excited state of the atom to the ground state. Because the potential emission takes place involving two electrons ejecting from the target atom, the total energy transfer (the first ionization energy of the primary ion) must be at least equal to twice the work function of the target material, hence potential electron emission is only significant for positive ions of high ionization energies such as inert gas ion species. In addition the process is only plausible at low ion energies (<5 keV) due to decreasing interaction time at higher ion energies.

The kinetic emission process, on the other hand, is similar to the sputtering process in such that target electrons are excited through multiple ion scattering and energy loss in the target material. The excited electrons lose most of their energy in the form of heat in the solid but the ones near the surface (<10's of Å from the surface) may escape from the surface if their energy is higher than the surface binding energy. Kinetic electron emission typically dominates in general FIB operation and typical secondary electron yield per incoming ion is about 0.1-10. The energy and angular dependence of the secondary electron yield follow a similar trend seen with the ion sputtering yield described above.

1.1.3 FIB applications

Combined with the ability to focus a beam under 10 nm and exploiting various aspects of the ion-matter interactions, today's FIB machines are versatile and convenient one stop tools for high resolution imaging and device modifications involving both removal and deposition of material at the nanometer scale with high precision and reliability. The FIB machines are used to fabricate high aspect ratio nanopores, a pattern of photonic structures, and stress-free cross sections revealing thin material layers, locally remove or deposit conducting or insulating material literally nm by nm, perform patterned implantation without a mask, and generate and detect secondary signals from sample upon the bombardment of the ion beam. These are the essential FIB functions incorporated in a broad range of applications including high resolution scanning ion microscopy (SIM), secondary ion mass spectroscopy (SIMS), TEM sample preparation, thin film head (TFH) manufacturing, mask repair, integrated circuit (IC) failure analysis and edit, lithography, ion implantation, and others^[1-7]. Below SIM and FIB circuit edit (CE) are briefly reviewed to elaborate on the power and unique capabilities of the present day FIB machines.

Scanning Ion Microscopy (SIM)

The imaging process in the FIB follows the exactly same manner used in the SEM. A beam is finely focused and raster-scanned on a sample surface and an image is constructed by stitching a series of pixels with each pixel position synchronized with the physical beam scan position and the pixel intensity represented by a detected signal from the sample at that corresponding beam position. Hence, in general, the smaller the ion beam probe, the more detailed image can be generated given that the ion-sample interaction provides adequate signal to noise ratio ($>S/N \sim 5$).

Because of the significantly higher yield compared to other ion-induced secondary particles generated, FIB microscopy is predominantly based on detection of secondary electrons (typically with energies below 10 eV) similar to the conventional SEM imaging. The ion beam induced SE imaging, however, can provide much richer topographical and material contrast compared to the electron beam induced SE imaging, as much shallower penetration of ions into the sample material leads to much higher SE yield and higher sensitivity to different sample topography and materials (see Fig. 1.7 top). Also, because the ion penetration depth can be affected by the crystallographic orientation of the sample grains, the FIB SE imaging can show strong crystallographic (channeling) contrast (see Fig. 1.7 bottom) which makes FIB particularly useful for microstructural investigation, i.e. inspecting plastic deformation and stress-corrosion cracks in steel and the distribution of grain sizes in multi-crystalline materials^[19].

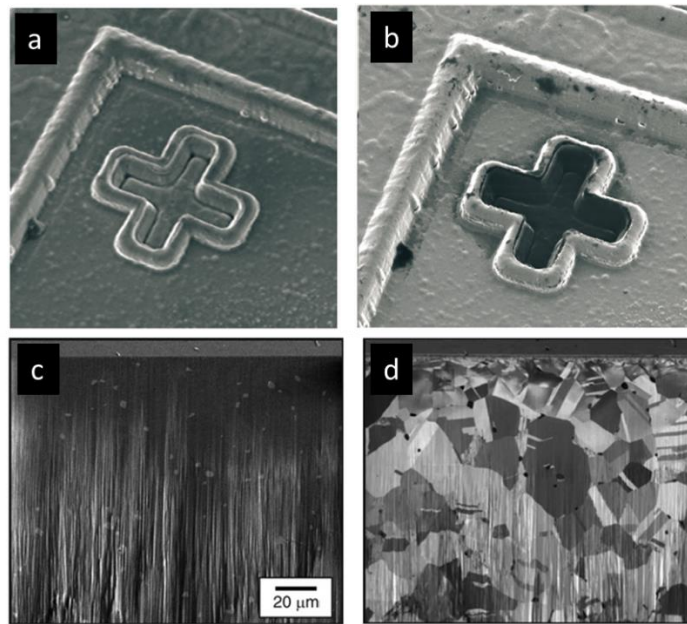


Fig. 1-7 Electron induced secondary (SE) electron imaging versus ion induced secondary electron (iSE) imaging. **Top:** an alignment cross imaged by SEM SE imaging (a) and He^+ iSE imaging (b). The iSE image of (b) clearly indicates that the material inside the cross is different from the outside (the material contrast). **Bottom:** SE (c) and iSE (d) images of an FIB-cut cross section in brass. Surface topography produced during the FIB milling is visible in both (c) and (d) but in (d) the grain structure is additionally visible due to iSE channeling contrast. Images (a) and (b) taken from Ref. [18] and (c) and (d) from Ref. [4].

Despite the unique SE imaging capabilities and additional contrast mechanisms offered by primary ions and secondary ions were well recognized earlier on, traditionally FIB was not regarded as an effective imaging tool due to poorer imaging resolution compared to the SEM and the lack of choices in light ion species. With the commercial FIB systems predominantly providing Ga^+ ion beams, imaging samples are inherently prone to chemical contaminations by Ga implantation as well as physical modifications by sputtering^[*]. For many Ga^+ based FIB machines, a SEM column is commonly integrated together in the same platform (known as the ‘dual beam’) to support for the imaging needs during and post FIB processing^[7,21]. However, in 2006 the invention of Helium ion microscope (HIM) by Alis Corporation (now a subsidiary of Zeiss) sparked a new interest in ion microscopy. With the new helium ion source based on the gas field ionization technology (more details provided in Section 1.2.2) the HIM now offers a sub-nanometer imaging resolution (0.24 nm, 25-75% edge rise), in fact, surpassing that of any SEM systems^[22] as well as virtually damage and contamination free imaging capabilities^[13, 23]. The new invention is indeed testimonial to how an ion source can improve the overall FIB machine performance and extend its usefulness. Considering the much smaller theoretical probe size and larger field of focus achievable with ion beams compared to electron beams due to the smaller wavelength, the FIB technology is poised to gain wider acceptance in inspection and metrology of three dimensional nano-scale structures and biological samples.

[*] An excellent account on the subject of material sputtering affecting the ion microscope image resolution can be found in the PhD thesis of Castaldo^[20].

FIB circuit edit (CE)

The unique capabilities of making smear- and stress-free cross-sections of structures composed of different material layers and adding both insulating and conductive materials at the nano-scale naturally make FIB a tool of choice when it comes to reviewing defects and rewiring in integrated circuits. The modern FIB tools offer not only the convenience and innovative technical solutions in circuit debugging but also provide tremendous economic advantage as FIB allows direct on-chip circuit modifications without needing to repeat fabrication steps that usually require expensive masks.

A couple of simple FIB circuit edit examples are shown below. In Fig. 1-8, an original wire track of an IC was cut by controlled FIB sputtering and the upper portion of the track was rerouted to an adjacent track to the left by a new metal strap deposited between two tracks in the middle. Fig. 1-9 shows a cross section of an access to the lower metal layer (metal 1) made while maintaining electrical isolation from the top metal layer (metal 2) by gas assisted FIB milling an access hole down to the lower metal layer first and then backfilling it with a FIB insulator deposition. After a smaller hole opened into the insulator, the hole was then refilled with a conductor (Pt) and a contact pad was created again by FIB metal deposition on the top surface.

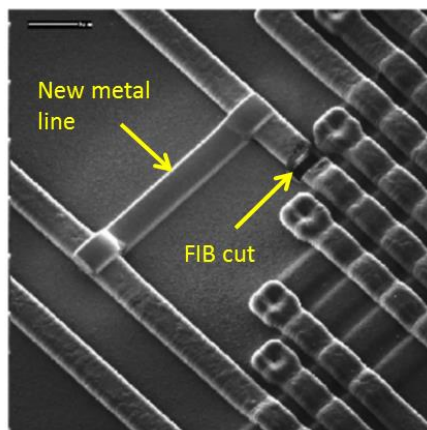


Fig. 1-8 Rewiring of an IC using FIB milling and deposition. Image adapted from Ref. [6].

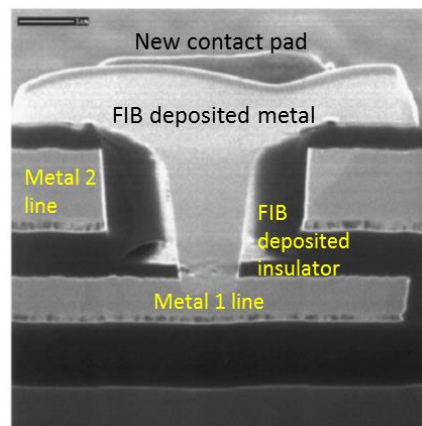


Fig. 1-9 Cross section showing a new contact made to metal 1 line after FIB cutting through metal 2 line. Image adapted from Ref. [6].

FIB technology has been adopted in chip development and manufacturing immediately after commercialization of FIB systems began in the 1980's. Naturally, the advancement of the IC technology over the years has demanded parallel progress in FIB performance and CE processing technology. Changes in component materials such as aluminum to copper wiring has required sophisticated gas assisted strategies for consistent milling^[24, 25]. Advancement in chip packaging (i.e. flip chip, 3D IC packaging) and increasing number of interconnect layers have meant creative ways of accessing the transistor devices and lower level interconnects from the back side of the silicon substrate^[26-29]. By far the more obvious challenge has been the requirement of smaller FIB probe sizes to cope with the shrinking circuit component geometry. This is elaborated in Fig. 1-10, which shows the FIB nano-machining capability required for addressing the minimum via size of the several past and current generation process nodes. Livengood *et al.*^[30, 31] point out that the minimum probe

size achievable from the current Ga LMIS based FIB machines (~7 nm FWHM) will no longer be sufficient for process nodes beyond 60 nm and CE will require a FIB probe size reaching 1 nm within the next 5 years if the Moore's law continues to hold.

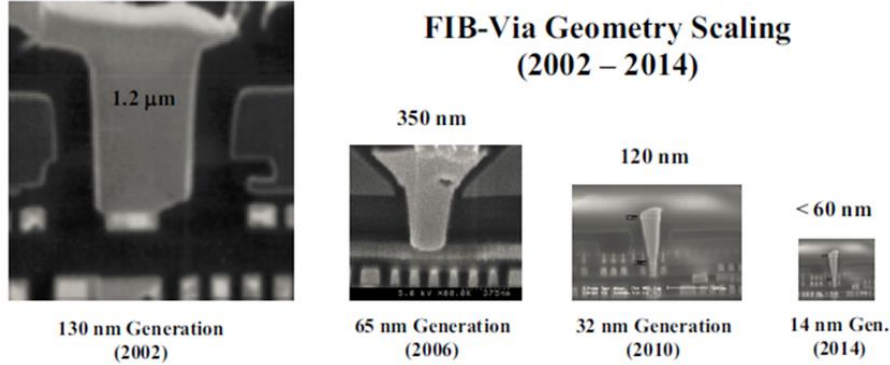


Fig. 1-10 Minimum FIB-via geometry requirements over time. In general the required via milling is about 3x4 times of the critical feature size. Image taken from Ref. [30]

1.1.4 Measure of FIB system performance

Defining and determining the FIB resolution of the smallest feature it can machine or image are not straightforward as the functionality of FIB manifest from physical interactions with matter that vary greatly with ion landing energy, ion incident angle, sample material, topography, and crystal structure, and surrounding gas environment as discussed previously. The end results can be also severely influenced by secondary processing effects such as the re-deposition during sputtering^[6] and information uncertainty associated with unwanted sample modifications during imaging^[20]. But what is clear is that, whether the FIB machine is used for imaging, sputtering, deposition, lithography, or implantation, for addressing small features with high throughput, the first obvious requirement for high resolution performance is a sufficiently small ion probe with as much current as possible. Therefore, the achievable probe size given an ion current is a convenient figure of merit that generalizes FIB machine performance.

The amount of current that can be delivered as an ion probe intrinsically depends on the reduced brightness B_r of the ion source and the size of the beam limiting aperture used in the FIB focusing column (see Fig. 1-11). The reduced brightness describes the amount of current I leaving from the object area A into a unit solid angle Ω when accelerated to the source side potential V_o . This is typically expressed as

$$B_r = \frac{I}{A\Omega V_o}. \quad (1.1)$$

With an aperture placed in front of the source that defines a solid angle, the probe current I_p entering the focusing column and eventually to the target is then

$$I_p = B_r \frac{\pi}{4} d_v^2 \pi \alpha_o^2 V_o, \quad (1.2)$$

where d_v is the object (virtual source) diameter and α_o the object angle defined by the beam limiting aperture.

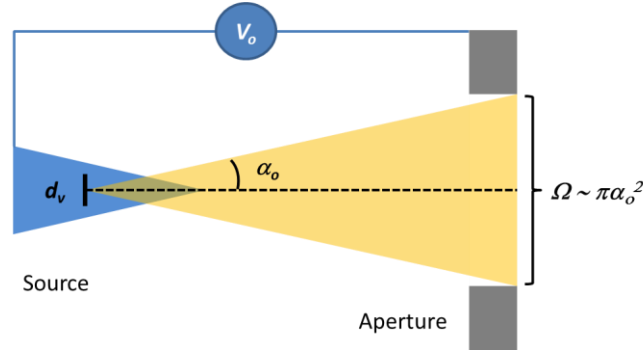


Fig. 1-11 Description of reduced brightness B_r . Ions from the virtual source diameter d_v are accelerated to the object side beam potential V_o into the solid angle Ω defined by the aperture. For a small object angle α_o , Ω is simply approximated to $\pi\alpha_o^2$.

The probe size d_p of a charged particle optics system including FIB is typically defined as^[32],

$$d_p = \{[d_I^{1.3} + (d_A^4 + d_S^4)^{1.3/4}]^{2/1.3} + d_C^2\}^{1/2}, \quad (1.3)$$

where d_I , d_A , d_S , and d_C are the contributions from the source image, the diffraction disk, the spherical aberration, and the chromatic aberration, respectively. Here, the d_p corresponds to the full width having 50% of the current (FW50) with each individual contributions defined as

$$d_I = Md_v, \quad (1.4)$$

where M is the magnification from the virtual source to the image plane and d_v the virtual source diameter,

$$d_A = 0.54 \frac{\lambda}{\alpha_i}, \quad (1.5)$$

where λ is the ion (or electron) wavelength and α_i the image half angle at the probe,

$$d_S = 0.18C_S\alpha_i^3, \quad (1.6)$$

where C_S the spherical aberration coefficient of the system, and

$$d_C = 0.34C_c \frac{dE}{V_i} \alpha_i, \quad (1.7)$$

where C_c is the chromatic aberration coefficient of the system, dE the full width at half maximum (FWHM) of the energy distribution of the source, and V_i the beam potential at the image plane.

Based on Eqs. 1.3 through 1.7, the optical system optimization for achieving an optimum probe size is then to balance the contributions between the magnified source image, the focusing lens diffraction which decreases with α_i and the chromatic and spherical aberrations which contrarily increase with α_i , in other words, simply to optimize α_i given a fixed M . However, this implies that there is an optimum object angle can be selected following the Helmholtz-Lagrange relation:

$$\frac{\alpha_i}{\alpha_o} = \frac{1}{M} \left(\frac{V_o}{V_i} \right)^{1/2}. \quad (1.8)$$

Subsequently, this indicates that there is a limit to how much ion current that can be focused into the optimum probe spot by the direct consequence of Eq. 1.2.

For typical FIB operation, the de Broglie wavelength of ions is extremely small so that the diffraction term is rather insignificant. Furthermore, for achieving a minimum probe size (~small

current), the image half angle is kept small so that spherical aberration contribution also becomes negligible (the α_i goes to cubic power). The probe size of the FIB system then becomes limited by the chromatic aberration contribution, in which case, the attainable minimum beam size becomes^[33]

$$d_p = \left(0.19 \frac{I_p C_c^2 dE^2}{B_r V^3} \right)^{1/4}. \quad (1.9)$$

From Eqs. 1.2 and 1.9, it's utterly clear that the intrinsic source properties B_r and dE fundamentally limit the FIB machine performance in terms of the beam size and the amount of current available in it.

1.1.5 Effect of coulomb interactions in FIB columns

The beam size characterization in the previous section is only limited to an ideal situation in which stochastic coulomb interactions between the neighboring particles in the system are absent^[**]. Because of the slow moving nature of the ions (at least compared to the electrons), FIB systems are prone to the influence of coulomb interactions and the probe size at the target can be much larger than what's expected by Eq. 1.3. The degradation can appear in two ways: (1) the repulsive forces between ions can increase the divergence of the beam. This is known as the trajectory displacement and the consequence is the broadening of the apparent virtual source size, which then causes loss in beam brightness and (2) the repulsive forces can also act longitudinally broadening the energy spread of the ions. This is known as the Boersch effect and this degrades the beam performance by increasing the chromatic aberration contribution. These effects can't be completely eliminated since the presence of charged particles is required in the instruments considered here but the proper implementation in the design of the focusing column as well as the source can minimize the effect. The general rule of thumb is to reduce or eliminate any unnecessary current and reduce the interaction time^[35]. These can be easily implemented in the focusing optics region by applying a beam limiting aperture (BLA) and acceleration tube and reducing the overall column length^[36, 37], however in the source region it is usually difficult to do so as the interactions are typically the highest near the emitting site and the emission conditions (i.e. total emission and extraction field) of the sources are often determined by the requirements of the ionization mechanism and not flexible to be varied due to operational stability. The Ga liquid metal ion source (LMIS), which will be discussed more in detail in Section 1.2.1, is a good example illustrating the severity of the problem. For operational stability Ga LMIS' typically operate with $\sim\mu\text{A}$ of total emission even though only $\sim\text{nA}$ of current is utilized for actual FIB processing. The consequences of the high emission current are the blurring of the virtual source size to ~ 50 nm although the actual emitting site is only a few nm wide^[38] and the energy spread of ≥ 5 eV although the initial energy spread is believed to be smaller than 1 eV^[39]. For minimizing coulomb interaction at the source, a gas ion source would be a better choice compared to a field emission based source such as the LMIS as the emission current can be usually adjusted easily by changing gas pressure without needing to change voltages on the focusing optics.

[**] For most complete theoretical analysis of coulomb interactions, refer to the work by Jansen^[34].

1.2 Existing ion sources for high resolution FIB applications

In addition to high reduced source brightness and low energy spread required for high resolution FIB capability, commercially useful ion sources must provide good current stability, reliability, life time, and the ease of use. Presently, there are only two types of ion sources, namely the liquid metal ion source and gas field ionization source meeting these stringent requirements and capable of providing sub-10 nm FIB probes.

1.2.1 Liquid Metal Ion Source (LMIS)

Interestingly enough the development of LMIS originated from charged ion droplet research for spacecraft propulsion systems back in 1960's by Krohn^[40], but soon after discovering the property of spray ion emission rather than charged liquid droplets, LMIS was quickly adapted into a focusing column by Krohn and Ringo^[41] and Seliger *et al.*^[42]. First commercialization of FIB based on LMIS began in the early 1980's and to date, the Ga-LMIS has been the most successful and widely used FIB source in the commercial machines, owing to its high source reduced brightness ($\sim 1 \times 10^6$ A/m²srV), simplicity and reliability.

As shown in Fig. 1-12, the construction of a LMIS is very simple and compact, consisting of a sharpened needle (tip end radius of ~ 10 μ m), typically made of tungsten, with a liquid metal reservoir attached to the filament structure on the base. For operation, the reservoir is first heated to allow flowing of the metal to the tip end. Upon applying a high negative voltage (~ -10 kV) with respect to the tip on the nearby extractor electrode, the metal in a molten state is then drawn into a conical shape known as the Taylor-Gilbert cone on top of the tip by the balance of the electrostatic and surface tension forces. Due to the high electric field (10^{10} V/m) induced at the sharp apex of the liquid metal cone ions begin to form through a quantum mechanical tunneling process known as field evaporation^[43].

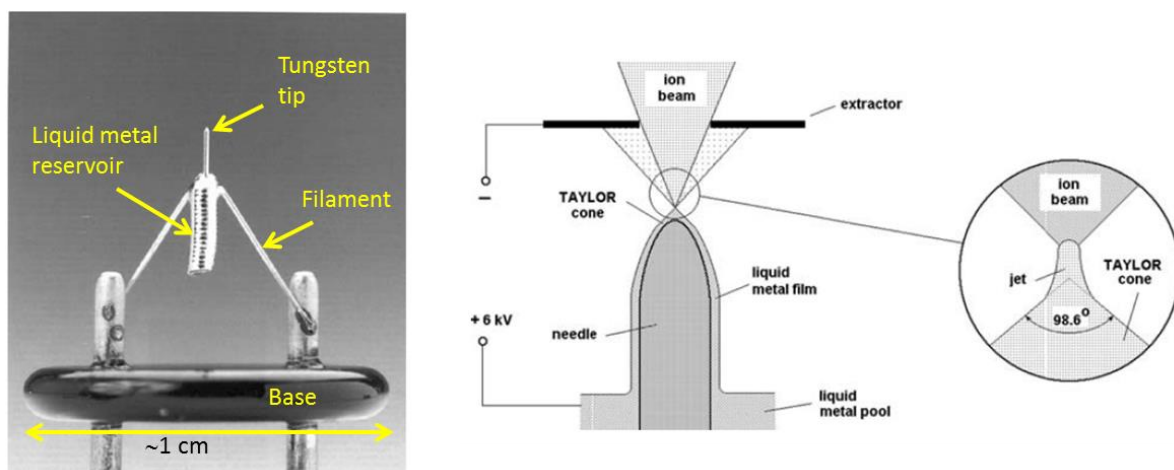


Fig. 1-12 Needle type LMIS (left) and ion emission process (right). Images adapted from Refs. [44] and [45].

The usable reservoir materials are typically metal species having a high surface tension, a low vapor pressure at its melting point, and non-volatile with the tip substrate (i.e. no corrosion). To date, a wide variety of metal species including Al, As, Au, B, Be, Bi, Cs, Cu, Ga, Ge, Fe, In, Li, Pb, P, Pd,

Si, Sn, U, and Zn have been tried and even in the form of alloys (GaAs, Au/Si, Au/Si/Be, Pd/As/B) which gives the possibility of varying ion species when used with a mass separator^[1]. However, for commercial uses Ga is irrefutably favored as its low melting point (29.8 °C) enables stable operation without heating for many hours and its low vapor pressure (<10⁻⁸ mmHg at melting point) allows long life time (>1500 hours)^[6].

The amount of current typically drawn from a Ga LMIS is about 2 μA attuned for operational stability (emission stability <2% per hour) and a flat angular distribution of the ion current but only up to tens of nA that arises from the central region of the extracted beam is used for FIB processing typically limited by the spherical aberrations of focusing optics^[6]. Although the radius of the emitting apex is believed to be 1.5-3 nm, because of the significant coulomb interactions introduced by the high total emission current close to the emission site, the ions appear to originate from a virtual source diameter of ~50 nm. The interactions are also responsible for its relatively high energy spread of ~5 eV which essentially limit the minimum probe size in a typical FIB optics setup to about 5-10 nm^[6]. Being relatively high in mass, Ga ions provide a good sputter rate (0.05-0.7 μm³/nC for 25 keV Ga⁺), hence the Ga-LMIS has been predominately used for nanofabrication purposes, however, being a metallic species, Ga ions can induce contamination leading to changes in electrical, magnetic, and optical properties of the sample.

1.2.2 Gas Field Ionization Source (GFIS)

The GFIS is similar to the LMIS in that the ionization is induced by the application of a high-potential electric field created from placing a sharp tip structure (a field emitter) close to an extractor electrode but operationally very different as the ionizing atoms are gaseous rather than molten metals coated the tip surface. In GFIS, neutral gas atoms or molecules are attracted to the positively biased tip end by polarization forces and the ions are formed by field ionization^[6, 46] in which an electron from the gas atom tunnels to the field emitter. Furthermore, the field emitter is typically maintained at a cryogenic temperature (<77 K) to enhance the density of atoms in the high field region and to decrease the thermal motion (energy) of the atoms/ions via thermal accommodation. The ions, accelerated away from the tip by a high electric field (~10¹⁰ V/m) with a negligible de Broglie wavelength and transverse velocities, appear to originate from a very small virtual source size (<1 nm) with good beam parallelism, which eventually gives rise to very high beam brightness (>10⁹ A/m²srV). It's been claimed that a nanometric protrusion (aka 'super tip') formed on a regular tip after special geometric manipulation can yield a reduced brightness reaching ~10¹¹ A/m²srV^[47].

To avoid secondary scattering processes (i.e. the charge transfer) the source is generally forced to operate at a low background gas pressure (0.01- 1 mtorr). This generally limits the maximum current output of a GFIS to ~10-20 pA but this is an advantage in terms of minimizing the coulomb interactions. Because of the exponential dependence of the tunneling process on the electric field, stable tip geometry and controlling temperature fluctuations and gas impurities are critical for the emission stability and the source lifetime.

Despite the GFIS development^[48, 49] for FIB applications preceding the LMIS, the commercialization of the technology didn't materialize until recently due to technical difficulties in improving the reliability of the source. In 2006, a FIB system incorporating a He-based GFIS was introduced by ALIS and it has demonstrated sub-1 nm probe size. The inert and light ion species,

high reduced beam brightness ($2 \times 10^9 \text{ A/m}^2\text{srV}$), and low dE ($< 1 \text{ eV}$) characteristics of the He-GFIS can provide exceptional imaging resolution with marginal sample damage and contamination although its low sputtering rate and low probe current ($< 20 \text{ pA}$) are found to be inadequate for FIB machining applications. The success is mainly attributed to the development of a proprietary process which produces a pyramidal apex ending in three atoms, known as the 'trimer', at the end of a round tungsten tip as shown Fig 1-13. The atomically sharp apex provides field enhancement that localizes the gas ionization only near the trimer. The pyramidal shape is also found to be stable for providing short term emission stability better than 1% during high resolution image acquisition (\sim minutes) and the fact that the trimer can be repeatedly renewed (*in situ* in a matter of few minutes) allows a long term use (\sim many months) of a single source^[50].

To extend the use of GFIS to FIB machining applications, gases other than He have been tried but the success has been very limited so far. Helium is the best suited for the GFIS technology because it has the highest ionization energy of all elements and requires a relatively high electric field strength ($\sim 4.4 \text{ V/\AA}$) to ionize. The high electric field strength tends to ionize any gas impurities before reaching the tip, which helps preserving the emission sites. Given that the GFIS is based on atomic emission, any adsorption of impurities can abruptly terminate the emission causing beam instability. Currently GFIS using Ne (which has the second highest ionization energy) is being actively developed^[31, 51] but at the moment the long term operation is limited to only ~ 10 hours^[52]. The general consensus is that gases other than He and Ne would not be practical for commercial GFIS.^[31, 51]

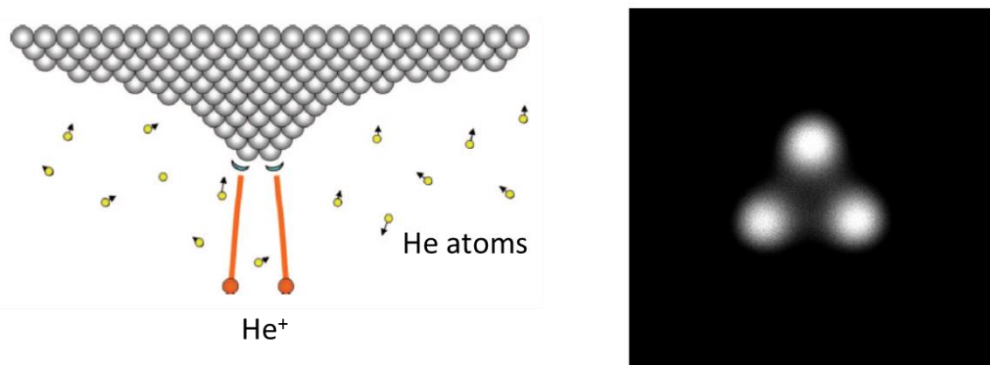


Fig. 1-13 (Left) Illustration showing a pyramidal apex built on a tungsten tip. Due to field enhancement, He atoms predominantly become ionized near the apex. (Right) emission pattern from the trimer. During operation, the emission from a single atom is simply selected by using an aperture. Adapted from Ref. [50].

1.3 About this thesis

As discussed above, modern FIB machines are versatile and widespread instruments integral to various applications involving inspection and both removal and deposition of materials at the nanometer scale. Because their functionalities are directly dependent on the ion-matter interactions, for addressing small features effectively, the FIB machines must be able to provide sufficiently small ion probes with high current. Moreover, in the application point of view, given the

current industry trend of ever increasing complexity and diversity in the materials being processed and requiring higher sensitivity in dimensional and contamination control as well as high throughput, it is highly desired that FIB instruments to also provide a wide spectrum of ion species, preferably selectable based on the application requirements. The LMIS and the GFIS, the most advanced ion sources available for the commercial FIB machines today, are capable of meeting the stringent FIB optical performance, lifetime, and reliability requirements but only for a few specific ion species due to the fundamental limitations in the ionization mechanisms that they rely on.

It's the aim of this PhD research work to develop an alternate ion source equally impressive in terms of the beam brightness, energy spread, and general usability as the current state-of-the-art FIB sources but also with flexibility to deliver a wide variety of ion species, ranging from low to high in mass, inert and reactive, and all selectable *in situ*. The new source, named 'Nano-Aperture Ion Source' or 'NAIS' for short in this thesis, is based on the novel concept originally proposed by Kruit and Tondare^[53,54]. It utilizes the direct electron impact gas ionization scheme, which is already a widely used and proven technique for producing a variety of ion species, but departing from the conventional designs using this technique, the proposed source is configured with a high performance Schottky electron focusing column and a miniaturized gas chamber in order to fully optimize the source performance suitable for FIB applications. The rest of this thesis is dedicated to describe all the research activities and presents the results achieved in developing the new source. Table 1-4 lists key source parameters that we expect from the NAIS.

Table 1.4 Target performance of the NAIS compared to the current state-of-the-art FIB sources.

	Current state-of-the-art FIB sources		Expected for Ar NAIS
	Ga LMIS [6]	He GFIS [23,50]	
Ionization mechanism	Field evaporation	Gas field ionization	Direct electron impact gas ionization
Max. B_r (A/m^2SrV)	$\sim 10^6$	$\sim 10^9$	$\sim 10^7$
dE (eV _{FWHM})	5-10	< 1	< 1
Max. Probe current (nA)	$\sim 20-50$	~ 0.02	~ 1
Compatible ion species	Al, Au, Be, Si, Pd, B, P, As, Ni, Sb	Ne	H, He, Ne, Kr, Xe, O, virtually any gas

The thesis is organized as follows:

After a brief review of the FIB technology and high brightness ion sources in this introductory chapter, Chapter 2 discusses our novel approach utilizing the conventional electron impact gas ionization scheme to develop a competitive ion source for high resolution FIB applications. The basic concept and design of the new ion source are presented and the fundamental source properties roughly estimated based on the ideal gas chamber conditions and the performance of the existing Schottky electron gun technology are also given. In Chapter 3, the performance of the new ion source is further investigated in detail through numerical simulations. First, gas simulations using the Monte Carlo technique are performed to understand the gas particle density distribution in the

interaction region of the gas chamber and then incorporating the gas simulation results, ion trajectory simulations are performed to calculate the achievable beam current, ion energy distribution, and the reduced brightness of the ion beam arising from the gas chamber. The gas chamber conditions are systematically varied to optimize the ion source performance. Chapter 4 summarizes our development efforts in fabricating the miniaturized gas chambers for the new ion source. Two different gas chamber designs are investigated and detailed fabrication methods and the results of the prototype build are presented. A great deal of time during this research had been dedicated to laboratory work on constructing experimental setups and characterizing the ion beams arising from the prototype miniaturized gas chamber. The description of the experiments and the results are presented in Chapter 5. Although the main scope of this PhD research is to develop an ion source, at the end, the source is intended to be used in a focused ion beam system. Its true performance should be measured and verified in an actual FIB system. In Chapter 6, design details of integrating a prototype NAIS in a commercial FIB column and expected column performance are discussed.

The core of this thesis is based on the following scientific papers:

1. D. S. Jun, V. G. Kutchoukov, and P. Kruit, Ion beams in SEM: an experiment towards a high brightness low energy spread electron impact gas ion source, *J. Vac. Sci. Technol. B* **29** (2011) 06F603-1
2. D. S. Jun, V. G. Kutchoukov, C. T. H. Heerkens, and P. Kruit, Design and fabrication of a miniaturized gas ionization chamber for production of high quality ion beams, *Microelectron. Eng.* (2012), <http://dx.doi.org/10.1016/j.mee.2012.03.024>
3. D. S. Jun and P. Kruit, Proof-of-concept experiments for the Nano-Aperture Ion Source, to be submitted
4. D. S. Jun and P. Kruit, Simulated source performance of the Nano-Aperture Ion Source, to be submitted

References

- [1] J. Melngailis, Critical review: Focused ion beam technology and applications, *J. Vac. Sci. Technol. B* **5** (2), 469 (1987)
- [2] S. Reyntjens, R. Puers, A review of focused ion beam applications in microsystem technology, *J. Micromech. Microeng.* **11** (2001)
- [3] A. A. Tseng, Recent developments in micromilling using focused ion beam technology, *J. Micromech. Microeng.* **14** (2004)
- [4] C. A. Volkert and A. M. Minor, Focused ion beam microscopy and micromachining. *MRS Bulletin*, 32, 389-399, (2007)
- [5] J. Gierak, Focused ion beam technology and ultimate applications, *Semicond. Sci. Technol.* **24** (2009)
- [6] J. Orloff, M. Utlaut, L. Swanson, *High Resolution Focused Ion Beams: FIB and its applications*, (Kluwer Academic/Plenum Publishers, New York 2003)
- [7] L. A. Giannuzzi and F. A. Stevie, *Introduction to Focused Ion Beams: Instrumentation, Theory, Techniques and Practice* (Springer, New York, 2005)
- [8] V. N. Tondare, Quest for high brightness, monochromatic noble gas ion sources, *J. Vac. Sci. Technol. A* **23**, 1498 (2005)
- [9] P. Sigmund, Theory of sputtering I: sputtering yield of amorphous and polycrystalline targets, *Phys. Rev.*, 184(2), (1969)
- [10] J. F. Zeigler, J. P. Biersack, and U. Littmark, *The Stopping and Range of Ions in Solids* (Pergamon, New York, 1984), Vol. 1
- [11] www.SRIM.org
- [12] S. Tan, R. Livengood, D. Shima, J. Notte, and S. McVey, Gas field ion source and liquid metal ion source charged particle material interaction study for semiconductor nanomachining applications, *J. Vac. Sci. Technol. B* **28**, C6F15 (2010)
- [13] D. J. Maas and R. van Gastel, Helium ion microscopy, *Springer Series in Surface Sciences* Vol. 51, 461-497, (2013)
- [14] D. Joy, Multi-beam ion microscopy, *Microscopy Today*, Vol. 20, Issue 05, 10-15, (2012)
- [15] I. Utke, P. Hoffmann, and J. Melngailis, Gas-assisted focused electron and ion beam processing and fabrication, *J. Vac. Sci. Technol. B* **26**, 1197 (2008)
- [16] K. Ohya and T. Ishitani. "Imaging using electrons and ion beams", in *Focused Ion Beams Systems, Basic and Applications*, ed. N. Yao, Cambridge University Press, 2007, chap. 4.
- [17] Baragiola, R. A. Principles and mechanisms of ion induced electron emission, *Nucl. Instr. and Meth. in Phys. Res. B* **78**, 223 (1993).
- [18] J. Morgan, J. Notte, R. Hill, B. Ward, An introduction to the helium ion microscope, *Microscopy Today*, Vol. 14, No 4, (2006)
- [19] J. Li, Focused ion beam microscope, *Journal of Metl*, Vol. **58**, No. 3, 27-31 (2006)
- [20] V. Castaldo, High resolution scanning ion microscopy, PhD thesis, Delft University of Technology, 2011
- [21] P. Sudraud, G. Ben Assayag, and M. Bon, Focused-ion-beam milling, scanning-electron microscopy, and focused-droplet deposition in a single microcircuit surgery tool, *J. Vac. Sci. Technol. B* **6**, 234 (1988)
- [22] Carl Zeiss press release, Nov. 21, 2008, www.zeiss.com

- [23] R. Hill, F. H. M. Faridur Rahman, Advances in helium ion microscopy, Nucl. Instrum. Methods A **645**, 96-101 (2011)
- [24] J. Casey, M. Phaneuf, C. Chandler, M. Megorden, and K. Noll, Copper device editing: Strategy for focused ion beam milling of copper, J. Vac. Sci. Technol. B **20**, 2682 (2002)
- [25] Y. Drezner, Y. Greenzweig, and A. Raveh, Strategy for focused ion beam compound material removal for circuit editing, J. Vac. Sci. Technol. B **30**, 011207 (2012)
- [26] D. Niles, R. W. Kee, and C. Rue, Full-thickness backside circuit editing for ASICS on laminated packages, JMEPEG **19**, 819 (2010)
- [27] T. Liu, C. Chen, S. Liu, M. Chang, and J. Lin, Innovative methodologies of circuit edit by focused ion beam on wafer-level chip-scale-package devices, J. Mater. Sci: Mater. Electron, Vol. **22**, 1536 (2011)
- [28] P. Gounet, M. Mercier, and D. Serre, Failure analysis of Through-Silicon-Vias aided by high-speed FIB silicon removal, Proceedings of 16th IPFA, pp 94-99 (2009)
- [29] M. Abramo, N. Antoniou, D. L. Barton, K. N. Hooghan, and R. H. Livengood, FIB backside isolation techniques, Microelectronics Failure Analysis Desk Reference, Supplement, p1 (2001)
- [30] R. Livengood, S. Tan, P. Hack, M. Kane, and Y. Greenzweig, Focused ion beam circuit edit-a look into the past, present, and future, Microscopy and Microanalysis, Vol. **17**, S2, 672-673, (2001)
- [31] R. Livengood, S. Tan, R. Hallstein, J. Notte, S. McVey, and F. Faridur Rahman, The neon gas field ion source-a first characterization of neon nanomachining properties, Nucl. Instrum. Meth. Phys. Res. A, Vol. **645**, No. 1, pp.136-140 (2011)
- [32] J. E. Barth and P. Kruit, Addition of different contributions to the charged particle probe size, Optik. **101(3)**. 101 (1996)
- [33] P. Kruit, M. Bezuijen and J. E. Barth, Source brightness and useful beam current of carbon nanotubes and other very small emitters, J. Appl. Phys., **99**, 024315 (2006)
- [34] G. H. Jansen, *Coulomb Interactions in Particle Beams*, Advances in Electronics and Electron Physics, suppl. 21 (Academic Press, London, 1991)
- [35] P. Kruit and G. H. Jansen, in *Handbook of Charged Particle Optics* (First Edition), edited by J. Orloff, (CRC Press, New York, 1997), Chapter 7
- [36] X. Jiang and P. Kruit, Comparison between different imaging modes in focused ion beam instruments, Microelectron. Eng. **30**, p 249 (1996)
- [37] M. Rauscher and E. Plies, Impact of Coulomb interactions on the performance of a low energy focused ion beam system, J. Appl. Phys., **97**, 064908 (2005)
- [38] C. W Hagen, E. Fokkema, and P. Kruit, Brightness measurements of a gallium liquid metal ion source, J. Vac. Sci. Technol. B **26**, 2091 (2008)
- [39] W. Knauer, Energy broadening in field emitted electron and ion beams, Optik **59**, 335 (1981)
- [40] V. E. Krohn, Liquid metal droplets for heavy particle propulsion, ARS Electrostatic Propulsion Conference, Monterey, CA, Vol. 3-4, 1960
- [41] V. E. Krohn and G. R. Ringo, Ion source of high brightness using liquid metal, Appl. Phys. Lett. **29**, 479, (1974)
- [42] R. L. Seliger, J. W. Ward, V. Wang, and R. L. Kubena, A high-intensity scanning ion probe with submicrometer spot size, Appl. Phys. Lett. **34**, 310 (1979)
- [43] L. C. Wang and H. J. Kreuzer, Kinetic theory of field evaporation of metals, Surface Science, Vol. **237**, 337 (1990)

- [44] S. K. Guharay, J. Orloff, and M. Wada, Ion beams and their applications in high-resolution probe formation, *IEEE Transactions on Plasma Science*, Vol. **33**, 1911-1930,(2005)
- [45] J. A. Eichmeier, M. K. Thumm (Eds.), *Vacuum Electronics Components and Devices*, (Springer 2008)
- [46] R. G. Forbes, in *Handbook of Charged Particle Optics* (2nd Edition), edited by J. Orloff, (CRC Press, New York, 2008), Chapter 3
- [47] S. Kalbitzer, Bright ion beams for the nuclear microprobe, *Nucl. Instrum. Meth. Phys. Res. B* **158**, 53 (1993)
- [48] J. Orloff and L. W. Swanson, Study of a field-ionization source for microprobe applications, *J. Vac. Sci. Technol.* **12**, 1209 (1975)
- [49] R. Levi-Setti, Proton scanning microscopy: feasibility and promise, *Scanning Electron Microscopy*, 125 (1974)
- [50] B. Ward, J. A. Notte, and N. P. Economou, Helium ion microscope: A new tool for nanoscale microscopy and metrology. *J. Vac. Sci. Technol. B*, **24**(6) (2006)
- [51] F. H. M. Rahman, S. McVey, L. Farkas, J. A. Notte, S. Tan, The prospects of a subnanometer focused neon ion beam, *Scanning* Vol. 33, 1-6 (2011)
- [52] J. Notte, F. H. M. Rahman, S. M. McVey, S. Tan, R. Livengood, *Microsc. Microanal.* 16 (Suppl. 2), 28 (2010)
- [53] P. Kruit and V. N. Tondare, Particle-optical apparatus equipped with a gas ion source, European Patent 06220357.0
- [54] V. N. Tondare, Towards a high brightness, monochromatic electron impact gas ion source, PhD thesis, Delft University of Technology, 2006

2 ■ The Concept of Nano-Aperture Ion Source (NAIS)

For high resolution FIB processing, an ion source with high brightness and low energy spread is essential. In many FIB applications, it is also desired that a variety of ion species to be available and selectable *in situ* to optimize for ion imaging, milling, and deposition, all without changing the source. In this chapter, an ion source that is capable of meeting all these requirements is proposed. The Nano-Aperture Ion Source (NAIS), named after the unique physical feature incorporated in the gas chamber design, is a gas ion source based on the widespread electron impact ionization technique. However, unlike the conventional electron impact gas ion sources, the new source is fitted with a miniaturized gas chamber and a Schottky electron gun to produce high ion current from a small ionization volume. General descriptions on the source construction and the mechanism of operation are presented and then potential source properties are estimated considering the electron impact ionization characteristics of rarefied gases and the performance of the existing Schottky electron gun technology.

2.1 Introduction

Focused Ion Beam (FIB) systems have been indispensable tools in the semiconductor industry, materials science, and many research and applications fields of the nanotechnology sectors because they can image and manipulate nanometer-scaled structures. Similar to Scanning Electron Microscopes (SEMs), FIB systems can provide imaging capability using secondary electron signals from the sample but in addition to providing a larger depth of focus and an alternative contrast mechanism using secondary ion signals, the FIB system offers an unparalleled capability of removing materials in the nanometer scale. Some of the key applications of the FIB systems utilizing this unique capability include mask repairs, TEM sample preparations, IC failure analysis, defect characterization, and device modification ^[1].

Since the early 1980's, gallium based liquid metal ion sources (Ga LMIS) have been the standard for commercial FIB systems because of their reliable operation with high reduced brightness ($\sim 1 \times 10^6$ A/m²srV), good current stability ($< \pm 2$ % on a minute scale), and long life time (~ 400 μ A-hours/mg) ^[1-3]. However, the inherent destructive nature of the gallium ions inevitably results in sample modification making it undesirable for high resolution imaging and inspection applications. Additionally, the gallium LMIS has a relatively high energy spread of 5-10 eV limiting the minimum probe size of the Ga FIB system to be about 10 nm at 30 keV ^[1,3]. Furthermore, its chemical activity and staining can lead to changes in electrical and magnetic performance, material crystalline change, and chemistry changes in samples. ^[1]

As the dimensions of the chip components continue to shrink and the demand for more advanced tools to image and manipulate the materials to the atomic scale increases, there has been a growing interest in improving the performance of the FIB systems by developing an ion source with high brightness, low energy spread combined with operation with a broad range of noble ion species and ion currents. Over the course of the past decade, a number of research efforts have emerged to develop non-contaminating FIB source using various methods such as plasma ^[5-7], laser photoionization ^[8-11], and gas field ionization ^[12-14] techniques. Unfortunately some fundamental problems exist in each of these techniques and so far none of these sources is posed to replace the current state-of-the-art Ga LMIS in the commercial FIB systems. Conventional plasma sources have shown to provide reliable production of a variety of noble ion species but their inherent high temperature operation yields a relatively low reduced brightness to compete against the LMIS. Some progress has been achieved in developing a laser ion source using magneto-optical trap (MOT) but researchers are currently facing a difficulty in achieving high brightness. It's speculated that the loss in brightness comes from an increase in the transverse temperature of the ion beam from coulomb forces while being extracted in the ionization volume ^[9,11]. The relatively slow loading rate of the MOT, which eventually limits the extractable current (~ 160 pA for chromium ion beam ^[11]) and its complicated aligning and tuning of laser beams to trap and photo-ionize gas atoms raise some practical concerns. Recently the helium ion microscope based on gas field ionization source (GFIS) from Zeiss has sparked a new interest in ion microscopy. With its light mass and high brightness from gas field ionization, the helium microscope offers exceptional imaging quality but so far the gas species is limited to only helium for reliable operation. With a usable beam current of 1 fA-100 pA and light ion, however, it's inadequate for an effective sputtering tool. The development of a GFIS using heavier gas such as Neon has turned out to be technically difficult due to emission instability and short life time associated with the ionizing gas having a lower ionization energy compared to typical impurities found in the source region ^[13, 14].

The next generation ion source for the commercial FIB systems should provide uncompromising performance over all of the fundamental and practical source properties, namely the reduced brightness, energy spread, noise, beam stability, lifetime, and reliability, at least comparable to what the current Ga LMIS offer, while providing a variety of ion species that can be chosen for a specific application without time-consuming modifications (i.e. breaking high vacuum) on the tools. In the following, a novel ion source based on electron impact gas ionization intended to meet all of these requirements is presented.

2.2 Electron impact ionization

Electron impact ionization is an elementary process of charged particles involving the transfer of potential energy to an atom during inelastic collision with a moving electron, leading to the conversion of a neutral atom or molecule into an ion (Fig. 2-1). For the ionization to occur, the impact electrons must have an energy exceeding the target atom's ionization energy (eV_i). Key advantages in this technique are the fact that virtually any gas can be used to produce ions and the design can be kept relatively simple at the minimum requiring only a stream of energetic electrons and a gas source. For these reasons electron impact gas ionization is commonly employed in many ion sources used in a variety of applications including secondary ion mass spectrometry, ion implantation, ion lithography, material sputtering, and even accelerator injection and fusion.

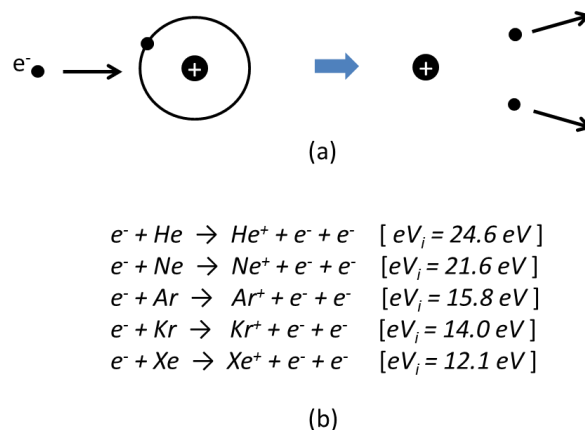


Fig. 2-1 (a) Production of a positive ion by electron impact and (b) ionization energies (eV_i) of noble gases.

An elementary ion source design^[15] utilizing direct electron impact scheme is shown Fig. 2-2. In this design electrons are supplied by two heated tungsten filaments and accelerated towards the anode made of a stainless steel tube of 10 mm inner diameter. A gas is injected axially into the ionization region via a stainless steel capillary (0.1 mm inner diameter) and is ionized by the electrons entered through the entrance apertures of the anode. The use of the capillary somewhat reduces the dimensions of the ionization region (the pressure falls quadratically with the distance from the capillary), thus relatively low energy spread ($< 1 \text{ eV}$) can be achieved but this also means generally low gas density available in the interaction region. Moreover, with the crude design of which the shape and size of the electron beam only mildly optimized by the electron repeller, this

source yields a very low rate of electron-neutral collisions, which leads to a reduced source brightness only reaching $\sim 1 \text{ A/m}^2\text{srV}$.

A much more elaborate design aiming for higher reduced source brightness by providing a higher impact electron current density has been proposed by Barth *et al.* [16]. The design, shown in Fig. 2-2, also utilizes gas effusion from a small aperture to keep the interaction region restricted to dimensions of a few μm but a fairly high electron current is provided into the interaction region using thermionic emission based 2π electron gun and an intricate magnetic mirror system. With the possible impact electron current reaching 1 mA, the authors concluded that the ion source is capable of providing a reduced brightness up to $10^4 \text{ A/m}^2\text{srV}$ although it has never been verified.

It should be pointed out that many plasma ion sources, which essentially rely on electron impact gas ionization for igniting and sustaining the plasma, are widely available and generally offer improved performance in terms of the current output and the beam brightness when compared to the conventional direct electron impact ion sources. In fact, RF plasma sources [7, 17-19] have been successfully adapted to FIB systems for processes requiring fast material removal with micro-beam resolution (i.e. Through Silicon Via (TSV) and flip chip cross sectioning). With probe currents available up to a few microamperes compared to tens of nanoamperes for Ga LMIS equipped FIB, the Xe plasma FIBs have demonstrated a significant throughput increase by a factor of 20 to 100 times compared to the processing speed achieved with conventional Ga^+ ion beams. However, adverse effects from generally high (elevated) ion temperature, modulation in the plasma potential, and inherent coulomb interactions typically limit the reduced source brightness of plasma sources to $\sim 10^4 \text{ A/m}^2\text{srV}$ and the energy spread above 5 eV, inadequate for sub-10 nm high resolution FIB processing.

Considering the simplicity and reliability in the production of ions from any gas, room temperature operation which extends benefits of much easier operation and adaptation to FIB systems, plus the low energy spread capability, the non-plasma mode, direct electron impact gas ion sources look very appealing and practical for FIB implementation, however, as noted with the two prior arts above, significant improvement in the source reduced brightness must take place.

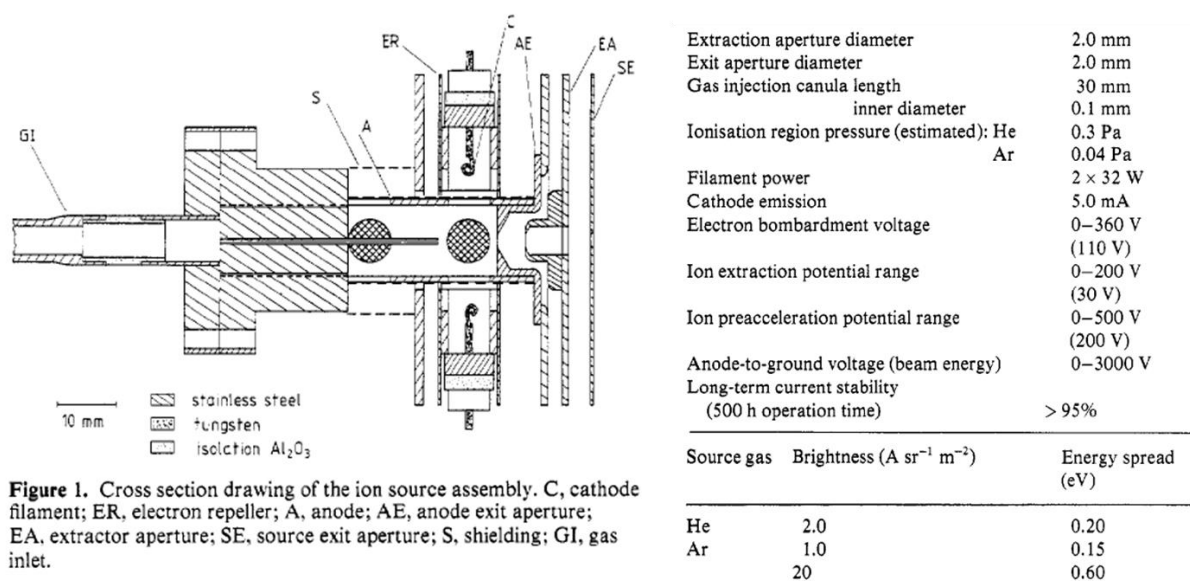


Fig. 2-2 A direct electron impact gas ion source developed by Barthels *et al.* [15].

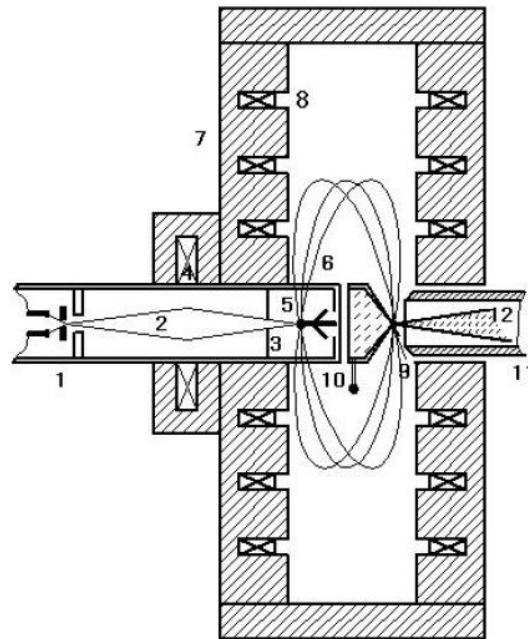


Fig. 2-3 A high brightness direct electron impact gas ion source design proposed by Barth *et al.* ^[16]. An electron beam (2) from a conventional electron gun (1) is focused through an aperture (3) using a magnetic lens (4) onto a tungsten sphere (5). With the magnetic mirror-lens system (7, 8), the thermionic electrons from the sphere (6) are accelerated and focused into the gas (9) effusing from the chamber (10) and ionize. Ions (12) are accelerated by the electrode (11).

2.3 Nano-Aperture Ion Source (NAIS)

2.3.1 The source concept

NAIS relies on a small volume based direct electron impact gas ionization similar to the two prior arts discussed in the previous section but instead of gas effusion, it utilizes trapped gas in a miniaturized gas chamber. Fig. 2-4 describes the components and illustrates the concept of our source in its most simplistic view. Essentially, the ion source is comprised of a sub-micron scaled gas chamber and an electron gun. Our preferred electron gun is equipped with a Schottky emitter because along with its reliability, it's known for high brightness that can provide a stable high current (>100 nA) focused to a small probe size (<100 nm). The gas chamber can be viewed as a pair of two thin parallel conductive membranes separated by a spacing l . The membranes are electrically isolated by a thin layer of an insulator (PMMA, Si_3N_4 , SiO_2 , etc.). A small bias voltage between the membranes is applied to extract the ions. A pair of small apertures (aka the double-aperture) is placed on the stacked membranes by a FIB so that electrons can enter from one aperture and ions can exit out of the other along with the unscattered electrons. The transmitted electrons are repelled while the ions are further accelerated by an ion accelerator placed downstream from the gas chamber. Ideally, the apertures should be kept as small as possible to minimize the neutral gas

atoms to escape but also need to be carefully selected to maximize the input electron current and the output ion current.

The miniaturization of the gas chamber is necessary because the ionization volume needs to be kept small to provide a small virtual source size thus yielding high brightness. Another reason is that in order to minimize the loss in brightness due to ion-ion interactions inside the gas chamber, a high electric field is needed for quick extraction of the ions, but at the same time, a low bias voltage is preferred in order to keep the ion energy distribution low. In order to satisfy these conditions, the gas chamber spacing needs to be as small as possible.

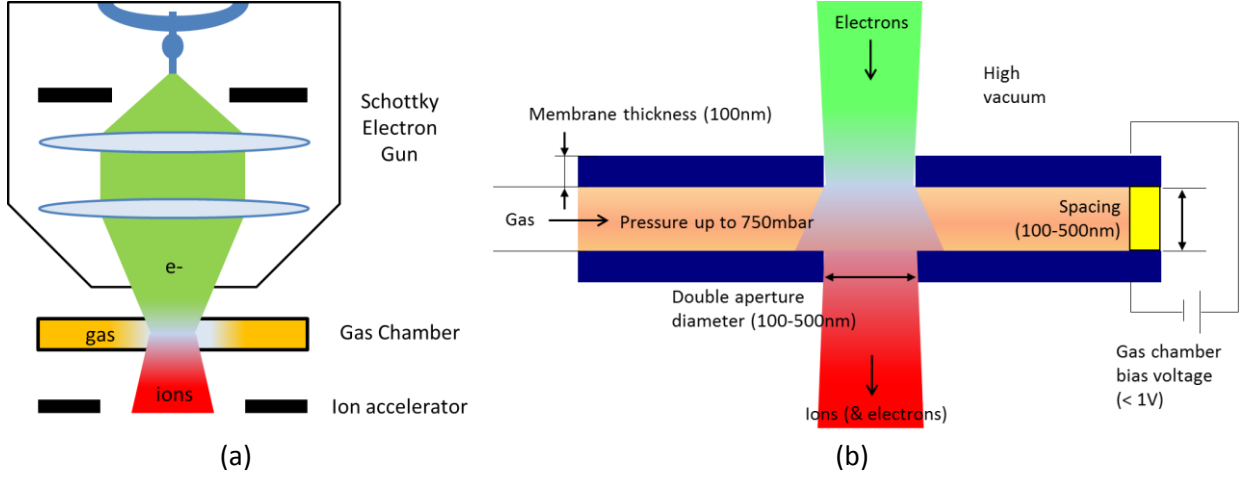


Fig. 2-4 (a) Schematic of NAIS and (b) target gas chamber dimensions.

2.3.2 Electron impact gas ionization in a dilute gas

Considering the gas atoms as rigid spheres and the energetic electrons of density n_e moving in the z -direction through a dilute gas of density n_o (Fig 2-5), the number of collisions per unit volume dn_e occurring between the incident electrons and gas atoms of electron impact ionization cross section $\sigma(X)$ within a distance dz is given by

$$dn_e = -n_o n_e \sigma(X) dz \quad (2.1)$$

The total number of collisions per unit volume occurring over a distance l is then

$$\int_{n_e(z=0)}^{n_e(z=l)} \frac{dn_e}{n_e} = -\int_0^l n_o \sigma(X) dz,$$

which reduces to

$$n_{e(z=l)} = n_e e^{-n_o \sigma(X) l} \quad (2.2)$$

where $n_{e(z=0)}$ and $n_{e(z=l)}$ are the densities of electrons at $z=0$ and $z=l$, respectively.

Since the quantity $\sigma(X)$ is relatively small (i.e. very few incident electrons collide with neutrals), Eq. 2.2 can be approximated to

$$n_{e(z=l)} = n_e (1 - n_o \sigma(X) l) \quad (2.3)$$

Further rearranging and conveniently expressing Eq. 2.3 in terms of the number of ions produced N_i [$=N_e - N_{e(z=l)}$] from the total of incident electrons N_e instead of the densities n_e and $n_{e(z=l)}$ gives:

$$\frac{N_i}{N_e} = n_o \sigma(X) l \quad (2.4)$$

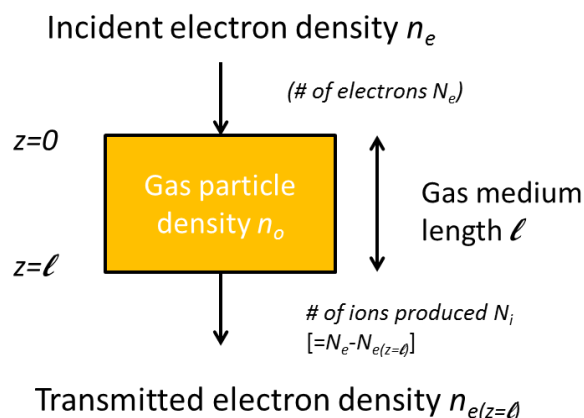


Fig. 2-5 Electron impact ionization in a dilute gas.

2.3.3 Theoretical source performance

Ion production inside the gas chamber

Ideally the new ion source is operated in the dilute gas situation such that the mean free path λ of gas atoms is about equal to the characteristic length of the gas chamber (i.e. gas chamber spacing l). In other words, the gas pressure near the ionization volume inside the gas chamber is preferably kept at the upper limit of the molecular gas flow regime (Knudsen number $K_n = \lambda/l = 1$) so that a maximum number of ions can be produced while preventing ion-neutral and ion-ion interactions which could reduce the source brightness. For $\lambda=l$, Eq. 2.4 can be re-written as

$$\frac{N_i(X)}{N_e} = \frac{\sigma(X)}{\sqrt{2}\pi d^2} \quad (2.5)$$

where d is the molecular diameter of a given gas atom. Since the ion current is proportional to the number of ions $N_i(X)$ and the electron current the number of electrons N_e the right hand side of Eq. 2.5 represents the maximum ionization efficiency provided that the gas pressure inside the gas chamber is kept in the molecular flow regime. For Argon gas, $d=0.369$ nm^[20] and $\sigma(Ar^+)=0.783 \times 10^{-20}$ m²^[21] for 1 keV incident electron energy, the maximum ion current produced inside the gas chamber is expected to be approximately 1.3 % of the input electron current. Estimated ionization efficiencies for other noble gas ion species are listed in Table 2-1.

Table 2-1 Ionization efficiencies for noble gas ion species assuming $\lambda=l$. Molecular diameters from Ref [20] and ionization cross sections from Ref [21, 22]

	Molecular diameter d (nm)	Ionization cross section at 1 keV ($\times 10^{-16}$ cm ²)	Ionization efficiency (%)
Ions	He ⁺	0.22	0.124
	Ne ⁺	0.255	0.321
	Ar ⁺	0.369	0.783
	Kr ⁺	0.427	0.984
	Xe ⁺	0.487	1.21

Theoretical source reduced brightness (B_r)

For charged particle beams the reduced brightness B_r is defined as the amount of current emitted from a source per unit area per unit solid angle normalized by the beam acceleration potential V . This definition is also equivalent to:

$$B_r = \frac{J}{\Omega V} \approx \frac{J}{\pi \alpha^2 V} \quad (2.6)$$

where J is the current density and Ω is the solid angle enclosing all the rays that emerge with a small beam half angle α from the source.

Under the assumption that the velocity distribution of the emitted particles emerging is semi-Maxwellian, Langmuir^[23] showed that the theoretical maximum current density J_{max} of a thermionic source can be expressed as

$$J_{max} = \frac{eV}{kT} \sin^2 \alpha \quad (2.7)$$

where e is the electric charge, k is the Boltzmann's constant, and T is the cathode temperature.

Using Eqs. 2.6 and 2.7 and assuming a small beam half angle ($\sin \alpha \sim \alpha$), the maximum reduced brightness of the NAIS that can be achieved with an average current density J_i is then

$$B_r = \frac{eJ_i}{\pi kT} \quad (2.8)$$

For the NAIS the ions can only form at the plane of contact with the electron beam area and for a very narrow gas chamber spacing the ion current density is directly proportional to the electron current density but differed by a factor of the right hand side of Eq. 2.5. In this case, Eq. 2.8 can be simplified to

$$B_r \approx 2.84 \frac{\sigma(X)J_e}{d^2} \quad (2.9)$$

for the reduced brightness unit in A/m^2srV , $T=293$ K, and the mean free path of the gas atoms matched to the gas chamber spacing ($\lambda =l$). It's clear from Eq. 2.9 that for maximizing reduced source brightness it's critical to provide the highest input electron current density as possible. However, because both ionization cross section (Fig. 2-8) and the electron current density are dependent on the electron energy, first, a careful examination on the achievable probe current density as a function of beam energy for an electron gun equipped with a Schottky emitter is necessary and thereafter an electron energy that compromises between the ionization cross section and the electron current density to maximize the reduced brightness can be determined.

For minimizing the spot size for a given amount of the probe current, an intricate balancing between the object angle and image angle of an electron gun is necessary under various conditions. In Ref [24] Kruit *et al.* have provided simple analytical equations to estimate four different regimes: (1) the chromatic aberration C_c of the probe lens dominates a system, (2) the spherical aberration C_s of the probe lens dominate, (3) the brightness does not play role but the chromatic aberration of the gun lens needs to be balanced with the chromatic aberration of the probe lens, and (4) the spherical aberration of the gun lens needs to be balanced with the spherical aberration of the probe lens. Following the steps provided in Ref [24], the possible current density of a gun with a Schottky emitter for the electron acceleration voltages of 100 to 1000 V are calculated and presented in Fig. 2-7. The input parameter values used for the calculation such as reduced brightness, virtual source size, angular intensity, and energy spread for typical Schottky sources and the aberration coefficients of typical gun lens are taken from Ref [25]. For the aberration coefficients C_s and C_c of the probe forming lens we have used more conservative values of 0.3 mm for 100 V and 1 mm for 1000 V and varying linearly with the acceleration voltage for the voltages in-between.

Fig. 2-8 shows the estimated reduced source brightness as a function of the incident electron energy for singly charged ion beams of helium, neon, argon, krypton, and xenon gas. The values are calculated using Eq. 2.9 with the electron current densities from Fig. 2-7 and the published partial ionization cross sections of those gases found in Ref [21, 22]. The results indicate reduced source brightness of our source can be more than an order of magnitude higher than the Ga LMIS. Note that the maximum reduced brightness arises with an incident electron energy around 300-500 eV although the ionization cross sections of these gases typically peak around 50 eV.

It should be also noted that the ionization volume is expected to be almost entirely contained inside the gas chamber. A Monte Carlo simulation study by Peatross and Meyerhofer^[26] indicates that the gas particle density outside the double-aperture is extremely small even for a higher pressure up to $l/\lambda=10$. Since the NAIS is intended to operate within the molecular flow regime, ion-ion collisions and charge transfer outside the gas chamber should be negligible having no adverse effect on the source brightness and ion energy spread.

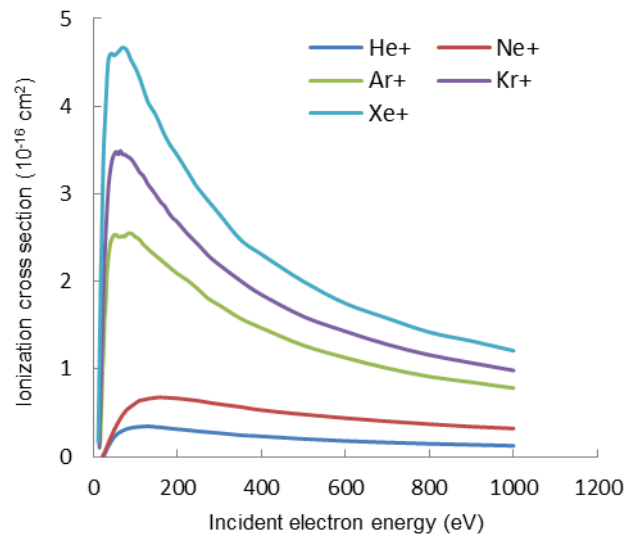


Fig. 2-6 Ionization cross section as a function of incident electron energy for He^+ , Ne^+ , Ar^+ , Kr^+ , and Xe^+ . (Data from Atomic and molecular collisions group, Rice university ^[22])

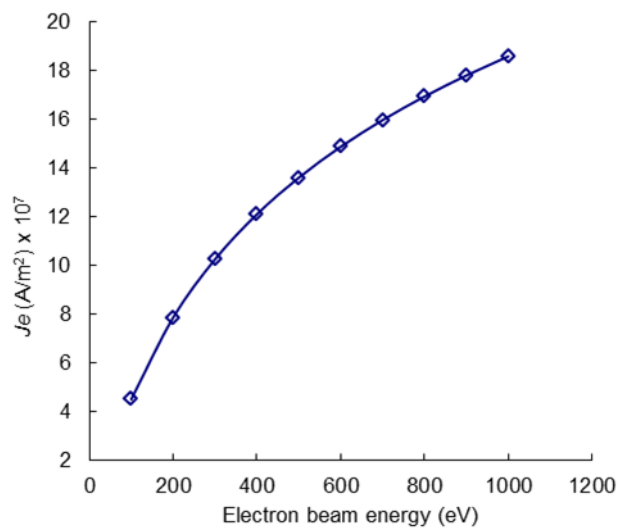


Fig. 2-7 Electron current density as a function of the beam energy for an electron gun equipped with a Schottky source.

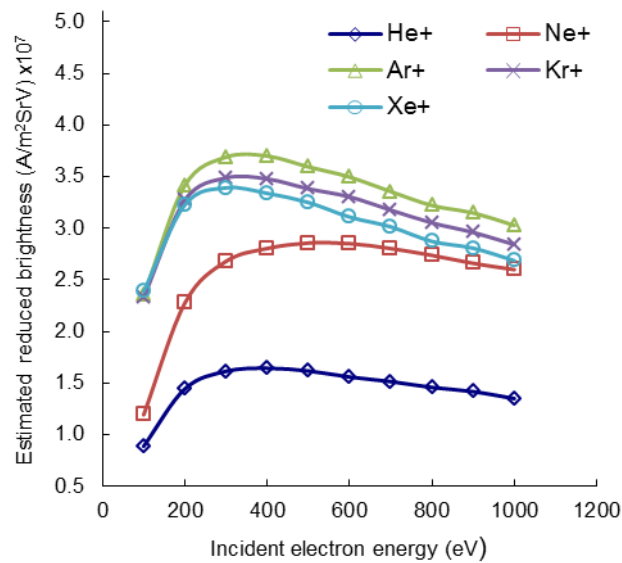


Fig. 2-8 Estimated reduced source brightness for NAIS using helium, neon, argon, krypton, and xenon gas.

Ion energy spread (dE)

For the new ion source it is preferred to have a large extraction field inside the gas chamber to reduce the ion flight time so that the probability of charge transfer and coulomb interactions caused by ion-ion collisions decrease. One attractive feature about the miniaturized gas chamber design is that even a small bias voltage can generate a relatively large field inside the gas chamber. For a spacing of 100 nm, only 0.3 V is necessary to create an e-field of $\sim 3 \times 10^6$ V/m, which is a moderate field below the threshold for field-induced breakdown over the insulating medium between the membranes. The argon ion flight time across the 100 nm spacing at such field is approximately 0.083×10^{-9} sec implying that only one ion at a time can form and exit the gas chamber for an ion current up to almost 2 nA. Under these circumstances, ion-ion coulomb interaction inside the gas chamber becomes negligible and the energy distribution would only depend on the angular spread set by the initial thermal motion of the ions at the time of ionization and the spatial distribution of the ions along the beam axis within the extraction field inside the gas chamber. Judging from the fact that the average thermal energy of gas particles at room temperature (~ 0.04 eV for argon) is much lower than the energy of a typical ion gained by the bias voltage (0.3 V for 100 nm spacing), it is anticipated that the energy spread of the new ion source is mostly governed by the gas chamber bias voltage and the magnitude approximately equal to charge e times the magnitude of the bias voltage.

2.4 Conclusions

A gas ion source suitable for both high resolution focused ion beam milling and imaging applications is proposed. The general source concept is to extract positively charged ions from a miniaturized gas chamber where neutral gas atoms become ionized by direct electron impact. To enhance gas ionization the new source incorporates a high current density electron beam from a Schottky electron gun. The use of a very small gas chamber and a very narrow electron beam (< 100 nm) allows for a very small ionization volume, which, in turn, can yield a bright ion beam from a small virtual source size with low energy spread. After considering feasible performance of the Schottky electron gun at low energies (500-1000 eV), we conclude that the NAIS can possibly provide beams of noble gas ion species with maximum ion current reaching ~ 1 nA range with a reduced source brightness exceeding 1×10^6 A/m²srV and an energy spread below 1 eV.

Acknowledgement

This research is supported by the “Stichting voor Fundamenteel Onderzoek der Materie (FOM)”, which is financially supported by the “Nederlandse Organisatie voor Wetenschappelijk Onderzoek” and FEI Company.

References

- [1] M. Utlaut, in *Handbook of Charged Particle Optics* (First Edition), edited by J. Orloff, (CRC Press, New York, 1997), Chapter 11
- [2] L. A. Giannuzzi and F. A. Stevie, *Introduction to Focused Ion Beams: Instrumentation, Theory, Techniques and Practice* (Springer, New York, 2005)
- [3] V.N. Tondare, Towards a high brightness, monochromatic electron impact gas ion source, PhD thesis, Delft University of Technology, 2006
- [4] J. Gierak, A. Septier, and C. Vieu, Design and realization of a very high-resolution FIB nanofabrication instrument, *Nucl. Instrum. Methods Phys. Res. A* **427**, 91 (1999)
- [5] L. Scipioni, D. Stewart, D. Ferranti, and A. Saxonis, Performance of multicusp plasma ion source for focused ion beam applications, *J. Vac. Sci. Technol. B* **18**, 3194 (2000)
- [6] Q. Ji, T. –J. King, K. –N. Leung, and S. B. Wilde, Production of various species of focused ion beam, *Rev. Sci. Instrum.* **73**, 822 (2002)
- [7] N. S. Smith, P. P. Tesch, N. P. Martin, and R. W. Boswell, New ion probe for next generation FIB, SIMS, and nano-ion implantation, *Microscopy Today* (2009), 17: 18-23 Cambridge University Press
- [8] J. L. Hanssen, E. A. Dakin, J. J. McClelland, and M. Jacka, Using laser-cooled atoms as a focused ion beam source, *J. Vac. Sci. Technol. B* **24**, 2907 (2006)
- [9] S.B. van der Geer, M. P. Reijnders, M. J. de Loos, E. J. D. Vredenburg, P. H. A. Mutsaers, and O. J. Luiten, Simulated performance of an ultracold ion source, *J. Appl. Phys.* **102**, 094312 (2007)

- [10] B. J. Claessens, M. P. Reijnders, G. Taban, O. J. Luiten, and E. J. D. Vredenburg, Cold electron and ion beams generated from trapped ions, *Phys. Of Plasmas* **14**, 093101 (2007)
- [11] A. V. Steele, B. Knuffman, J. J. McClelland, and J. Orloff, Focused chromium ion beam, *J. Vac. Sci. Technol. B* **28**, C6F1 (2010)
- [12] J. Notte, R. Hill, S. McVey, L. Farkas, R. Percival, B. Ward, An introduction to Helium Ion Microscopy, *Microsc. Microanal.* (2006), 12: 126-127
- [13] J. Notte, F. H. M. Rahman, S. M. McVey, S. Tan, and R. Livengood, The Neon Gas Field Ion Source – stability and lifetime, *Microsc. Microanal.* **16**, 28 (2010)
- [14] R. H. Livengood, S. Tan, R. Hallstein, J. Notte, S. McVey, F. H. M. Rahman, The neon gas field ion source – a first characterization of neon nanomachining properties, *Nucl. Instr. And Meth. A* (2011), doi:10.1016/j.nima.2010.12.220
- [15] H. Barthels, J. Grosser, and H. P. Neitzke, Electron bombardment ion source with small energy spread and high brightness, *J. Phys. E: Sci. Instrum.* **19** (1986)
- [16] J. E. Barth, C. B. de Gruyter, E. Koets, P. Kruit, P. E. van der Leeden, J. B. Le Poole, and K. D. van der Mast, Gas ion source for focused beams, *Microelectron. Eng.* **3**, 147 (1985)
- [17] P. Tesch, N. Smith, N. Martin, and D. Kinion, High current focused ion beam instrument for destructive physical analysis applications, *Proceedings from the 34th ISTFA 2008*
- [18] T. Hrnčir, F. Lopour, M. Zadrazil, J. Jiruse, A. Delobbe, O. Salord, P. Sudraud, Novel plasma FIB/SEM for high speed failure analysis, 3D tomography and other applications, *Proceedings from the 15th EMC 2012*
- [19] www.fei.com/products/fib/vion
- [20] A. Roth, *Vacuum Technology* (2nd Edition), Elsevier Science BV, The Netherlands, 1990
- [21] R. Rejoub, B. G. Lindsay, and R. F. Stebbings, Determination of the absolute partial and total cross sections for electron-impact ionization of the rare gases, *Phys. Rev. A* **65**, 042713 (2002)
- [22] Electron impact ionization cross section data from:
www.ruf.rice.edu/~atmol/electron_data.html
- [23] D. B. Langmuir, Theoretical limitations of cathode-ray tubes, *Proc. Inst. Radio Eng.* 25 (8), 977-991 (1937)
- [24] P. Kruit, M. Bezuijen and J. E. Barth, Source brightness and useful beam current of carbon nanotubes and other very small emitters, *J. Appl. Phys.*, **99**, 024315 (2006)
- [25] L. W. Swanson and G. A. Schwind, in *Handbook of Charged Particle Optics* (First Edition), edited by J. Orloff, (CRC Press, New York, 1997), Chapter 2
- [26] J. Peatross and D. D. Meyerhofer, Novel gas target for use in laser harmonic generation, *Rev. Sci. Instrum.*, **64**(11), 3066 (1993)

3 ■ Simulated Performance of the Nano-Aperture Ion Source

Source performance of the NAIS is investigated through computer simulations. First, gas simulations based on the steady state free molecular gas flow are performed to calculate the gas particle density distribution inside and outside of the gas chamber and to study how the gas chamber dimensions influence the distribution. The main objective of the gas simulation is to verify that the proposed NAIS gas chamber design can sufficiently confine a high gas density inside the gas chamber and the leakage through the double-aperture is rather insignificant. Secondly, ion trajectory simulations are performed to calculate the source reduced brightness and ion energy distribution with the rate of ion transmission through the gas chamber taking into account. The ion trajectory simulations also incorporate the gas simulation results in defining initial ion conditions in the interaction region. This simulation study looks into intricate details on the impact of the gas chamber dimensions and gas temperature on the beam current output, ion energy distribution, and reduced brightness and the role of the gas chamber bias voltage in optimizing the ion source performance.

3.1 Introduction

The core concept of the Nano-Aperture Ion Source is a small volume based electron impact gas ionization utilizing a miniaturized gas chamber. A narrow gas chamber spacing (100-500 nm) and a small diameter of the incident electron beam (100 nm) keep the ionization volume very small. Ideally, the gas chamber pressure is maintained at the threshold of molecular flow (i.e. gas mean free path~gas chamber spacing) to achieve a maximum ionization rate while circumventing ion-neutral and ion-ion collisions. The narrow gas chamber spacing combined with low gas chamber bias voltage (<1 V) operation avert from forming a plasma, thus ions are kept at room temperature unless the gas is intentionally cooled down.

In the previous chapter, the source reduced brightness and the energy spread of the new ion source are estimated based on several assumptions. The source brightness is estimated using the Langmuir brightness equation ($B_r = eJ/\pi kT$, see Chapter 2 Section 2.3.3) with the ions assumed to originate from a planar emitting surface having the same area as the beam area of the incident electrons traveling through the gas chamber. This assumption was made considering that the gas chamber spacing is very small and ion production outside the gas chamber is thought to be negligible based on the results of a study by Peatross and Meyerhofer^[1]. Additionally, all ions created inside the gas chamber are simply assumed to exit and become a useful current although it is certain that some ions would get 'lost' due to collisions with the gas chamber membranes and even exit through the electron entrance aperture. The brightness approximation using the Langmuir equation also ignores the detail that the amount of the ion current exiting the gas chamber would vary depending on the bias voltage applied between the membranes and the dimensions of gas chamber features such as the double-aperture diameter, spacing, and membrane thickness.

The ion energy distribution of the new ion source is expected to be mainly depending on the spatial distribution of the ions along the beam axis within the extraction field inside the gas chamber, considering that the average thermal energy of gas particles at room temperature (~0.04 eV for argon) is much lower than the average kinetic energy that ions would gain as accelerating through the gas chamber. The net energy spread is simply estimated to be on the order of the gas chamber bias voltage times the electric charge e , again, from the assumption that the ions are most likely to 'start' from somewhere between the membranes and not from the outside of the gas chamber.

In this chapter, source properties of the NAIS are numerically investigated through computer simulations with the subtle details overlooked in the previous estimation taking into account. Gas simulations using the Monte Carlo method are performed to determine the gas leakage rate through the double-aperture and the amount of gas subject to ionization both inside and outside of the gas chamber. Additionally, incorporating the gas simulation results, ion trajectory simulations are performed to estimate possible ion current output, ion energy spread, source reduced brightness and virtual source size and to investigate how they are influenced by the gas chamber dimensions, temperature and the bias voltage. Ultimately, the study is to verify whether the energy spread of NAIS can be indeed very small ($dE < 1$ eV) and the source reduced brightness predicted by the Langmuir brightness equation ($B_r > 1 \times 10^6$ A/m²srV) is plausible.

3.2 Simulation approach

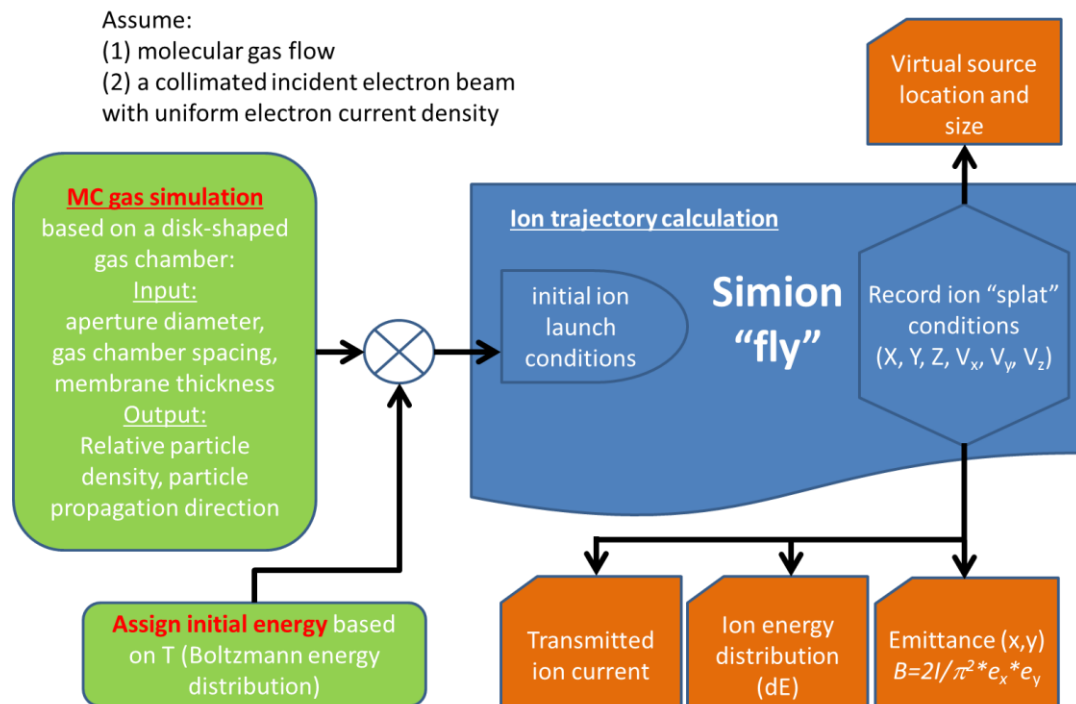


Fig. 3-1 Computer simulation steps for calculating the basic source properties of the NAIS.

Fig. 3-1 describes the general work flow of the simulation study. Basically, the study is undertaken in two separate simulation steps – first the gas simulation and then the ion trajectory simulation using SIMION optics software^[2]. In the first part, a Monte Carlo based computer code is developed to simulate free molecular gas flow in the proposed miniaturized gas chamber. A large number of test particles are injected and their trajectories tracked to evaluate the amount of gas loss through the double-aperture and the relative gas particle densities throughout the gas chamber. The code is written so that the aperture diameter, gas chamber spacing, and membrane thickness can be varied.

In the second part, the gas chamber is modeled as two rotationally symmetric electrostatic lens electrodes using SIMION. SIMION is capable of calculating ion trajectories in the electrostatic fields and recording ion positions and velocities at a user specified test plane. For simplicity, the incident electron beam is assumed to have a uniform current density and enter the gas chamber perfectly collimated and with a round cross section. The subsequent implication is that the gas particle density distribution within the interaction volume (=gas volume exposed to the electron beam) essentially represents the ion density distribution, provided that the electron impact ionization rate is relatively low (i.e. ionization in a dilute gas) and the multiple scattering by a single electron is negligible (i.e. short gas chamber spacing). Under these conditions, the results from the gas simulation can be directly used to define initial ion positions and the direction of the propagation at the gas chamber in the SIMION optics bench. Each ion is then given an initial energy that is randomly chosen based on a Boltzmann energy distribution at an assumed gas temperature before launching into the electrostatic field created by a gas chamber bias voltage.

The rate of ion transmission through the gas chamber is simply determined by counting the number of ions made through the ion exit aperture and dividing it by the total number of ions launched.

During the ion trajectory simulation, ions transmitted through the ion exit aperture are further accelerated by an ion accelerator potential. For convenience the ion accelerator is set as a simple potential surface placed perpendicular to the beam axis at a distance away from the gas chamber. It is also used as a test plane where ion positions and velocities are recorded upon arrival. The ion energy spread is deduced from the distribution of the ion velocities and the reduced source brightness based on the beam emittance calculated at the test plane.

Tracing back the slopes of individual rays from the test plane to the point where they cross the optical axis provides the locations of the virtual crossover formed by the ion extraction field. Because the ions have different intrinsic thermal energies and emerge from a finite ionization volume, there exists a spread in the crossover locations. The location where the spread is the smallest along the plane perpendicular to the optical axis is commonly regarded as the virtual source plane and the diameter of the spread as the virtual source size.

More details on the each simulation step and the results are provided in the following sections.

3.3 Gas simulations

3.3.1 Steady state molecular flow gas simulation using the Monte Carlo method

A defining characteristic of the molecular gas flow is that the mean free path (λ) of the gas is long compared to the characteristic dimension (L_{ch}) of the retaining vessel such as a pipe diameter. This regime is conveniently denoted by a dimensionless Knudsen number $K_n > 1$ from the following definition:

$$K_n = \lambda / L_{ch}$$

Another important characteristic that defines the molecular gas flow is that the gas particles move independently of each other (i.e. no inter-particle collisions) so that the gas dynamics is entirely determined by the gas-wall collisions. The gas particles travel straight line until they are stopped by a wall. The particles are then promptly scattered, however, into a new direction with no relation to the direction of incidence as the wall surfaces are microscopically 'rough'. The flow of gas particles in this regime is purely statistical based on the geometry of the walls, therefore the Monte Carlo (MC) computational technique is highly appropriate and commonly utilized for characterization of the gas conductance and particle density distribution of diverse and complicated vessel shapes. In general, the method of this technique is rather simple and implemented by injecting a test particle into a retaining vessel and following over its probable path, however, for the results to be statistically significant, the simulation requires a large number of test particles. The local particle density can be calculated based on the frequency of the particles traveling in that specific local volume and the overall conductance of the gas system can be represented by the notion of the transmission probability^[1,3-5].

The gas chamber of the NAIS can be simply regarded as two parallel plates with concentric holes separated by a small distance. In practice, the gas chamber is constructed by sandwiching two thin membranes processed through silicon based lithography steps on a thin layer of dielectric material such as PMMA, Si₃N₄, or TEOS (detailed fabrication methods are given in Chapter 4). The

void that can be filled with gas is actually created by etching a gas flow channel on the insulating layer and therefore, the thickness of the dielectric layer sets the gas chamber spacing and the shape of the gas channel. The two flat membranes define the gas retaining boundaries. The channel is strategically etched to connect from a window where gas is introduced and extend all the way to cover the membrane area where the gas chamber apertures would be fabricated later by FIB machining. Fig. 3-2 shows the etched gas channel in the shape of dumb-bell on the PMMA layer of a prototype device.

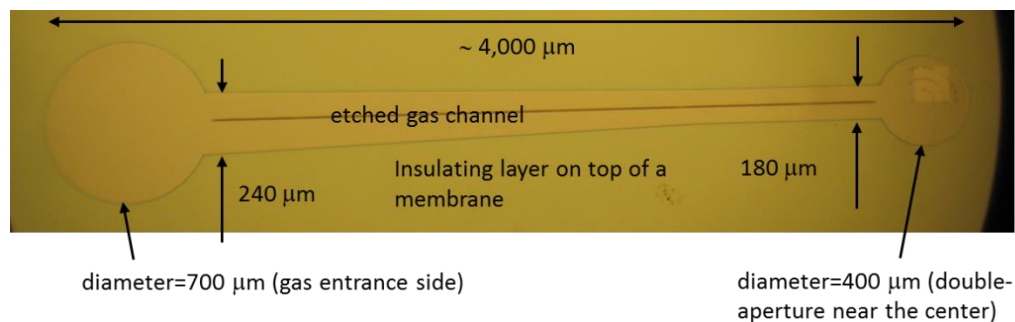


Fig. 3-2 Gas channel etched on PMMA. The shape of the gas retaining surfaces in the NAIS gas chamber is defined by the gas channel created between the two flat membranes.

Our primary interest in the gas simulation is to evaluate the relative particle density distribution in the region of the gas-electron interaction and to verify that the dimensions in the proposed gas chamber design are sufficient to maintain a high particle density inside the gas chamber while the density outside of the double-aperture remains relatively small. Knowing the exact conductance through the gas channel is not of a primary concern here as in practice the gas pressure in the interaction region can be estimated based on the amount of ion current produced from the incident electron beam current supplied and it can also be adjusted if necessary by simply changing the pressure at the gas inlet. Also, given that the gas particle trajectories in the molecular flow regime are strictly governed by random scattering events off the gas chamber surfaces and not by their previous paths, the relative particle density in a local volume depends on the geometry of the local surfaces within the sight of the particles, not by the shape and dimensions of the surfaces placed far away. For these reasons, only the circular section at the end of the gas channel covering the membranes is considered as the gas chamber for the simulation. Additionally, in an attempt to reduce computation processing time, the outer diameter of the gas chamber is scaled down. The layout of the simplified gas chamber model is shown in Fig. 3-3.

The gas simulation begins with a particle introduced from the side entrance window of the disc shaped gas chamber. The computer code is written so that the particle starts from anywhere on the entrance window plane randomly chosen based on a uniform distribution and injected into the gas chamber also at a random angle. The particle is assumed to move in straight line between encounters with the gas chamber walls (example particle traces shown in Fig. 3-4). When the particle encounters the gas chamber boundaries, it rebounds in a new direction based on a Lambertian distribution^[6] (aka the Knudsen cosine distribution). The volume inside the gas chamber and outside near the double aperture is subdivided into many smaller elemental volumes and the

count is kept for each elemental volume when a particle travels through it. Upon the particle either exiting through either aperture or returning back to the entrance window, a new particle is launched. The process continues until a large number of particles (20,000+) exit through the double-aperture. The entire simulation is also repeated for gas chambers with varying gas chamber spacing (SP), membrane thickness (TH), and aperture diameter (AP).

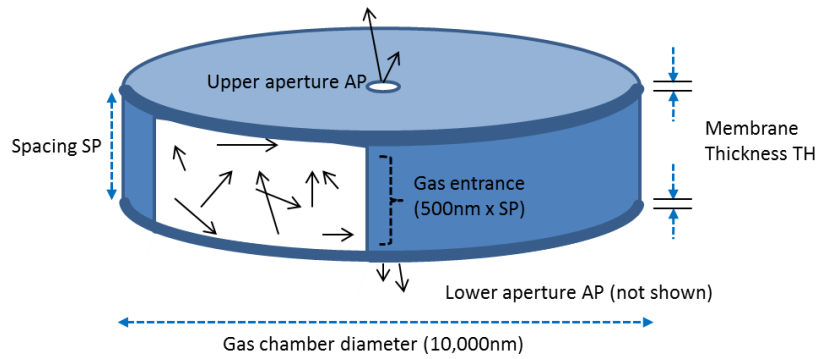


Fig. 3-3 Simplified gas chamber model for the simulation.

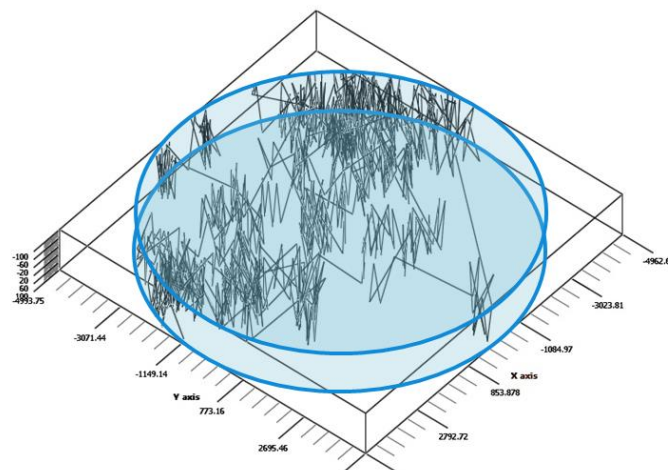


Fig. 3-4 Simulated trajectories of a particle inside the gas chamber model. The particle path is only determined by the particle-wall collisions and remittance based on the cosine distribution.

3.3.2 Gas simulation results

The effect of the gas chamber aperture diameter, the membrane thickness and the gas chamber spacing on the particle transmission probability is shown in Fig. 3-5. The transmission probability is determined from the ratio of the number of particles that exited through the double-aperture to the total number of the test particles launched. It comes as no surprise that the transmission probability increases with the diameter of the double-aperture. Given a fixed entrance

window size and a double-aperture diameter, the increase in the membrane thickness lowers the transmission probability as the extra length of the membrane wall surface creates more resistance to the gas flow. It is also shown that the increase in the gas chamber spacing given a fixed double-aperture size also reduces the transmission probability. This can be explained by the fact that increasing the gas chamber spacing consequently increases the relative entrance window size, thus increasing the probability for the particles to exit through the entrance window rather than the double-aperture. In all conditions considered here, the calculated leakage rate through the upper aperture is about the same as through the lower aperture reflecting on the symmetry of the double-aperture design.

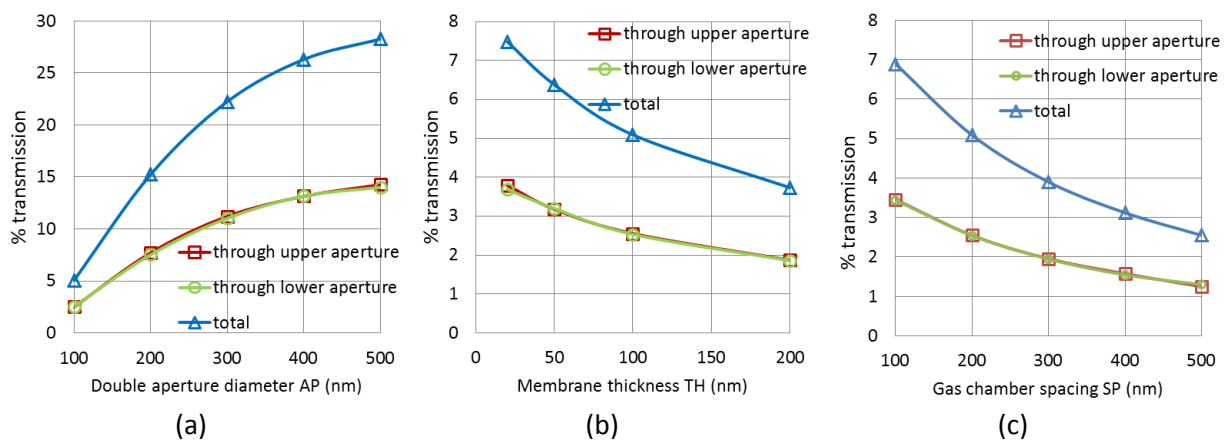


Fig. 3-5 Transmission probability that gas particles exit through the double-aperture: as a function of the double-aperture diameter AP given TH=100 nm and SP=200 nm (a), as a function of the membrane thickness TH given AP=100 nm and SP=200 nm (b), and as a function of the spacing SP given AP=100 nm and TH=100 nm (c). For all calculations, the gas chamber outside diameter is assumed to be 10 μm and the gas entrance window size of 500 nm x SP.

Fig. 3-6 shows a cross section of a gas chamber with a contour plot indicating the total number of times that particles intersected each elemental volume during gas simulation. The gas chamber dimensions are set to AP=100 nm, SP=200 nm, and TH=100 nm and each elemental volume $5 \times 5 \times 5 \text{ nm}^3$. In steady state, the particle frequency to a specific elemental volume can be regarded as the probability that a particle can be found in that specific location, therefore the contour plot basically represents the relative particle density distribution. It is visually clear that the particle density distribution in the vicinity of the gas chamber apertures changes considerably. The plot also clearly indicates that a small but steady number of gas particles are expected to be found just outside of the double-aperture.

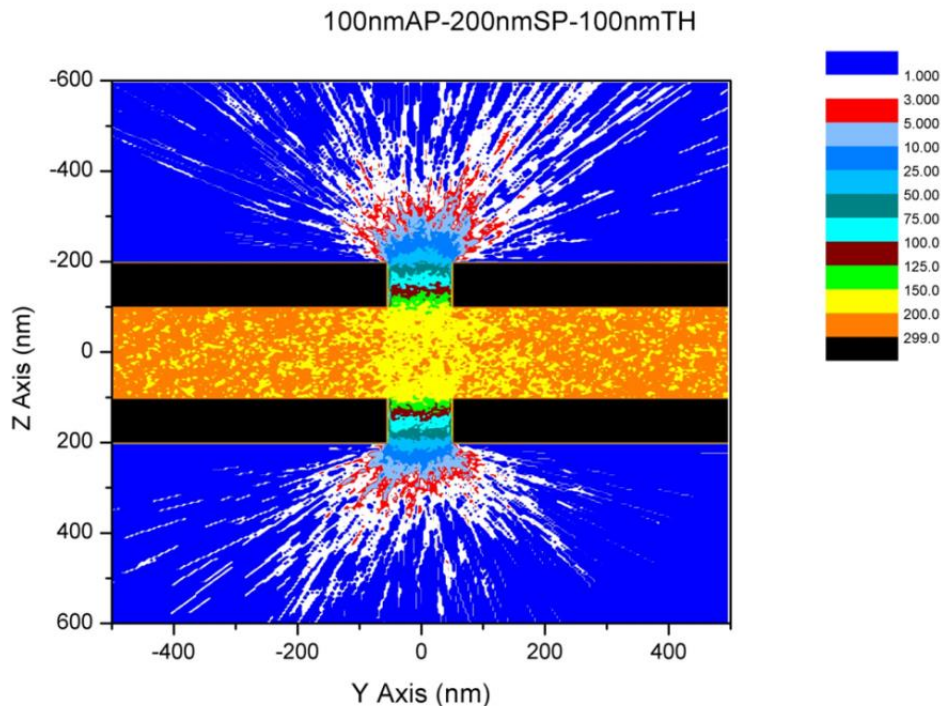


Fig. 3-6 A contour plot showing the total number of times that particles frequented each of the elemental volumes ($5 \times 5 \times 5 \text{ nm}^3$) pre-defined in a gas chamber having dimensions AP=100 nm, SP=200 nm, and TH=100 nm.

As already seen with the transmission probability, the particle density distribution can vary significantly with gas chamber dimensions. The simulation results showing the effect of the gas chamber aperture diameter, the gas chamber spacing, and the membrane thickness are summarized in Figs. 3-7 through 3-9. The results in each case are presented in two different ways – the distribution along the radial line (the radial distribution, along the Y-axis at $Z=0$ in the figures) from the entrance window to the center of the gas chamber and to the opposite edge of the gas chamber and the distribution along the line that goes through the center of the double-aperture (the axial distribution, along the Z-axis at $Y=0$). In both cases, the density is normalized to the density found at the particle entrance window. In general, the density in the radial direction drops very quickly just after the entrance window as the gas chamber space opens up and then stays relatively flat or gradually decreases towards the center before dipping again near the double-aperture. Axially, the relative particle density is the highest at the center between the membranes and then drops in the outward direction. Of the different gas chamber features and their dimensions considered here, it is evident that the aperture size has the most significant impact on the rate of the particle density fall both in the radial and axial direction. For small aperture sizes ($\sim AP \leq SP$) the particle density appears to stay almost uniform between the inner membrane walls and then drops in the outward direction, sharply through the aperture walls and then quickly diminishes just outside the aperture edge. For large aperture sizes ($\sim AP > SP$), however, the density starts out at much lower in the middle, falls steadily to the inner aperture edge and through the aperture walls, and finally diminishes at a distance farther away from the outer aperture edge. Overall, the outcomes of the gas simulations are found to be in good agreement with the results found by Peatross and Meyerhofer ^[1].

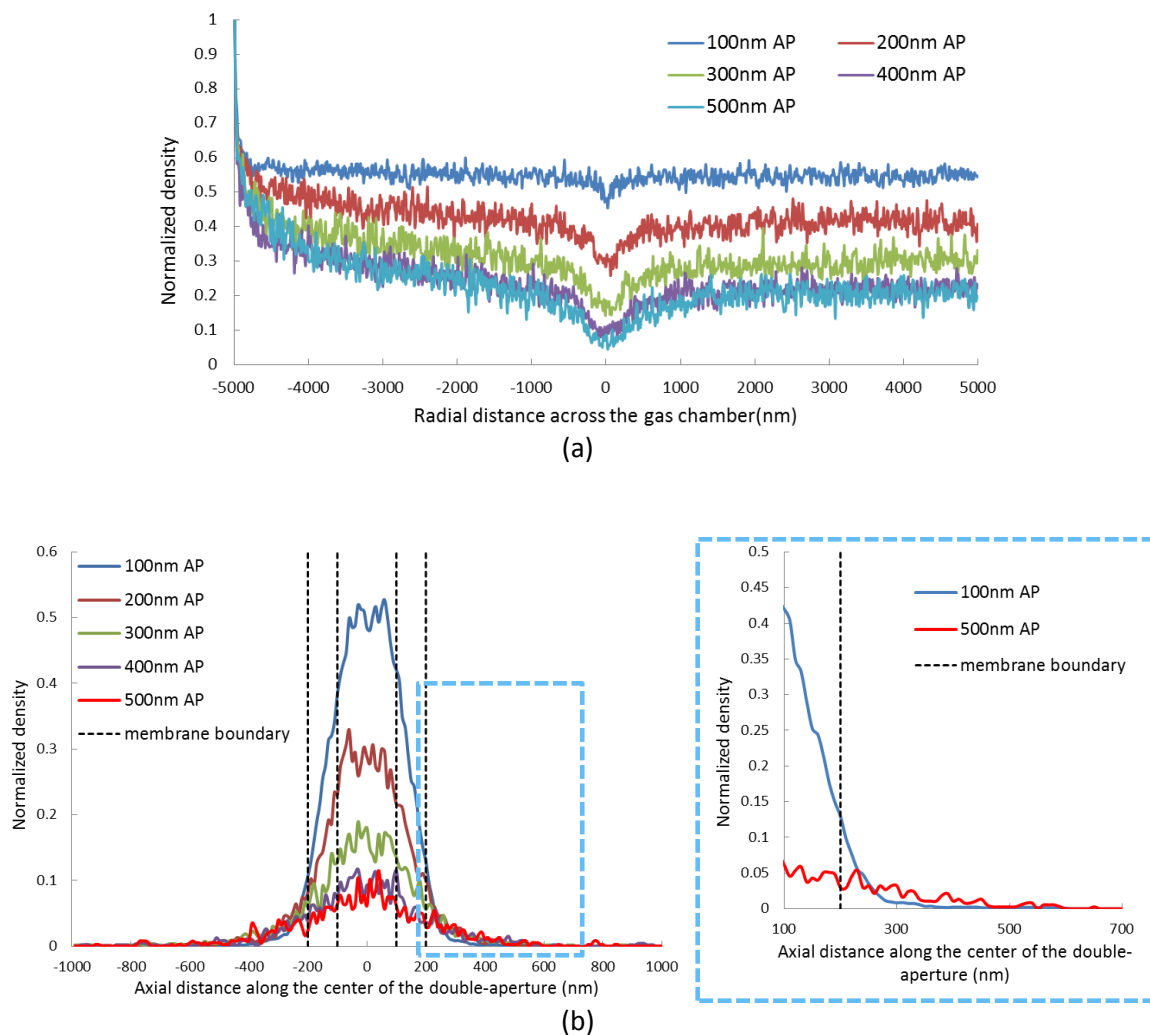


Fig. 3-7 Effect of the double-aperture diameter AP on the particle density distribution (given SP=200 nm and TH=100 nm): (a) Radial particle density distribution and (b) axial particle density distribution.

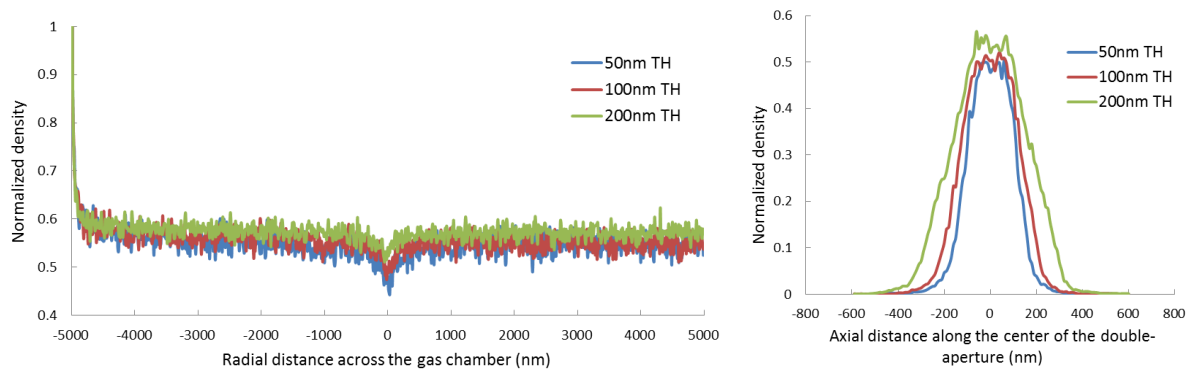


Fig. 3-8 Radial (left) and axial particle distribution (right) dependence on the membrane thickness TH (given AP= 100 nm and SP=200 nm).

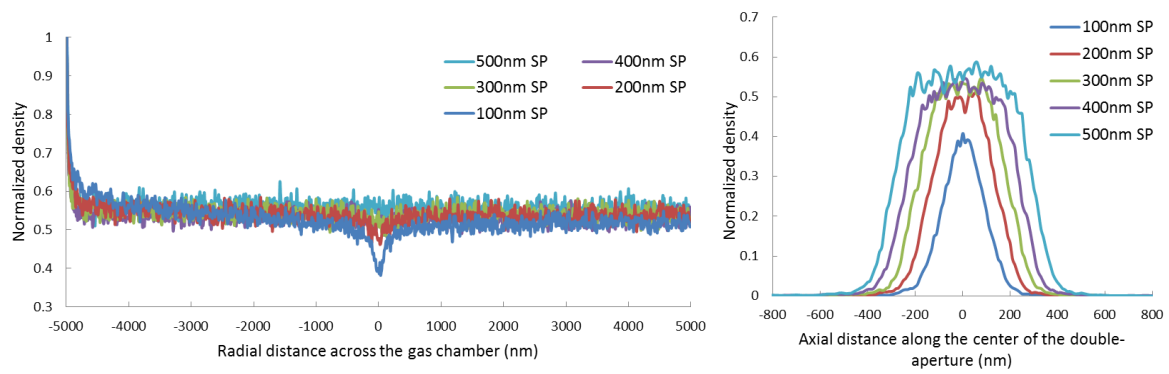


Fig. 3-9 Radial (left) and axial particle distribution (right) dependence on the gas chamber spacing SP (given AP= 100 nm and TH=100 nm).

3.4 Ion trajectory simulations

The gas simulation results in the previous section reassure the particle loss through the gas chamber apertures can be maintained very small and indicate that the majority of the gas particles reside within the gas chamber bouncing off from one surface to another. At each bounce, the particles are subject to new propagation directions along with new thermal velocities which can be generalized by the Maxwell-Boltzmann statistics. Due to the very large difference in mass, the interaction with impact electrons leaves the pre-collision gas particle velocity and direction of propagation undisturbed; however, the trajectory of the newly formed ions thereafter can be manipulated by an external electrostatic field. For the NAIS, a gas chamber bias voltage is applied to steer and accelerate the ions toward the ion exit aperture. Given that a potential difference is applied between the two parallel membranes with concentric apertures the gas chamber essentially resembles a two electrode electrostatic lens system and the ‘focusing’ capability of the gas chamber would greatly depend on the initial conditions of the ions, the gas chamber bias voltage, and the geometry of the gas chamber.

Fig. 3-10(a) is an instance showing ions initialized in a gas chamber modeled in SIMION. In this case, the gas chamber is modeled to have AP=200 nm, SP=200 nm, and TH=100 nm. For all ion trajectory simulations presented here, the ionization volume is assumed to be defined by the gas particles exposed to a perfectly collimated electron beam having a uniform current distribution in a 100 nm round beam spot. Under this assumption, the gas particle densities found from the gas simulations are directly used to define the initial ion positions in the SIMION simulations. Each ion inherits the same direction of propagation recorded during the gas simulation but it is given an initial ion energy randomly selected based on a Boltzmann distribution at an assumed temperature. Once the ions ‘fly’ through the gas chamber extraction field and exit, they are further accelerated by an ion accelerator with a constant field of 1×10^6 V/m. In an attempt to keep the SIMION ion bench to a reasonable size, the ion accelerator is modeled as a simple equipotential surface of 1 V placed perpendicular to the optical axis (z-axis) of the ion bench, 1 μm away from the gas chamber. The equipotential surface is also set as a test plane to record the x-y positions and velocities of the ions passing through. Fig. 3-10(b) shows the trajectories of ions through an ion extraction and acceleration field. It is evident that not all ions make it through the ion exit aperture.

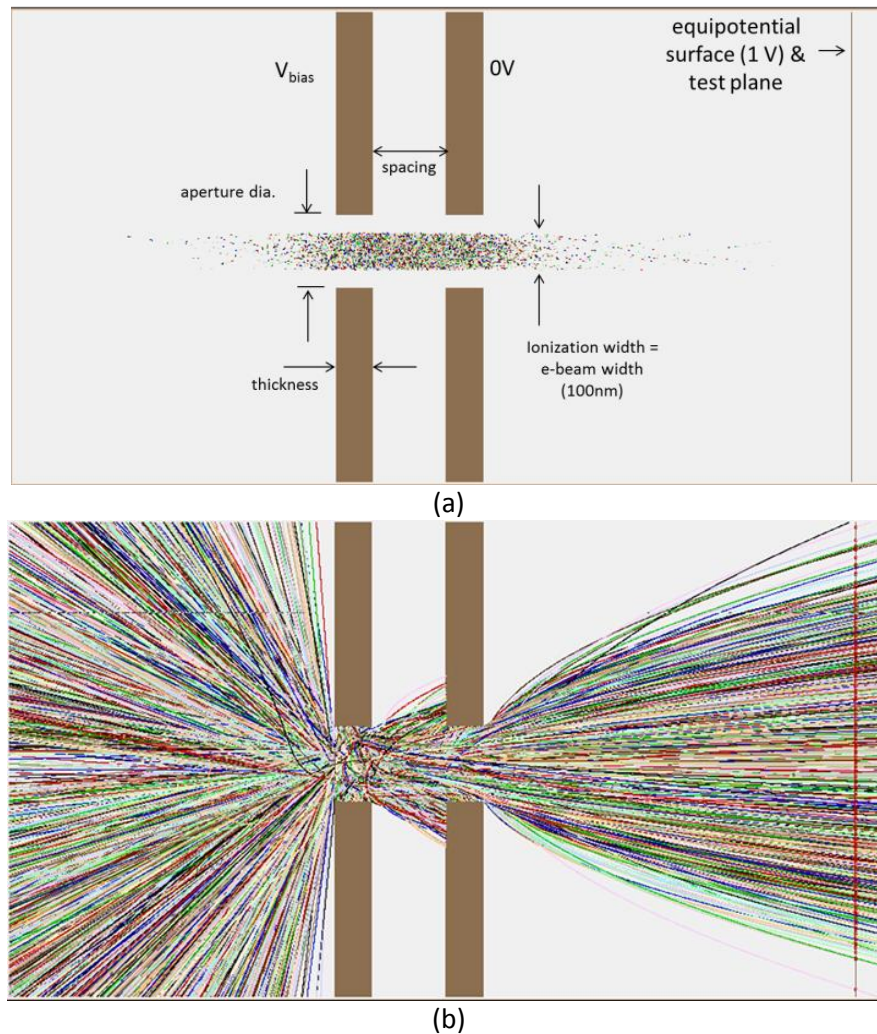


Fig. 3-10 SIMION ion trajectory simulation: The gas chamber is modeled as two rotationally symmetric lens electrodes and the ions are initially placed according to the particle densities found from the gas simulation (a) and simulated ion trajectories (b).

3.4.1 Ion transmission

In defining the ion transmission rate as the ratio between the number ions made through the ion exit aperture and the total number of ions launched, the ion trajectory simulations have shown that certainly 100% ion transmission is not possible for the NAIS because the ions forming outside the electron entrance aperture, though small in number, are effectively shielded from the ion extraction field. Furthermore, the ions having relatively high initial thermal energies can even exit through the electron entrance aperture^[*] or accelerate toward the ion exit aperture at large diverging angles so that many of them become stopped by the gas chamber walls (Fig. 3-10(b)). However, the simulation results show that the ion transmission (beam current output) can be optimized in several different ways.

^[*] For the ranges of the gas chamber bias voltage and the gas chamber dimensions considered for the simulations, it is found that the ion loss through the electron entrance aperture can range 2-10% for $T=293$ K.

Gas cooling is not a requirement for the current NAIS design, but this is shown to be an effective way to boost the NAIS performance, particularly for enhancing the ion transmission rate while keeping the gas chamber bias voltage low. A cooler gas means lower intrinsic thermal energies for the ions, which effectively decreases the angular spread of ions within the gas chamber when accelerated by an extraction field (i.e. increased the current density at the ion exit aperture plane). The simulation results in Fig. 3-11(a) show that cooling a room temperature gas to 77 K (liquid nitrogen temperature) can almost double the current output for a given bias voltage.

Clearly, the gas chamber bias voltage is an important parameter for the NAIS as it provides the flexibility to control the output current by changing the angular spread of the beam, however it should be reminded that in practice high gas chamber bias voltages can yield field induced discharges. Upon limiting the field between the gas chamber membranes to 3×10^6 V/m, the simulation results indicate that the gas chamber spacing should be kept small in order to maximize the ion transmission rate (Fig 3-11(b)). This also offers an added benefit of requiring a small gas chamber bias voltage (for the same field) which enables low energy spread operation. This will be further addressed in the next section.

Although the supporting data not presented here, the membrane thickness can also make a small impact on the ion transmission as it can change the 'angle of view' for the ions. The thinner the membrane, the higher the ion transmission (several % increase going from 200 nm to 100 nm), but in reality, the reliability in fabrication and mechanical stability under a gas load would be more important factors to consider when it comes to determining the membrane thickness.

Obviously, increasing the ion exit aperture size is a good option to increase the ion transmission rate drastically (Fig 3-11(c)), but as shown by the gas simulations, it increases the gas density outside the gas chamber which can cause adverse effects on the source brightness and ion energy distribution. This will be also discussed in detail later.

It should be pointed out that the results of the ion trajectory calculations are similar whether the initial ions are positioned based a uniform gas particle density distribution or accordingly by the results of the gas particle density simulations (Fig 3-11(a) and (b)). The uniform gas density here implies an ideal condition in which the gas particles fill the gas chamber uniformly and no particles exist pass the outside edge of the apertures. The similarity in the result also indicates that the gas leakage through a miniaturized gas chamber with a small double-aperture is sufficiently small so that the particle distribution within the gas chamber appears to be 'almost' uniform.

The ion (current) density profiles of beams extracted from the gas chamber at several different bias voltages are show in Fig. 3-12. The results are obtained by dividing the beam cross sections acquired at the SIMION test plane into many sub-sections having an equal shape and area (40×40 nm²) and counting the number of ion trajectories intersecting each sub-section area. The figures show the distribution of the total number of particles per sub-section (particle density) along the two orthogonal directions (X and Y) across the beam spots. As shown, the current density distribution appears to be Gaussian and remains that way even when the total beam current (the area under the curve) is changed by varying the gas chamber bias voltage.

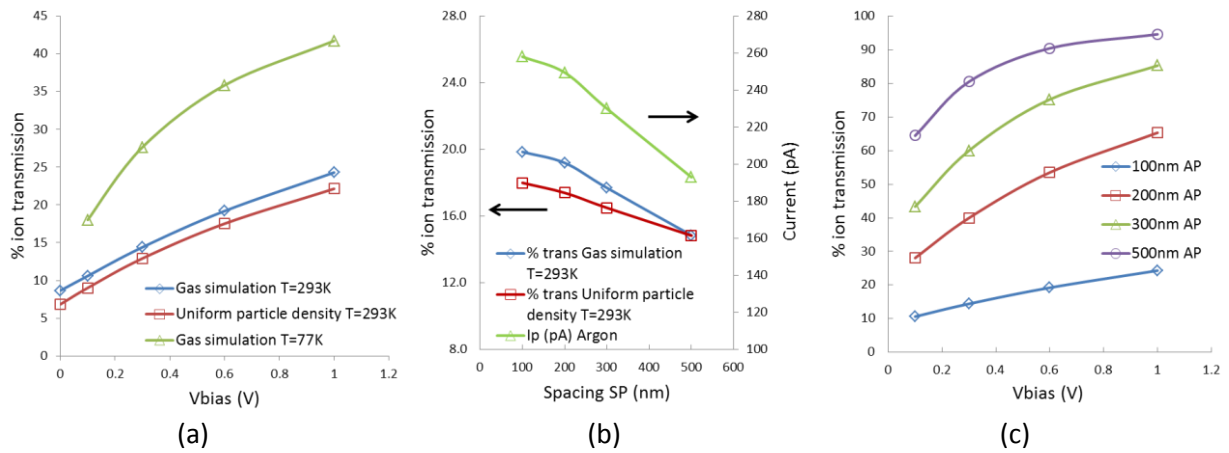


Fig. 3-11 Ion transmission rates through the ion exit aperture under different gas chamber conditions: (a) As a function of gas chamber bias voltage for two different gas temperatures $T=293\text{ K}$ and $T=77\text{ K}$. For $T=293\text{ K}$ two different initial ion distributions assumed: (1) initial ion positions set based on the gas simulation results ('Gas simulation') and (2) ions positioned uniformly inside the interaction volume within the gas chamber boundaries ('Uniform particle density'). Gas chamber dimensions $AP=100\text{ nm}$, $SP=200\text{ nm}$, $TH=100\text{ nm}$. (b) As a function of gas chamber spacing: given $AP=100\text{ nm}$ and $TH=100\text{ nm}$. The bias voltage is adjusted so that the e-field between the membranes is constant ($3 \times 10^6\text{ V/m}$) for all spacings. The ion currents (I_p) are determined based on the assumption that a total current of 1.3 nA is produced from the gas ionization (argon) and factoring in the calculated % transmission. (c) As a function of gas chamber bias voltage for several aperture diameters: given $SP=200\text{ nm}$ and $TH=100\text{ nm}$.

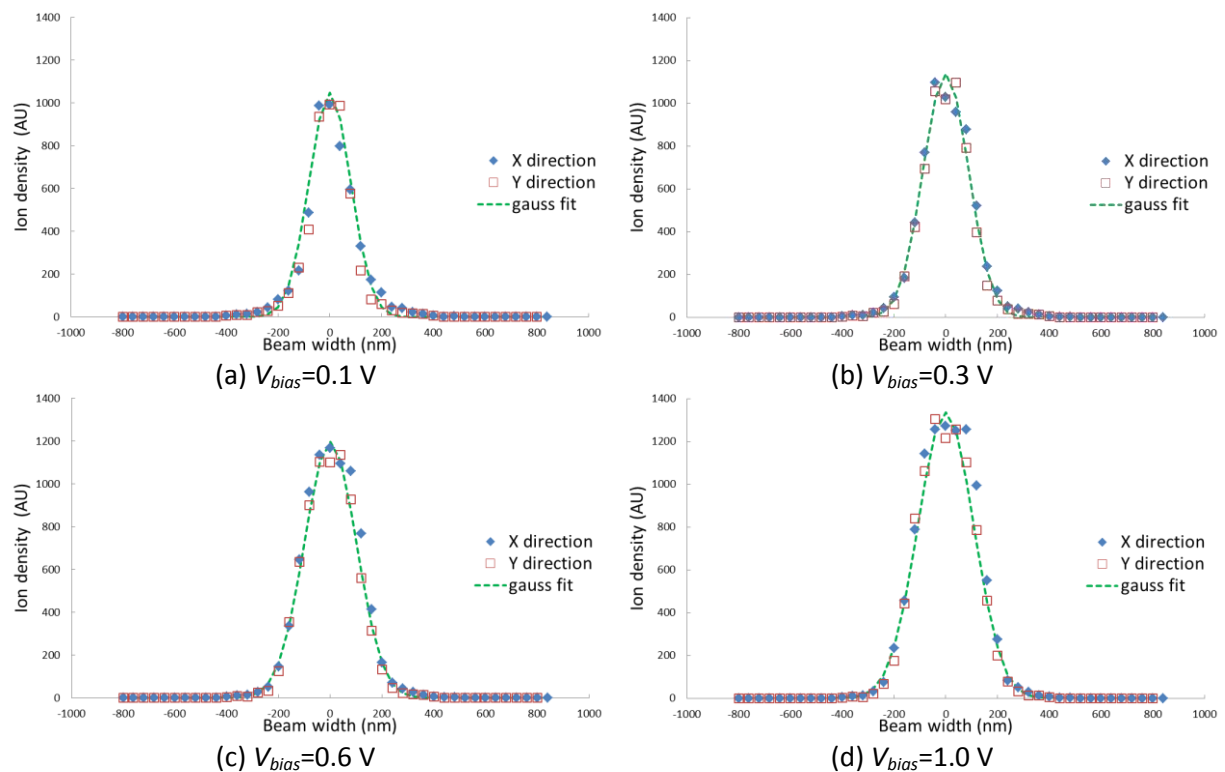


Fig. 3-12 Calculated ion (current) density distributions of beams extracted from the gas chamber at several different bias voltages. The distributions appear to be Gaussian. Given gas chamber dimensions $AP=100\text{ nm}$, $SP=200\text{ nm}$, and $TH=100\text{ nm}$.

3.4.2 Energy spread

Fig. 3-13 and Fig. 3-15 show the energy distributions of the ions crossing the 1 V equipotential surface set on the SIMION ion bench. The ions arrive at the test plane with different energies mainly because they start from different locations in the gas chamber. The ions starting out from the back-end of the gas chamber (the electron entrance aperture side) gain in kinetic energy while accelerated by the gas chamber bias voltage plus additional kinetic energy through the ion acceleration field whereas the ions starting out from the front-end (the ion exit aperture side) just have the latter portion. As expected the ion trajectory simulation results show that the overall width of the ion energy spread generally follows the magnitude of the gas chamber bias voltage applied but interestingly when the ion extraction field is very weak ($V_{\text{bias}} \sim 0$ V), the ion acceleration field can also make an impact. This behavior is seen in Fig. 3-13(a) in which case the dE is bigger than what can be expected from the intrinsic ion thermal energy distribution at room temperature alone. It is found that this is due to the ion acceleration field (1×10^6 V/m) sufficiently penetrating through the ion exit aperture and extracting some ions.

Perhaps the most surprising result revealed by the ion trajectory simulation is the development of a secondary peak in ion energy distribution when the gas chamber bias voltage is turned up high. At low bias voltages, the ion energy distribution curve typically entails a narrow peak (the primary peak) centered on the low energy side as the majority of the ions exit the gas chamber originate from the front side of the gas chamber (i.e. ions closer to the ion exit aperture have a higher transmission probability – the proximity effect). As the bias voltage increases, a second peak starts to appear on the high energy side of the curve. A further investigation has shown that this is caused by the lens effect of the gas chamber when the bias voltage is relatively high. A large potential difference between the membranes creates dense equipotential surfaces bulging through the electron entrance aperture, which ‘focus’ many more ions from the back-end of the gas chamber into the ion exit aperture compared to the ions from the middle, thus creating a sharper increase in the number of ions transmitting with high energies. Fig. 3-14 illustrates this lens effect through simple examples.

Similar to the results already seen with the ion transmission calculations in the previous section, the dE results calculated from the ion trajectory simulations assuming a uniform gas density distribution in the gas chamber and from those using the gas simulation results directly are found to be in close agreement. Only significant difference between them is seen at the tail of the distribution in which the calculation based on the gas simulation results exhibits an extended tail on the low energy side that comes from the ions started outside of the gas chamber. The difference at the other end is unnoticeable due to the fact that the ions from behind the electron entrance aperture have an inherently small probability to transmit through the gas chamber.

Lowering the intrinsic ion thermal energies by gas cooling has already shown to be efficient for extracting more ions but because the average kinetic energy that ions would typically gain from the gas chamber extraction field is still much greater, for the overall width in ion energy distribution it makes hardly any difference (Fig. 3-13). However, because the ions with lower intrinsic thermal energies lead to a smaller angular spread in the ion extraction and have higher sensitivity to the lens effect, the gas cooling allows many more ions originating from the backside of the gas chamber to transmit through. For this reason, the ion distribution plots for $T=77$ K in Fig. 3-13 display more of an up-slope trend in the mid-to-high ion energy range whereas the distribution plots for $T=293$ K generally display a down-slope trend before the secondary peak.

It is also found that the gas chamber spacing and the double-aperture size can have influences on the ion energy distribution. Fig. 3-15(a) shows simulated energy distributions of ion beams from three gas chambers of same aperture size and membrane thickness, but different spacing. As the applied bias voltage is also same (1 V), the base widths of all three energy distributions are pretty much identical, but because of the effective ion extraction field strength changes with the different gas chamber spacing, there is a considerable shift in the number of mid-to-high energy ions that show up in the distributions. The size of the double-aperture, on the other hand, can influence both the ion distribution width and shape. In Fig. 3-15(b), it is shown that the increasing the aperture size results in a much longer tail on the low energy side due to an increased ionization farther outside the ion exit aperture. Moreover, for the large apertures ($\sim AP > SP$), because the gas (and ion) density is the highest at the center between the membranes and falls rather fast out toward the ion exit aperture, the ion energy distribution is generally centered on the medium energy side without featuring the two distinctive peaks that are commonly seen with gas chambers having small apertures ($\sim AP \leq SP$).

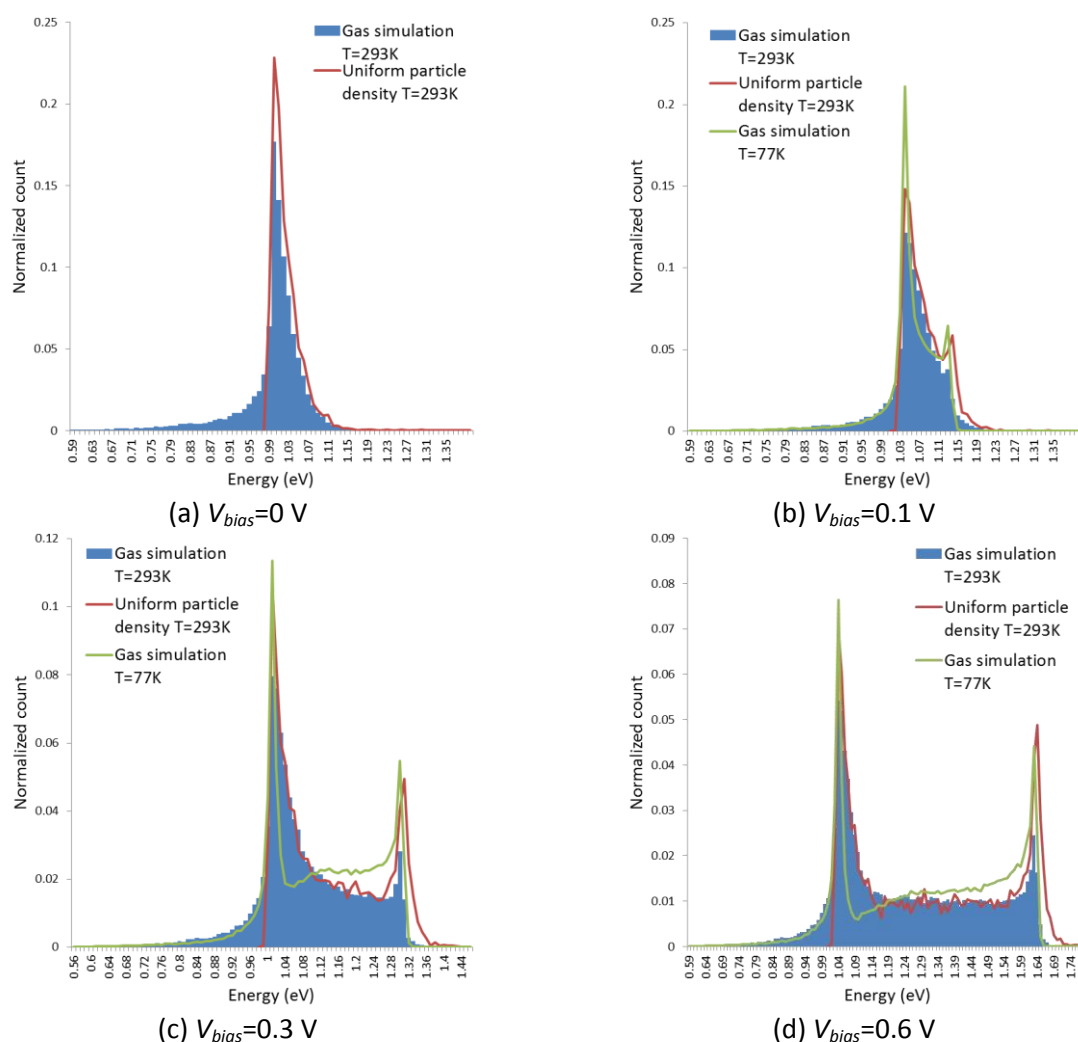


Fig. 3-13 Ion energy distributions calculated from the SIMION simulation results ($AP=100\text{ nm}$, $SP=200\text{ nm}$, and $TH=100\text{ nm}$). The overall width of ion energy distribution (dE) is mainly influenced by the gas chamber bias voltage (V_{bias}). The calculations assuming a uniform gas particle density also show similar outcomes as the calculations based on the gas simulation results.

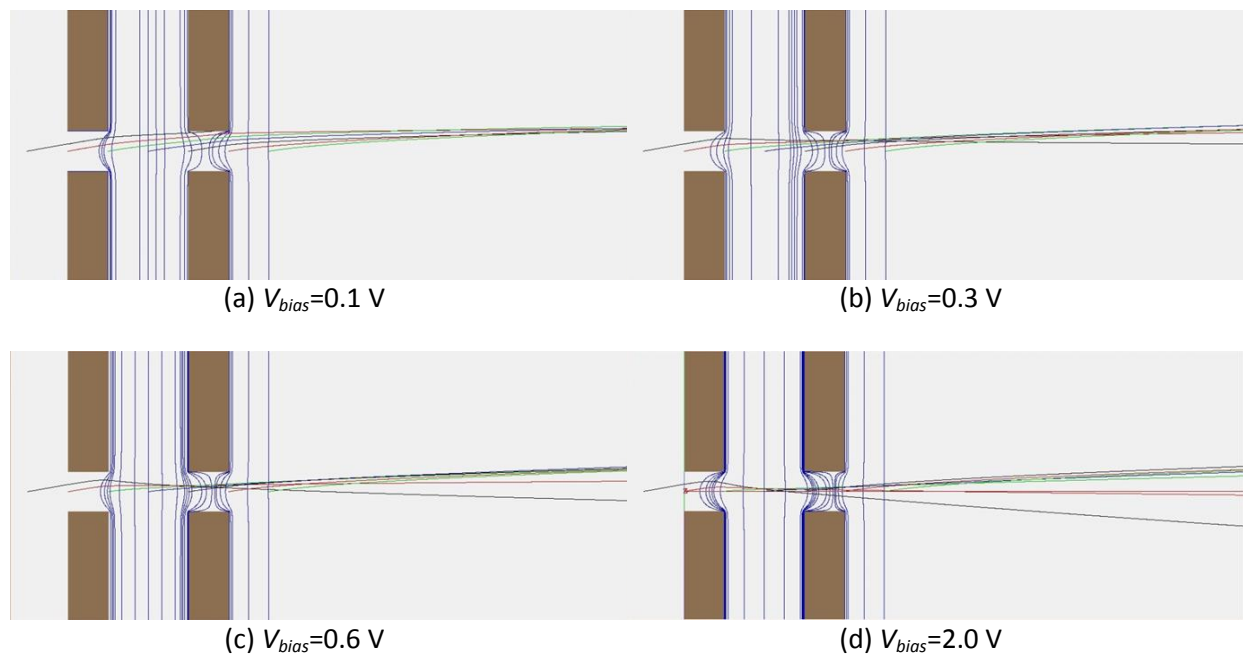


Fig. 3-14 The lens effect of the gas chamber: test ions are assigned with a same initial energy and half-angle but positioned at different locations along the gas chamber axis. It is evident that the ions from the back-end of the gas chamber become deflected more as the bias voltage increases.

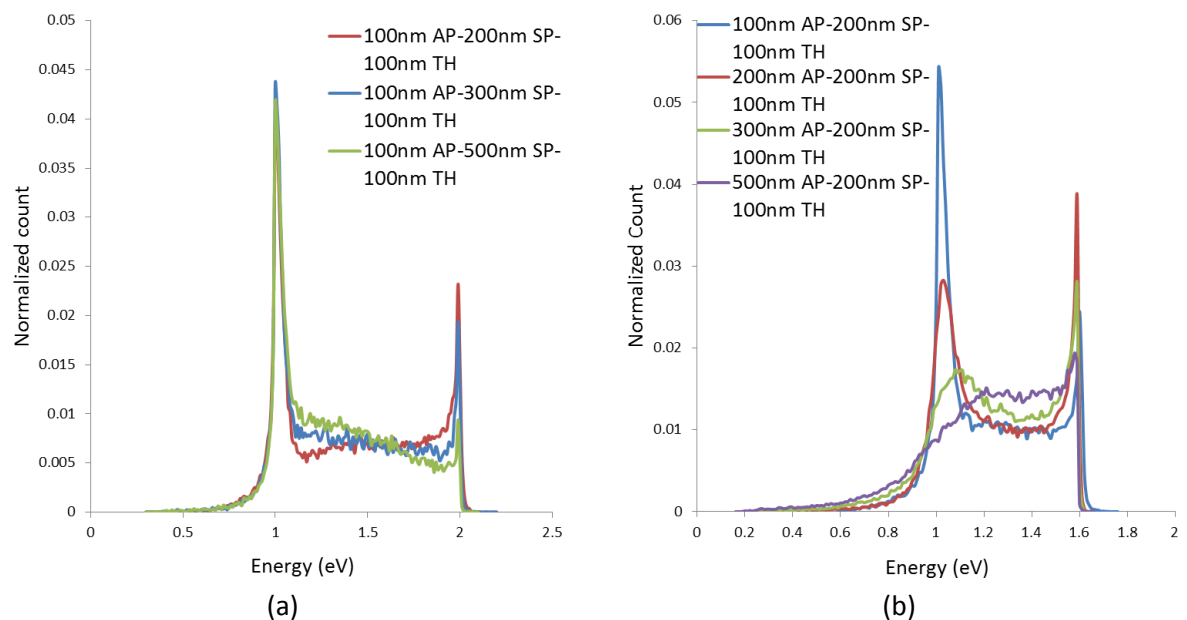


Fig. 3-15 Effect of the gas chamber spacing (a) and the double-aperture size (b) on the ion energy distribution. The gas chamber bias voltage is fixed at 1 V in (a) and 0.6 V in (b). All based on the gas simulation results and $T=293$ K.

3.4.3 Source reduced brightness

The brightness of charged particle beams equals to the amount of current (I) emitted from a source per unit area (A) per unit solid angle (Ω). In simpler terms, it basically quantifies the current density and the degree of parallelism in a beam. All particle beam sources, including the NAIS as discussed in the previous section, are prone to some amount of intrinsic velocity spread. Beams with large random transverse velocity components produce a large spread in angle relative to the axis of propagation, leading to high beam emittance or poor beam parallelism which limits the ability to focus, and ultimately resulting in low beam brightness.

In a system where x and y denote the two Cartesian coordinates perpendicular to the beam direction z , the transverse angle x' (or y') of an individual particle of paraxial beams that move with constant energy can be represented by taking the ratio between the transverse velocity V_x (or V_y) and the forward velocity V_z . Rather than dealing with the orbit of each individual particle in a beam, the overall beam parallelism can be generalized by using the concept of emittance^[7]. Emittance by definition is the effective area or the product of the beam's width and divergence relating to the random velocity spread in the trace space plane x - x' (or y - y'). Due to the diffusive nature of the distribution, the emittance of N -particle system is typically calculated using the moments of the particle distribution. The root-mean-square (rms) emittance in x - x' (and similarly for y - y') is written as:

$$\varepsilon_{x(rms)} = \sqrt{\overline{x^2 x'^2} - (\overline{xx'})^2} \quad (3.1)$$

where

$$\begin{aligned} \bar{x} &= \frac{1}{N} \sum_{i=1}^N x_i, & \bar{x}' &= \frac{1}{N} \sum_{i=1}^N x'_i, \\ \overline{x^2} &= \frac{1}{N} \sum_{i=1}^N (x_i - \bar{x})^2, & \overline{x'^2} &= \frac{1}{N} \sum_{i=1}^N (x'_i - \bar{x}')^2, \\ \overline{xx'} &= \frac{1}{N} \sum_{i=1}^N (x_i - \bar{x})(x'_i - \bar{x}'). \end{aligned}$$

In ideal conditions without any non-linear forces the density of particles or the area occupied by a given number of particles in the trace space remains constant and the beam emittances can be utilized in defining the beam brightness. For the beams having Cartesian symmetry in the transverse direction the reduced brightness of a beam with current I normalized by the beam acceleration V_{acc} is typically expressed as^[7]:

$$B_r = \frac{I}{A\Omega V_{acc}} = \frac{I}{8\pi^2 \varepsilon_{x(rms)} \varepsilon_{y(rms)} V_{acc}} \quad (3.2)$$

Fig 3-16(a) and (b) are the trace space plots at the 1 V test plane of a diverging beam from a gas chamber configured to AP=100 nm, SP=200 nm, TH=100nm and $V_{bias}=0.6$ V. The finite area under the elliptical beam boundary is an indication that individual particles in the distribution have different transverse velocities. Due to the symmetry in the NAIS design, the distributions in the x - x' and y - y' are essentially identical.

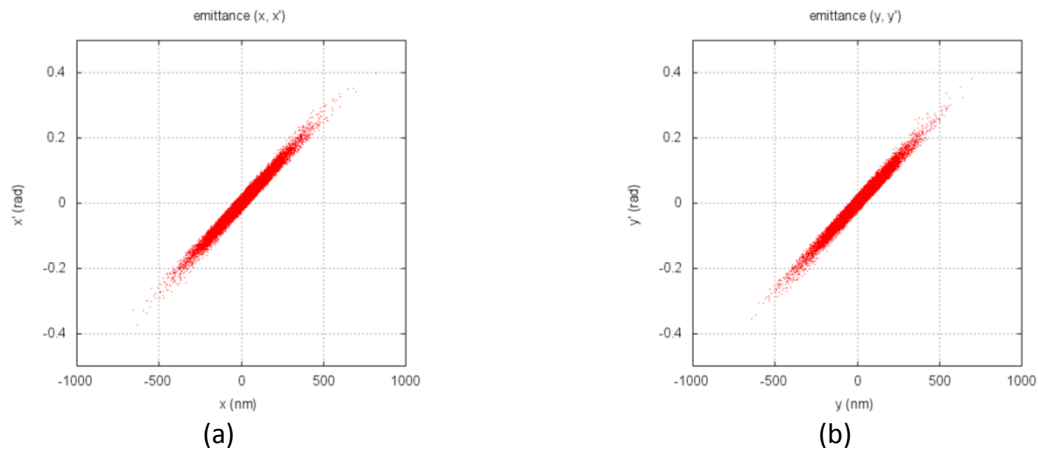


Fig. 3-16 Trace space plots ($N=100,000+$) of a ion beam recorded at the 1 V test plane (AP=100 nm, SP=200 nm, TH=100 nm and $V_{\text{bias}}=0.6$ V). The particle distributions traversed in the southwest direction indicate that it is a diverging beam both in x and y direction.

Figs. 3-17 through 3-20 show the calculated ion beam current, emittance, and reduced brightness of the NAIS under various aperture, spacing, gas temperature, and bias voltage conditions. The calculations assume for argon as the source gas, at the optimum gas pressure condition ($K_r=1$), and ionized by a 1 keV incident electron beam of 100 nA uniformly distributed in a 100 nm diameter (equivalent to a current density $J_e \sim 1.27 \times 10^7$ A/m²). Under these conditions the total current produced from gas ionization is expected to be ~ 1.3 nA based on the ionization efficiency for argon gas given in Table 2.1 of Chapter 2. The ion beam current actually exiting the gas chamber is calculated by factoring in the ion transmission probability estimated from the ion trajectory simulations to the assumed total ionization current. The emittance is calculated based on the ion trajectory and velocity information found at the test plane and applying to Eq. 3.1. The reduced brightness of the transmitted ion beams is calculated using Eq. 3.2.

Incidentally, even though the assumed current density of the incident electron beam for the analysis is somewhat conservative, being about a magnitude lower than the theoretical limit calculated in Chapter 2, the simulation indicates that the NAIS can provide a maximum reduced brightness nearing $\sim 2 \times 10^6$ A/m²srV at room temperature. In addition, the result is in line with the theoretical expectation based on the Langmuir brightness model assuming the same electron current density. The simulation results, however, also make it clear that this level of reduced brightness is only achievable for gas chambers configured to optimum dimensions and after carefully adjusting the gas chamber bias voltage to balance between the beam current and the emittance. Of the various conditions evaluated here, AP=100 nm, SP=200 nm, TH=100 nm and $V_{\text{bias}}=0.6$ V are found to be optimal. There are several other interesting details to point out:

As already seen before, increasing the gas chamber bias voltage generally yields a higher ion beam current as the acceleration reduces the angular spread of the ions toward the ion exit aperture. With no bias voltage, the ion transmission is mostly limited to the ions initially positioned near or outside the exit aperture. Although small in numbers, these ions generally retain transverse velocity components prescribed by the Maxwell-Boltzmann statistics at the assumed gas temperature. Turning up the bias voltage from zero initially decreases the beam emittance as the ions making through the aperture tend to have low transverse velocity components which then narrows the overall distribution (see Fig. 3-21), however, at some point, this becomes offset by the

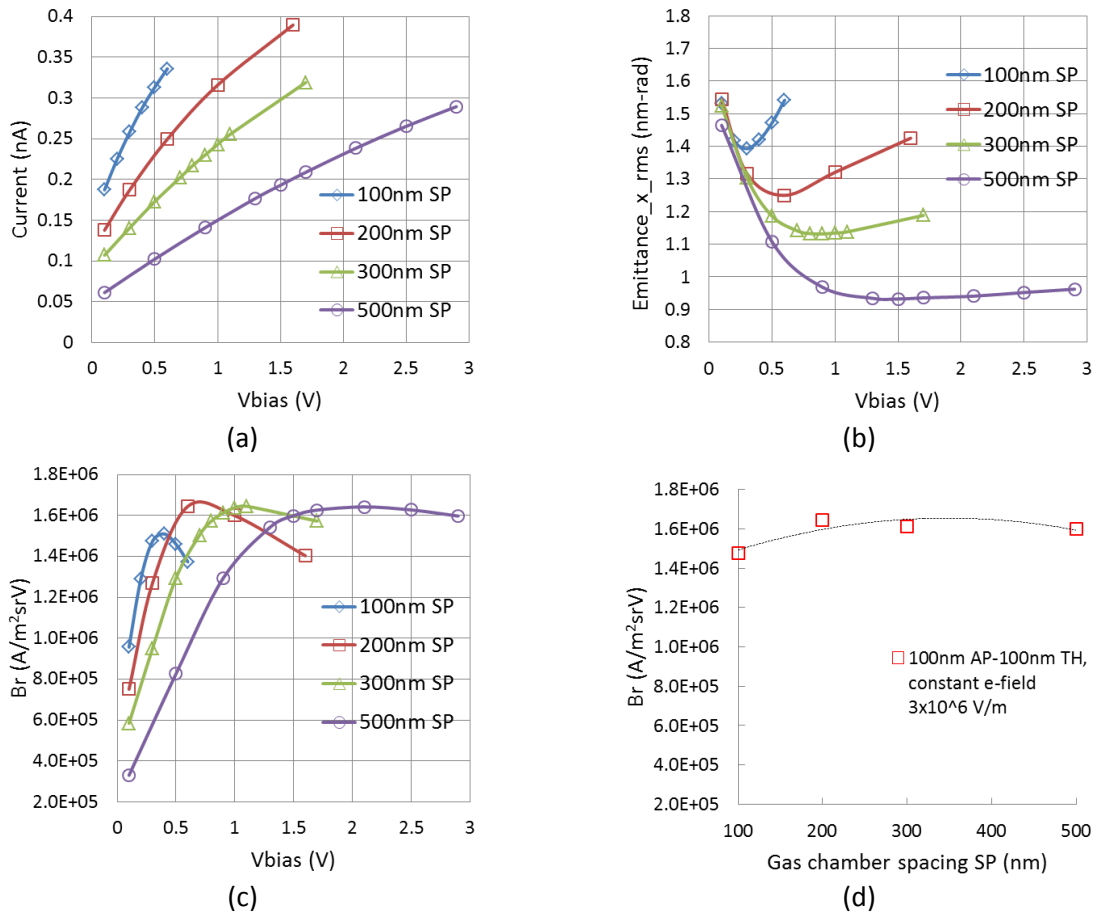


Fig. 3-17 Calculated ion current output (a), emittance (b), and reduced beam brightness (c, d). Given AP=100 nm, TH=100 nm, and SP is varied from 100 to 500 nm. Initial ion positions set according to the simulated gas particle density results. The ion beam current is calculated assuming the total ionization current of 1.3 nA and factoring in the ion transmission probabilities calculated from the simulation results. The emittance is calculated using Eq. 3.1 and the reduced brightness using Eq. 3.2. Only the emittance results in x-x' are shown but the results for y-y' are found to be more-or-less the same following the design symmetry. The gas chamber bias voltage is adjusted for a fixed E-field of 3×10^6 V/m for the results in (d). For all calculations $T=293$ K is assumed.

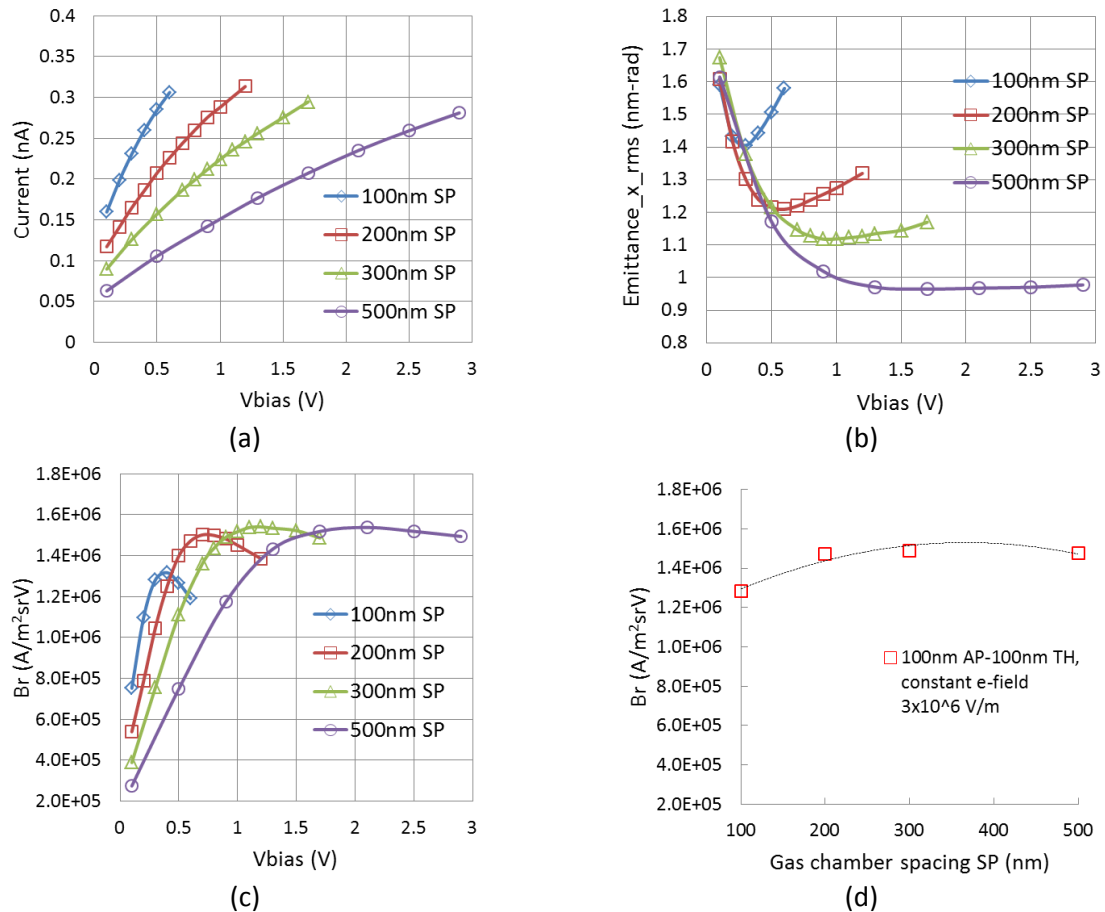


Fig. 3-18 Calculated ion current output (a), emittance (b), and reduced beam brightness (c, d). The calculation methods and the simulation conditions are identical to those in Fig. 3-18 except that a uniform particle density distribution is assumed for determining initial ion positions.

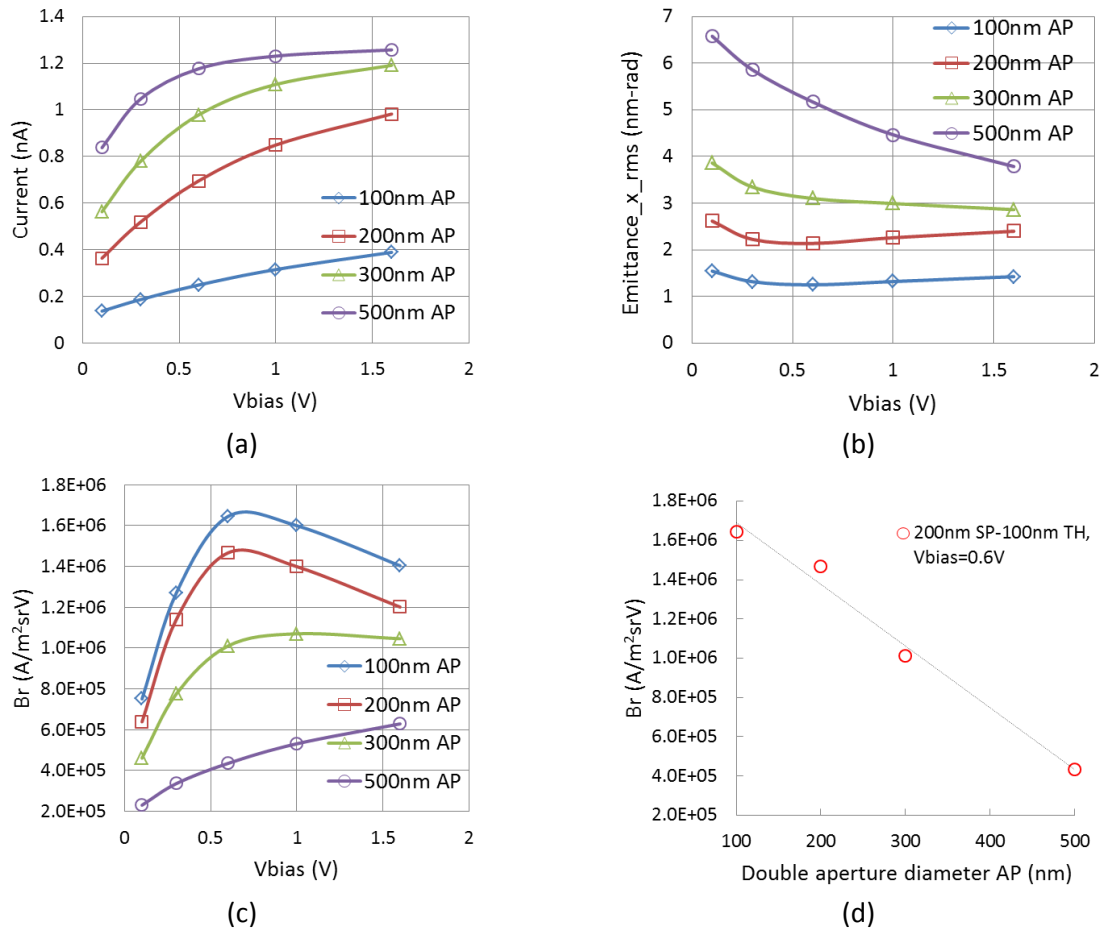


Fig. 3-19 Calculated ion current output (a), emittance (b), and reduced beam brightness (c, d). Given SP=200 nm, TH=100 nm, and AP is varied from 100 to 500 nm. Initial ion positions set according to the simulated gas particle density results. The results in (d) assumes for a fixed gas chamber bias voltage of 0.6 V. For all calculations T=293 K is assumed.

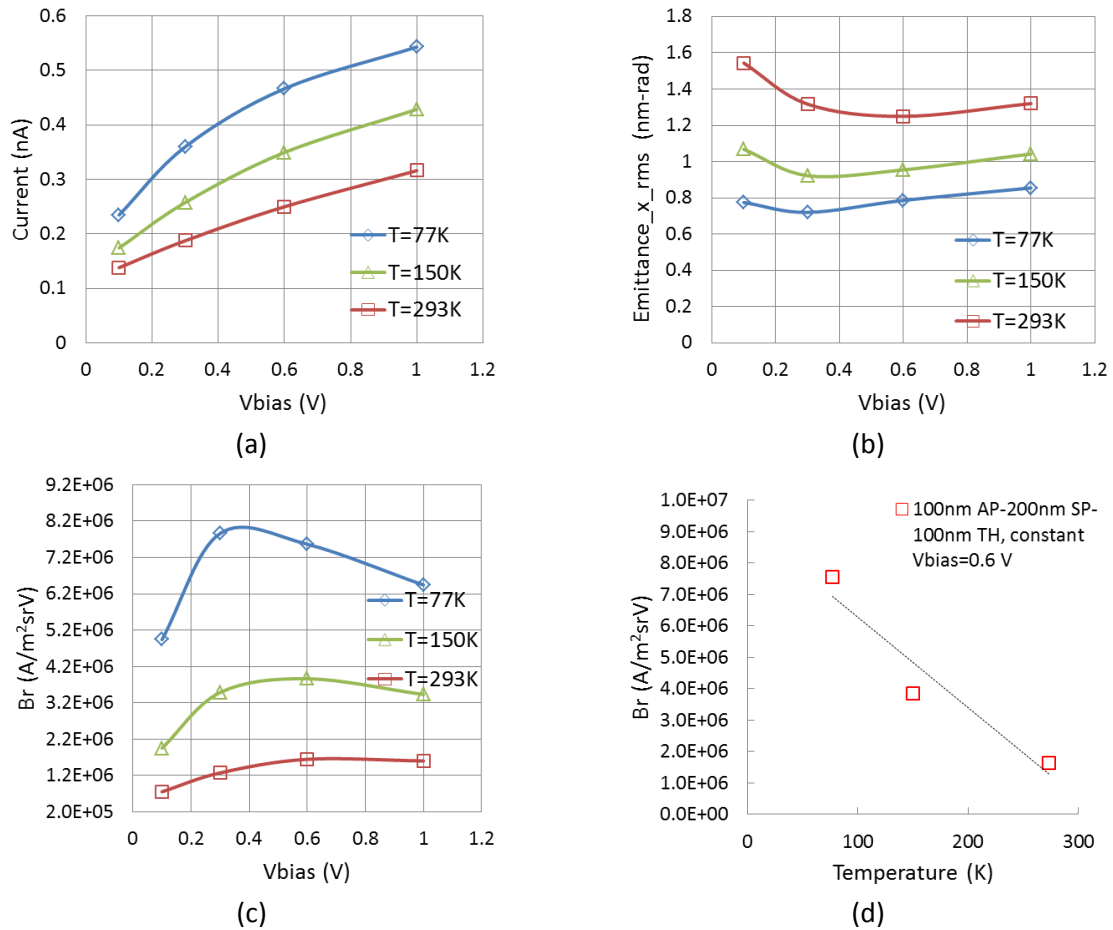


Fig. 3-20 Effect of the source temperature on the transmitted ion current (a), emittance (b), and reduced beam brightness (c, d). Given AP=100 nm, SP=200 nm, and TH=100 nm. Initial ion positions set according to the simulated gas particle density results. The results in (d) assumes for a fixed gas chamber bias voltage of 0.6 V.

gradual increase in the transverse velocity spread as more ions are allowed to transmit and also by the aberrations from the lens effect of the gas chamber. Because the emittance grows at a faster rate than the current, the beam brightness eventually decreases with the bias voltage. Figs. 3-17 and 3-19 clearly indicates that the transition takes place for the emittance and brightness differs depending on the gas chamber dimensions.

Here, one important concept to realize is that the distribution of the transverse velocity components essentially defines the beam divergence or beam solid-angle Ω of the NAIS. Shown above is that the gas chamber aperture limits ion beam current but it can also effectively lower the beam solid angle, in which case, it can possibly provide a very high angular intensity ($=I/\Omega$). This is a crucial aspect in understanding why the reduced beam brightness concluded in this section can be comparable to that of the Langmuir brightness model in Chapter 2 even though the output current considered in both models are very different.

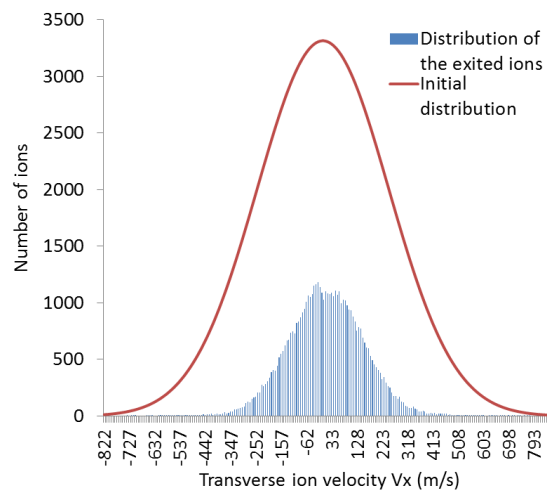


Fig. 3-21 Transverse velocity distributions of the ions initially assigned in the ionization volume (red) and the ions exited the gas chamber (blue). AP=100 nm, SP=200 nm, TH=100 nm, $V_{\text{bias}}=0.6$ V, and argon gas @T=293 K. Note that the area under the curve represents the total number of ions in each case.

Given a fixed incident electron beam diameter, the ratio between the gas chamber aperture size (AP) and the spacing (SP) is found to be a useful factor in generalizing the source performance including beam brightness. Both AP and SP, along with the gas chamber bias voltage, obviously affect the amount of the current exiting the gas chamber as they limit the ‘angle of view’ for the ions. Similarly, both influence the beam emittance by limiting the overall beam divergence angle (hence the beam size at the test plane) out of the gas chamber. It can be generalized that a combination of a large aperture diameter and a small spacing ($AP > SP$) yields a relatively high current but with a relatively low beam brightness while a combination of a small aperture and a large spacing ($AP < SP$) yields a relatively small current but with a relatively high beam brightness.

Note that the calculation results shown in Fig. 3-18 are from the simulations based on the uniform gas particle density. Again, the results are very similar to those from the simulations using the results from the gas simulations.

The simulation results in Fig. 3-20(d) confirm that the source reduced brightness of the NAIS is approximately inversely proportional to the source temperature just as predicted by the Langmuir brightness equation.

Lastly, all the results presented here are only applicable for argon gas. Ion beam current and the reduced brightness of other noble gas species should scale relatively to the ionization efficiencies given in Table 2.1.

3.4.4 Virtual source size

Ions emerge from the NAIS gas chamber with slightly varying angles relative to the axis of propagation due to a spread in the random transverse components of the intrinsic thermal velocities and that the extraction field strength is not completely uniform within in the gas chamber. Also, because the ions emerge from a volume, not from a plane, the virtual source size is likely to be larger than the beam diameter of the incident electron beam.

Fig. 3-22 illustrates a virtual source defined by projecting the tangents to the ion trajectories back to the location where they form a waist. Figs. 3-23 and 3-24 show details on how the virtual source size and its location are affected by the gas chamber bias voltage, spacing and aperture size. In summary, the virtual source is found to form slightly behind the gas chamber (opposite to the beam propagation direction) and that, at low bias voltages, the diameter of the ion exit aperture appears to be the more accurate indicator for the virtual source diameter than the diameter of the incident electron beam. Initially the virtual source becomes smaller as the bias voltage is increased but at some point, it starts to increase due to the increasing spread in the ion transverse velocities and the increasing particle transmission rate from the back side of the gas chamber.

Based on the results shown in the figures, the virtual source size of the NAIS can be approximated to the diameter of the incident electron beam only when the aperture is also comparable to the electron beam size.

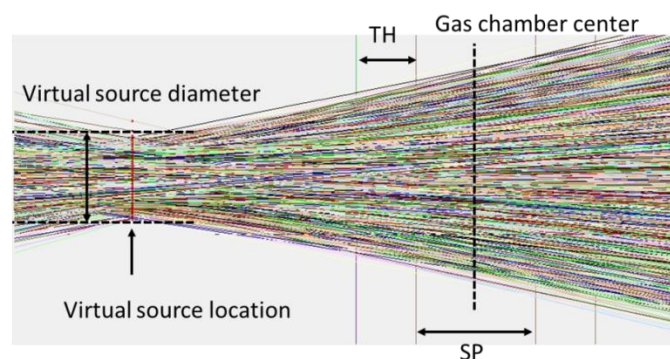


Fig. 3-22 Tangent lines to the particle trajectories at the test plane traced back toward the source.

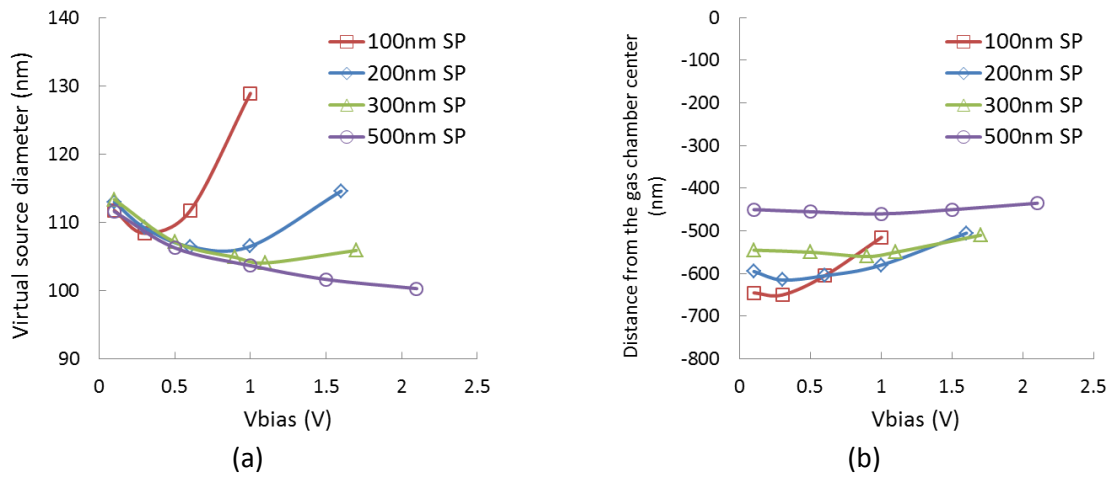


Fig. 3-23 Virtual source size (a) and location (b) as a function of the bias voltage for various gas chamber spacings (given AP=100 nm, TH=100 nm, T=293 K). The diameter of the fully collimated incident electron beam is assumed to be 100 nm.

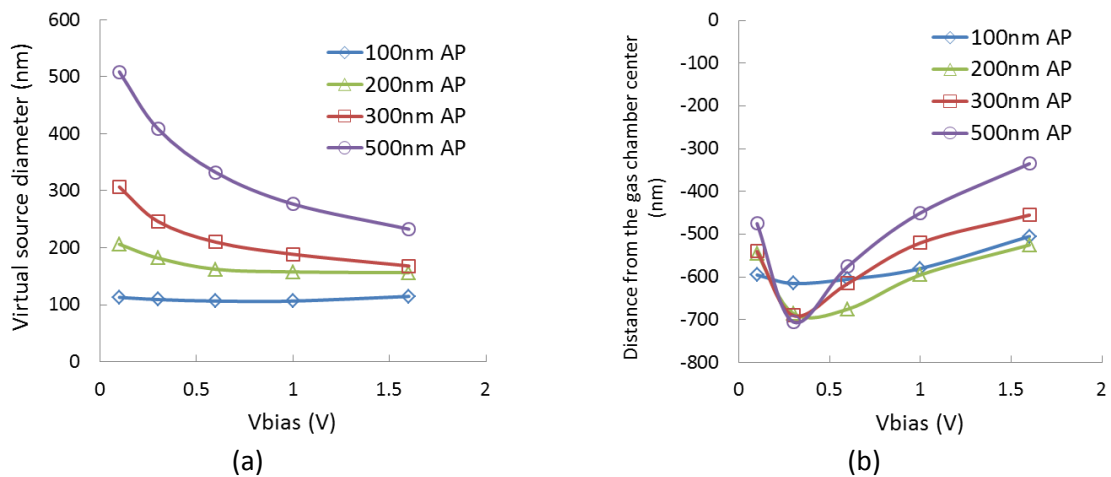


Fig. 3-24 The virtual source size (a) and location (b) as a function of the bias voltage for various gas chamber aperture sizes (given SP=200 nm, TH=100 nm, T=293 K). The diameter of the fully collimated incident electron beam is assumed to be 100 nm.

3.5 Further work

Two additional topics on which further simulation work could be beneficial are: (1) evaluating the performance of the asymmetrical double-aperture configuration and (2) exploring for high gas pressure operation ($k_n < 1$) to increase the overall source current.

The present simulation study has clearly shown that the performance of the NAIS strongly depends on the gas chamber geometry, in particular the double-aperture size. So far all the results are based on the symmetrical gas chamber configuration having two identical aperture size, however it would be very interesting to repeat the simulation work for gas chambers having two different aperture size. Because the gas particle density distribution would be asymmetrical and the

lens effect would be somewhat different in the asymmetrical configuration, the distribution of the ion transmission from the front/middle/back of the gas chamber would also be different. It may be possible to utilize the asymmetrical design to reduce the bimodal ion energy distribution without sacrificing output beam current and the reduced brightness.

The work carried out in this chapter has been strictly limited to a gas flow in the free molecular flow regime in order to simplify the condition for non-ion-neutral collisions. However, inside the gas chamber, because the ions are quickly accelerated and on average they are moving much faster than the neutral gas atoms inside the gas chamber, it would be possible to increase the gas pressure by at least $\sim\sqrt{2}$ times and still avoid ion-neutral collisions. Obviously, the crucial and challenging part of the investigation will be including gas neutral-neutral collisions in the gas simulation model and re-evaluating the neutral density distribution in the gas chamber.

3.6 Conclusions

One of the variables that play a critical role on the performance of the NAIS is the density of neutral gas atoms in the interaction region of the miniaturized gas chamber. Because the NAIS incorporates a gas chamber with a pair of apertures, the gas particle density distribution within the gas chamber is expected to be non-uniform and extending out through the apertures. Monte Carlo gas simulations based on the steady state free molecular gas flow are performed to quantify the gas particle density distribution and to investigate its dependence on the double-aperture size, the membrane thickness, and the gas chamber spacing. The gas simulation results indicate that in general the gas chamber aperture diameter needs to be kept on the order of the spacing or smaller ($\sim AP \leq SP$) for maintaining a high gas density inside the gas chamber while allowing only a marginal amount of gas leakage through the double-aperture.

By assuming that the current inside the incident electron beam is uniformly distributed and that the ionization occurs in a dilute gas filled small volume, the particle density distribution found from the gas simulation can be used directly to define the spatial distribution of the ions 'born' within the interaction region. With the initial positions known with respect to the geometry of a gas chamber, ions are then given initial energies based on an assumed gas temperature and their trajectories under the influence of a gas chamber extraction field are investigated using a commercial ion optics simulation program. The ion trajectory simulation directly provides the rate of ion transmission through the ion exit aperture and individual ion positions and velocities along the trajectories, which are then used to estimate the amount of current, ion energy distribution, and the reduced beam brightness of an ion beam arising from a NAIS gas chamber.

It is found through simulations that the gas chamber bias voltage, dimensions, and temperature are also critical variables that influence on the beam current output, ion energy distribution, and reduced brightness. However, the gas chamber bias voltage is particularly important as it can single-handedly influence all three source parameters at once and can be easily adjusted during source operation. Increasing the gas chamber bias voltage generally increases the current output, but also increases the energy spread. If the bias voltage is too high, it can also decrease the beam brightness. Implementing a larger aperture size is another way to increase the current output, however this also reduces the beam brightness. The simulation results suggest that the best way to enhance both the current output and beam brightness is by lowering the gas temperature.

Given the incident electron beam having a diameter of 100 nm we find that the optimum chamber dimensions that provide the best source reduced brightness are ~ 100 nm in aperture diameter, ~ 200 nm in spacing and ~ 100 nm in membrane thickness. Based on these gas chamber dimensions, argon gas at room temperature, and a 1 keV impact electron beam of 100 nA, the simulation results have shown that the NAIS is capable of providing a maximum ion beam current up to 300 pA, an energy spread well below 1 eV, and the reduced brightness $\sim 2 \times 10^6$ A/m²srV.

Overall, the outcomes of the simulation study confirm that the gas chamber bias voltage effectively determines the energy spread of the NAIS and the maximum reduced brightness estimated based on the Langmuir brightness equation is reasonably accurate.

Acknowledgment

This research is supported by the “Stichting voor Fundamenteel Onderzoek der Materie (FOM)”, which is financially supported by the “Nederlandse Organisatie voor Wetenschappelijk Onderzoek” and FEI Company.

References

- [1] J. Peatross and D. D. Meyerhofer, Novel gas target for use in laser harmonic generation, *Rev. Sci. Instrum.*, **64**(11), 3066 (1993)
- [2] www.simion.com
- [3] D. H. Davis, Monte Carlo calculation of molecular flow rates through a cylindrical elbow and pipes of other shapes, *J. Appl. Phys.* **31**, 1169 (1960)
- [4] D. J. Santeler, New concepts in molecular gas flow, *J. Vac. Sci. Technol. A* **4** (3) (1986)
- [5] A. Roth, *Vacuum Technology* (2nd Edition), Elsevier Science BV, The Netherlands, 1990
- [6] J. Greenwood, The correct and incorrect generation of a cosine distribution of scattered particles for Monte-Carlo modeling of vacuum systems, *Vacuum* **67**, 217-222 (2002)
- [7] M. Reiser, *Theory and Design of Charged Particle Beams* (2nd Edition), (Wiley, 2008)

4 ■ Miniaturized Gas Chamber Design and Fabrication

We present two different gas chamber designs, each incorporating a different MEMS micromachining technology. The first design, known as the double-chip design, follows a relatively straightforward method of fabricating a thin metal membrane on a substrate chip using the bulk-micromachining technology and then combining two different chips to form a single gas chamber. The second design, which is called the single-chip design and is still in the alpha phase of development, follows a fabrication method based on the surface micromachining technology in which all the gas chamber features (two membranes and a gas channel in-between) are built on a single substrate chip. In addition to detailing and highlighting the differences in the fabrication steps of each design, we report our current progress in the prototype fabrication and testing.

4.1 Introduction

The use of a miniaturized gas ionization chamber is the underlying concept that differentiates the Nano-Aperture Ion Source from traditional electron impact gas ion sources both in terms of design and performance. The sub-micron features of the gas chamber are unique and essential for providing high quality ion beams suitable for high resolution FIB applications. Developing a reliable fabrication method of the gas chamber, therefore, is a critical step towards building a prototype ion source and demonstrating the new source concept.

Putting it simply, the miniaturized gas chamber can be described as a micro device consisting of two thin parallel plates separated by a small spacing (the gas chamber spacing) set by a thin layer of an electrically insulating material. The gas chamber includes a pair of small concentric apertures (the double-aperture) for providing passage for electrons and ions to enter and exit the gas chamber and an additional hole for feeding gas into the gas chamber. Fig. 4-1 illustrates the basic layout of the gas chamber design and specifies our target dimensions.

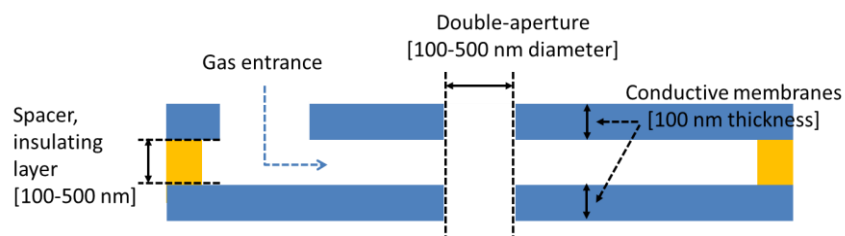


Fig. 4-1 Basic layout of the miniaturized gas chamber and target dimensions.

Naturally, employing Micro-Electro-Mechanical Systems (MEMS) techniques^[1,2] is an obvious choice when it comes to fabricating devices with sub-micron features. MEMS fabrication techniques are highly specialized micromachining processes that provide tremendous advantages in making small structures with detailed features under tight dimensional control. They also offer cost advantages of batch manufacturing with very high reliability and reproducibility. Traditionally, MEMS technology has been dominantly used in manufacturing of small sensors and actuators for consumer electronics and automobiles, but nowadays, the application of MEMS technology to improve instruments of charged particle optics are also becoming increasingly visible^[3-5].

In this project we specifically incorporate bulk micromachining and surface micromachining technologies^[6,7] for fabricating miniaturized gas chambers. These are two commonly utilized MEMS micromachining technologies suitable for fabricating structures involving thin membranes. The bulk micromachining involves the selective removal of the substrate material in order to leave behind the desired geometries of the miniaturized functional components. Comparatively, the surface micromachining involves the deposition of a thin film (the sacrificial layer) which is initially used as a structural layer but later removed to release an actual functional component(s). Both technologies are commonly accompanied by oxidation, diffusion, ion implantation, chemical vapor deposition (CVD), sputtering, lithography, and etching for thin film layers and substrate manipulations.

In the following we present fabrication methods of two distinctly different gas chamber designs – namely the double-chip design and the single-chip design. The double-chip design is based on the bulk micromachining technology and the single-chip on the surface micromachining technology. We highlight the differences in each design and detail the results in prototype

fabrication. In addition to our current progress, and we provide an outlook on our future gas chamber development efforts.

4.2 The double-chip design

The double-chip gas chamber design follows a straightforward method of combining two pre-fabricated chips called the ‘upper’ and ‘lower’ chip. Each chip is at first processed on different wafers for fabricating a very thin metal membrane (~100 nm) using bulk micromachining techniques but later stacked and glued together to form a complete gas chamber. Although each chip has a slightly different footprint size (7.5 x 10.4 mm for the *upper*, 11.4 x 11.4 mm for the *lower*) and a different mask layout resulting in different geometrical features and sizes, both chips essentially go through the same fabrication method. The written descriptions on the fabrication steps below are generalized to apply to both chip fabrication, however any geometric differences between the upper and lower chip are clearly indicated in the figure(s) describing each step.

4.2.1 Fabrication process

Step 1: Si₃N₄ layering and fabrication of etch masks

The upper and lower chips are fabricated using 300 μm thick silicon <100>-oriented wafers. The wafers are coated with 100 nm LPCVD (low pressure chemical vapor deposition) Si₃N₄ that later functions as a mask and a spacer. To fabricate metal membranes, a gas entrance window, and alignment windows, both lower and upper chip wafers are first spin-coated with the positive ZEP-520 electron-beam resist (spun at 1000 rpm) and then baked for 30 min at 175 °C. In the following step, the photoresist is exposed with a dose of 300 μC/cm² using EBPG (electron beam pattern generator Vistec 5000+, 100 keV). After the wafers are developed in n-butyl acetate for 90 sec and rinsed in MIBK:IPA (9:1), the patterned Si₃N₄ (by the e-beam resist mask) is dry-etched (using 25 sccm CHF₃ and 25 sccm Ar at 50 W RF power and 8 μbar pressure, Leybold Hereaus parallel plate RIE etcher). After this step the resist is removed by dipping the wafers in HNO₃. Fig. 4-2 represents the cross sections of the upper and lower chips at the end of Step 1.

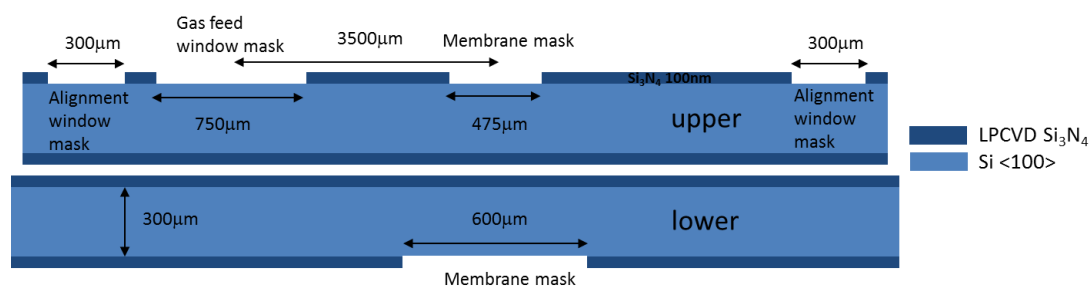


Fig. 4-2 Si₃N₄ layering and fabrication of membranes, gas feed, and alignment window masks.

Step 2: Wet etching and metallization

In this step the wafers are etched in KOH solution (1 kg KOH/ 2.5 liter H₂O) at 95 °C. After etching, 5 metal layers - 2-5 nm Cr, 60 nm Mo, 10 nm Pt, 10 nm Au and 20 nm Mo - are evaporated (by using a metal evaporator Temescal) one by one on the processed side of the wafers to form a membrane layer (Fig. 4-3). Our experience has shown that such a combination of metal layers reliably results in wrinkle-free metal membranes (see section 4.2.2 for details).

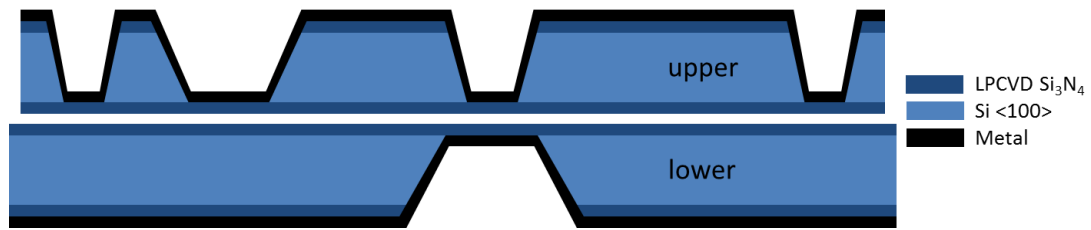


Fig. 4-3 After KOH etching and metal deposition.

Step 3: Etching to form the metal membranes, gas channel, and alignment markers

To release the metal membranes and create the gas channel and alignment markers (the alignment markers apply to the lower chip section only) from the Si_3N_4 layer, a photoresist is spun on both wafers on the flat side which has not been processed yet. The same photoresist ZEP-520 and the same EBPB process used in Step 1 are applied again to define etching areas. After the exposure and development, the unprotected Si_3N_4 area is etched in AMS 100 Bosch until the metal layer is reached. In this step the gas channel is created in the Si_3N_4 layer and the full-metal membranes are exposed on both the upper and bottom chips as shown in Fig. 4-4. On the lower chip, special alignment markers are additionally exposed. The cleaning of the photoresist takes place in an oxygen plasma stripper (Tepla). Figs. 4-5(a) and (b) are optical images showing two different areas along the etched gas channel on the upper chip.

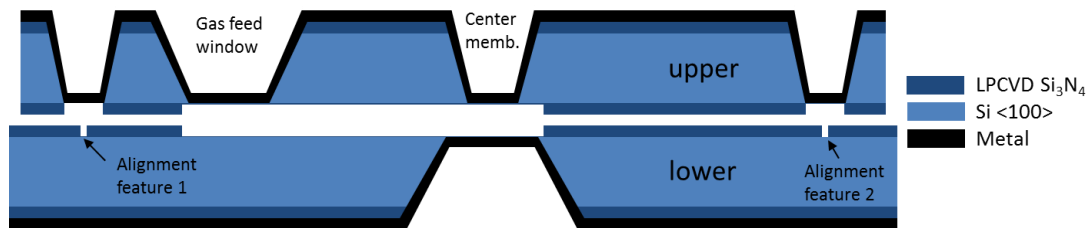


Fig. 4-4 The metal membranes are exposed and the gas channel and two alignment markers (on the lower chip only) created after Si_3N_4 dry etching.

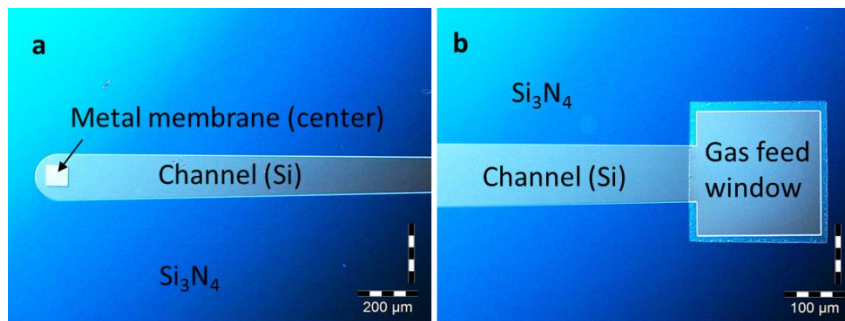


Fig. 4-5 Optical images showing the etched gas channel on the upper chip near the center metal membrane area (a) and the gas feed window area (b). The gas channel etched on Si_3N_4 actually starts from the gas feed window and extends all the way including the center metal membrane area. Although not shown, the gas channel etched on the lower chip coincides to the upper chip when stacked together.

Step 4: Membrane alignment and gluing

The metal membranes covering the gas entrance and alignment windows of the upper chip can easily be opened up by puncturing with a sharp needle. The upper and lower chips are loaded in a special alignment/glue fixture, and while watching under an optical microscope, the upper chip is moved carefully until the two alignment markers inscribed on the lower chip are visible through the corresponding alignment windows (see Fig. 4-6). Once aligned, the chips are clamped down and high vacuum compatible glue (Tra-Bond 2248, Tra-Con Company) is applied along the entire edges of the upper chip and in the alignment windows for gas sealing (Fig. 4-7).

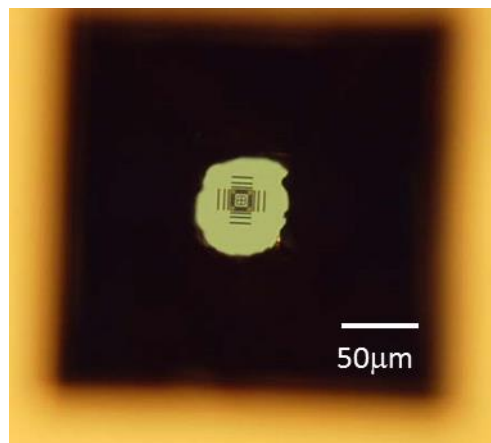


Fig. 4-6 *Optical image:* optical microscope view of a cross-shaped alignment marker of the lower chip showing through an alignment window of the upper chip.

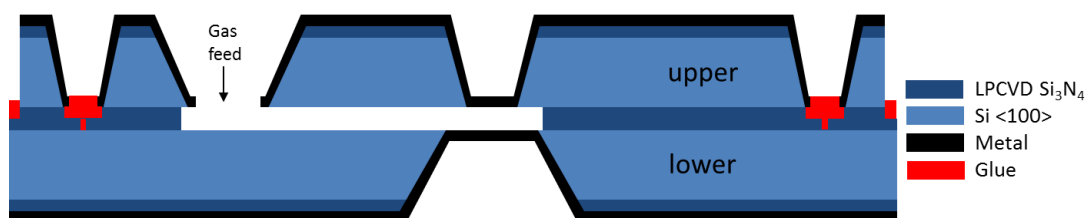


Fig. 4-7 After the membrane alignment and gluing.

Step 5: Double-aperture FIB milling

In the final step, a double-aperture (100-500 nm in diameter) on the aligned metal membranes is fabricated using a conventional FIB system (100 pA, 30 keV, 5 to 60 sec, FEI Quanta™ 3D FEG Dualbeam). Fig. 4-8 illustrates the cross section of the gas chamber at the end of this step. Fig. 4-9 shows SEM and optical images of completed gas chambers.

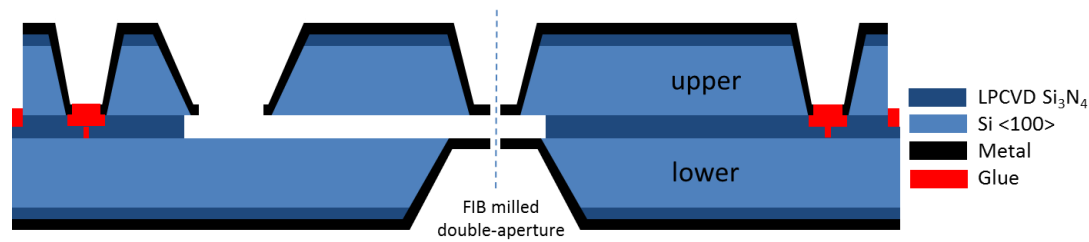


Fig. 4-8 Electron and ion entrance and exit apertures (the double-aperture) are fabricated on the metal membranes using a conventional FIB machine.

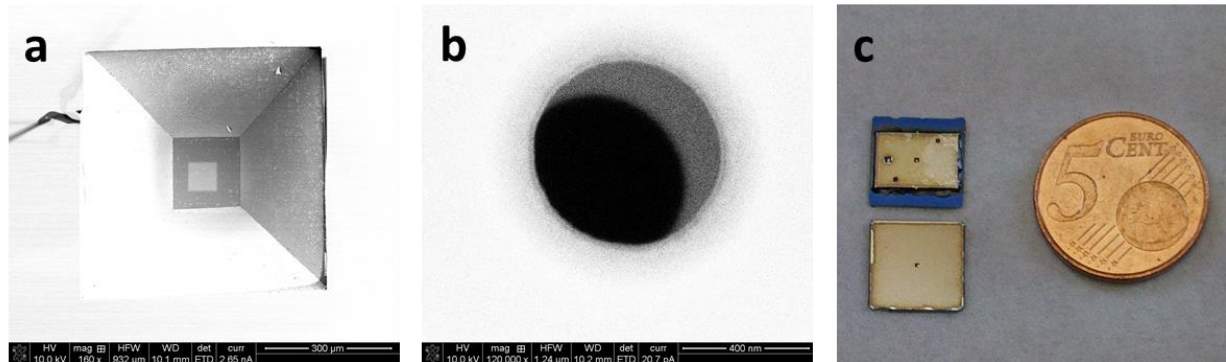


Fig. 4-9 SEM micrographs: (a) The upper chip membrane clearly showing through the larger membrane of the lower chip. (b) A tilted view of a double-aperture (fabricated by FIB milling) clearly showing a small separation between the metal membranes. Optical image: (c) Top and bottom view of the completed double-chip gas chambers.

4.2.2 Membrane buckling due to internal stress and oxidation

In the design of the gas ionization chamber two thin conducting membranes confine gas and gas ionization and also create an extraction field to guide the ions out of the gas chamber when a gas chamber bias voltage is applied. In the case of the double-chip design, a full metal membrane is created on each chip by removing the underlying Si_3N_4 layer deposited on the Si substrate. Our preferred material for the metal membrane is molybdenum as it's known for high strength and good electrical conductivity and vacuum compatibility^[8,9]. For metallization, the deposition by evaporation is favored over sputtering because the lower operating temperature and pressure during the evaporation process generally leads to lower internal stress in the deposited metal layer. A membrane thickness of 100 nm is targeted as our experience has shown difficulty keeping the thinner membranes intact through the entire gas chamber fabrication process. Although the thick membranes would be beneficial considering mechanical stability under gas load, membranes thicker than 100 nm are not desirable in our case as the ion transmission out of the gas chamber would become greatly reduced.

However, earlier on we noticed that 100 nm thick molybdenum membranes prepared through evaporation often experience buckling after some time. This is not a desirable effect since the buckling can change the gas chamber spacing and at worst, it can cause an electrical short between the membranes or even burst. We conclude that the buckling is the result of increased internal stress caused by oxidation in the atmosphere as we found that some membranes of a same

fabrication batch showed no sign of buckling as long as kept in vacuum while the ones exposed to air often show wrinkling in the matter of hours or days (see Fig. 4-10).

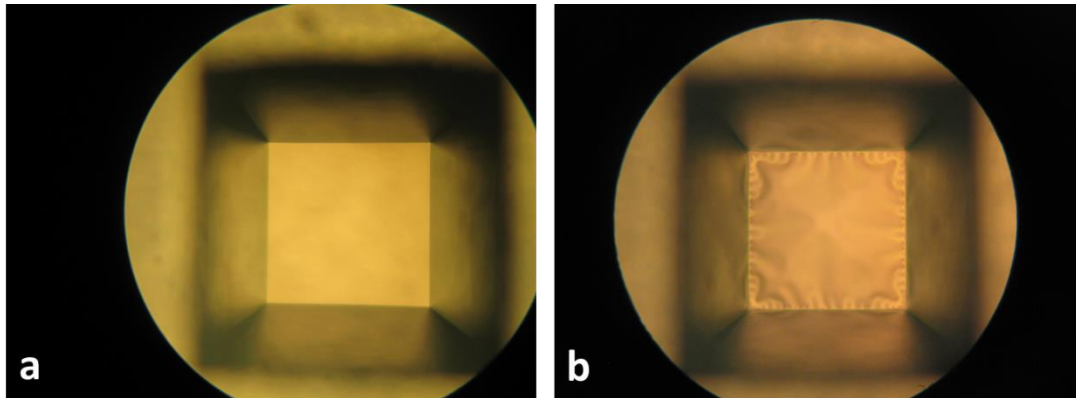


Fig. 4-10 Molybdenum membrane buckling over time: (a) Just after the fabrication process and (b) 5 days later. The membrane dimensions $\sim 400 \times 400 \mu\text{m}$.

Further investigation indicated the buckling effect is dependent on the thickness of the molybdenum layer exposed to atmosphere. Applying the same membrane etching technique described in Step 3 of Section 4.2.1 in a simplified flat membrane testing experiment (see Fig. 4-11), it was found that a molybdenum layer thinner than 20 nm shows good resistance to buckling when exposed to the atmosphere. Our solution for producing a 100 nm thick flat metal membrane based on molybdenum material is, therefore, to adding other thin film layers for extra thickness but limit the thickness of Mo layer on the air side to 20 nm. Experimentally we found that combining five different metal layers - 2-5 nm Cr, 60 nm Mo, 10 nm Pt, 10 nm Au and 20 nm Mo - reliably yields a flat membrane of 100 nm thickness and stays flat even after a long exposure in the atmosphere. The 60 nm thick Mo deposited beneath Pt and Au doesn't seem to cause any problem as it is well protected from direct exposure to the atmosphere. Table 4-1 lists different molybdenum thickness and several different combinations of other thin film materials that we tried with molybdenum and the outcome on the flatness when the membranes are exposed to the atmosphere.

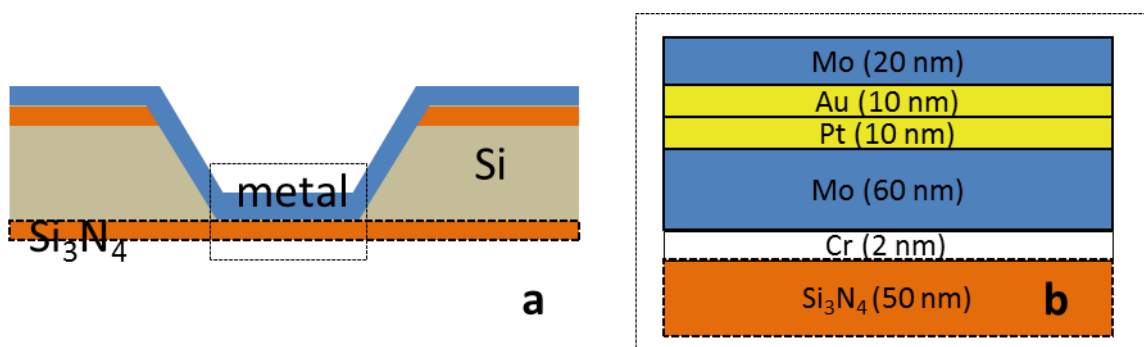


Fig. 4-11 Molybdenum membranes with different thickness and combinations of molybdenum and other thin film materials are tested for membrane flatness. In each case, the metal layer(s) is evaporated on the backside of the Si_3N_4 membrane ($380 \times 380 \mu\text{m}^2$, 50 nm thick) and then the lower Si_3N_4 layer is dry-etched.

Table 4-1. Summary of the flat membrane test results (thickness in nm). Note that thin films were deposited on a 50 nm thick Si_3N_4 base layer sequentially following the order of materials appearing from left to right. Therefore, the first Mo column indicates the molybdenum layer hidden beneath other thin films and only the last Mo column indicates the thickness of molybdenum prone to air exposure. After the deposition(s), the Si_3N_4 layer was etched away and membranes were inspected for its flatness over a two-month period.

Cr	Mo	Pt	Au	Mo	Results
2	-	-	-	500	Wrinkled
2	-	-	-	200	Wrinkled
2	-	-	-	150	Wrinkled
2	-	-	-	100	Wrinkled
2	-	-	-	75	Wrinkled
2	-	-	-	20	Flat
2	60	20	-	20	Wrinkled
2	20	-	60	20	Wrinkled
2	60	10	10	20	Flat

4.2.3 The double-chip gas chamber spacing issues

The gas chamber spacing can be measured by direct FIB cross-sectioning (see Fig. 4-12 for example) or simply back-calculated from SEM images of the double-aperture taken at two different tilt angles. The spacing correlates to a change in the amount of an aperture (*the lower*) edge showing through the other aperture (*the upper*) when the gas chamber is tilted by a certain amount. The latter method is quite advantageous as it is non-invasive and even an *in situ* measurement for a pressurized gas chamber is possible.

Employing both techniques we determine that the gas chamber spacing of our first prototypes based on the double-chip design typically ranges from 1 to 2.5 μm although the fabrication process flow is designed for 200 nm. The larger-than-expected spacing is caused mostly by glue seepage between the two chips and particle contamination during the fabrication process (Fig. 4-13).

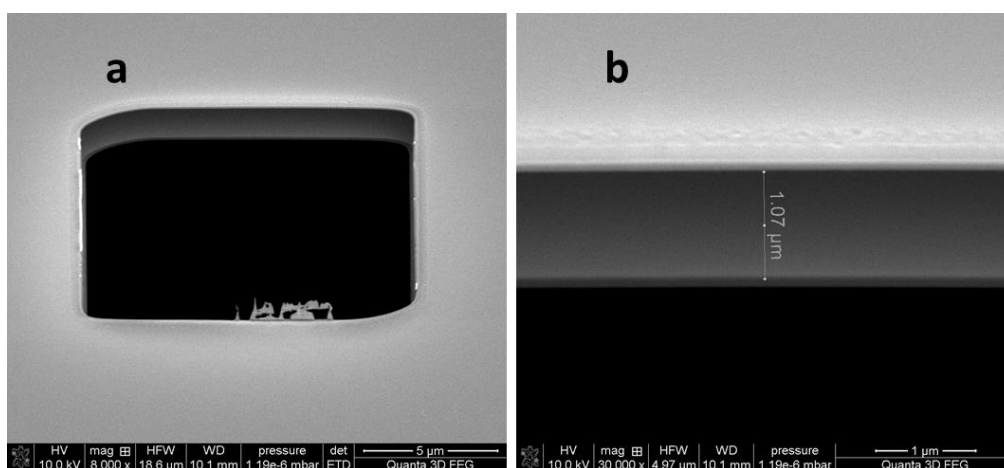


Fig. 4-12 Gas chamber spacing measurement by FIB cross-sectioning. *SEM micrographs*: (a) Tilted view of a cross sectioned area and (b) gas chamber spacing measurement using SEM.

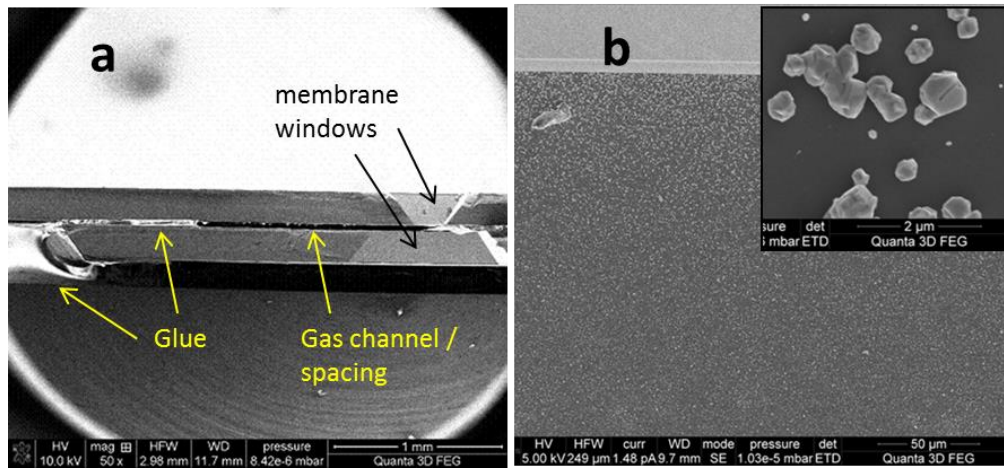


Fig. 4-13 Two culprits for the larger-than-expected gas chamber spacing. *SEM micrographs:* (a) glue seepage between the two chips and (b) micron-sized particles often found on the substrate chips. The particles shown in (b) are Fe and believed to originate from a contaminated KOH etching bath.

An additional increase in the gas chamber spacing can result when membranes are exposed to high differential gas pressure causing membrane load deflection. A simple test performed to demonstrate this behavior is shown in Figure 4-14. A 100 nm thick membrane with visible wrinkles was placed on a vacuum setup. While the top side of the membrane stayed exposed to the atmosphere, lowering the vacuum pressure underneath the membrane stretched the membrane (caused by the load deflection) and the wrinkles began to disappear.

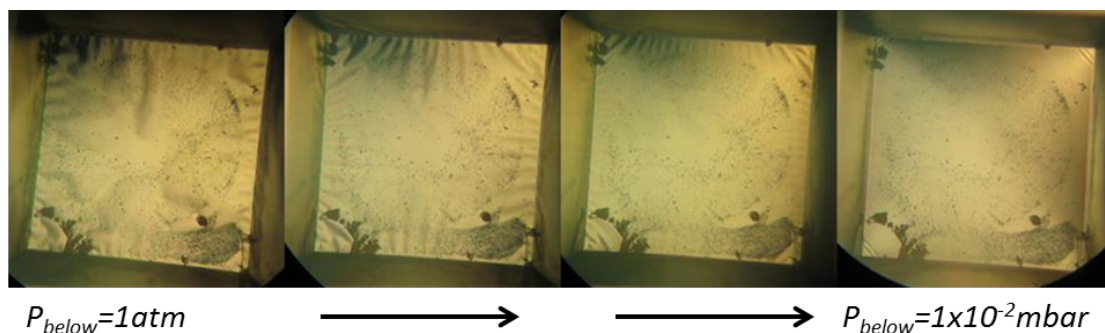


Fig. 4-14 Disappearing of the wrinkles of a 100 nm thick membrane (250 x250 μm) due to ‘stretching’ (or load deflection) when the gas pressure (P_{below}) under the membrane is gradually lowered while the pressure above is at atmospheric pressure.

For a quantitative analysis applied to our actual gas chamber design, a test setup was configured on a tiltable SEM stage to image the double-aperture at various tilt angles while the gas chamber is pressurized. Fig. 4-15 shows a series of double-aperture SEM images of a prototype gas chamber at different gas chamber pressures (while the background SEM chamber pressure in the $\sim 10^{-6}$ mbar). It’s evident that the amount of the lower aperture edge showing through the upper aperture is changing as the result of changing gas chamber spacing. The gas chamber consisted of square membranes of 120x120 μm (*upper*) and 70x70 μm (*lower*). The measured spacing increase as a function of the gas chamber pressure is shown in Fig. 4-16. As a point of reference, theoretical

calculations of the spacing increase for a gas chamber with evaporated molybdenum membranes under the same geometric conditions are also shown. The theoretical calculations are based on the analytical equations given in Ref. [10] in which the load deflection of a square membrane is described in terms of the membrane width W and thickness t , Young's modulus E , Poisson's ratio ν , the residual stress σ and the gas pressure P . For our analysis, we assume generally accepted values of $E=320\text{ GPa}$ and $\nu=0.31$ for the molybdenum thin film. Yoder *et al.* [11] has investigated the residual stress of the evaporated molybdenum film and found that it can range from 0.34 to 1.44 GPa depending on the evaporation process. If the typical molybdenum material properties are assumed for our metal membranes (our metal membrane is 80 % molybdenum), the results in Fig. 4-16 suggest that the residual stress in our membrane is estimated to be about 0.85 GPa. In such case, we infer that the load deflection induced gas chamber spacing increase becomes almost negligible ($< 13\text{ nm}$) even at our maximum operating gas chamber pressure of 750 mbar if the membranes size is reduced to $< 10\times 10\ \mu\text{m}$ (Fig. 4-17).

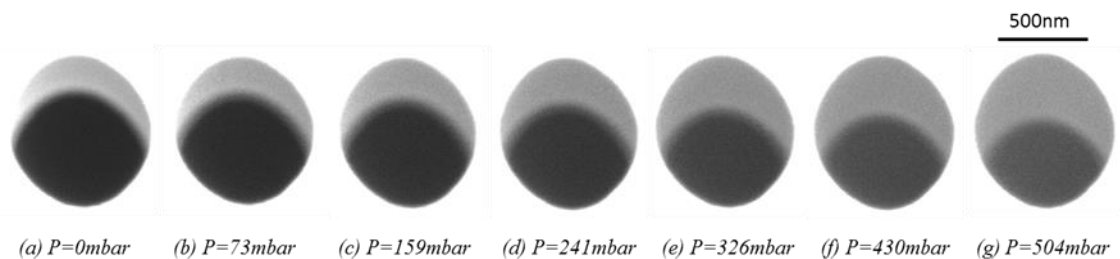


Fig. 4-14 SEM images of the double-aperture showing a gradual increase in the gas chamber spacing when the gas chamber pressure is gradually increased.

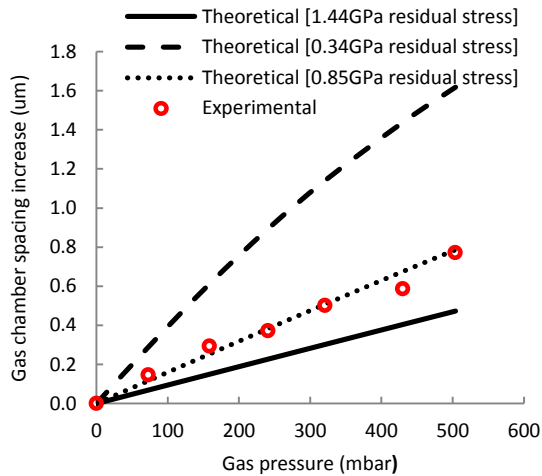


Fig. 4-16 Dependence of the gas chamber pressure on the gas chamber spacing for a gas chamber having square membranes of $120\times 120\ \mu\text{m}$ (upper) and $70\times 70\ \mu\text{m}$ (lower) and $t=100\text{ nm}$.

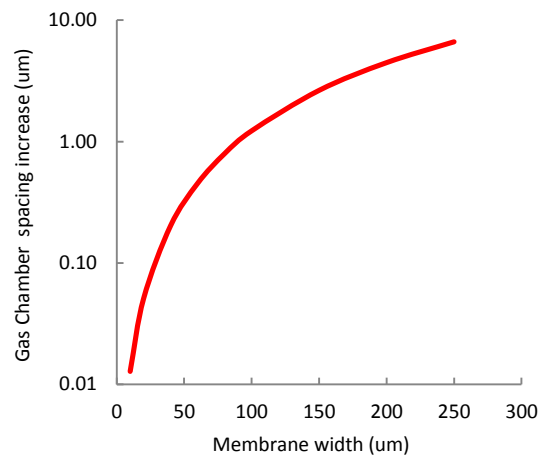


Fig. 4-17 Gas chamber spacing increase from the membrane load deflection as a function of the square membrane width assuming $t=100\text{ nm}$, $E=320\text{ GPa}$, $\sigma=0.85\text{ GPa}$, $\nu=0.31$, and $P=750\text{ mbar}$.

4.2.4 Prototype evaluation and future improvement

The fabrication techniques involved in the double-chip design are relatively simple and can yield highly reproducible results. After some adjustments to the membrane material and thickness,

the current fabrication recipe has been established to yield flat 100 nm thick full metal membranes. These membranes are also shown to be strong and fully capable of handling a differential gas pressure of at least 1 atmosphere and fully compatible for use in a high vacuum environment. Our calculation shows that the gas pressure induced load deflection of the membrane can be sufficiently minimized by adjusting the size of the membrane.

A number of prototype gas chambers have been already used for the NAIS proof-of-concept experiments and their performance evaluated. They all have sufficiently shown to function as gas ionization chambers and extract ions in response to an applied gas chamber bias voltage. Details of the experiments and the test results are available in Chapter 5.

Overall, the straightforwardness of the fabrication method, and the robustness, reproducibility, and reliability of the double-chip design are very attractive, however resolving the gas chamber spacing issues remains to be the last puzzle before releasing the design. We have identified both gluing and particle contamination to be the main sources for the larger-than-expected gas chamber spacing with the current fabrication procedures, however, the gluing seems to be the much bigger issue as the particle contamination should be resolved by conducting fabrication and assembly in a more strict and cleaner environment (i.e. going from the current Class 10,000 to Class 100 cleanroom). Apart from trying to reduce glue seepage by using a better gluing fixture and using a high viscosity glue, two possible glue-less approaches are proposed.

One possible approach is to use a mechanical means to encapsulate and clamp down to keep the gas chamber pieces together. The encapsulation can be combined with gas supply tubing and O-rings which can be strategically placed to make gas and vacuum sealing. The idea is illustrated in Fig. 4-16.

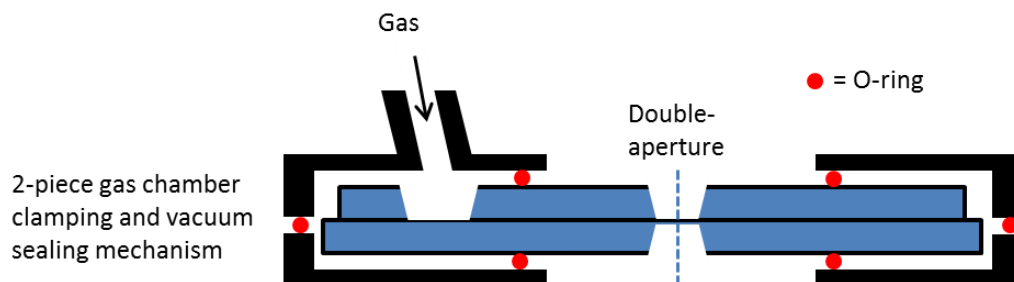


Fig. 4-16 Mechanical design of clamping the double-chip based gas chamber instead of gluing. The O-rings provide vacuum sealing.

Another possibility to eliminate gluing is to join the wafer chips by direct wafer bonding ^[12]. The wafer bonding is a widely used technique for joining silicon-to-silicon wafers but in recent years the method has been extended to join two wafers with a LPCVD Si₃N₄ interface (up to 1 μm thickness) ^[13-15]. The work in Ref. [15] suggests that annealing temperature as low as 400 °C can create a bonding strength exceeding 2 Jm⁻² between the LPCVD Si₃N₄ interfaces. The wafer bonding process may be implemented in-line with the rest of membrane fabrication process, in which case the exposure to particle contamination should be reduced significantly. However, it should be noted that the bonding ability is limited by surface roughness (preferred mean roughness < 0.5 nm) and the curvature of the wafers.

4.3 The single-chip design

In this section we detail the fabrication method of the single-chip design. This design is an alternative, yet more elegant and simpler approach compare to the double-chip design as this requires no post-fabrication membrane alignment step and addresses the gas chamber spacing issue of the double-chip design by fabricating a gas channel and membrane structures on a single chip. The single-chip design employs surface micromachining techniques and starts with creating a sacrificial layer sandwiched by two thin membranes on a single substrate. Later in the process, the sacrificial layer is removed to create a series of empty cavities between the thin membranes that later serves as the gas channel. This surface micromachining provides precise dimensional control in the vertical direction as the sacrificial layer thickness is defined by deposited film thickness which can be accurately controlled. The design also incorporates a large membrane that extends the entire gas channel area and ensures automatic alignment to the opposite membrane by design. The design also includes an array of pillars between the membranes for preventing load deflection and membrane collapse.

4.3.1 Fabrication process

The process flow given below is specific to the gas chamber with the target spacing of 200 nm. The spacing can be adjusted by varying the thickness of the TEOS sacrificial layer and processing time. Table 4-2 lists the key processing variables that can be substituted for production of gas chambers with 500 and 1000 nm spacing.

Table 4-2. Substitutable processing parameters for different gas chamber spacing.

TEOS thickness (nm) (~ gas chamber spacing)	Oxidation processing time (min)	BHF etching time (min:sec)	Ti evaporation thickness (nm)
200	26	9:30	300
500	65	8:45	550
1000	130	8:30	1050

Step 1: SiO₂ (TEOS) and Si₃N₄ layering

Starting with a 4" silicon <100>-oriented wafer (300 μm) with a 80 nm thick LPCVD Si₃N₄ layer, the wafer is first cleaned in HNO₃ for 10 min followed by additional dipping in boiling hot HNO₃ (69.5 %, 110 °C) for another 10 min. A layer of 200 nm TEOS (tetra-ethyl-ortho-silicate) is deposited using an oxidation furnace (Tempress oven, 26 min @700 °C) followed by another 50 nm vapor deposition of Si₃N₄ (LPCVD, Tempress).



Fig. 4-17 At the end of Step 1. The Si wafer is deposited with TEOS and Si₃N₄ thin films.

Step 2: Fabrication of etch access holes on the upper Si_3N_4 layer

ZEP-520 e-beam-resist is spin-coated (1000 rpm) on top of the uppermost Si_3N_4 layer and baked at 175 °C for 30 min. An array of 1 μm access holes with a pitch of 3 μm are written on the resist using EBPG (electron beam pattern generator Vistec 5000+, dose 1000 $\mu\text{C}/\text{cm}^2$ at 100 keV). The access holes are later used to etch the sacrificial layer. After developing the resist in n-butylacetate for 90 sec and rinsing in MIBK:IPA (9:1), the patterned Si_3N_4 layer by the ZEP resist mask is dry-etched. (25 sccm CHF_3 and 25 sccm Ar at 50W RF power and 8 μbar pressure, Leybold Hereaus).

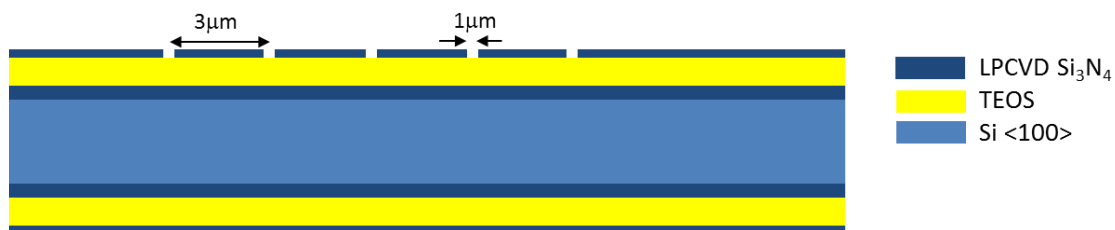


Fig. 4-18 Etch access holes patterned and dry etched on the uppermost Si_3N_4 layer (Step 2).

Step 3: Etching in BHF

The wafer is dipped in Triton X-100 for 1 min to improve the wettability of the surfaces (it improves the uniformity of the etching in the next step). The wafer is then dipped in BHF (buffered HF, 5 (40%) NH_4F : 1 (49%) HF) to remove most of the sacrificial layer (200 nm TEOS). The BHF etches the TEOS layer isotropically under the masking layer (Si_3N_4) through the access holes. Etched cavities grow over time but when the etching is stopped on time (approximately after 9 min 30 sec for 200nm TEOS), the etched cavities become inter-connected but leaves un-etched portion of the TEOS as an array of pillars (see Fig. 4-19 and Fig. 4-20). The wafer is then rinsed in water and baked in an oven (90 °C, 5 min) to dry.

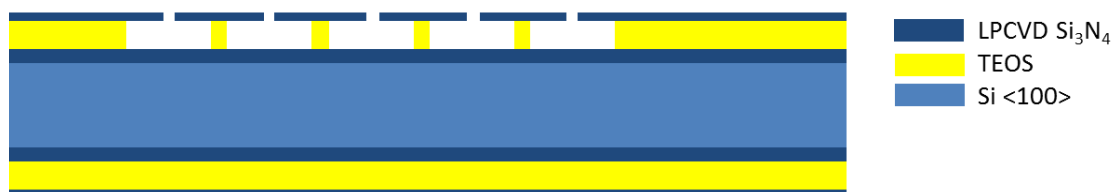


Fig. 4-19 At the end of Step 3. Side view of the etch cavities and pillars created by BHF. The pillars support the Si_3N_4 layer on top.

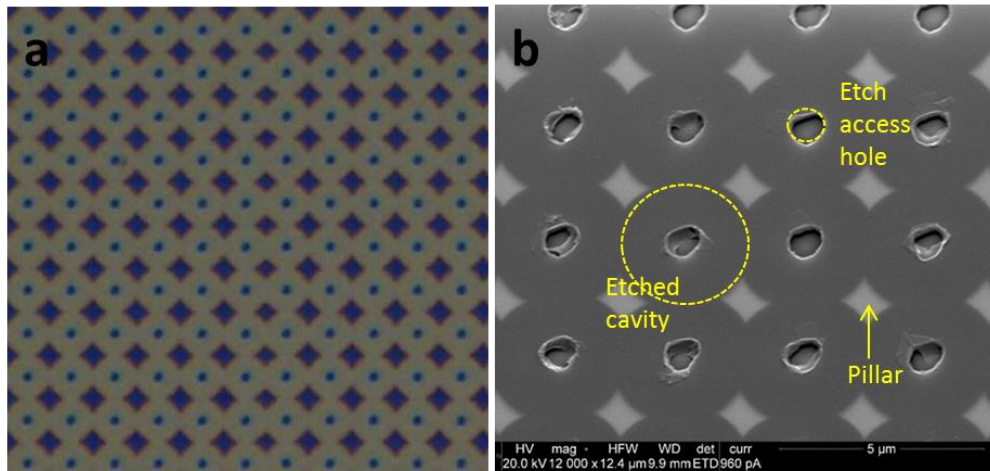


Fig. 4-20 Optical image (a) and SEM micrograph (b) showing an array of etch access holes, inter-connected etch cavities, and leftover 4-point star shaped TEOS pillars after BHF etching.

Step 4: Plugging etch access holes

Spin coat ZEP-520a (1000 rpm) on top of the Si_3N_4 masking layer with the etch access holes and develop in n-amylacetat for 15 min. Rinse with MIBK:IPA=9:1 for at least 30 sec. Evaporate (Temescal) approximately 300 nm of Ti on top of the photoresist (Fig. 4-21). Leaving the wafer in anisole for about 24 hrs ensures lift-off of the deposited Ti on the masking layer (Si_3N_4) but leaves Ti partly closing up the access holes. After rinsing in IPA, additional 50 to 100 nm PECVD (plasma enhanced chemical vapor deposition) Si_3N_4 (HiQ, 4 min 17 sec) is evaporated to close the access holes completely (Figs. 4-22 and 4-23).

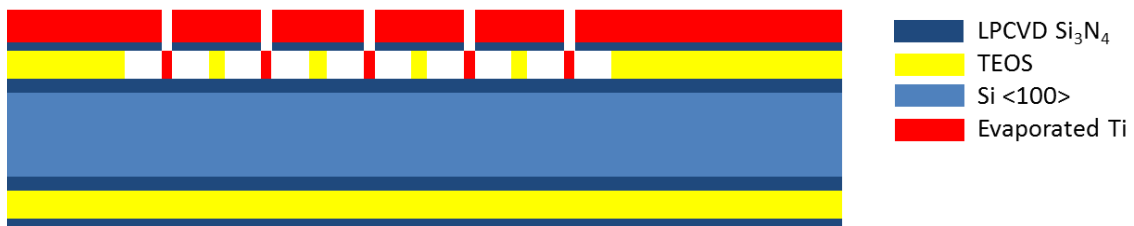


Fig. 4-21 Evaporated Ti almost fills up the etch access holes.



Fig. 4-22 After lifting off of the evaporated Ti from the Si_3N_4 masking layer, 50 to 100 nm PECVD Si_3N_4 is additionally evaporated to completely close the etch access holes.

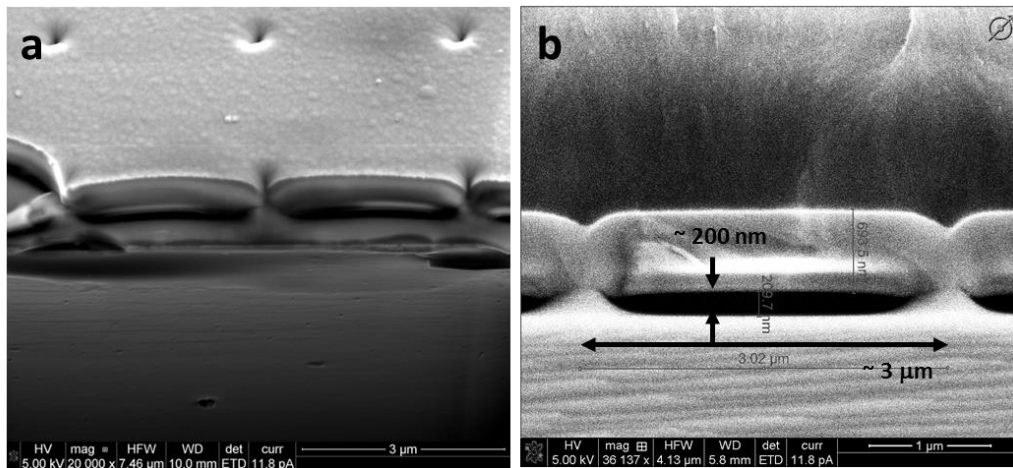


Fig. 4-23 SEM micrographs: Cross section views of the etched cavities and plugged etch holes from different angles.

Step 5: First metal layer

5 nm Cr (adhesion layer) and 20 nm Mo are evaporated (Temescal) to create a metal layer on top of the PECVD Si₃N₄ layer.

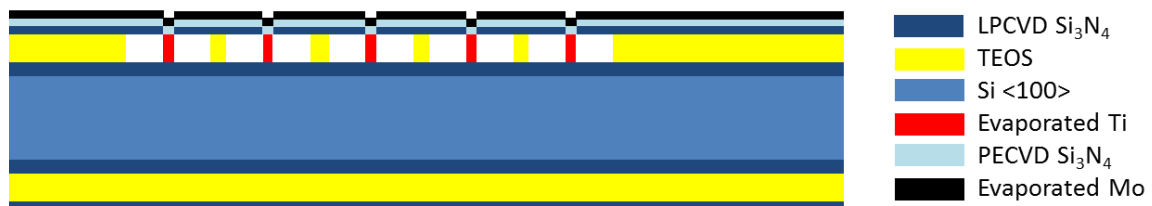


Fig. 4-24 After Cr and Mo evaporated on top of the PECVD Si₃N₄ layer.

Step 6: Adding gas feed and membrane window and second metal layer

Spin-coat AZ5214 photoresist (2000 rpm, ~2 μm thickness) on the back side of the wafer followed by baking at 120 °C for 2 min and additionally at 90 °C for 10 min. After 10 sec UV lithography, masks for the gas feed and backside membrane are now defined. Develop AZ5214 in MF321 for 70 sec and rinse the wafer in water for 30 sec. Dry-etch the exposed Si₃N₄ (Leybold Hereaus, for 7 min 30 sec, 25 sccm CHF₃ and 25 sccm Ar at 50 W RF power and 8 μbar pressure). Strip off the AZ514 in anisole. Etch in KOH (90 °C, ~3.5 hrs) in the AMMT holder and allow no KOH on the front side (the surface micro-machined side). 5 nm Cr (adhesion layer) and 20 nm Mo are evaporated (Temescal) to create a metal layer.

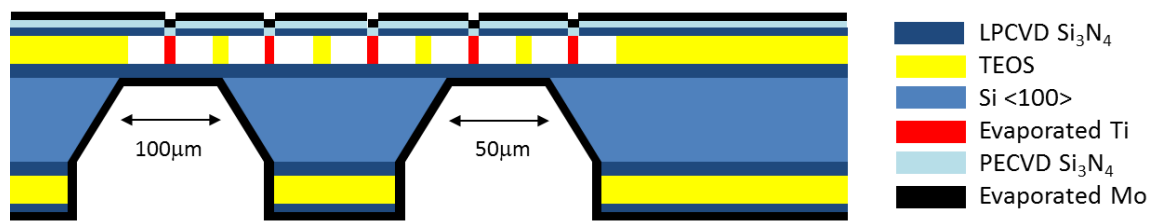


Fig. 4-25 In Step 6, the gas feed and back side membrane windows are created by KOH etching and covered with Cr and Mo metal layers.

Step 7: Opening gas feed window and FIB milling a double-aperture

A double-aperture (100-500 nm) is fabricated by FIB machining (100 pA, 30 keV, 5 to 60 sec, FEI Quanta™ 3D FEG Dualbeam). For this version of the gas chamber, a FIB probe should be positioned to mill between the access hole plugs and the TEOS pillars. The membrane of the gas feed window can be also removed by FIB milling. Refer to Figs. 4-26 through 4-29 for visual examples and additional details on this step.

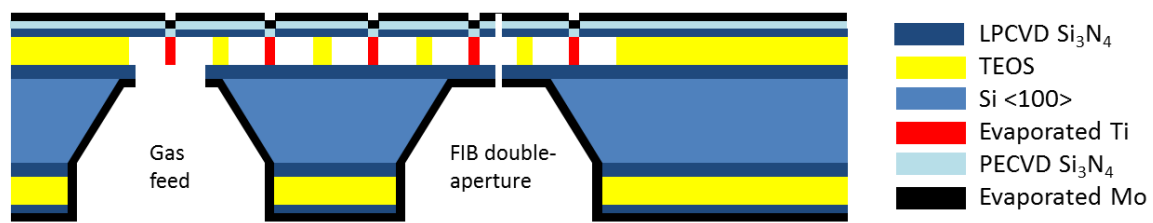


Fig. 4-26 In the last step, the double-aperture is fabricated and gas feed window membrane is opened by FIB milling.

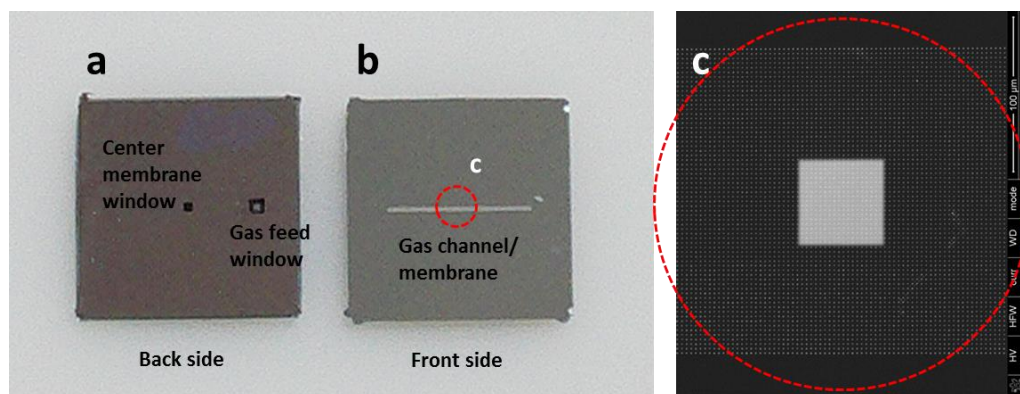


Fig. 4-27 Optical images showing the front and back side of a completed prototype (a, b). The gas channel/membrane built on the Si substrate on the front side extends all the way from the gas feed window and passes over the center membrane window of the back side. By design, the membranes on the both sides overlap. The center membrane on the back side is clearly visible through the gas channel membrane on the front side when inspected under SEM (c).

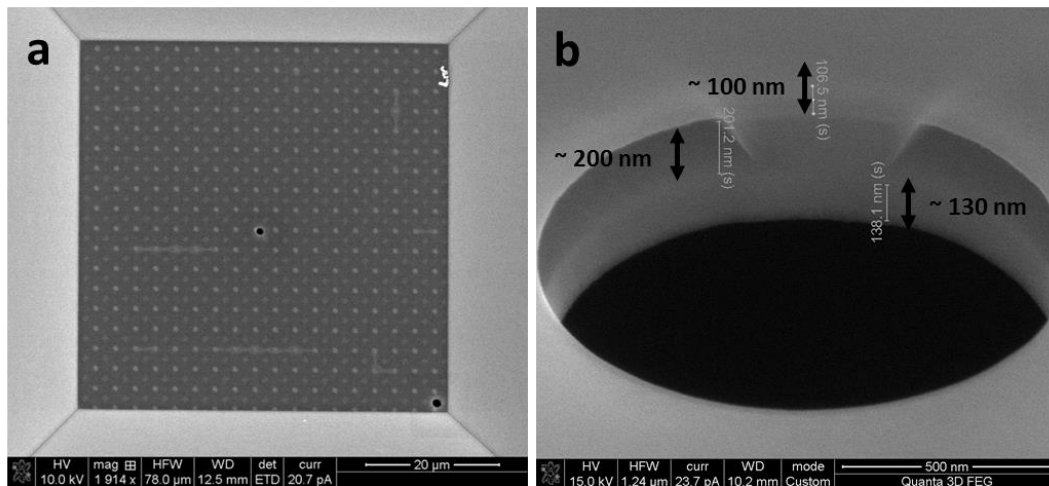


Fig. 4-28 SEM micrographs: (a) Looking down on the center membrane on the back side of the prototype gas chamber of Fig. 4-27. Two double-apertures, one in the center and the other in the lower right corner, are FIB milled between the TEOS pillars and etch plugs. (b) Close-up view on the double-aperture in the middle.

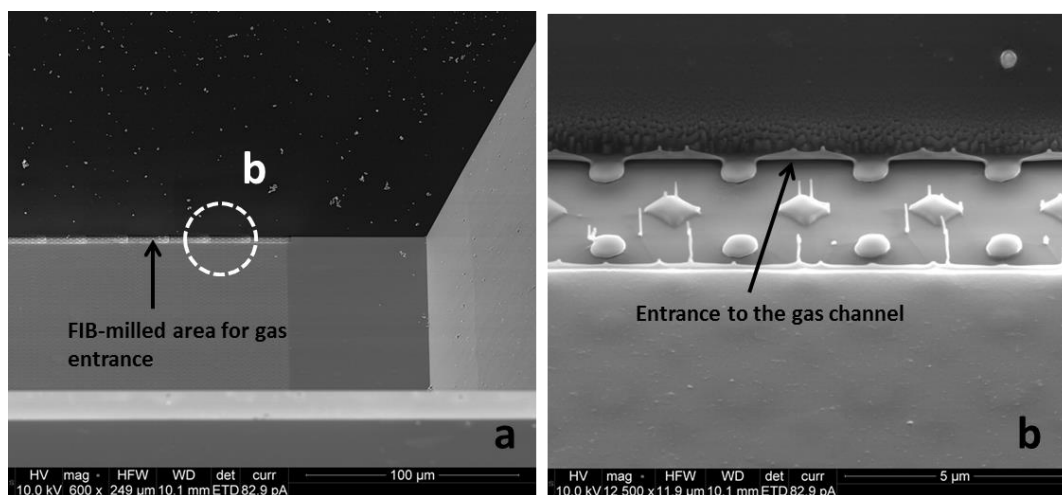


Fig. 4-29 SEM micrographs: (a) A portion of the gas feed window membrane is removed by FIB milling. This creates a gas entrance to the gas channel. (b) A magnified view of the circled area in (a). The gas channel (inter-connected etch cavities), TEOS pillars, and etch hole plugs are visible through the milled area.

4.3.2 Prototype evaluation and future improvement

The idea of the single-chip based gas chamber is new. It was conceived after encountering the gas chamber spacing issue of the double-chip design. Rather than just addressing the immediate concern and trying to find solutions only within the double-chip design, an alternate design was sought for overall design improvement. The single-chip design idea turned out to be quite attractive

as it could address the gas chamber spacing issue and also simplify the overall manufacturing process by eliminating post-fabrication assembly.

The fabrication process recipe provided above is our first try at demonstrating the construction of the miniaturized gas chambers based on the surface micromachining techniques. The recipe is newly developed and at the time of writing, only a couple of prototype wafers have been processed, thus very limited experimental results are available. However, the several prototype gas chambers that were inspected and tested so far have shown many promising results.

FIB cross-sectioning has shown the dimensions of the gas cavities are very uniform, evenly distributed, and all within the design target dimensions (see Fig. 4-23 for example). When the gas chambers were pressurized with argon gas and introduced with energetic electrons, signs of argon gas ionization were very apparent (Fig. 4-30). This sufficiently proves that the etched TEOS cavities properly function as a continuous gas channel all the way up to the double-aperture area. Moreover, stable background vacuum pressure in the test setup was observed when gas was leaked in to the gas chamber, indicating that the BHF etch hole plugs are leak tight. *In situ* SEM inspection also has shown no noticeable membrane deflection when high gas pressure is applied to the gas chamber, approving the TEOS pillar support design.

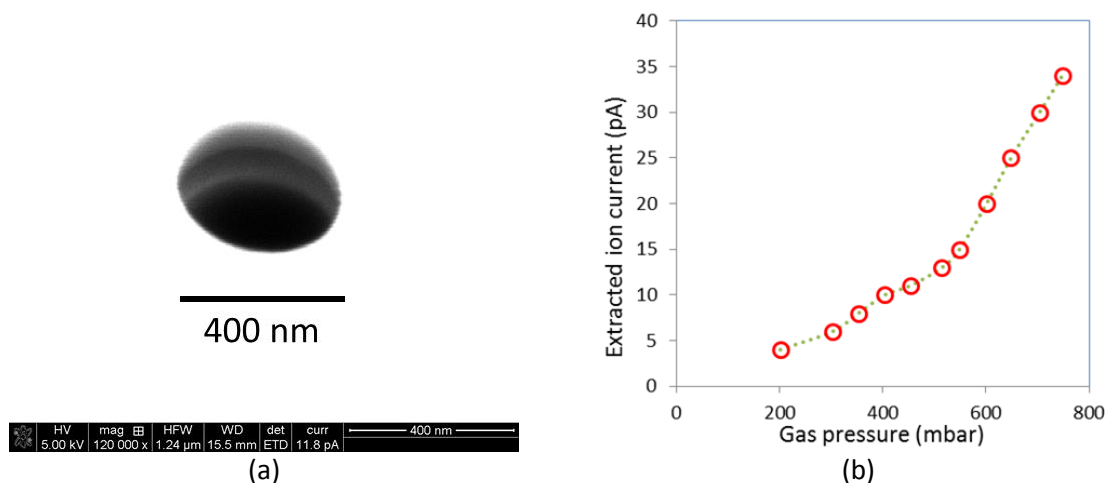


Fig. 4-30 (a) SEM micrograph showing the double-aperture of a prototype gas chamber of the single-chip design (spacing ~200 nm). (b) Argon ion current measured from the gas chamber of (a). The input electron current was about 10 nA at 1 keV.

Although the prototype testing so far have shown the verification of gas ionization, good gas chamber structural integrity, and full compliance to the gas chamber spacing specification, the effect of the gas chamber bias voltage on ion extraction has not yet been established. The increase of the extracted ion current responding to the increase of the gas chamber bias voltage was confirmed with the prototype gas chambers of the double-chip design, but currently not with the single-chip design prototypes. Judging from the clearly open circuit connection between the two membranes when checked with an ohmmeter, the electrical contact to and electrical conductivity along the membrane are thought to be the problem. In the present design, the gas chamber membranes are a mixture of thin metal (Cr/Mo) and Si_3N_4 layers. This incomplete metal membrane design was initially chosen due to some material processing restrictions on some of the equipment that we use and

initially we were mainly interested in demonstrating the design idea behind the surface micromachining before optimizing it. Trying to keep the overall membrane thickness to ~100 nm in the current design, only 20 nm thick metal layer was incorporated into the design. It is speculated that this 20 nm evaporated Mo layer may not provide good contact with the gas chamber bias contact pin or/and continuous coverage all around the membrane. An obvious way to verify this will be adding more metal and testing again.

Going forward with the design, full metal membrane is highly recommended for making the single-chip design more robust and perhaps resolving the gas chamber bias voltage issue. According to the data compiled by Willams *et al.*¹⁶, the etch rate of evaporated molybdenum in 5:1 BHF solution (5 40% NH₄F: 1 49% HF) is less than <0.3 nm/min (considerably slower than TEOS), suggesting the replacement of the current Si₃N₄ wet etch mask with molybdenum should be feasible.

4.4 Conclusions

In this chapter the detailed fabrication methods of the double-chip and the single-chip gas chamber design are given. The overall structural configuration of the gas chamber sought after through both designs is essentially the same. Our target is to produce a structure consisting two ~100 nm thick membranes separated by a small spacing of 100 -500 nm that can be filled with gas, however, each design tries to achieve this from a different MEMS micromachining approach.

In the case of the double-chip design, each membrane is fabricated on a substrate chip first by bulk micromachining and then a complete gas chamber is formed by aligning and gluing two different substrate chips. The gas chamber spacing, in this case, is created by a small gap set by thin layers of Si₃N₄ between the chips. On the other hand, in the single-chip design, a TEOS layer sandwiched by two thin membranes is first fabricated on a single substrate chip and then later using the surface micromachining technology, the TEOS layer is etched away leaving an empty space between the membranes. Essentially the thickness of the TEOS determines the gas chamber spacing in this case.

We find that the double-chip design is reliable and reproducible and the prototypes have shown to fully function as gas ionization chambers and extract ions. However, the current assembly approach using glue has presented difficulties in meeting our gas chamber spacing target. We plan to investigate different glue-less approaches such as mechanical clamping and wafer bonding to resolve the issue.

Although the fabrication method is much more involved and complicated for the single-chip design, it has shown that the surface micromachining technology is very effective in achieving our target gas chamber spacing. In addition, the single-chip design simplifies the overall manufacturing process by requiring no post fabrication gas chamber membrane alignment. Still further design optimization and more experimental evaluations are needed but at this point, the single-chip design looks to be a promising alternative to the double-chip design.

Acknowledgements

The author gratefully acknowledges Dr. Vladimir G. Kutchoukov for his leading role in the development of the miniaturized gas chambers and fabrication of the prototypes. The author also acknowledges Carel Heerkens and Dr. Fredrik Creemer for helpful discussions. All fabrication work was conducted in Van Leeuwenhoek Laboratory and DIMES. This research is supported by the “Stichting voor Fundamenteel Onderzoek der Materie (FOM)”, which is financially supported by the “Nederlandse Organisatie voor Wetenschappelijk Onderzoek” and FEI Company.

References

- [1] J. W. Judy, *Microelectromechanical systems (MEMS): fabrication, design and applications*, *Smart Mater. Struct.* **10** 1115, (2001)
- [2] T. M. Adams and R. A. Layton, *Introductory MEMS: fabrication and applications*, (Springer US, 2010)
- [3] B. van Someren, M. J. van Bruggen, Y. Zhang, C. W. Hagen, and P. Kruit, *Multibeam electron source using MEMS electron optical components*, *J. Phys. : Conf. Ser.* **34** 1092 (2006)
- [4] P. Kruit, *The role of MEMS in maskless lithography*, *Microelec. Eng.* **84**, 1027 (2007)
- [5] Y. Shi, S. Ardanuc, and A. Lal, *Micro-Einzel lens for wafer-integrated electron beam actuation*, *MEMS, IEEE Conf.* (2013)
- [6] G. K. Fedder, *MEMS fabrication*, *Proc. Int. Test Conf.*, 691-698 (2003)
- [7] *Micromachining Techniques for Fabrication of Micro and Nano Structures*, Edited by M. Kahrizi, (InTech, 2012)
- [8] R. A. Holmwood and R. Glang, *Vacuum deposited molybdenum films*, *J. Electrochem. Soc.* Vol. **112**, 82 (1965)
- [9] G. Gordillo, F. Mesa, and C. Calderon, *Electrical and morphological properties of low resistivity Mo thin films prepared by magnetron sputtering*, *Brazilian Journal of Physics*, Vol. **36**, 3B p.982-985 (2006)
- [10] D. Maier-Schneider, J. Maiback, E. Obermeier, *A new analytical solution for the load-deflection of square membranes*, *J. Microelectromech. Syst. Integr.* **4** 238-241 (1995)
- [11] K.B. Yoder, A.A. Elmustafa, J.C. Li, R.A. Hoffman, D.S. Stone, *Activation analysis of deformation in evaporated molybdenum thin films*, *J. Phys. D: Appl. Phys*, **36**(7), 884 (2003)
- [12] Q. Y. Tong and U. Gosele, *Semiconductor wafer bonding: recent developments*, *Materials Chemistry and Physics*, **37**, 101-127 (1994)
- [13] K. Reck, C. Ostergaard, E. V. Thomsen, and O. Hansen, *Fusion bonding of silicon nitride surfaces*, *J. Micromech. Microeng.* **21** (2011)
- [14] S. Sanchez, C. Gui, and M. Elwenspoek, *Spontaneous direct bonding of thick silicon nitride*, *J. Micromech. Microeng.* **7** (1997)
- [15] C. L. Hsu, G. Pandraud, J. F. Creemer, P. J. French, P.M. Sarro, *Low temperature LPCVD SiN direct bonding for sensors*, *Proceedings of the STW annual workshop on semiconductor advances for future electronics and sensors (SAFE 2005)* (pp. 162-166)
- [16] K. R. Williams, K. Gupta, and M. Wasilik, *Etch rates for micromachining processing part II*, *Journal of Microelectromechanical Systems*, Vol. 12, No. 6 (2003)

5 ■ Ion beams in SEM: the proof-of-concept experiments

The concept of NAIS is introduced in Chapter 2 and the critical ion source properties investigated extensively through gas and ion trajectory computer simulations are presented in Chapter 3. Numerically the results are in line with our expectations and support that NAIS is a viable noble gas ion source capable of providing both high brightness and narrow energy spread suitable for high resolution FIB applications. In Chapter 4, two different methods of fabricating miniaturized gas chambers using nanofabrication techniques are discussed. Although the fabrication process involving gluing has caused difficulties in meeting the target gas chamber spacing, gas chambers based on the double-chip design are readily and reliably produced and sufficient for experimental investigations.

In this chapter, we detail our experimental efforts to demonstrate the concept of NAIS. An improvised NAIS prototype was devised inside a commercial SEM. A prototype gas chamber was filled with gas inside the SEM specimen chamber and gas ionization was induced by simply focusing a SEM probe into it. An ion beam was then extracted by applying a bias voltage across the gas chamber. Although the experimental setup couldn't be configured to meet all of our desired NAIS design specifications, the setup was certainly adequate in validating the basic functionality of the miniaturized gas chamber design and demonstrating that NAIS is capable producing different noble gas ion species. Additionally, the setup was configured to measure extracted ion current and ion energy spread. The SEM test setup was eventually developed into a mini-FIB system to demonstrate focusing of an ion probe for imaging and milling.

5.1 Experimental setup

A number of proof-of-concept experiments (aka the ‘SEM experiments’) with the goals of demonstrating the idea of generating ion beams from a miniaturized gas chamber using noble gases and evaluating the performance of such ion beams were conducted in a commercial SEM (FEI Quanta™ 3D FEG^[1]). A SEM was chosen as an experimental platform because its specimen chamber can double as a simple vacuum testing space with the benefits of quick venting and pump-down as well as of the possible SEM imaging for *in situ* visual feedback during experiment. But more importantly, the SEM can provide a high current density electron beam that can be used to test our miniaturized gas chambers for gas ionization. Simply speaking, the general scheme of the SEM experiments entails to: (1) install a miniaturized gas chamber inside the SEM specimen chamber, (2) configure a gas line to the gas chamber and leak in gas, (3) create ions by focusing an electron probe of the SEM into the gas chamber, (4) extract ions by applying a bias voltage across the gas chamber, and (5) measure ion beam properties such as ion current, stability, energy spread, etc..

Fig. 5-1(a) shows the Quanta system used for the experiments and Fig. 5-1(b) a schematic overview describing the ion source test setup configured inside the Quanta SEM specimen chamber. Several variations in the setup exist depending on the specificity and the objective of the experiment but in general, it consists of two main sections – the gas chamber housing and a detection module. The gas chamber housing holds a prototype gas chamber and connects it to the gas line fed from a gas bottle placed outside of the SEM chamber. An O-ring is used to make a leak tight connection between the gas feed window of the gas chamber and the gas line. The gas chamber housing also includes an electrode called ion accelerator, which is used to accelerate the ions from the gas chamber towards the detection module while repelling any electrons transmitted through the gas chamber apertures. This sufficiently prevents any mixing of electrons in ion detection. Below the gas chamber housing, a detector module is placed for measuring ion beam properties. For measuring ion beam current, a Faraday cup is utilized, for visualizing ion beam patterns, micro-channel plates (MCP) combined with a phosphor screen, and for assessing ion energy distribution, an energy analyzer. The SEM experimental setup was eventually developed into a mini FIB system by adding focusing lenses, beam scanning octupole deflectors, and a secondary electron detector below the gas chamber housing.

The gas chamber housing is typically mounted on an extension arm that is connected to X-Y piezo stages (M-663, Physik Instrumente) or in some cases, directly on the SEM stage. In either case, the stage control enables a rough alignment of the gas chamber to the electron column during experiment. For precise alignment, the gas chamber is imaged by the SEM, the gas chamber aperture located, and then the electron probe is aligned to the center of the gas chamber aperture using the beam shift function of the SEM. The electron beam can be kept scanning over the gas chamber aperture to supply a pulsed electron beam into the gas chamber or can be switched to spot mode to supply a steady stream of electrons.

Gas load to the gas chamber is controlled by a manual leak valve placed along the gas line outside the SEM chamber. A vacuum pressure gauge suitable for all gas types (DCP 3000, Vacuubrand) is placed near the leak valve to monitor the amount of gas being leaked in to the gas chamber.

A typical SEM probe current applied for gas ionization ranged anywhere from 6 to 15 nA at a beam energy of 1 keV (the Quanta SEM in analytic mode, with spot number between 2 and 5). The available probe current varied depending on the ever changing status of the SEM in terms the

emitter total emission drift and the spatial beam drift within the column and the quality of consequent column realignment. Based on the edge resolution analysis of secondary electron images using FEI image software [2], the beam diameter of the electron probe ranged between 50 nm to 100 nm (12-88% rise distance or FW50) for currents between 6 and 15 nA at 1 keV.

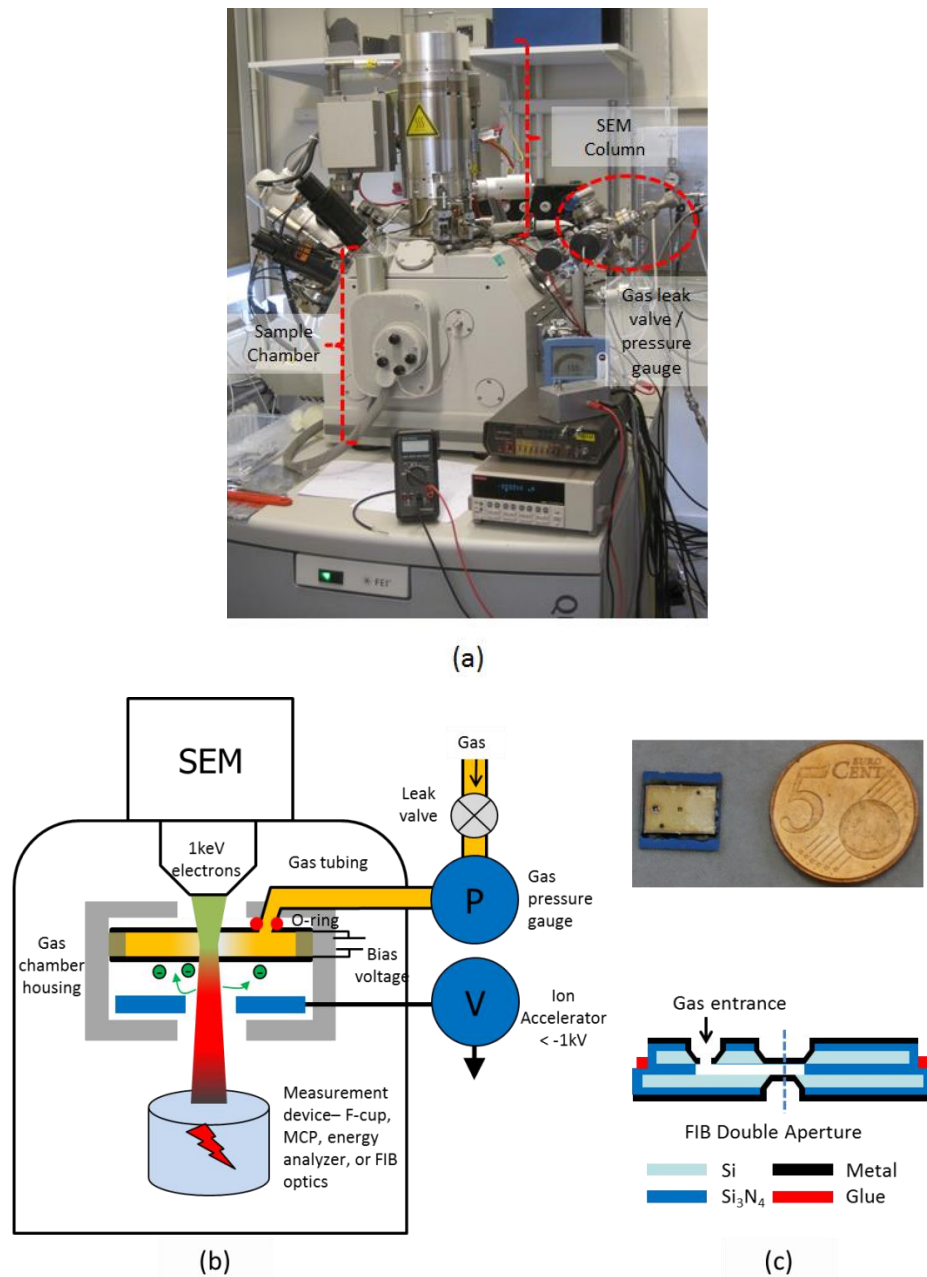


Fig. 5-1 (a) FEI Quanta™ 3D FEG system utilized as a test platform to demonstrate the concept of NAIS, (b) simple sketch describing the ion source experimental setup built inside the Quanta system, and (c) image of a prototype gas chamber based on the double-chip design and cross section illustrating the gas chamber material components.

The gas chambers used for the experiments are prototypes of our 1st generation gas chamber design, also known as the double-chip design (Fig. 5-1(c)). These are glued structures of two silicon substrates, each holding a 100 nm thick molybdenum metal membrane prepared through

several steps of metal evaporation, e-beam lithography, and wet-etching. Additional 100 nm thick Si_3N_4 layer is deposited on top of the moly layer and then later dry-etched to create a gas channel. After the membranes and gas channels are aligned and the substrates glued together, a double-aperture is fabricated using conventional FIB machining to create entrance and exits apertures for electrons and ions (See Ch. 4 of this thesis for details). Table 5-1 lists all the prototype gas chambers used for the experiments and their relevant dimensions.

Table 5-1. Prototype gas chambers based on the double-chip design used for the SEM experiments

Gas chamber	Spacing (μm)	Aperture diameter (μm)
GC1	2.3	1.5
GC2	1.4	1.0
GC3	2.0	0.8
GC4	2.0	1.0

5.2 Ion beam pattern imaging

Although qualitative, a simple and effective way of demonstrating the ‘beam’ formation of ions is by capturing a projected beam pattern from an ion source. Fig. 5-2(a) illustrates the method incorporated in the SEM test setup just to do such. A dual microchannel plate (MCP, chevron style, 10 μm channel diameter, HRBIS-10000, Beam Imaging Solutions) was placed below the ion accelerator and ions entering the MCP are converted to secondary electrons with a total amplification up to $\sim 10^7$ (@ maximum 2 kV across the MCP). By accelerating the secondary electrons emitted from the MCP onto a phosphor screen (P43, aluminum overcoat on Pyrex disc, Beam Imaging Solutions), a projection of the ion beam from the source can be viewed. Due to the limited viewing angle through the view ports of the SEM, a 45-deg mirror was necessary to redirect the image pattern to an observing camera outside the SEM chamber.

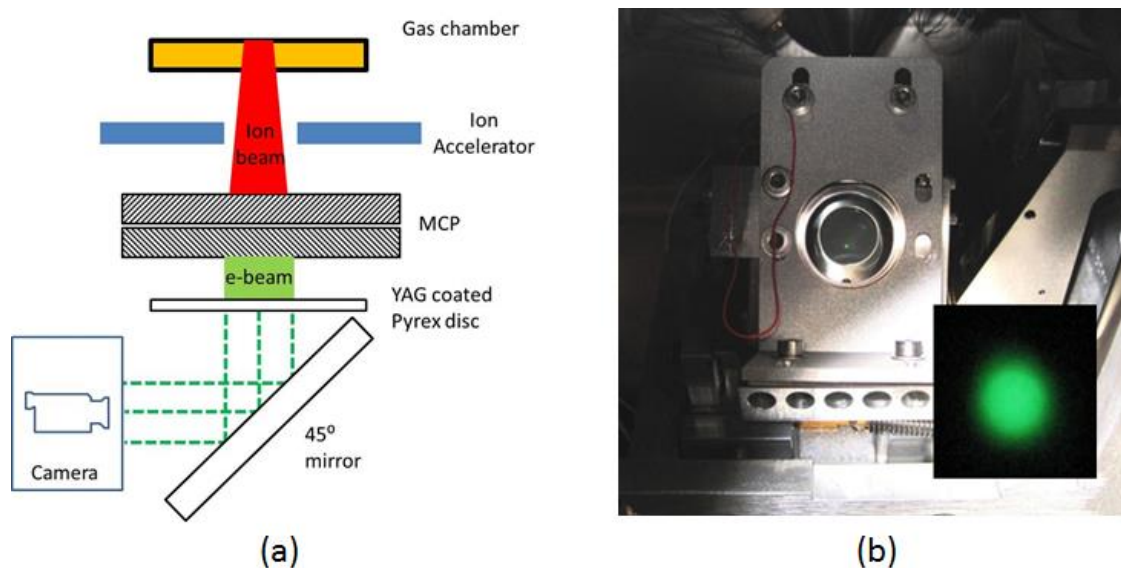


Fig. 5-2 (a) Schematic of the ion beam pattern imaging setup and (b) Photos of the actual imaging setup and an argon ion beam pattern (inset) captured by a digital camera.

Fig. 5-2(b) shows the actual test setup and an argon ion beam pattern captured on a digital camera through a SEM viewport. The exact magnification of the image is unknown but the diameter of the beam pattern was estimated to be about 2 mm. Similar beam patterns were also observed using helium and xenon gas. It was quite apparent that the intensity of the beam pattern strongly depended on the gas pressure, the amount of the electron beam focused into the gas chamber, and the gas chamber bias voltage. When the electron beam was put in spot mode, a steady beam pattern was observed but when the electron beam was scanned over the double-aperture, pulsed ion beam signals corresponding to electron beam scan speed were seen. These observations are only qualitative, but they sufficiently prove that the ionization took place inside the miniaturized gas ionization chamber and indicate that ions emerge from such a device form a beam with ‘some’ source brightness.

5.3 Ion beam current

5.3.1 Beam current measurement

The amount of current extracted from the gas ionization chamber was directly measured using a Faraday cup system shown in Fig. 5-3. A Faraday cup (made of Poco graphite, cup diameter/length aspect ratio $\sim 1:12$) connected to a high precision current meter (Keithley 485 Picoammeter) was placed just below the gas chamber housing. In order to ensure that the current measured in the cup reflects only the ion current and not the electron current passing through the gas chamber, the Ion Accelerator potential was set above the electron beam potential to act as an electron mirror and prevent any electrons to transmit through (see Fig. 5-4).

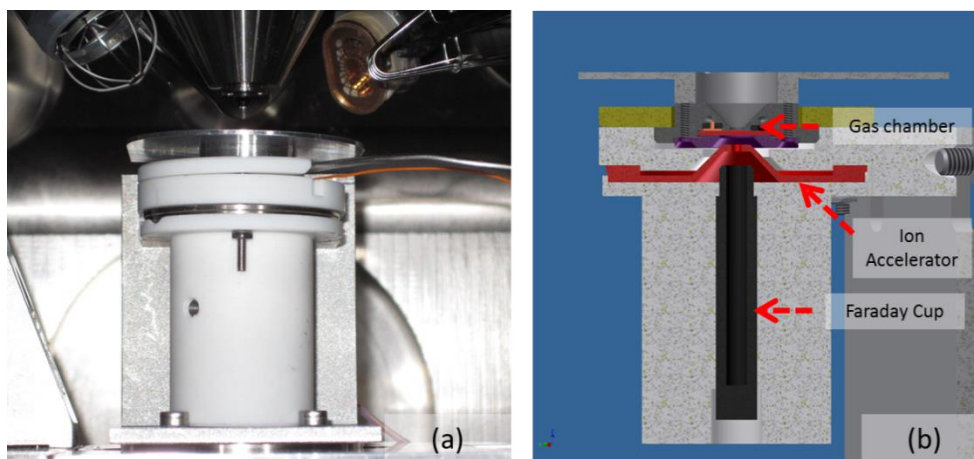


Fig. 5-3 (a) Ion beam current measurement setup. (b) Cross section of the setup. The ion current is measured using a Faraday cup installed below the Ion Accelerator.

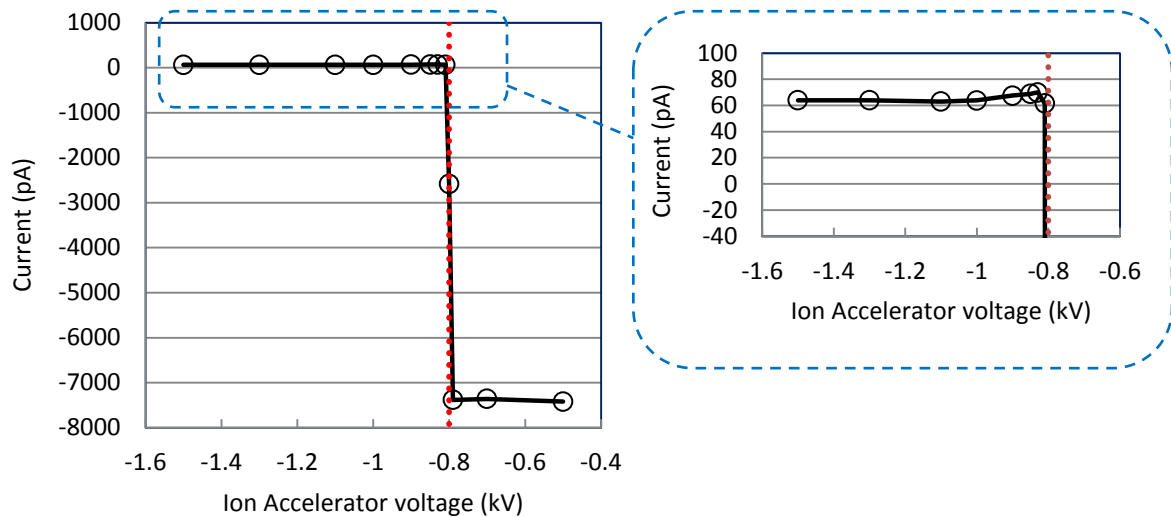


Fig. 5-4 Effect of the Ion Accelerator bias on the ion current measurement. The Faraday cup was kept at slightly above the ground potential (+100 V) and the Ion Accelerator bias was gradually varied to transmit or repel the incoming electron beam (~7600 pA, 0.8 keV). The incoming ion beam was ~65 pA.

Fig. 5-5 shows the measured extracted ion beam current as a function of the gas pressure for helium, argon, xenon, and air. Consistent with the theoretical expectations discussed in Chapter 2, the results clearly indicate that the amount of ions generated from the gas chamber depends on the gas pressure and the gas species. The dependence on the gas species comes from the fact that each gas has a different electron impact ionization cross section for a given incident electron beam energy. The figure also clearly shows that the ion current increases as the gas pressure increases but it eventually peaks and starts to drop when the gas pressure is high enough to limit the mean free path of ions inside the gas chamber. Note that the gas pressure where these peaks occur in is different for each gas, corresponding to the fact that the mean free path of each gas is different at a given gas pressure.

The experimental measurement also verified that the amount of ion current produced from the gas chamber also strongly depends on the incident electron beam energy. This follows the fact that the ionization cross section of the gases also varies with the energy of the incident electron. Fig. 5-6 shows the ionization efficiency (the extracted ion current divided by the input electron current) measured for argon gas as a function of the incident electron beam energies measured between 800 and 1500 V. The measured ionization efficiency curves follow the ionization cross section curves^[3,4] very well, indicating the linear relationship between the ion production and the gas ionization cross section.

The gas chamber bias voltage is another factor that has a considerable impact on the amount of ion current extracted from the gas chamber. The angular spread set by the initial thermal motion of the ions at the time of ionization and the electric field between the two membranes influence on the transmission of ions through the ion exit aperture. As expected, the results in Fig. 5-7 indicate that the extracted ion current increases with the gas chamber bias voltage until the ion beam size becomes comparable to the exit gas chamber aperture size. The figure also shows that even with zero bias voltage a noticeable amount of ions are extracted. Although no electric field is produced between the gas chamber membranes, a field from the Ion extractor (~ 1×10^6 V/m) still can sufficiently penetrate through the gas chamber aperture and pull some ions out.

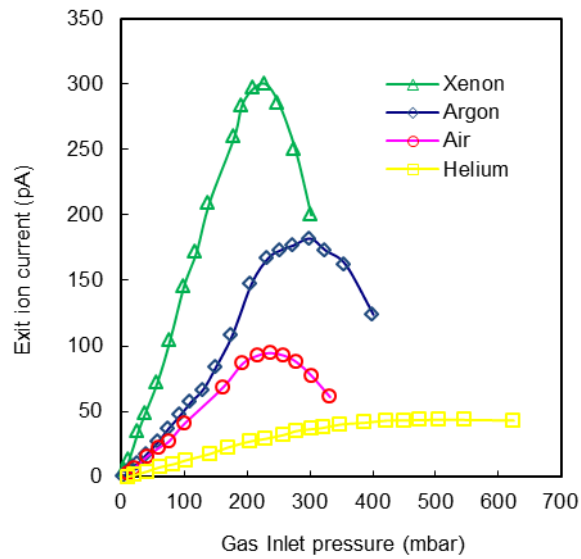


Fig. 5-5 Measured ion beam current as a function of gas pressure for argon, helium, xenon, and air (using Gas chamber GC1, SEM probe current ~14 nA @1 keV, the ion accelerator set at -1.25 kV).

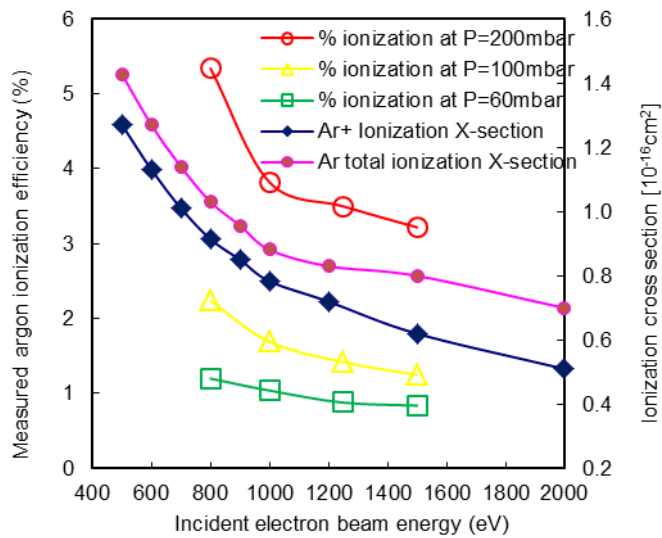


Fig. 5-6 Measured ionization efficiency as a function of the incident electron beam energy -- argon gas, using GC2, SEM probe current 6 to 9 nA depending on the electron beam energy, the ion accelerator set at 25% above the electron beam potential. Ar⁺/Ar total ionization cross sections cited from Refs. [3] and [4].

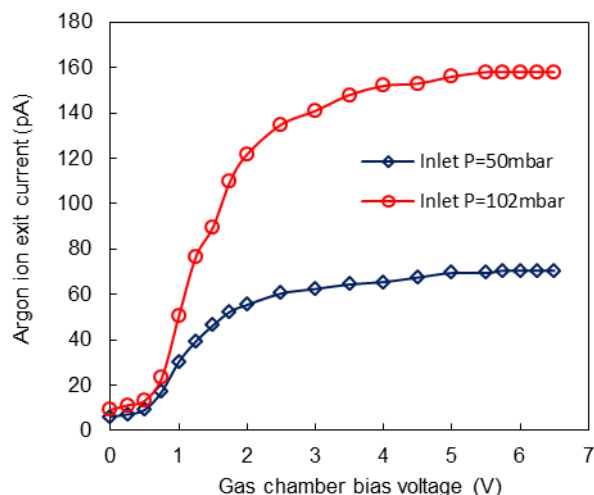


Fig. 5-7 Measured ion current as a function of the gas chamber bias voltage (argon gas, using GC2, SEM probe current ~ 9 nA @1 keV, Ion extractor set at -1.25 kV).

5.3.2 Beam current stability

From a theoretical standpoint, two essential drivers playing a direct role in the beam current stability of the NAIS are the stabilities of the incident electron beam current and the gas pressure. In this regard, it's quite reasonable to expect superb beam current stability from the NAIS since the NAIS utilizes a Schottky electron emitter which is well known for excellent current stability and the miniaturized gas chamber design only allows very small gas leakage through sub-micron sized gas chamber apertures. The current stability of a Schottky emitter can be better than 1% per hour if ring collapses can be avoided and good vacuum environment is maintained around the source ^[5,6]. As for the gas pressure, assuming molecular flow, the conductance (C) through an orifice with an area A is about $11.6 \cdot A$ ($L/(sec \cdot cm^2)$) ^[7]. For a miniaturized gas chamber with two 100 nm diameter holes, the total conductance is about 9.11×10^{-10} L/sec. Assuming a gas tank with 1 liter capacity connected to the gas chamber and no gas leakage other than the loss through the gas chamber apertures into the surrounding vacuum, the total time it takes to lose 1 % of gas is about 1,500 hours, suggesting that the ion current drift due to gas pressure drift can be indeed extremely small.

However, during the experiments it's often observed that that the actual ion beam current stability can vary from one gas chamber to another, and in some cases, it can be considerably worse than expected. Fig. 5-8 shows a short term argon current stability of a prototype NAIS (using GC2) measured in the SEM. Although the pressure change over an hour period was about 1 %, the current drift was more than 15 % over the same period. The gas pressure change in this case was a lot more than what's described above due to the larger gas chamber aperture size (1 μ m diameter instead of 100 nm) and much smaller gas volume. It turned out that the current drift was mostly caused by the electron beam spatially drifting from the center of the aperture towards an aperture edge over time. When the electron beam was re-aligned to the center, the ion beam current fully recovered. It is speculated that the charging of the particle contaminants on or near the double-aperture (see Fig. 5-9) can attribute to the electron beam spatial drift, hence the variability in the current stability seen with different gas chambers is explainable. We routinely see 1-3 % stability per an hour on the gas chambers with clean surfaces. Further study is necessary to understand the long

term stability of the NAIS and determine the life time of NAIS and the end-of-life mechanism but it appears that the drift of the electron beam may need to be continuously monitored and compensated if there is no solution for the charging behavior.

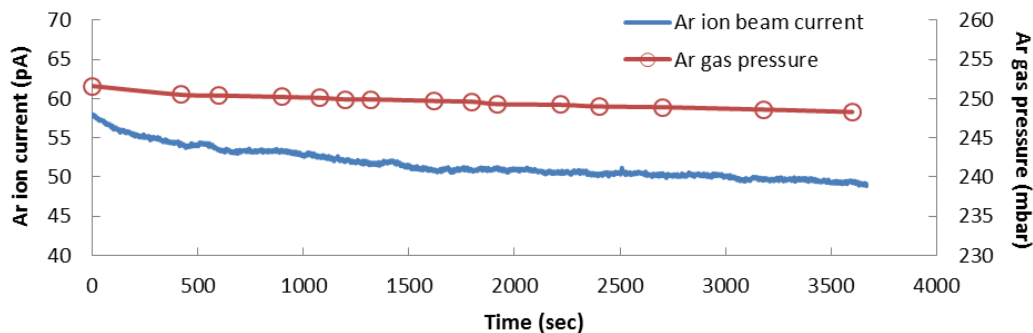


Fig. 5-8 Measured short-term ion beam current stability (GC2, argon gas)

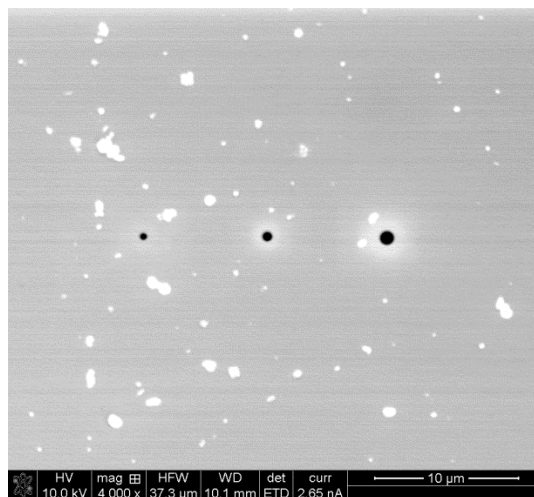


Fig. 5-9 Particle contaminants and charging seen on Gas chamber GC2.

5.3.3 Current distribution and angular intensity

Angular current density or simply angular intensity (I') is a measure of the current emitted into a solid angle (Ω). It can be calculated from measuring current transmitted (I) through a known aperture size (diameter D) placed a distance (L) away from the source. For a small acceptance half angle of the aperture ($D \ll L$) it can be approximated to

$$I' = \frac{I}{\Omega} = \frac{I}{\pi(D/2L)^2} \quad (5.1)$$

Fig. 5-10 shows a current contour profile of an argon ion beam acquired by sweeping a 40 μm aperture over a beam pattern and measuring the current through it. Based on the gas chamber-to-aperture distance of 8.25 mm and the measured current of 28.1 pA, the calculated angular intensity at the center of the beam pattern is about 1.52 $\mu\text{A}/\text{sr}$. The incident electron beam current into the gas chamber was about 12.5 nA at 1keV and both the ion accelerator and the aperture were

set at -2 kV with respect to ground during the measurement. Fig. 5-11 shows one-dimensional current profiles along the arbitrary X and Y lines going through the beam spot in Fig. 5-10. The measurement shows a reasonably nice fit with Gaussian curves, in good agreement with the simulation results in Chapter 4.

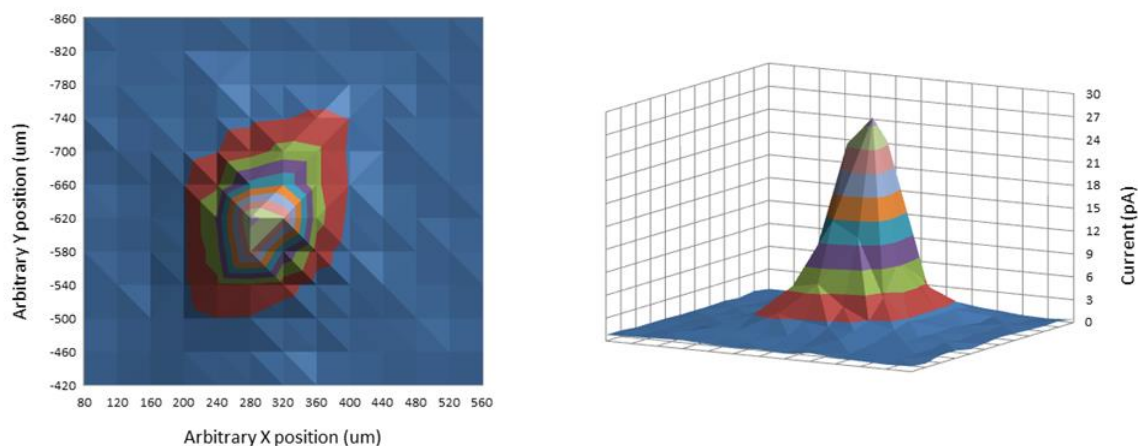


Fig. 5-10 Current distribution of an argon ion beam. The distribution is measured by raster-scanning a small apertured Faraday cup over a beam pattern.

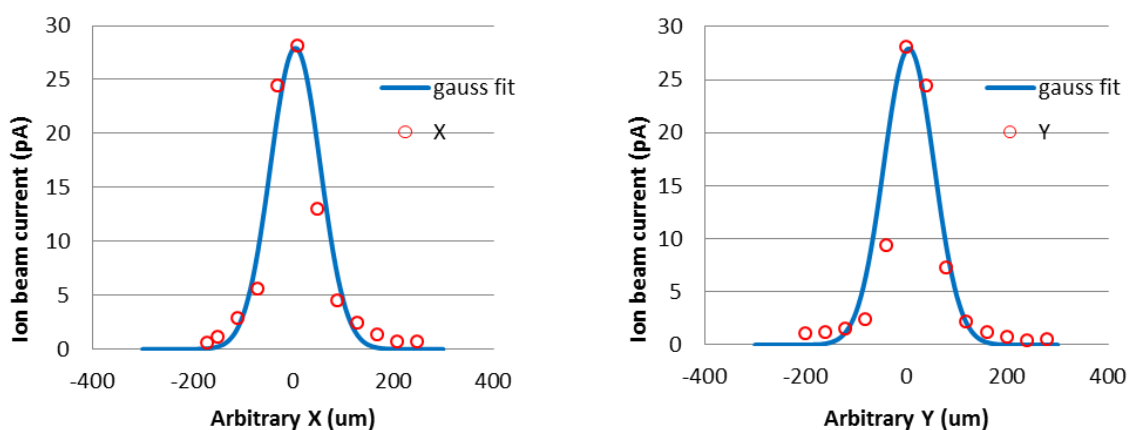


Fig. 5-11 One-dimensional ion beam current distributions along X and Y lines going through the center of the beam pattern of Fig. 5-10 fitted with Gaussian curves.

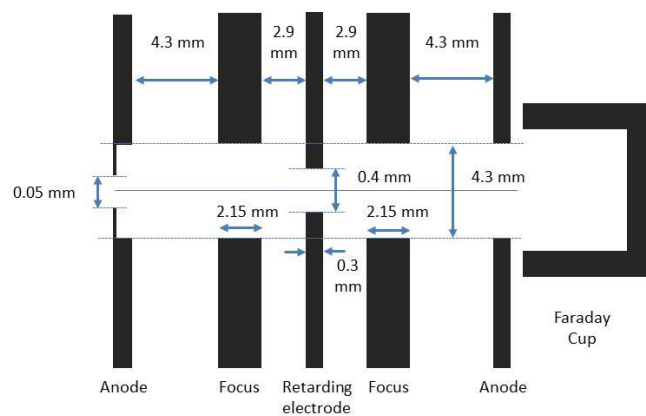
5.4 Energy spread

5.4.1 Retarding field energy analyzer

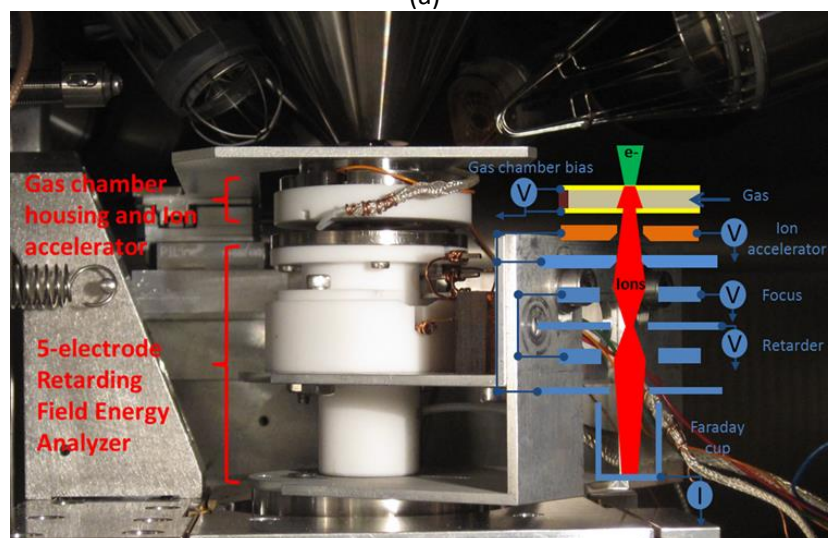
Energy spread dE of an ion (or electron) beam can be measured by several different techniques – using deflection of charged particles in electric and/or magnetic fields, measuring the time it takes for particles to travel between two known points (the time of flight method), or using retarding fields to discriminate against low energy particles and let only particles of sufficiently high energy pass to the collector^[8,9]. For our purpose, the technique of using retarding fields is chosen since an electrostatic retarding field energy analyzer is relatively simple to design and operate but

more importantly, it can be built in compact size that can be implemented within small space available in the SEM experimental setup.

Fig. 5-12 shows the 5-electrode retarding field energy analyzer built to fit in the SEM experimental setup. The analyzer, which is based on the 1961 Simpson paper ^[10], consists of an anode with an entrance aperture, a first focus electrode, retarding electrode, a second focus electrode, and an exit aperture electrode. The entrance aperture and exit aperture electrodes are designed to be biased at the ion accelerator potential and both focus electrodes at a same bias potential, thus making it essentially two immersion lenses placed back-to-back in a mirrored arrangement. The first part decelerates and focuses the incoming beam to a real image at the retarding plane and the second part accelerates the beam again to form another real image at the exit aperture. Only the ions with enough energy are allowed to transmit through the retarding electrode and be collected in the Faraday cup placed following the second immersion lens. The spread in the ion energy distribution can be calculated from measuring the rate of change of the transmitted ion current through the analyzer with respect to the retarding electrode voltage.



(a)



(b)

Fig. 5-12 (a) Schematic drawing of the 5-electrode retarding field energy analyzer and (b) image of the energy analyzer mounted in the NAIS SEM experiment setup. The analyzer mounted on the SEM stage can be tilted, rotated, and x-y-z translated to align to an ion beam.

During the design stage, the performance of the energy analyzer was thoroughly checked through optics simulations and once built, it was first tested against charged particle beams that have been already well characterized and documented by other researchers. For optics simulations, the analyzer design was transcribed to the optics bench of the SIMION program ^[11] and the performance was determined by comparing the assigned energy spread of the ions at the moment of the launch with the energy spread derived from tracking the number of particles transmitted through the retarding electrode while the retarding plate potential barrier was systematically varied by a small voltage step. The assigned energy spread of the ions and the energy spread back-calculated from the responses of the analyzer should be same if the design is perfect. Fig. 5-13 (a) shows the optics design in SIMION and an example ray tracing through it and Fig. 5-13 (b) shows the simulation results comparing the assigned Gaussian ion energy distributions (dE ranging from 20 to 110 meV_{FWHM}) to the corresponding energy distribution measured by the analyzer. For the simulation 10,000 ion particles are randomly launched within a beam acceptance half angle of 3.81 mrad with a 5 keV mean energy. Based on the simulation results we determined that the focus electrode voltage should be set at 3-4 % of the anode voltage (= the incoming beam potential) for the optimum resolution ^[12], and the energy analyzer is fully capable resolving a Gaussian FWHM greater than 70 meV, which is sufficient for characterizing the dE of NAIS.

Experimentally, the energy analyzer was tested to measure the energy spread of beams from a Schottky electron emitter and a gallium LMIS. The measurements were made directly in the Quanta dual beam system that the whole NAIS experiments are based in. The experimental setup was similar to what's shown in Fig. 5-12 (b) but without the NAIS gas chamber setup. The analyzer was placed on the sample stage of the SEM and then moved and tilted facing directly either the electron probe of the SEM column or the ion probe of the FIB column. Fig. 5-14 shows the results of the measurements. For the Schottky source we measured ~1 eV_{FWHM} and for the Gallium LMIS ~6 eV_{FWHM}, which are in good agreement with the measurements by other researchers ^[13-16].

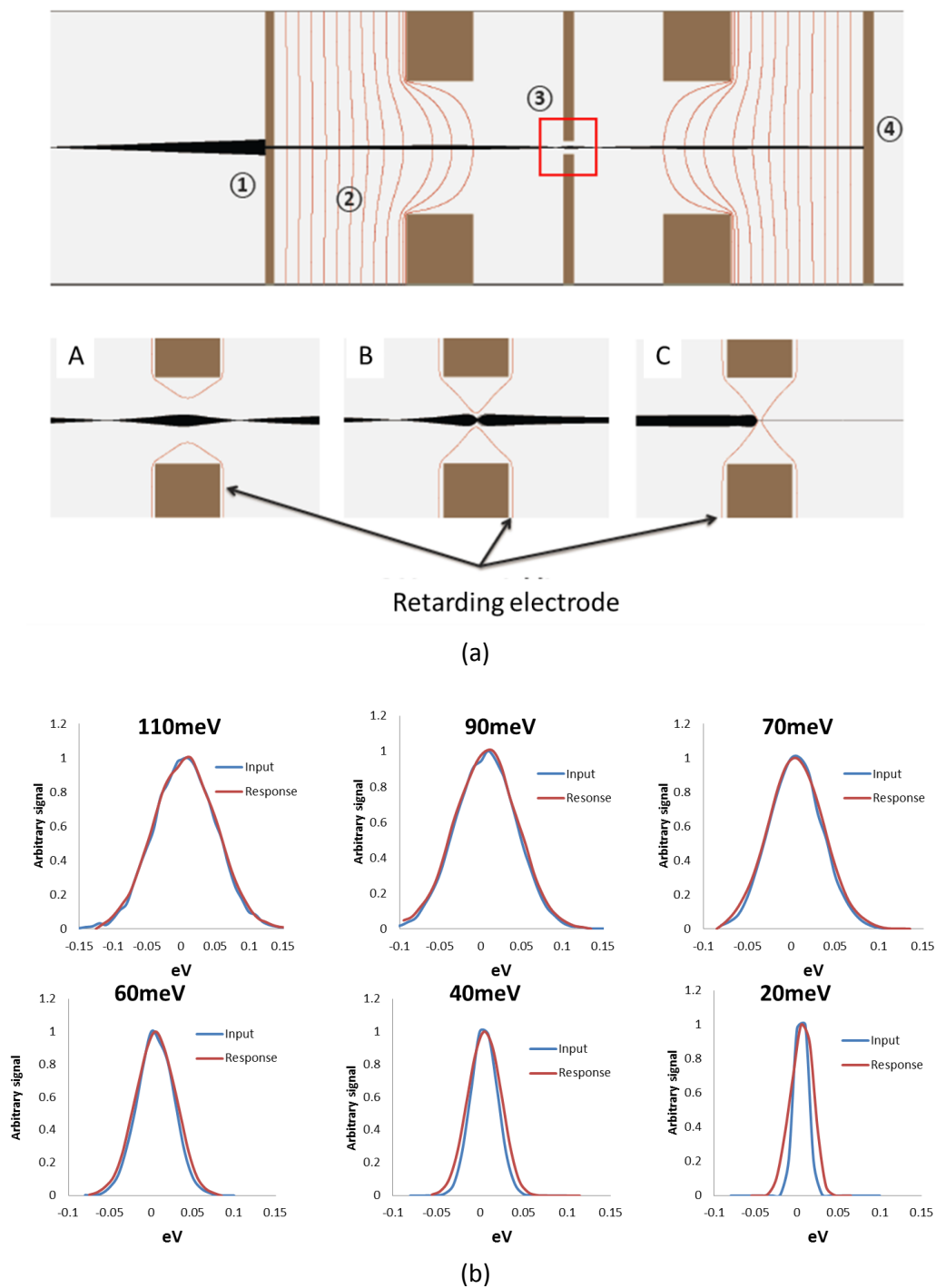


Fig. 5-13 The energy analyzer design was evaluated using SIMION. (a) example ion trajectories through the energy analyzer (A: 100% ion transmission through the retarding electrode, B: ions beginning to be repelled, C: 100% repelled) and (b) The resolution of the design was determined by comparing the assigned ion energy distribution of the ions at the moment of a launch (blue line) and the distribution constructed from the ion transmission responses to the varying retarding electrode voltage (red line).

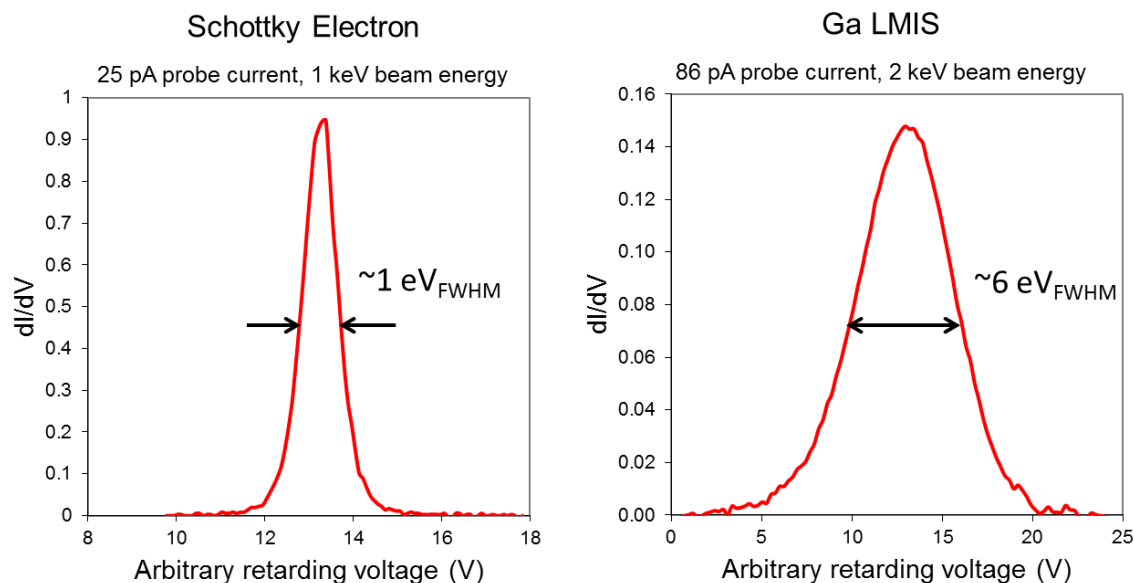


Fig. 5-14 The energy spread measurements of a Schottky electron beam and a Gallium LMIS ion beam in the Quanta dual beam.

5.4.2 Results

Energy spread measurements of an argon ion beam produced from the gas chamber *GC3* are shown in Fig. 5-15. Fig. 5-15(a) shows the measured ion beam current transmitted through the retarding plate aperture as a function of the retarding plate voltage under different gas chamber bias voltage settings and Fig. 5-15(b) the ion current curves in Fig. 5-15(a) differentiated with respect to the retarding voltage. The experimental results are very convincing that the gas chamber bias voltage has strong influence on the ion energy spread; in fact, as predicted from the simulation study in Chapter 3, the overall width of the energy spread is on the order of the magnitude of the gas chamber bias voltage with an exception for zero bias – the energy spread with zero bias looks much the same as the energy spread with 1V bias. This is due to the contribution of the electric-field ($\sim 1.25 \text{ V}/\mu\text{m}$) from the Ion Accelerator sufficiently penetrating into the gas chamber through the ion exit aperture ($\sim 1 \mu\text{m}$) and mimic as if a small bias voltage is applied. Similar effect on the ion beam transmission has already been discussed in Section 5.3.1.

The experimental results also clearly show the development of the secondary peak on the high ion energy side when the gas chamber bias voltage is relatively high. The simulation study has already shown that this happens due to increasing ion transmission from the back side of the gas chamber as a stronger focusing effect develops near the electron entrance aperture as the higher gas chamber bias voltage increase the electric fields between the aperture membranes.

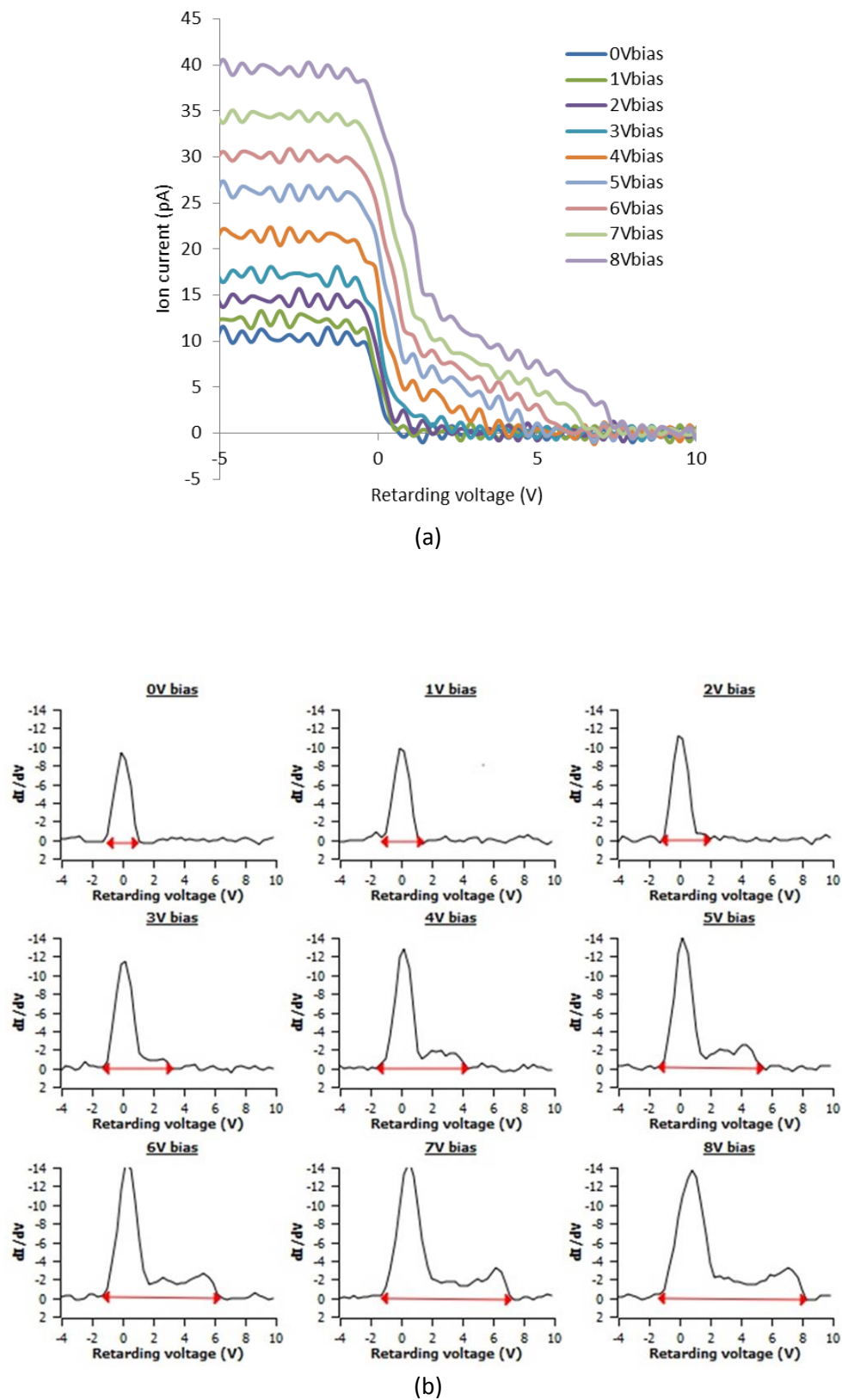


Fig. 5-15 Energy spread measurement using GC3, P=50 mbar, argon gas: (a) Measured ion beam current transmitted through the retarding plate aperture as a function of the retarding plate voltage and (b) the current in Fig. 5-16 (a) differentiated with respect to the retarding voltage.

The influence of the gas pressure on the ion production inside and the extraction out of the gas chamber has been well-thought-out in the design of NAIS and the subject also has been experimentally measured and presented in Section 5.3.1. The energy spread measurements also revealed that the gas pressure can influence the ion energy distribution. Fig. 5-16 shows the measured ion energy distributions at 3 different argon gas pressures - 50, 100, and 200 mbar. Considering the gas chamber spacing of GC3 is 2 μm , the gas pressure of 50 mbar corresponds to be near the molecular flow threshold (*Knudsen number* $Kn \sim 1$). The higher gas pressure would mean the inter-atomic and ion-neutral collisions become more likely and can lead to charge transfer between the ions and neutrals. The measurements in Fig. 5-16 indicate the broadening of the primary peak while the secondary peak is waning off when the gas pressure is significantly increased. The weakening secondary peak is the direct result of the declining number of high energy ions that originates from the back side near the electron entrance aperture due to ion-neutral collisions; however, ion-neutral collisions can yield new ions, which in turn, increase the number of ions originating from the middle and front side of the gas chamber (near the ion exit aperture) and broaden the overall width of the primary peak.

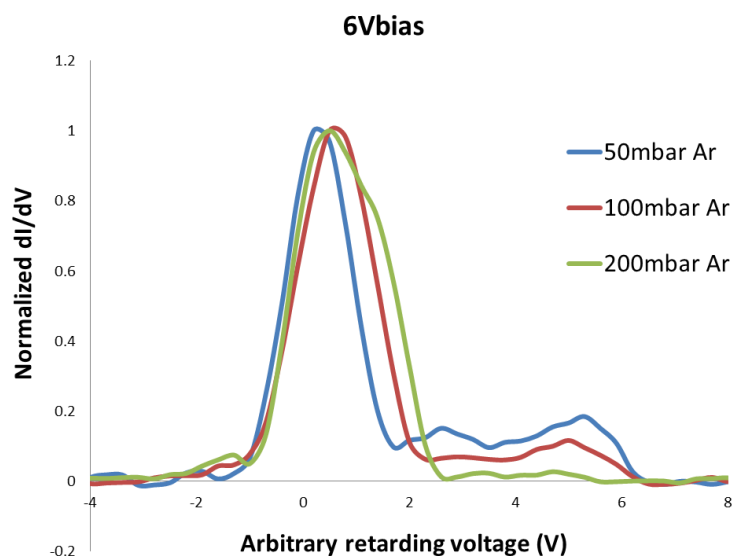


Fig. 5-16 Effect of gas pressure on the ion energy distribution (argon gas, GC3, gas chamber bias voltage fixed at 6 V).

5.5 FIB in a SEM: first ion imaging and milling using a NAIS

The experimental work up until this point has been mainly concerned with characterizing ion beams just as they emerge from the miniaturized gas chambers without needing to form a small probe as our primary objective has been to verify the basic functionality of the miniaturized gas chamber and demonstrating the generation of stable ion beams of noble gas species. Now that we have sufficiently established reliable ion extraction with ion current and energy spread on par with our theoretical expectations, attention is now turned to investigate the practicality of a small ion probe derived from a NAIS. The SEM experimental setup is one step further extended to include ion focusing optics and deflectors to form a small ion probe on sample for imaging and milling small features.

Fig. 5-17 is a simple sketch describing the new ion probe forming experimental setup (the 'mini-FIB') in the SEM and Fig. 5-18 a CAD illustration detailing the components layout. Similar to the earlier experiments, ions emerge from the gas chamber and accelerated by Ion Accelerator but in the new setup a gun lens (C1) is added to collimate the ion beam. The entire gas chamber housing assembly including C1 is mounted on the Piezo controlled extension arm capable of providing coarse alignment of the gas chamber to a SEM electron probe. The probe forming optics assembly and an imaging sample, on the other hand, were installed on the SEM stage. This enables mechanical movement of the ion probe forming optics to the ion beam emerging from C1 for alignment. The probe forming optics incorporated in this experiment is originally a prototype objective lens assembly of a mini electron column developed by FEI Company. Although the entire section stands about 50 mm tall, the assembly includes two-electrode objective lens, double scan octupole deflectors, and a built-in scintillator for thru-the-lens secondary electron detection capability. The amount of current landing on the sample was controlled by the strength of C1 and the size of the beam defining aperture (BDA) placed just above the probe forming optics. The imaging sample used was a simple silicon grid. A small Faraday cup was added below it for measuring ion probe current. Ion imaging was possible by collecting and converting secondary electron signals generated from the sample to photon signals using the scintillator. The light signal is further amplified by a photo-multiplier tube (PMT) before being synched to scanning and imaging electronics.

A huge challenge in designing and implementing this experiment was configuring high voltages for the test setup. Because the SEM normally operates with a target fixed at ground potential, the gas chamber membrane just below the electron probe forming lens was fixed at ground potential and the other membrane up to several volts below ground potential using a battery. Such configuration means that the entire ion optics components including the scan octupole deflectors and the ion beam target must be biased to negative high voltage inside the SEM vacuum chamber sitting at ground potential in order to accelerate and focus the ion beam. Due to high voltage design constraints in the SEM chamber and the limitations in the high voltage floating of the scanning electronics, the maximum acceleration voltage for the mini-FIB was limited to 5 kV.

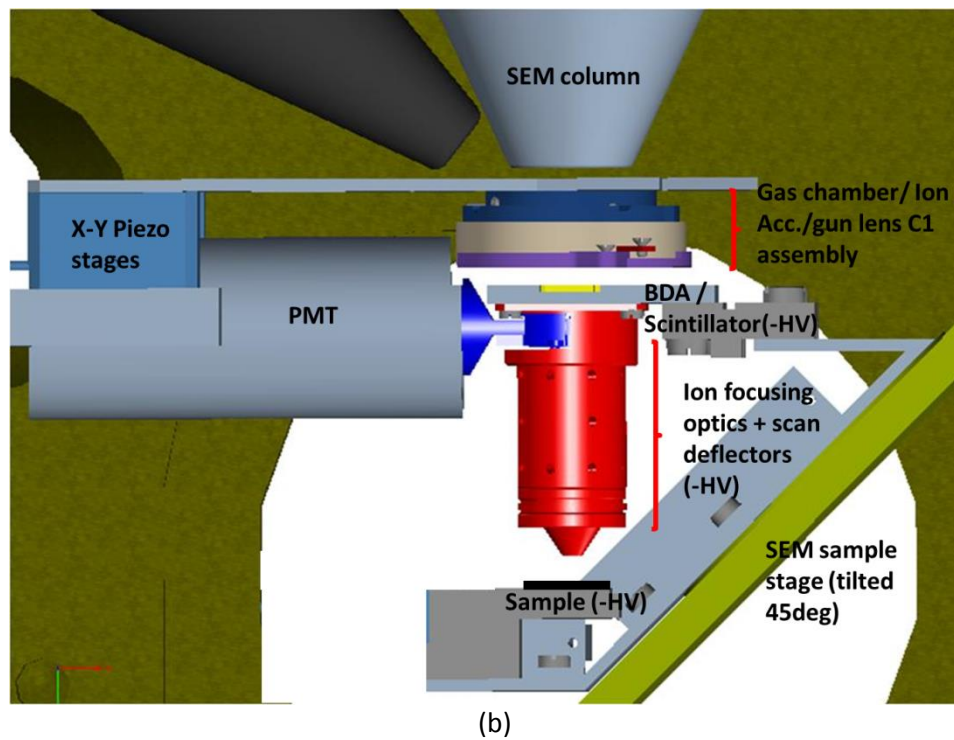
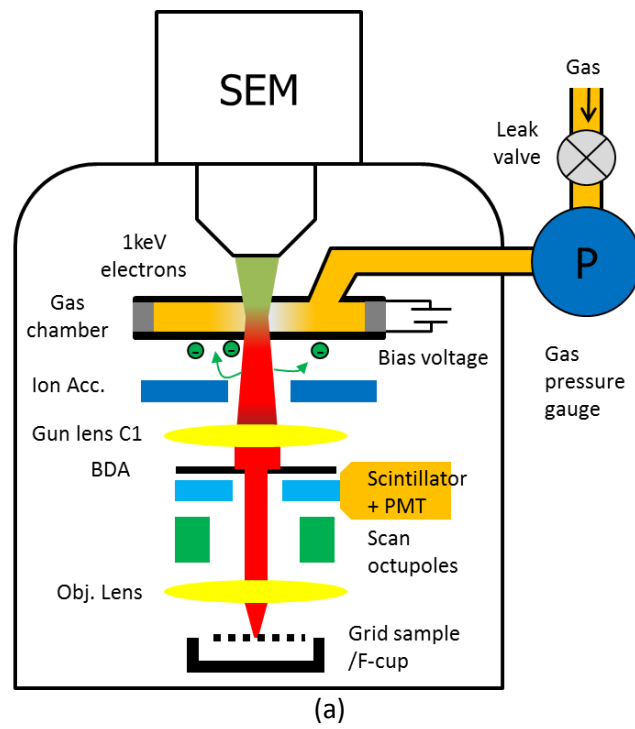


Fig. 5-18 (a) Schematic describing ion probe forming setup (the ‘mini-FIB’) in the SEM and (b) CAD illustration detailing the main components of the mini-FIB.

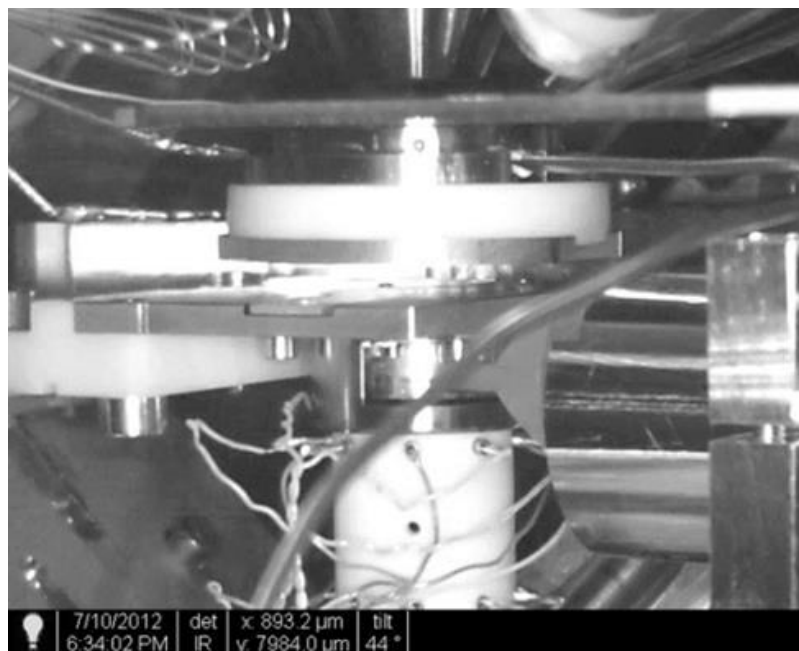
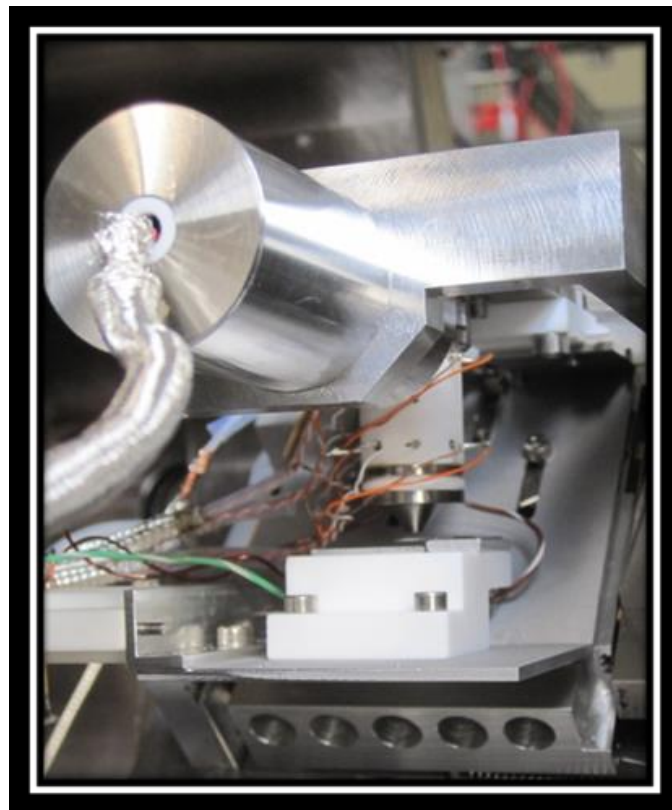


Fig. 5-19 The mini-FIB system in the SEM.

5.5.1 First FIB images

An improvised mini-FIB system incorporating the NAIS concept was built (Fig. 5-19) and for the first time ever, images using a focused argon ion beam generated from a miniaturized gas chamber were obtained. The images shown in Fig. 5-20 are of a silicon grid structure (35 μm grid bar width, 130 μm pitch), taken with approximately 70 pA of argon ions (Gas chamber GC4, 200 mbar argon gas, 8 nA SEM probe, 3 V gas chamber bias voltage) at a 5 keV beam energy. The probe current was measured in the Faraday cup placed just below the grid prior to imaging. The size of the BDA used for imaging was 40 μm in diameter and the sample was placed 3 mm below the mini-SEM objective lens (working distance WD = 3 mm). Fig. 5-21 illustrates the detailed mini-FIB optics layout and indicates the voltages applied to the column for imaging the silicon grid.

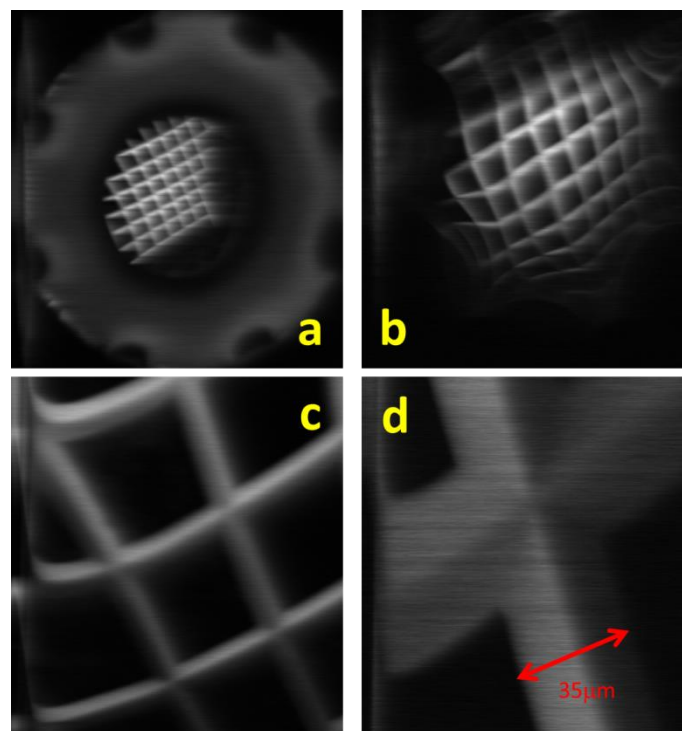


Fig. 5-20 First-ever FIB images using argon ions from a NAIS prototype (Gas chamber GC4, 70 pA, C1 at -500 V, 5 keV, 3 mm WD): (a) ion beam scanned over the upper octupole and (b) thru (d) silicon grid structure (130 μm pitch) at different scan magnifications.

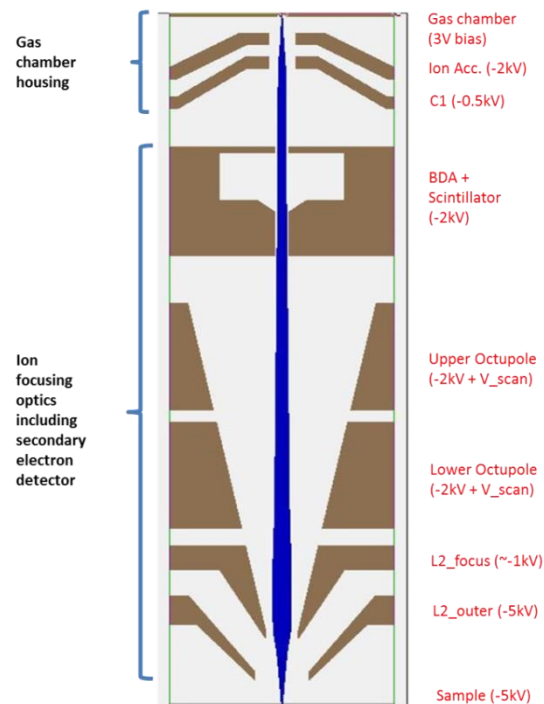


Fig. 5-21 Mini-FIB optics layout and voltage settings for the images in Fig. 5-20. All voltages are with respect to ground.

The grid images of Fig. 5-20 show obvious deviations from the rectilinear pattern of the silicon grid due to scan distortions. Unfortunately, there existed persistent mechanical misalignment and tilt between the upper gas chamber housing assembly and the lower probe forming optics that couldn't be simply corrected by SEM stage movement. Deviations in ion beam trajectory introduced by the optics misalignment also couldn't be corrected by electrostatic beam deflection using the octupole deflectors. In the end, the beam couldn't be properly aligned to the center of the final lens and scanned pivoting on its image principle plane, resulting poor imaging quality and magnification varying unevenly in the scan field.

5.5.2 First FIB milling

For demonstrating material removal by a focused ion beam, the silicon grid sample was replaced by a 100 nm thick molybdenum covered silicon nitride membrane in order to create a recognizable feature in a relatively short amount of time and make identification of the milled features much easier during inspection. Fig. 5-22 shows several images of the membrane sample and a couple of milled features on it. Both imaging and milling were performed under the same gas chamber settings and focusing voltage conditions used for imaging the silicon grid sample (Fig. 5-21) but with a larger probe current of 250 pA. The increase in current was done by changing the BDA diameter to 100 μm . Initially it was difficult to tune the beam as the membrane was blank and no reference features were available to set the focus. Varying the scan field of view to check on milling progress and changing the focus numerous times during milling led to very irregular shapes. Fig. 5-23 is a post-processing SEM inspection image of the milled features of Fig. 5-22. Once the ion beam was focused and tuned up as good as possible, milling in spot mode was attempted. Figure 5-7 shows a SEM image of the smallest spot-burn achieved with the focused argon ion beam.

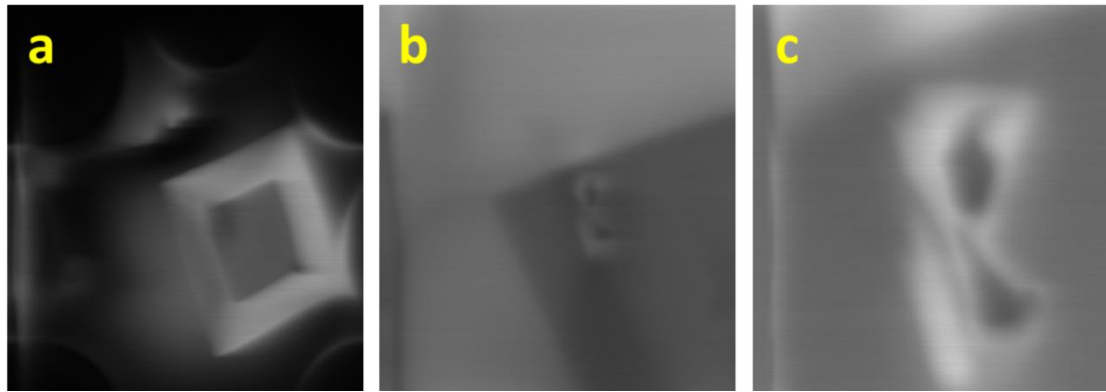


Fig. 5-22 Argon ion imaging and milling on a 100 nm thick molybdenum covered Si_3N_4 membrane (100 μm BDA, 250 pA, C1 at -500 V, 5 keV, 3 mm WD). (a) Large scan field view showing the entire membrane area. The darker area in the upper left corner of the membrane is where ion milling took place. (b)&(c) Zoomed views of the darker area. The two tear-drop shaped areas are where the argon ions milled through. The strange looking shapes are the result of zooming in and out multiple times while impatiently checking for the milling progress.

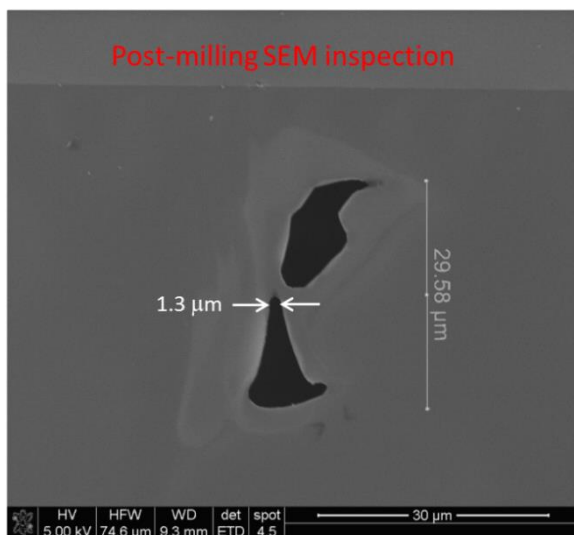


Fig. 5-23 SEM micrograph: SEM inspection of the FIB milled features of Fig. 5-22.

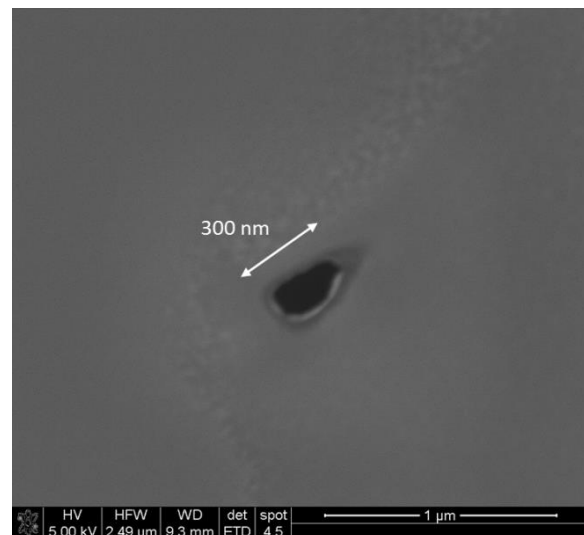


Fig. 5-24 SEM micrograph: the smallest spot-burn made on a thin membrane with a 250 pA, 5 keV argon ion beam.

5.6 Source reduced brightness

The reduced brightness (B_r) of an ion or electron source is an important quantity since it fundamentally determines the maximum amount of current that can be focused into a small probe. The source reduced brightness is often defined as,

$$B_r = \frac{4I}{\pi d_v^2 \Omega V_o} = \frac{4I}{\pi d_v^2 (\pi \alpha_o^2) V_o}, \quad (5.2)$$

where I is the current leaving from the source diameter d_v into a solid angle Ω , accelerated by the object side potential V_o . For a small beam acceptance half angle α_o , the solid angle can be approximated to $\pi\alpha_o^2$.

Because the reduced brightness is a conserved quantity throughout the particle optics system where coulomb interactions are negligible, in a situation involving a probe forming system, the reduced brightness of the source can be alternatively expressed in terms of the probe size d_i , the probe current I , the angular magnification M_α of the entire focusing optics, and the image side beam acceleration potential V_i :

$$B_r = \frac{4I}{\pi d_i^2 (\pi \alpha_o^2 M_\alpha^2) V_i} \quad (5.3)$$

Note that the probe size in Eq. 5.3 represents the magnified source image. For a non-source image dominant probe, aberration contributions should be subtracted from the total probe size.

In principle, using Eq. 5.3, the reduced source brightness of the NAIS can be estimated based on the current measured and beam size deduced from the mini-FIB experimental results and certain focusing optics parameters obtained from computer simulation. Unfortunately, the argon ion images shown in Figs. 5-20 and 5-22 are insufficient for an image analysis (i.e. edge resolution analysis) to extract meaningful and reliable beam size information as the images contain too much scan distortion. However, if we *loosely* take the diameter of the spot-burn (~ 300 nm) in Fig. 5-24 as the beam size for the 250 pA/5 keV beam used for the milling and apply the values of α_o and M_α in Table 5-2, which are obtained from computer simulation using EOD optics software^[17] (version 3.072), the apparent reduced beam brightness seen at the image plane is estimated to be about 3×10^3 A/m²srV. Note that the image half angle defined by the object half angle and the column angular magnification in Table 5-2 are sufficiently small, hence the aberration contributions to the overall beam size are relatively small. From the calculated column magnification of -0.55, the virtual source diameter, the apparent source size in which the ions appear to come from, is also estimated to be about 545 nm.

Table 5-2. Mini-FIB key optics parameters obtained from computer simulations.

Physical column settings	BDA dia. (μm)	40	100
	Probe current (pA)	70	250
	C1 voltage (V) wrt ground	500	500
	Beam energy (eV)	5000	5000
	Working dist. (mm)	3	3
EOD simulation results	Angular mag M_α	-1.15	-1.15
	Linear mag M	-0.55	-0.55
	Object angle α_o (mrad)	3.23	8.08
	Image angle α_i (mrad)	3.7	9.3
	Chromatic ab. coeff. (mm), image side	58	58
Spherical ab. coeff. (mm), image side	577	577	

The estimated reduced brightness and virtual source diameter above are quite contrary to what we are targeting for a NAIS, however, considering the sub-optimal gas chamber dimensions of the prototype gas chamber and the much lower electron current used for the experiment, the outcomes are not unreasonable. Theoretically the NAIS can provide a very high reduced brightness

by forming a small yet very intense ionization inside a miniaturized gas chamber. Our simulation results in Chapter 3 have shown that for a miniaturized gas chamber with spacing and aperture dimensions comparable to the beam width of the incoming electron beam, the virtual source size is on the order of the width of the incident electron beam. Hence, with our target NAIS gas chamber geometry of 100-200 nm spacing with 100 nm double-aperture diameter and an incident electron beam of 100 nm diameter, the expected source size is around 100 nm in diameter. In the mini-FIB experiment a gas chamber (*GC4*) with a much larger spacing (2 μm) and aperture diameter (1 μm) is used. The measured SEM probe applied to the gas chamber was on the order of 100 nm, however, due to ion emission arising from a much longer ionization volume (much longer in length and wider beam angle accepted by the much larger aperture size), the resulting virtual source size is much larger than the width of the electron beam. If we take one step further and assume the source diameter to be 100 nm instead of 520 nm for a 250 pA beam then the reduced brightness is roughly $8 \times 10^4 \text{ A/m}^2\text{srV}$. Furthermore, the reduced brightness analyzed here is based on the 250 pA argon ion beam produced from an 8 nA electron probe. We expect that an electron gun using a Schottky electron source can be optimized to focus more than 100 nA in a 100 nm probe spot. Because the brightness of the NAIS is directly proportional to the current density of the incident electron beam, if an electron probe of 100 nA were focused to the gas chamber used for the mini-FIB experiment, then the reduced brightness should increase by 12 times. This indicates that $B_r \sim 1 \times 10^6 \text{ A/m}^2\text{srV}$ is quite possible for the NAIS if the target gas chamber dimensions and incident electron current density requirements are met.

5.7 Conclusions

Our target NAIS is comprised of a sub-micron scale gas ionization chamber and an electron gun equipped with a Schottky electron emitter that can focus more than 100 nA of electrons into a sub-100 nm beam spot. Because the electron gun specifically designed to accompany a NAIS is currently being developed, an improvised NAIS prototype was devised inside a commercial SEM to perform several proof-of-concept experiments. The basic idea behind the improvisation entailed to installing a prototype gas chamber inside the SEM specimen chamber, filling it with a gas, and inducing gas ionization by simply focusing a SEM probe into it.

Albeit the SEM could provide much less electron current ($\sim 10 \text{ nA}$), the experimental setup was sufficient to demonstrate gas ionization inside miniaturized gas chambers by electron impact and the extraction of ion beams by applying a relatively small gas chamber bias voltage. We have shown that NAIS can easily provide beams of noble gas ions and verified that the amount of ion current generated from a miniaturized gas chamber depends on the gas pressure, gas ionization cross section, gas chamber bias voltage, and the incident electron current and beam energy, all in good agreement with our theoretical expectations. By incorporating a retarding field energy analyzer inside the SEM experimental setup, the ion energy spread of an ion beam arising from a prototype gas chamber has been characterized. We have verified that the ion energy spread strongly depends on the applied gas chamber bias voltage and shown that the energy spread $< 1 \text{ eV}_{\text{FWHM}}$ is possible for NAIS. Additionally, we have built a simple mini-FIB by incorporating an ion probe forming optics and scan deflectors in the SEM experimental setup and demonstrated for the first time ion imaging and milling using an argon ion beam arising from a miniaturized gas chamber. Lastly, the reduced source

brightness of NAIS is estimated based on the spot burn diameter and current measured from a focused argon ion beam and column parameters obtained from computer simulations. The estimated value is quite less than the target reduced brightness for the NAIS, however, it's well within reason considering the sub-optimal gas chamber dimensions and lower incident electron beam current used for the experiment.

Acknowledgement

The author would like to thank A. C. Wattjes, C. Barends, and G. Schotte for their technical assistance in designing and fabricating the parts necessary for the proof-of-concept experiments. The author would also like to thank the Beam Tech R&D group of FEI Company for providing the mini electron column components. This research is supported by the "Stichting voor Fundamenteel Onderzoek der Materie (FOM)", which is financially supported by the "Nederlandse Organisatie voor Wetenschappelijk Onderzoek" and FEI Company.

References

- [1] www.fei.com
- [2] FEI image software a proprietary program that calculates the beam size based on pixel intensity change along a line over an edge (edge resolution) of a SEM or FIB image. It's used to assess the imaging resolution of the FEI systems.
- [3] R. Rejoub, B. G. Lindsay, and R. F. Stebbings, Determination of the absolute partial and total cross sections for electron-impact ionization of the rare gases, *Phys. Rev. A* **65**, 042713 (2002)
- [4] P. L. Bartlett and A. T. Stelbovics, Calculation of electron-impact total-ionization cross sections, *Phys. Rev. A* **66**, 012707 (2002)
- [5] L. W. Swanson and G. A. Schwind, *Handbook of Charged Particle Optics*, 1st ed., edited by J. Orloff (CRC, New York, 1997), Chap. 2.
- [6] M. J. Fransen, PhD dissertation, Delft University of Technology, 1999
- [7] J. F. O'Hanlon, *A User's Guide to Vacuum Technology*, Wiley and Sons, New York, NY, 2003
- [8] W. Steckelmacher, Energy analysers for charged particle beams, *J. Phys. E: Sci. Instrum.* **6**, 1061 (1973)
- [9] H. Zhang, *Ion Sources* (Springer, 1999)
- [10] J. A. Simpson, Design of retarding field energy analyzers, *Rev. Sci. Instrum.* **32**, 1283 (1961)
- [11] www.simion.com
- [12] M. van der Heijden, Energy spread measurement of the Nano-Aperture Ion Source, Masters thesis, Delft University of Technology, 2012
- [13] H. S. Kim, M. L. Yu, M. G. R. Thomson, E. Kratschmer, and T. H. P. Change. Energy distributions of Zr/O/W Schottky electron emission. *J. Appl. Phys.*, **81**(1): 461-465, 1997

- [14] M. S. Bronsgeest, J. E. Barth, G. A. Schwind, L. W. Swanson, and P. Kruit, Extracting the Boersch effect contribution from experimental energy spread measurements for Schottky electron emitters, *J. Vac. Sci. Technol. B* **25**, 2049 (2007)
- [15] L. W. Swanson, G. A. Schwind, and A. E. Bell, Measurement of the energy distribution of a gallium liquid metal ion source, *J. Appl. Phys.* **51**, 3453 (1980)
- [16] J. C. Beckman, T. H. P. Chang, A. Wagner, and R. F. W. Pease, Energy spread in liquid metal ion sources at low currents, *J. Vac. Sci. Technol. B* **14**, 3911 (1996)
- [17] www.lencova.com

6 ■ Delft NAIS-FEI Sidewinder Integration: the concept and design

The proof-of-concept experiments performed inside a scanning electron microscope have successfully demonstrated the idea of the small volume gas ionization inside a miniaturized gas chamber by electron impact and provided the first experimental confirmation on reliable ion extraction and low energy spread capability of the NAIS. Now, for extending experimental investigation one step further and evaluating the new ion source performance in a reliable and more capable optics system, integration of a prototype NAIS into an FEI's Sidewinder ion column is planned. Although this plan simply requires replacing the existing Ga LMIS with a NAIS, the integration presents many design challenges involving high voltage, vacuum, and gas delivery due to significant differences between the two sources in terms of size and the mechanism of operation.

In this chapter design details of a NAIS prototype and the mounting scheme to the Sidewinder column are presented. An electron gun based on FEI's CLM and Mini-SEM column is designed to provide a current of 50 nA or more into a 100 nm beam spot. A new vacuum chamber is designed to house the prototype ion source to provide feedthrough connections for gas and high voltage and to interface with the existing Sidewinder chamber. The designed NAIS prototype is expected to provide a reduced brightness comparable to that of the Ga LMIS, but due to much lower energy spread, the newly designed ion column system should provide significant performance improvement over the conventional Ga-LMIS equipped Sidewinder.

6.1 Introduction

Encouraged by the positive outcomes from the numerical simulation work (Chapter 3) and the experimental success supporting the concept of the NAIS (Chapter 5), a plan for devising a full-scale FIB system incorporating a NAIS has emerged and preparation is currently underway. During the earlier stages of this project, an FEI Quanta™ 3D FEG DualBeam™ system, which combines a high resolution SEM column and a high resolution gallium FIB column, had been crucial in preparing miniaturized gas chambers and conducting proof-of-concept experiments. The FIB column was utilized for fabricating gas chamber apertures and the SEM for inspecting and measuring critical gas chamber dimensions. The specimen chamber of the dual beam was utilized as a vacuum test platform for carrying out a number of important experiments for evaluating the basic functionality, verifying mechanical stability of prototype gas chambers and characterizing the ion beams arising from them. The SEM column was, in fact, a part of the prototype ion source providing an electron beam for creating gas ionization in these experiments. Now, our new plan is to build a complete NAIS prototype and install it in a Sidewinder, the FIB column of the Quanta dual beam system, and test to evaluate full source capabilities of a NAIS in a commercial FIB system.

The Sidewinder (SW) ion column (Fig. 6-1) is a two-lens focusing column normally equipped with a gallium liquid metal ion source (Ga LMIS). It is capable of operating between 0.5 - 30 kV acceleration and delivering a wide current range of 1 pA - 65 nA. The column is capable of focusing 1 pA of ion current into ~7 nm diameter at 30 kV.^[1] The general plan is to remove the existing Ga LMIS and modify the source region of the SW to accommodate a prototype NAIS. The SW focusing optics below the source region will remain untouched to preserve the SW optics capability and maintain compatibility to the existing system software and control electronics.

The main purpose of the Delft NAIS-FEI Sidewinder integration is to demonstrate nanometer resolution imaging and milling performance using the new source concept. Although the expected reduced brightness of the new source is similar to that of the existing Ga LMIS, due to a considerably lower energy spread, we anticipate improved system performance from the modified Sidewinder, especially at low beam energies (< 10 keV). The integration will also allow us to study beam stability and lifetime of NAIS in a commercial system and to make direct performance comparisons against the Ga LMIS. Furthermore, the integration will offer opportunities exploring for high resolution FIB imaging and milling optimization based on gas selection, which not an available option with the standard Sidewinder column.

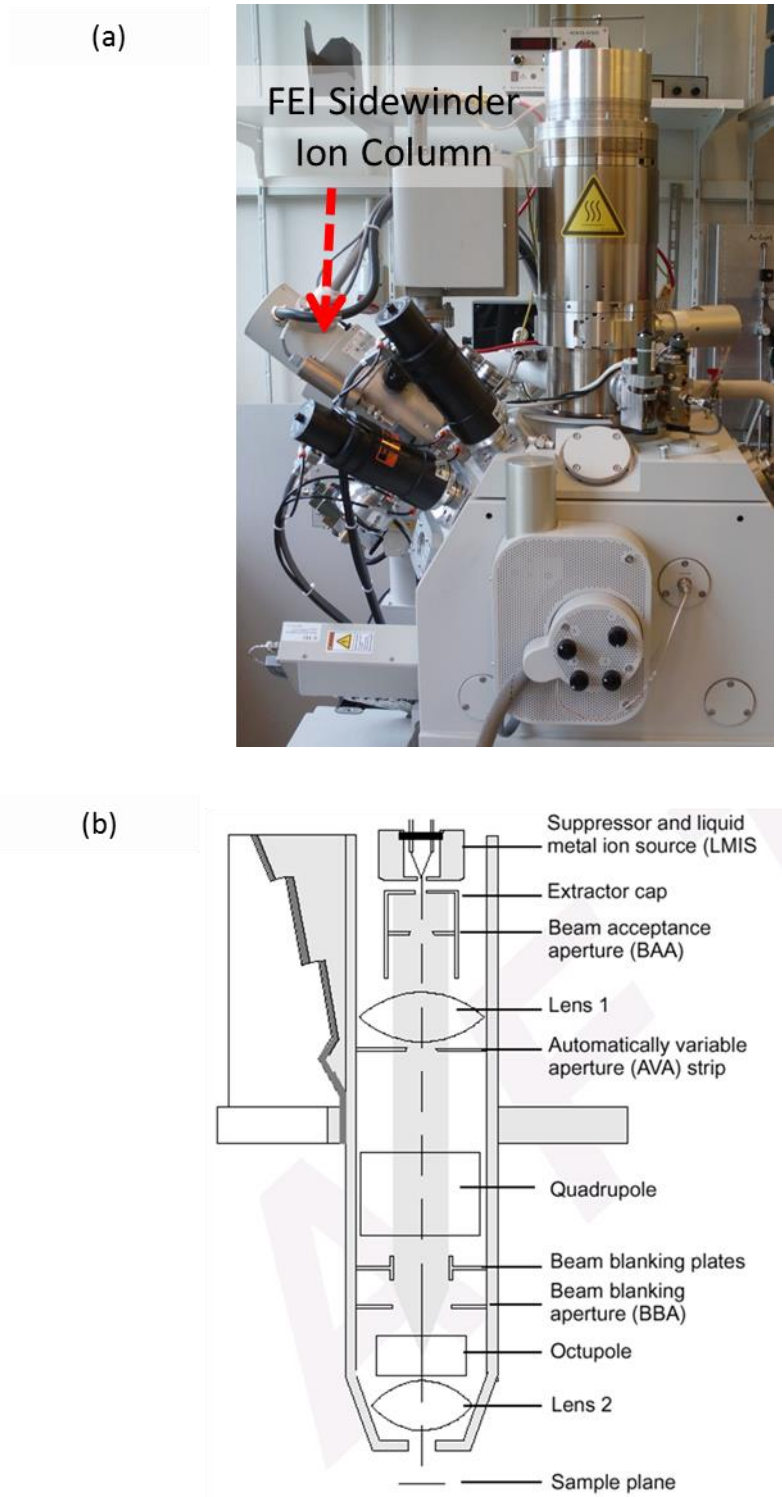


Fig. 6-1 (a) Sidewinder ion column of an FEI Quanta™ 3D FEG and (b) schematic describing main components inside the Sidewinder (adapted from Ref. [2])

6.2 Technical challenges

At first glance, the integration plan may seem straightforward and simple as the core of the work involves ‘only’ swapping the existing Ga LMIS with a NAIS prototype. However, many serious complications and technical challenges arise from the fact that the new source is radically different from the Ga LMIS in terms of physical shape and size and the way it operates. The new source requires different vacuum conditions and electrical arrangements, as well as requiring a gas connection in presence of high voltage. Significant changes to the source region of the Sidewinder column are inevitable, however, modifications to accommodate the new source need to be implemented without significant changes to the focusing optics of the Sidewinder (to preserve the Sidewinder focusing capability) as we want to keep the integration project as simple as possible and maintain compatibility to the existing system electronics and control.

The integration project presents three major technical challenges. The first one is to develop a Schottky electron focusing column that can provide a large amount of electron beam current into the entrance aperture of the miniaturized gas chamber. For achieving a reduced brightness comparable to that of the Ga LMIS ($\sim 1 \times 10^6$ A/m²srV), for using argon gas, for example, the electron column needs to be capable of delivering at least 50 nA of current into a 100 nm beam spot at 1 keV. Additionally, the electron column needs to include beam scanning and imaging capability to provide an easy and reliable way to locate and align an electron beam into the gas chamber aperture. For easier integration to the existing sidewinder chamber and preventing any interference with other peripherals on the Quanta dualbeam system, it is also desired that the overall dimensions of the electron column to be as small as possible.

The second challenge deals with the ‘packaging’ of the electron column and a gas chamber adequately so that the combination (referred as simply the ‘prototype NAIS’ hereinafter) can easily be mounted and complies with the Sidewinder optics. Because of its relatively large difference in size, it is not feasible to swap the gallium LMIS with a NAIS directly. Rather than redesigning the Sidewinder vacuum chamber to make a NAIS fit, the easier and more sensible approach is to design and manufacture a custom vacuum chamber that can hold a NAIS prototype and also can be added on to the existing Sidewinder gun chamber. For designing of the new chamber, however, many factors need to be considered. Due attention should be given to the UHV (ultra high vacuum) requirement of the Schottky source, proper high voltage isolation between the optical elements and the ground chamber walls, adequate arrangement of ports for the gas and electrical connections, external magnetic field shielding, components assembly procedures and internal gas hook-up and electrical wiring scheme. In addition, the design needs to include a mechanical means to move the ion source *in situ* for optical alignment as this is a feature available on the standard Sidewinder column.

The third challenge is developing and configuring high voltage (HV) power supplies and control electronics to operate the NAIS prototype together with the Sidewinder lens and beam energy power supplies. The standard Sidewinder operates at beam energies up to 30 keV by floating the ion source on its main beam supply. This means that the NAIS prototype including all of its driving power supplies must be directly referenced to the beam supply of the Sidewinder column and float all the way up to 30 kV. Because the NAIS prototype includes octupole deflectors for imaging the gas chamber double-aperture and aligning the electron beam into it, this also means that scanning electronics must be floated together. This requires the development of robust high

voltage scanning electronics as well as the control and imaging electronics that can interface with them safely.

Table 6-1 summarizes high level design requirements set on the NAIS-FEI Sidewinder ion column. Details on the design features and requirements are presented in the following section.

Table 6-1. Summary of the prototype ion column design requirements

Design aspects	Requirements
Electron focusing column	<ul style="list-style-type: none"> ▪ Schottky electron source based, electrostatic lens focusing ▪ Electron probe current /size: >50 nA/100 nm @1 keV ▪ Beam deflection for Imaging and e-beam/gas chamber aperture alignment ▪ Bakeable to >150 °C
NAIS ‘packaging’	<p>NAIS vacuum chamber:</p> <ul style="list-style-type: none"> ▪ Stainless steel (SS) 420 chamber material and welded ports for high voltage feedthroughs and gas connection ▪ mu-metal liners for shielding against external EM signals ▪ Bakeable to >150 °C <p>Vacuum:</p> <ul style="list-style-type: none"> ▪ Separated vacuum regions via differential pumping: Ultra high vacuum (UHV) for Schottky source: <1 x 10⁻⁸ mbar High vacuum (HVAC) for gas chamber and SW optics regions: <1 x 10⁻⁶ mbar <p>Gas delivery:</p> <ul style="list-style-type: none"> ▪ Gas chamber gas delivery up to 750 mbar, primarily noble gases ▪ Gas delivery in presence of high voltage (up to 30kV) <p>Optics alignment:</p> <ul style="list-style-type: none"> ▪ Form-scan (rotating table) alignment on all optics element assembly (Schottky emitter radial misalignment < 25 μm, all other optics elements < 5 μm) ▪ Electron beam alignment to the gas chamber by electrostatic deflection ▪ Moveable NAIS mechanism for mechanically aligning the ion source to the Sidewinder focusing optics
High voltage supplies and control	<ul style="list-style-type: none"> ▪ Sample at chamber ground (Quanta3D FEG chamber) ▪ Ion source (gas chamber) +1 kV to +30 kV wrt ground (corresponding to Schottky source 0 kV to +29 kV wrt ground), floated on the Sidewinder beam supply (HTSU) and controlled by Quanta3D software ▪ Electron gun power supplies (FEI FGUSU unit modified): Filament (3 A, 5 V), Suppressor (-2 kV), Extractor (6 kV), Gun Lens C1 (6 kV), Objective lens (15 kV), all Schottky source referenced ▪ Electron gun octupole supply (+/- 500V scan + shift + stigmation), floated on the electron extractor supply, custom software and control for scanning and imaging ▪ Sidewinder lens voltages and ion imaging controlled by the existing system electronics and software

6.3 Prototype ion column design

For convenience the Sidewinder column with a NAIS prototype is referred as the ‘protototype ion column’ hereinafter.

6.3.1 Schottky electron focusing column

The overall performance of the new ion source highly depends on the performance of the electron column that supplies an energetic electron beam into the gas chamber for ionization. For this reason, the new ion source design incorporates an electron column based on the Schottky source in order to maximize the electron current delivered into the gas chamber and maximize ion production. The design target for the electron column is to provide at least 50 nA into a spot of 100 nm at an energy of 1 keV. For having to include beam scanning octupole deflectors and an imaging signal detector such as a secondary electron (SE) detector, the desired electron column (design) essentially equals to a small scale, high current, low voltage SEM.

Fig. 6-2 illustrates the Schottky electron column designed for the prototype ion source. The design is actually the result of combining selective parts from two different products supplied by FEI Company. The upper section of the electron column is based on the FEI CLM electron gun which is used in FEI’s in-line process monitoring and metrology systems. It consists of a Schottky emitter, suppressor, extractor, beam acceptance aperture (BAA), gun lens (C1), and anode, all of which are stacked on the top of a large plate with a DPA (differential pumping aperture). Because the CLM gun is originally designed for low electron probe current operation (<4 nA), the BAA size is enlarged (80 μm diameter) to provide a probe current of 100 nA (based on the Schottky emitter angular intensity $I' = 0.5 \text{ mA/sr}$). Additionally, the gun lens (C1) is redesigned to balance the gun spherical aberration due to the increased beam acceptance angle.

The lower section of the electron column is based on FEI’s concept prototype called Mini-SEM. It’s a small scale column with full SEM capability. Although the entire lower section stands about 50mm tall, it consists of two-electrode objective lens, double octupole deflectors, and a scintillator for thru-the-lens secondary electron detection capability. Its relatively small footprint allows easy mounting below the DPA plate of the CLM column.

Fig. 6-3 shows the 1 keV column performance of the designed Schottky electron column simulated with EOD (Electron Optics Design, version 3.072) software ^[3]. The plot shows the FW 50 beam size (beam size containing 50% of current) calculated using the root-power-sum method ^[4] as a function of the C1 voltage. The results indicate that the minimum beam size achievable is about 46 nm for a probe current of 50 nA. This translates to the amount of current that can be delivered into a 100 nm gas chamber aperture is approximately 80 nA, exceeding our design target. The 1 KeV operating condition is chosen to maximize both electron current density achieved with a Schottky electron gun and the ionization cross section of noble gases. The calculation assumes an extraction voltage of 5 kV and the Schottky emitter angular intensity (I') of 0.5 mA/sr, and the image plane (the gas chamber) to be 2 mm below the Mini-SEM objective lens (i.e. working distance $WD = 2 \text{ mm}$). The virtual source size of the Schottky source is assumed to be 28 nm ^[5] and the energy spread of the electron beam to be $1 \text{ eV}_{\text{FWHM}}$ ^[6,7].

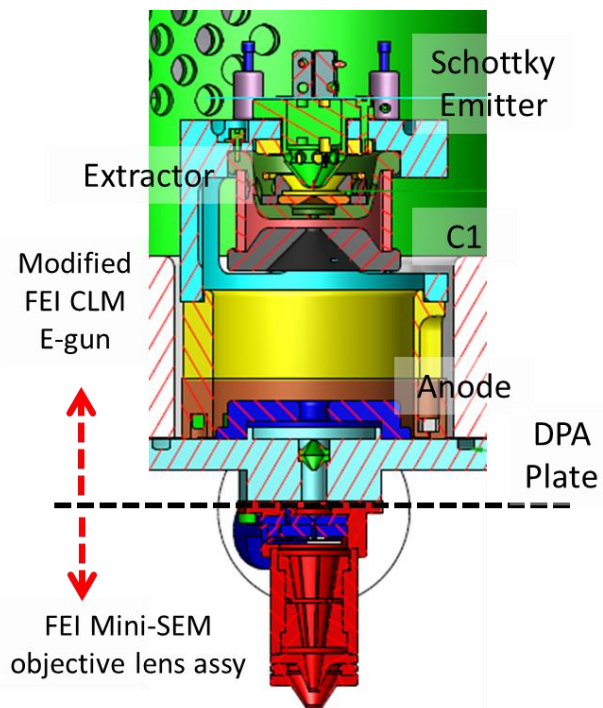


Fig. 6-2 Schottky electron column for the prototype NAIS

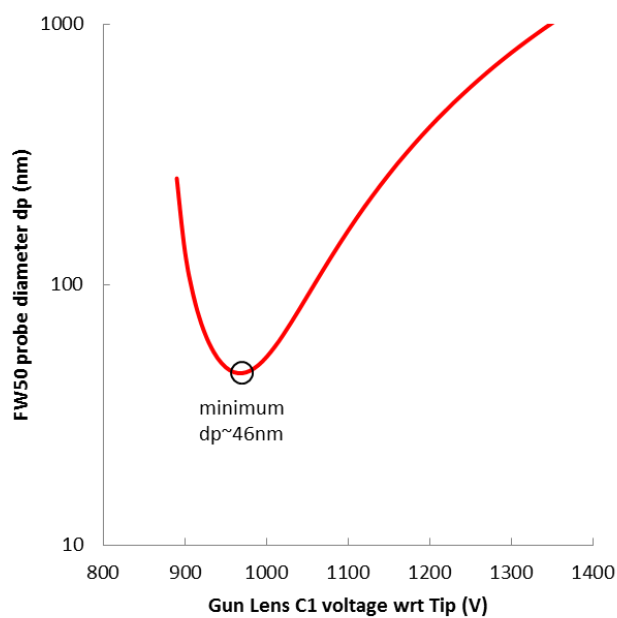


Fig. 6-3 Simulated performance of the Schottky electron column of Fig. 6-2.

6.3.2 NAIS 'packaging'

A key component required for the NAIS-Sidewinder integration project is the NAIS vacuum chamber. In the standard Sidewinder ion column, a Ga LMIS is held by the source end assembly that mounts from the top of the Sidewinder main vacuum chamber (see Fig. 6-4). Removing the source end assembly leaves relatively open space above the ion extractor, however, just not enough room for the entire NAIS structure and make all the necessary high voltage and gas connections in a safe manner. This issue is circumvented by keeping the NAIS prototype in a separate vacuum chamber (the NAIS vacuum chamber) and mounting the whole thing on top of the Sidewinder main chamber as shown in Fig. 6-5. The new chamber is designed to keep the entire NAIS assembly perched up inside its relatively wide body to give enough room for electrical and gas connections. This arrangement, however, alters the source location from the original Sidewinder optics geometry affecting the overall column magnification. The source is now located 100 mm farther way from the first lens (Lens 1) of the Sidewinder, but it is determined through optics simulations that this arrangement can still yield satisfactory ion column performance. More on the simulated optics performance of the prototype ion column will be discussed in detail in Section 6.4.

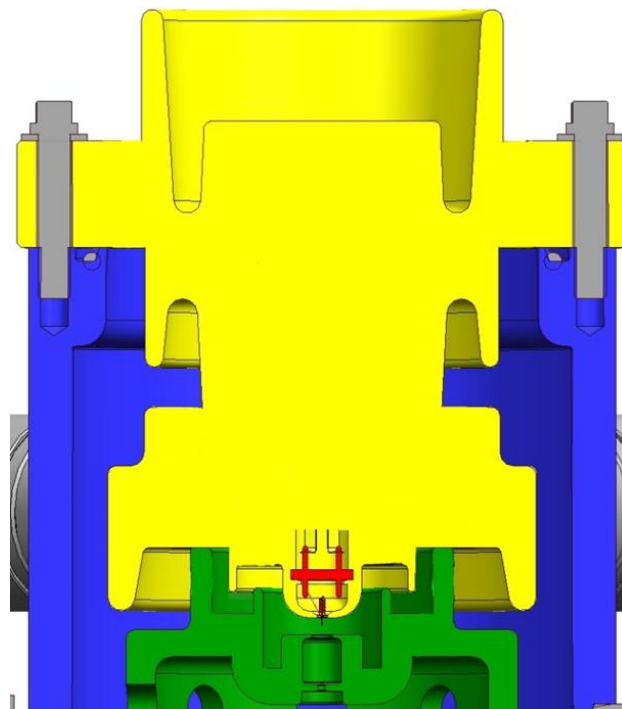


Fig. 6-4 CAD cross-section showing Ga LMIS (red) in the Source end assembly (yellow), and Extractor assembly (green) in the Sidewinder ion column chamber (blue).

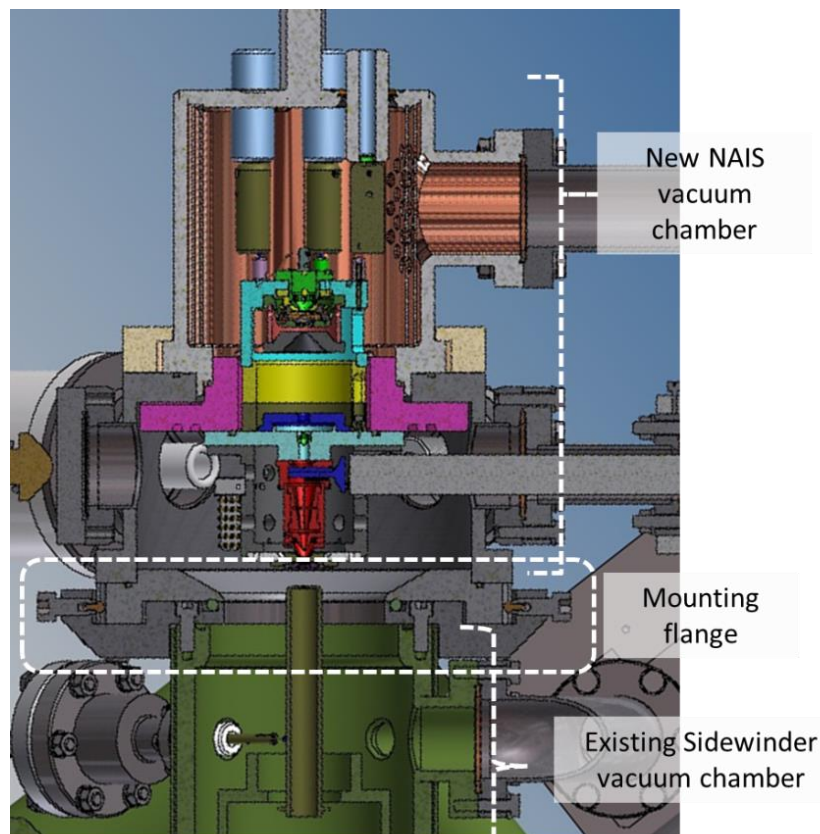


Fig. 6-5 CAD image illustrating the NAIS vacuum chamber design and mounting concept.

A. *NAIS vacuum chamber*

Details of the new NAIS vacuum chamber are shown in Fig. 6-6. The chamber is actually constructed of two separate pieces (*the upper and the lower*) clamped together with an O-ring in-between for vacuum sealing. The upper piece is a standard CLM gun chamber slightly modified to fit with the lower piece. It is made of stainless steel (SS 420) which is a widely used material for vacuum components due to its strength, tolerable machining and welding properties, and high magnetic permeability. It is also lined with two 1 mm thick internal mu-metal shields for additional magnetic shielding. The lower piece is a custom design with 8 conflat side ports (2- $\frac{3}{4}$ inch). It is also made of stainless steel (SS 420) and designed to be covered with a layer (1 mm thick) of mu-metal on the outside.

Electrical and gas connections are made through the top side of the vacuum chamber and also from the side. On top of the upper piece is a welded 5-pin high voltage feedthrough, rated to 45 kV. These pins are used for electrical connection to the upper section of the Schottky electron column that includes emitter filaments, suppressor, extractor, and the gun lens C1. High voltage connections to the rest of the Schottky electron column (octupole deflectors and the electron probe forming lens electrodes) and the gas chamber are made through the side ports of the lower piece of the vacuum chamber, along with the gas connection and transferring optical signals from the scintillator via a quartz glass rod. Fig. 6-7 shows the vacuum chamber ports layout for the high voltage, glass rod, and gas feedthroughs and Fig. 6-8 the actual electrical wiring in the Mini-SEM and gas chamber region of the prototype unit currently being assembled.

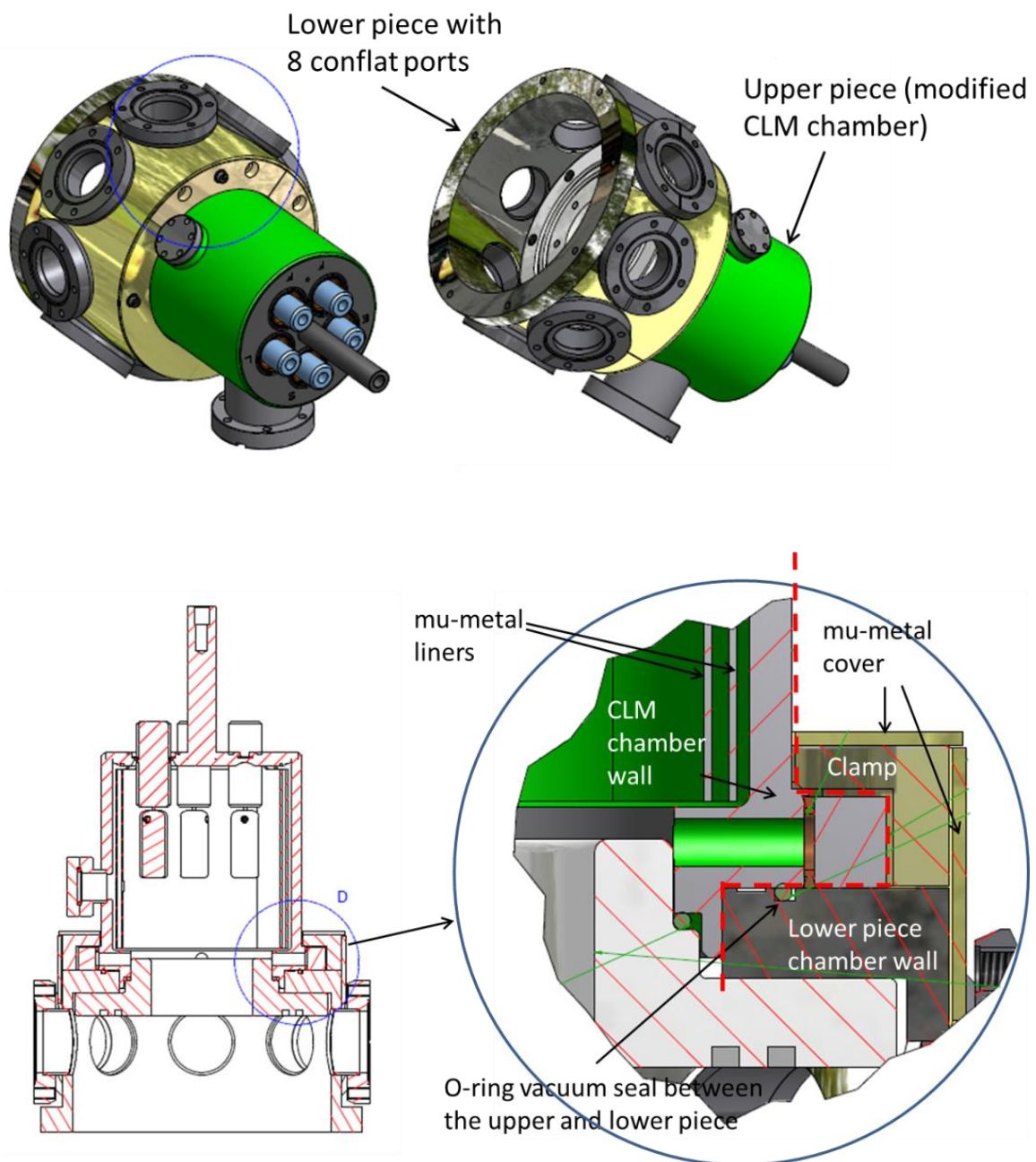


Fig. 6-6 Design details of the NAIS vacuum chamber.

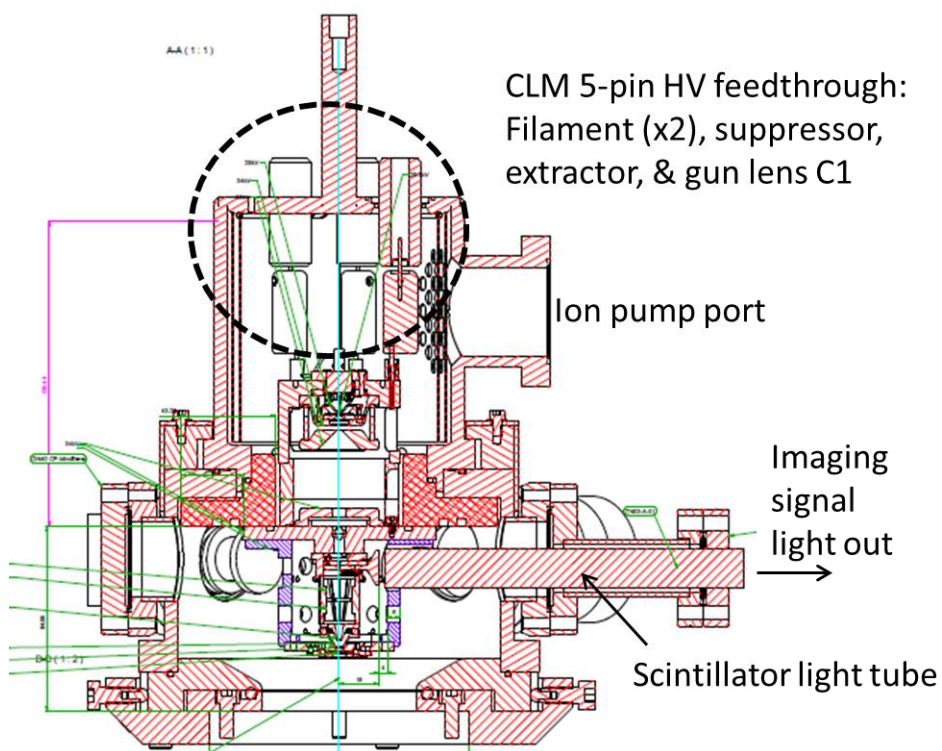
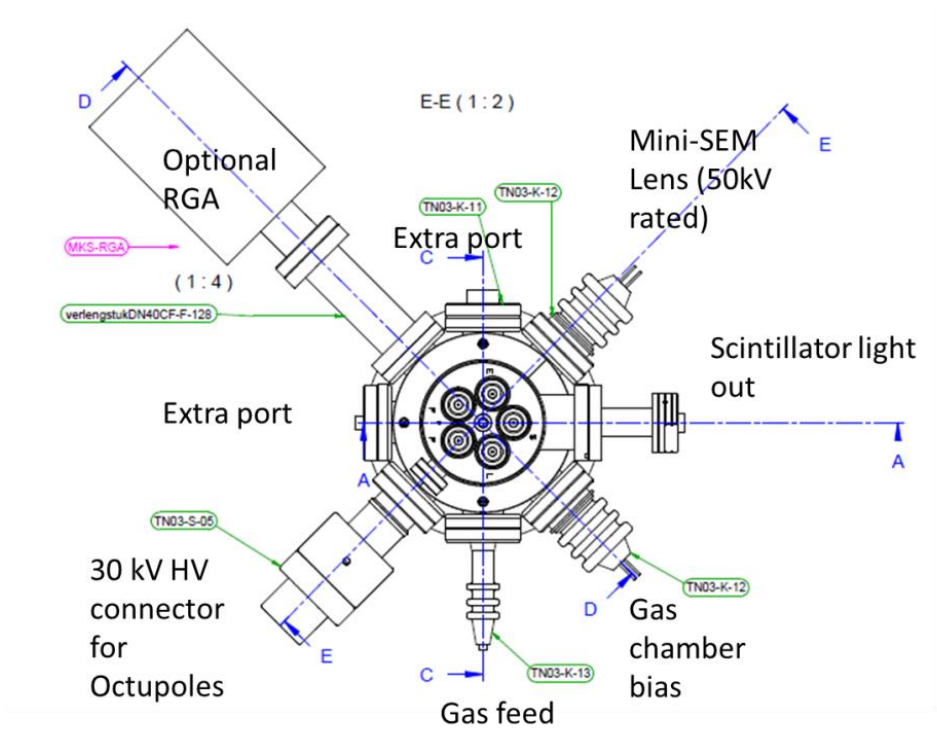


Fig. 6-7 Port arrangement for high voltage, light rod, and gas feedthroughs.

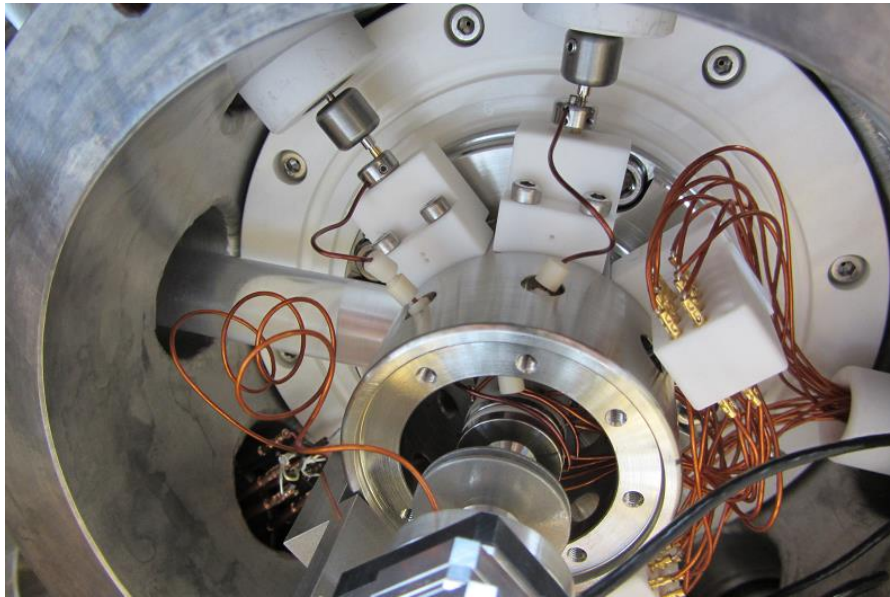


Fig. 6-8 Photo showing the electrical wiring inside the Mini-SEM-gas chamber region of the prototype unit.

B. Vacuum

The standard Sidewinder ion column is equipped with a 25 liter/sec ion pump that is sufficient to maintain a vacuum pressure in the low 10^{-6} mbar in the ion source and optics region during operation. Unfortunately, for the new prototype ion column the same vacuum arrangement is inadequate as the NAIS prototype includes a Schottky electron source. For stable emission, the Schottky source requires a vacuum condition below 1×10^{-8} mbar^[8].

To satisfy the UHV vacuum requirement of the Schottky electron source, the NAIS prototype is specifically designed to allow differential pumping to provide two different vacuum environments within the new vacuum chamber.

As shown in Fig. 6-9, inside the two-piece NAIS vacuum chamber, the CLM source module and the Mini-SEM objective lens assembly are divided on the DPA plate. The DPA plate is a metal plate with a small aperture (the DPA) that allows the passage of electrons while constricting gas flow. The DPA is specially designed to hold off up to three magnitudes of vacuum pressure difference. The DPA plate along with the entire Schottky electron gun sits on a ceramic bushing that is fastened on the lower chamber piece. The bushing is a high precision aluminum oxide part designed for multiple functions. In addition to providing high voltage isolation of the NAIS from the grounded chamber walls, the bushing, combined with the DPA/DPA-plate design and multiple O-rings, functions as a vacuum wall.

The upper piece of the NAIS chamber which encloses the Schottky electron emitter is mounted with a separate 25 liter/sec diode ion pump which is sufficient to achieve the required UHV pressure after a good bake. Below it, the standard 25 liter/sec ion pump that comes with the Sidewinder column satisfies the high vacuum requirement of the gas chamber region and the rest of the ion column.

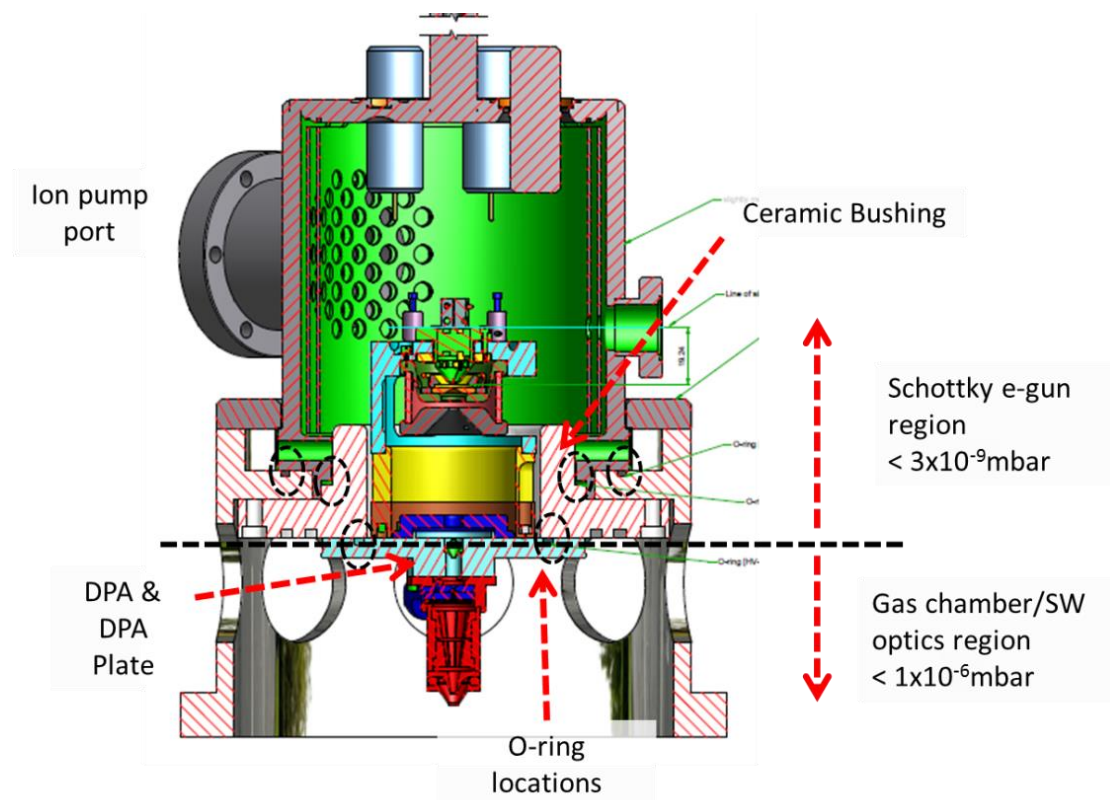


Fig. 6-9 Two different vacuum pressure regions in the prototype ion column.

C. Gas delivery

For operating the NAIS, almost up to an atmosphere of gas pressure is expected in the gas chamber. For fast switching of ion species, it is desired that the gas change is made quickly by pumping out the existing gas and leaking in a new, preferably without having to turn off the lower column voltage.

For the current version of the prototype ion column, gas is supplied to the gas chamber using gas tubing that originates from a gas tank placed outside of the ion column. Because the gas chamber is biased to voltage up to 30 kV during the ion column operation, a robust gas feedthrough design is needed to prevent high voltage breakdown via gas discharge as well as breakdown along the surface.

Paschen curves shown in Fig. 6-10 describe the gas discharge behavior of several noble gases between two parallel plate electrodes. The gas discharge breakdown voltage depends on both gas pressure and gap distance between the two electrodes. According to the figure, for operation at very high voltage, for example at 30 kV with argon gas, one obvious choice is to configure a setup so that the product of pressure and the gap distance is maintained to at least 2000 torr-cm. For this specification, a gap distance of only about 2 cm is sufficient to handle a 30kV difference at a gas pressure of 1000 torr, but for a gas pressure of 1 torr, the gap distance needs to be increased to 2000 cm. Considering the wide range of gas pressure (~ 1 to 570 torr) needed for operating the NAIS, such a long gap distance is very impractical to implement in our design.

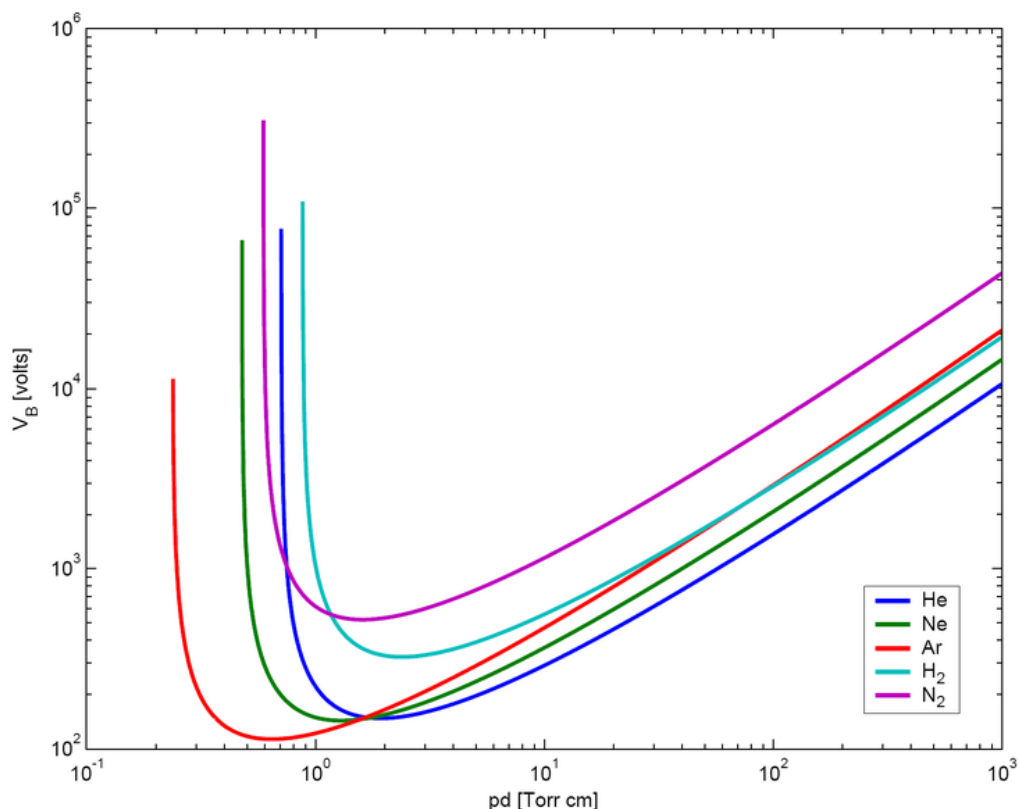


Fig. 6-10 Paschen curves of He, Ne, Ar, H₂, and N₂ (adapted from Ref. [9])

A much simpler and practical solution to prevent gas discharge induced HV breakdown is proposed and described in Fig. 6-11. The idea is essentially to limit the mean free path of the charged particles so that the charged particles mixed inside the gas don't gain enough energy to ionize the gas. Again, according to the Paschen curves in Fig. 6-10, an acceleration voltage below 100 V is not possible to result in discharge breakdown regardless the gas type and at any pressure. Assuming an insulation tube length between the two electrodes to be 6 cm and 30 kV applied across them (this exceeds the generally accepted HV design guideline of 10 kV/cm for electrical insulation along surface), limiting the mean free path of charged particles to below 200 μm should prevent gaining enough energy to ionize any neutrals by collisions. Physically filling the insulation tube tightly with insulating particles such as ceramic beads smaller than 200 μm diameter would be sufficient for this purpose.

This concept has been already tested in a simple laboratory experiment^[10]. Fig. 6-12 shows a prototype structure of 9 cm long plexiglass tube filled with alumina (Al₂O₃) beads of 1-100 μm in size. The test structure had no problem allowing gas flow of nitrogen, helium, and argon. The test structure also safely operated without any gas discharge breakdown in the pressure range of 1 mbar to 1 bar while a voltage difference of up to 30 kV was applied across the plexiglass structure.

Fig. 6-13 shows the final version of the high voltage gas feedthrough designed for the prototype ion column.

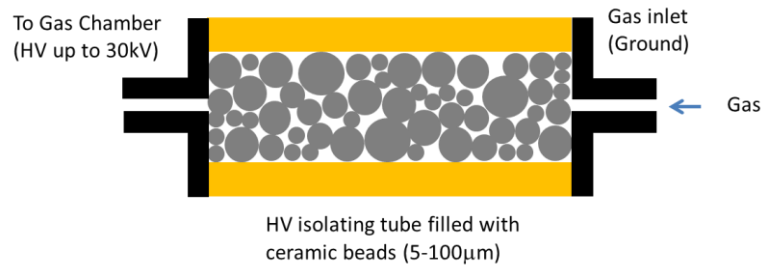


Fig. 6-11 The concept of high voltage gas feedthrough incorporating tiny ceramic beads. The design allows gas flow but prevents high voltage gas discharge by limiting the mean free path of the charged particles.



Fig. 6-12 High voltage gas feedthrough test structure built for testing the concept described in Fig. 6-11. The diode structure is made of plexiglass is about 9 cm long and filled with alumina beads (1-100 µm in diameter) inside. The structure showed no gas discharge breakdown in the gas pressure range 1 mbar to 1 bar while high voltage up to 30 kV was applied. The test gases were helium, nitrogen, and argon.

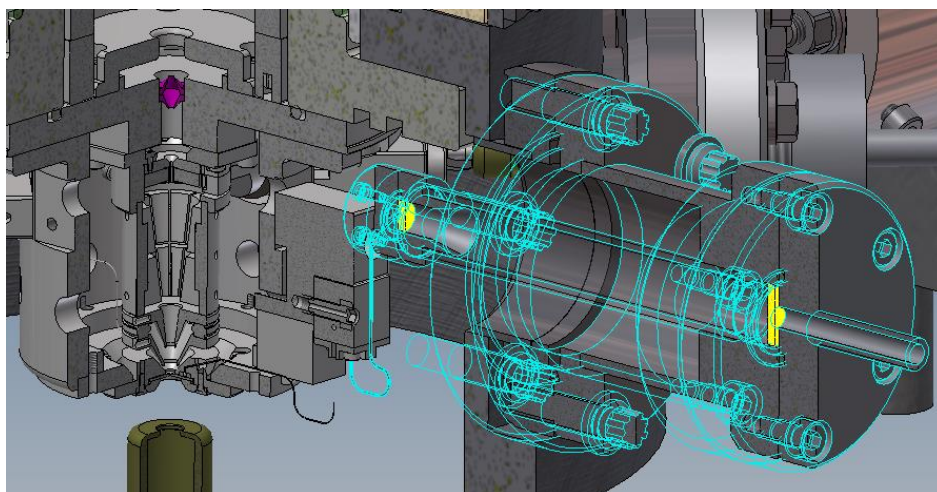


Fig. 6-13 High voltage gas feedthrough (outlined in blue) designed for the NAIS prototype ion column.

D. Alignment

Both CLM electron gun and Mini-SEM objective lens unit are initially built and tested at FEI before being assembled as a complete NAIS electron column in Delft. A special fixture utilizing a rotating table (see Fig. 6-14) is designed to assemble and align the modified CLM gun and the Mini-SEM optics on the DPA plate with very good accuracy. Overall, based on FEI's specification and our ability to align, all the optics elements including the Schottky emitter are aligned within $5\ \mu\text{m}$ (radial displacement) from each other.

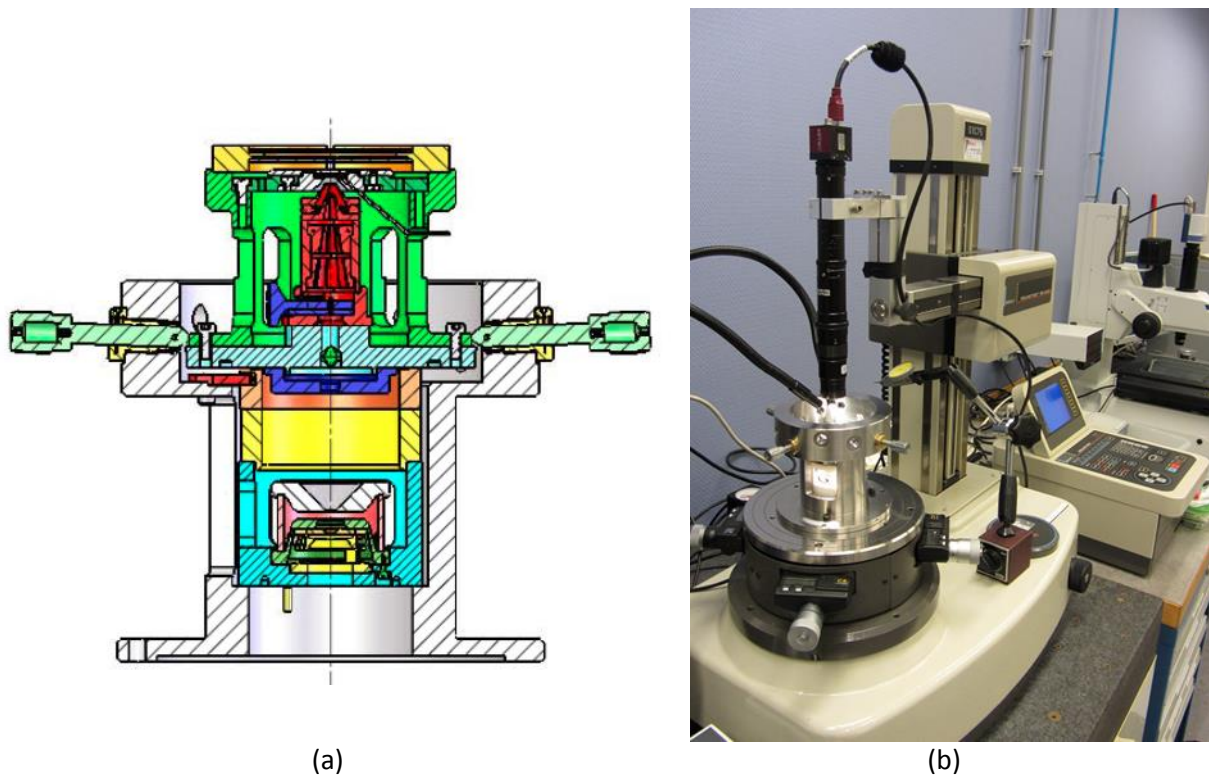


Fig. 6-14 (a) Fixture designed to align the CLM gun and Mini-SEM optics and (b) Mechanical optics alignment setup using a rotating table in Delft.

One major concern in the Schottky electron gun design is the possible loss of the electron beam current by being cut off by the DPA when the source is grossly misaligned and/or moves over time. Due to high operating temperature (1800 K), the Schottky emitter tip position can move gradually over time (about $25\ \mu\text{m}$ over one year estimated by FEI). Based on the operating parameters for the minimum electron beam diameter given in Section 6.3.1, our optics simulation using SIMION software indicate that the beam envelope diameter in the DPA region is expected to be $\sim 180\ \mu\text{m}$ and the source misalignment up to $45\ \mu\text{m}$ is tolerable before the electron beam transmission becomes affected by the DPA (see Fig. 6-15). Assuming all other components stay within $< 5\ \mu\text{m}$, the source drift shouldn't be an immediate concern.

Once the electron beam passes through the DPA, the beam trajectory can be corrected and aligned to the gas chamber using the Octupole deflectors of the Schottky electron gun. A vacuum chamber interface with mechanical screw adjustments is added between the NAIS vacuum chamber

and the Sidewinder vacuum chamber (Fig. 6-16) to provide alignment between the ion beam emerging from the gas chamber and the lens 1 of the Sidewinder column.

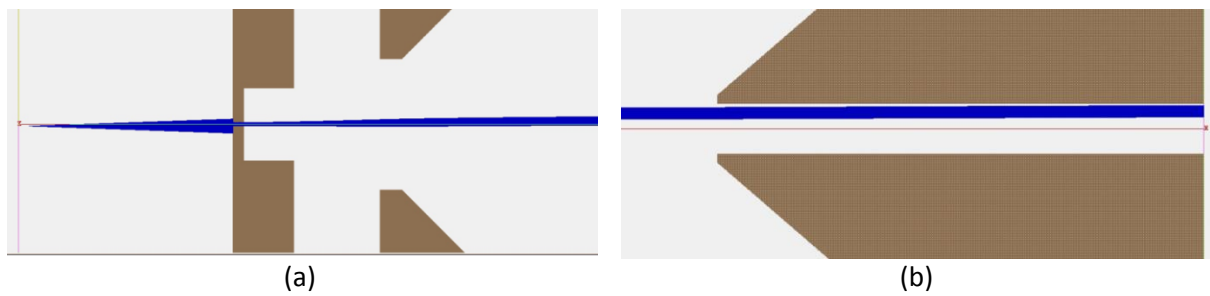


Fig. 6-15 SIMION optics simulation results showing the effect of Schottky emitter misalignment. (a) Electron trajectories from the Schottky electron emitter starting off by $45\ \mu\text{m}$. (b) The electron beam still clears through the DPA aperture diameter of $762\ \mu\text{m}$.

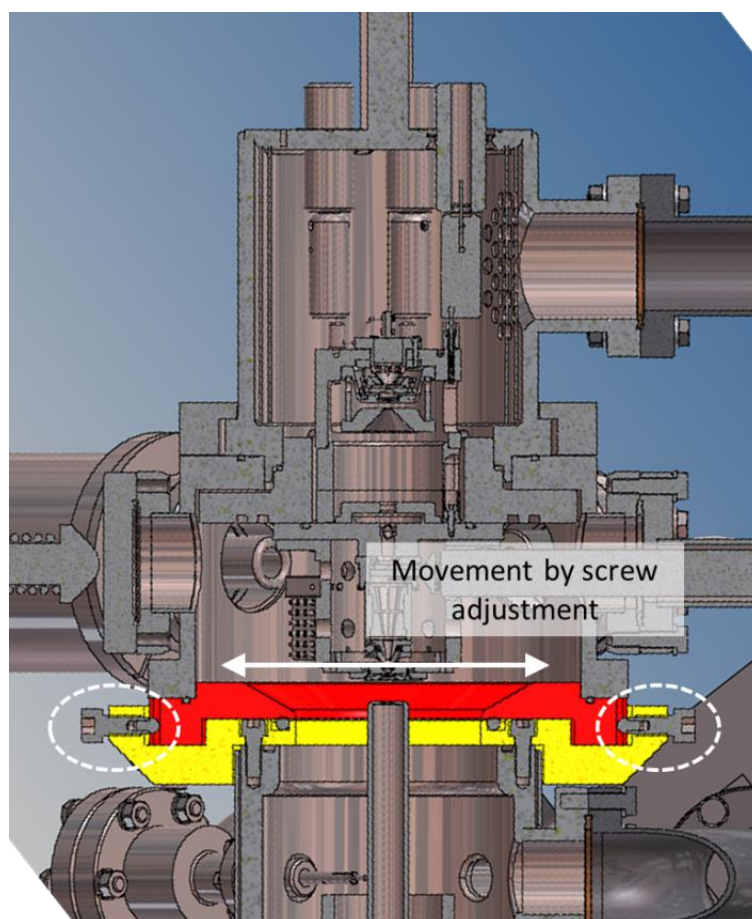


Fig. 6-16 Mechanical alignment of the ion beam to the Sidewinder optics by screw adjustments.

6.3.3 Optics layout and electrical power configuration

Fig 6-17 lays out the optics components of the ion column prototype and describes how the power supplies are configured to drive them. The CLM-Mini-SEM combination provides a 1 keV focused electron beam into the gas chamber for gas ionization. Ions produced inside the gas chamber are extracted by the gas chamber bias voltage and further accelerated by the Sidewinder extractor. The beam then gets collimated and focused by Lens 1 and Lens 2 of the Sidewinder column, respectively. The Sidewinder optics includes beam steering plates for alignment and a pair of octupole deflectors for scanning. Imaging signal detection and all of the ion beam adjustments between the Sidewinder Extractor and the target including the Sidewinder Lens 1 and Lens 2 focusing, electrostatic ion beam steering for alignment, ion probe stigmation, and scanning are set and controlled using the existing Quanta system power supplies and software.

The power to the Schottky electron source module (the CLM part) is provided by an FGSU (standard FEI electron gun power supply). Another modified FGSU is used to energize the Mini-SEM objective lens and to bias the gas chamber. Electron beam imaging of the gas chamber is possible by collecting and converting secondary electron signals generated from the gas chamber to photon signals using the scintillator. The light signal is further amplified by a photo-multiplier tube (PMT) before being synched to scanning and imaging electronics. The scanning octupole deflectors are to be operated by high voltage scanning power supplies developed in-house. A control software is also currently being developed to operate the Schottky electron gun and manage electron beam scanning and imaging.

Ion column optics performance and ion beam-solid interactions are greatly influenced by the landing energy of the ion beam, therefore the ability to vary the ion landing energy is a must feature for any FIB system to provide flexibility of tuning the ion beam for a specific application (milling, imaging, implantation, etc.). The standard operating beam energy range for the Sidewinder column is 0.5 keV to 30 keV and the landing energy is varied by adjusting the potential at the source while the target is fixed at ground inside the specimen chamber in the default system design. For operating a NAIS in a Sidewinder column in the same manner, this implies that the gas chamber needs to be floating at the beam potential along with the entire Schottky electron gun while a fixed potential difference of 1 kV is maintained between the Schottky source and the gas chamber. As shown in Fig. 6-17, this is achieved by having the FGSUs floating on a -1kV supply which is also floating on top of the Sidewinder main beam supply (+0.5 to 30 kV).

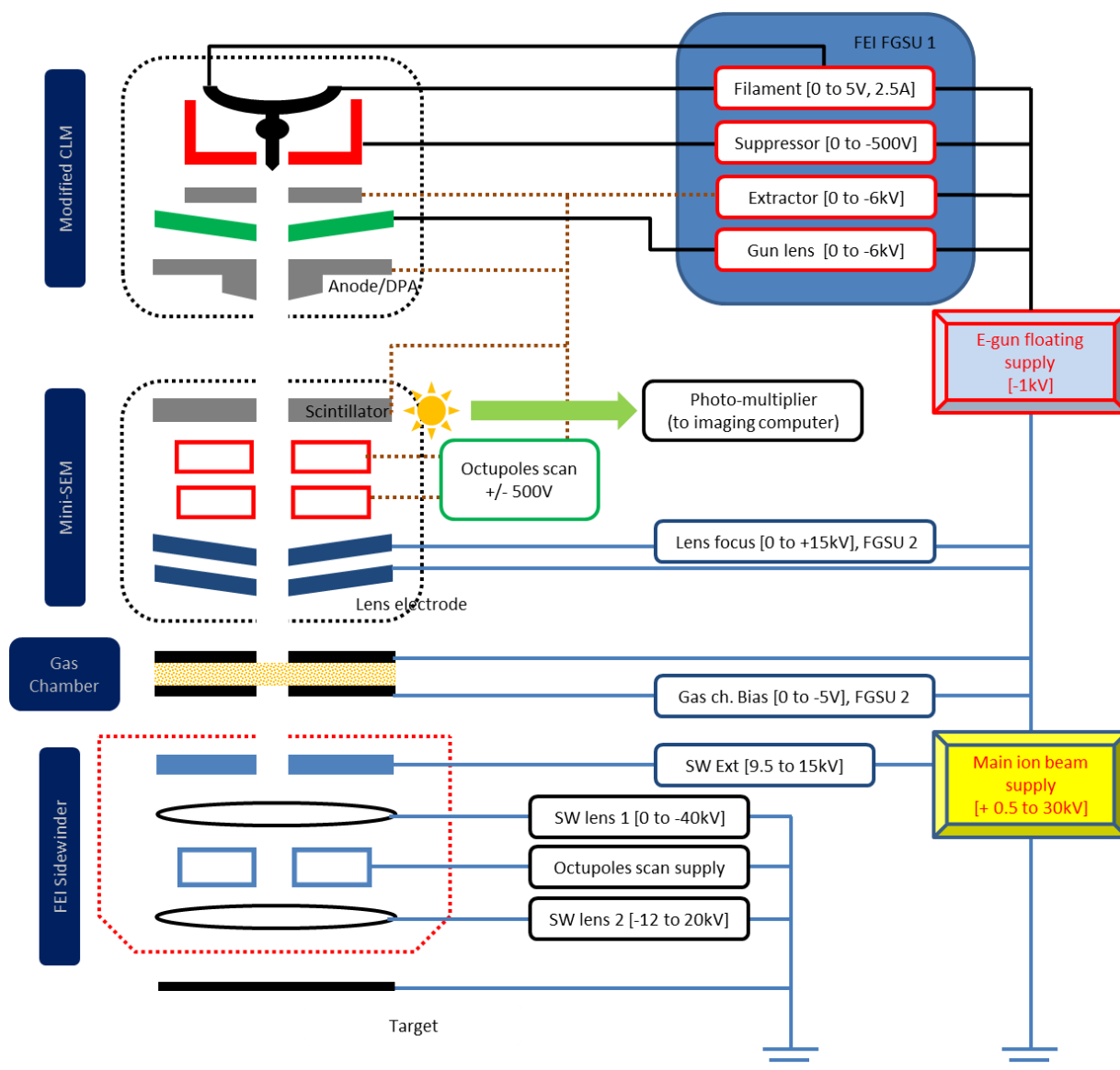


Fig. 6-17 Power supply configuration for the prototype ion column.

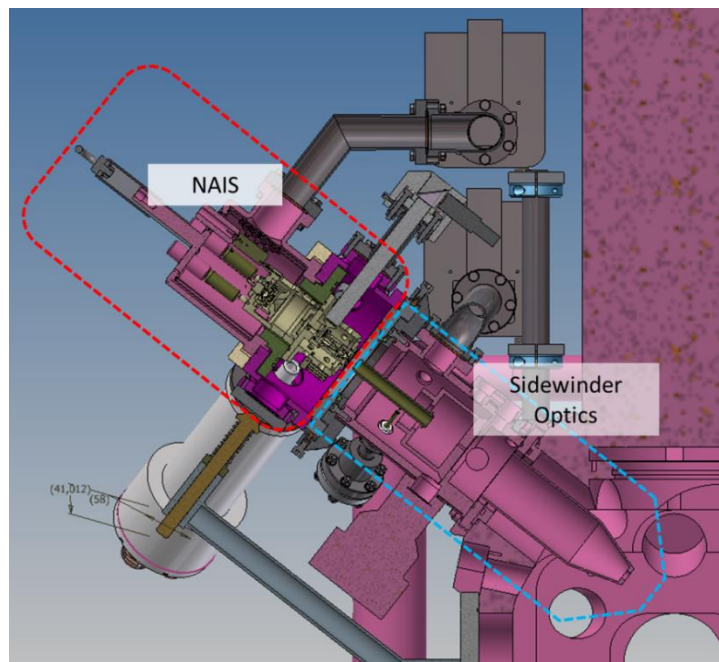
6.4 Predicted prototype performance

At the time of writing, the assembly of the prototype ion column has been completed and the system integration is underway. Upon installation, the column needs to be baked to obtain a UHV vacuum pressure in the Schottky source region. The experimental work will begin by verifying the Schottky e-gun probe size-current performance first and then detailed evaluation of the ion column performance. The evaluation will be primarily focused on measurements of the ion probe size-current performance in order to verify the expected source reduced brightness and energy spread and the characteristics of ion imaging, milling, and deposition using various gas species including the full range of noble gases. The prototype ion column will also provide opportunities to evaluate

source stability, reliability, and lifetime in an actual commercial FIB operating environment. Fig. 6-18 gives a first peek at the prototype ion column being prepared on a Quanta dualbeam system.



(a)



(b)

Fig. 6-18 (a) NAIS prototype ion column being integrated on to a FEI Sidewinder ion column and (b) CAD cross section.

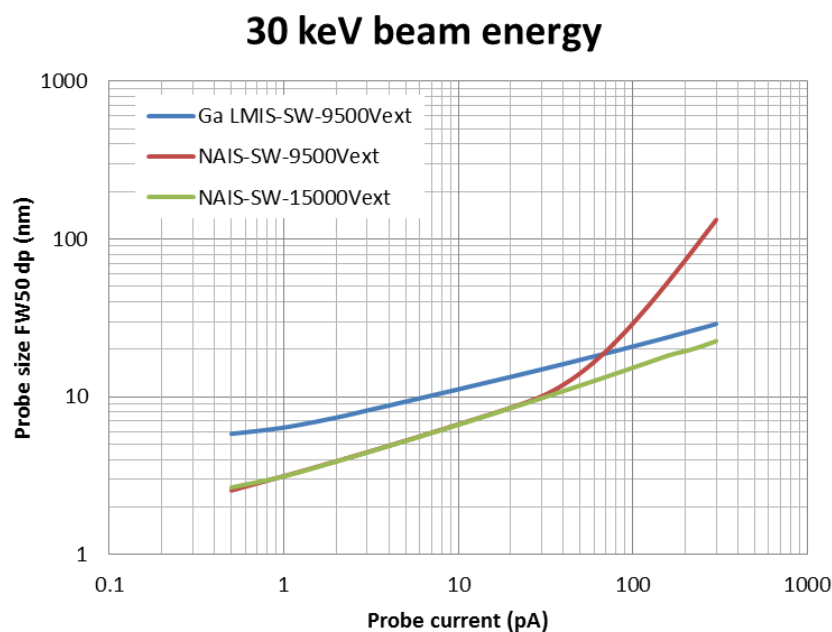
Predicted probe sizes of the prototype ion column as a function of probe current for operation at 30 keV and 5 keV are shown in Figs. 6-19 and 6-20. The probe size performance of the standard Ga LMIS based Sidewinder ion column are also given for comparison. The probe sizes indicated in the plots are beam diameters containing 50% of the beam current (FW 50) calculated using the root-power-sum method. They also represent minimum diameters achievable at each current after balancing the contributions between the demagnified source image and the focusing lens

aberrations as best as possible within the limits of the lens power supplies. All the calculations are based on the ion source parameters given in Table 6-2 and focusing lens aberrations and other optical parameters obtained using EOD optics software. Some key simulation results and corresponding beam size characteristics at several different currents at 5 keV and 30 keV are listed in Figs. 6-19 and 6-20. For the reason only considering small probe currents (< 300 pA) in the calculations, the coulomb interactions are assumed to be negligible^[11].

One major design modification to the prototype ion column from its original Sidewinder configuration beside the obvious source change is that the gas chamber is pushed back 100 mm from the original LMIS location, thus effectively increasing the distance between the source and Lens 1 by the same amount in the prototype. The modification was necessary to provide enough room for electrical wiring and gas hook-up in the areas of the lower optical section of the Schottky electron column and the gas chamber. Optically, this change allows higher demagnifying power in the prototype ion column, which in fact is a desirable effect considering the virtual source size of the NAIS is expected to be twice that of the Ga LMIS. According to the optics simulation results in Figs. 6-19 and 6-20, the prototype column can be pushed back to achieve significantly smaller source images compared to the standard Sidewinder without being overtaken by the chromatic contribution thanks to the much lower energy spread expected from NAIS (1 eV versus 5 eV of Ga LMIS).

One other relevant impact on the optics that results from the increased source-to-Lens 1 distance is the inevitable change of the Lens 1 focusing characteristics (i.e. image angle/ focusing distance) which can possibly present some limitation in controlling beam angle into Lens 2 and subsequently the half angle at the image. Within the limits of the existing Lens 1 power supply the prototype is forced to operate with an intermediate crossover forming between Lens 1 and Lens 2 when the ion extraction voltage is kept at the standard Sidewinder specification of 9500 V. For low or moderate beam energy operation (< 20 keV), the current Lens 1 power supply range is still sufficient to adjust the crossover location to achieve optimum image angles that balance between the source image and the aberration contributions for the entire probe current range considered for the initial testing (1 to 300 pA^[*]); however, for operation at higher beam energies, it is found that this can no longer be the case. This is evident in Fig. 6-19 showing that at the standard Sidewinder extraction voltage of 9500 V and the beam energy of 30 keV, for the currents above 30 pA, the NAIS prototype ion column operates in spherical aberration dominated mode and the overall beam size performance becomes much worse than the standard Sidewinder. One workaround for this issue is to increase the ion extraction to 15 keV (the limit of the exiting Sidewinder extractor supply) to help adjust the intermediate crossover to a favorable location by 'stiffening up' the ion beam before entering the Lens 1 focusing fields.

[*] 1 nA or even higher probe current is possible for NAIS with relatively high gas pressure, high gas chamber bias voltage, and larger ion exit aperture size at the expense of possible degradation in the reduced source brightness and energy spread. This mode is not considered for the initial testing of the prototype ion column.

**1 pA probe current**

	Vext (V)	Lens 1 (V)	Lens 2 (V)	α_o (mrad)	M	Cs (mm)	Cc (mm)	di (nm)	ds (nm)	dc (nm)	dp (nm)
Ga	9500	30000	10843	0.131	-0.104	902	92	5.22	0.06	3.67	6.39
NAIS	9500	44550	10721	0.065	0.023	911	95	2.34	0.63	1.69	3.15

10 pA probe current

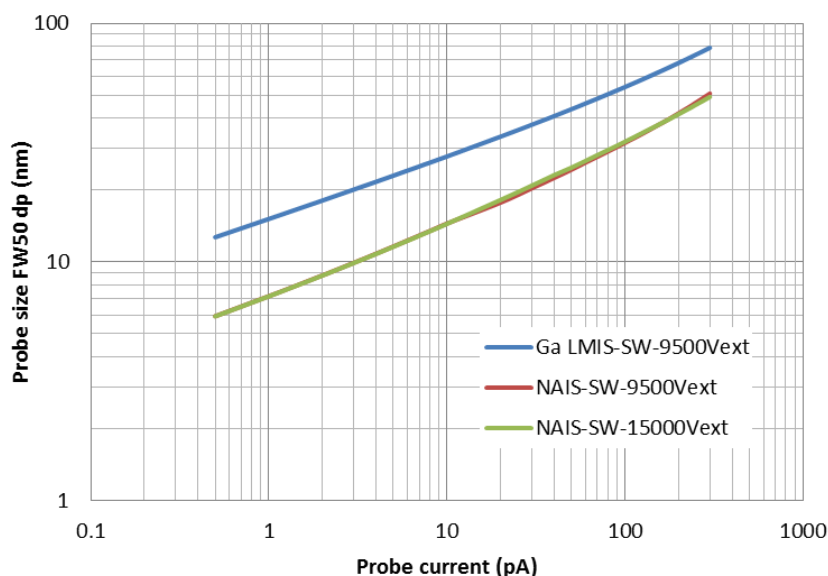
	Vext (V)	Lens 1 (V)	Lens 2 (V)	α_o (mrad)	M	Cs (mm)	Cc (mm)	di (nm)	ds (nm)	dc (nm)	dp (nm)
Ga	9500	41150	10869	0.415	-0.158	900	92	7.90	0.51	7.72	11.17
NAIS	9500	32600	10633	0.207	0.051	922	100	5.14	1.88	2.57	6.70

100 pA probe current

	Vext (V)	Lens 1 (V)	Lens 2 (V)	α_o (mrad)	M	Cs (mm)	Cc (mm)	di (nm)	ds (nm)	dc (nm)	dp (nm)
Ga	9500	50950	10939	1.312	-0.295	897	96	14.77	2.48	13.53	20.85
NAIS	9500	30000	10578	0.653	0.069	933	105	6.90	24.93	6.32	29.16
NAIS	15000	41750	10457	0.520	0.119	970	109	11.93	5.02	3.82	15.29

Fig. 6-19 Probe size-current performance of the NAIS prototype ion column and the standard Ga-LMIS Sidewinder ion column at 30 keV. EOD simulated optics parameters and the calculated beam size contributions for the probe currents of 1 pA, 10 pA, and 100 pA are given in the tables. [note: Vext=extraction voltage wrt the source, Lens 1 (2)= Lens 1 (2) focus voltage wrt the source, α_o =object half angle, M=linear magnification (positive indicates intermediate x-over), Cs=image side spherical aberration coefficients, Cc=image side chromatic aberration coefficient, di=source image diameter, ds=spherical aberration contribution, dc=chromatic aberration contribution, dp=total probe diameter (RPS, FW50)]

5 keV beam energy



1 pA probe current

	Vext (V)	Lens 1 (V)	Lens 2 (V)	α_o (mrad)	M	Cs (mm)	Cc (mm)	di (nm)	ds (nm)	dc (nm)	dp (nm)
Ga	9500	13500	13080	0.131	-0.212	999	37	10.60	0.11	10.80	15.15
NAIS	9500	18350	13345	0.065	0.052	1001	38	5.17	0.93	4.52	7.19

10 pA probe current

	Vext (V)	Lens 1 (V)	Lens 2 (V)	α_o (mrad)	M	Cs (mm)	Cc (mm)	di (nm)	ds (nm)	dc (nm)	dp (nm)
Ga	9500	16750	12980	0.415	-0.378	1002	39	18.92	0.61	20.04	27.68
NAIS	9500	14750	13497	0.207	0.107	1007	41	10.70	3.36	7.38	14.49

100 pA probe current

	Vext (V)	Lens 1 (V)	Lens 2 (V)	α_o (mrad)	M	Cs (mm)	Cc (mm)	di (nm)	ds (nm)	dc (nm)	dp (nm)
Ga	9500	18650	12802	1.312	-0.676	1039	45	33.80	3.51	41.09	54.08
NAIS	9500	9750	12576	0.653	-0.241	1060	43	24.15	9.71	10.86	31.58

Fig. 6-20 Probe size-current performance of the NAIS prototype ion column and the standard Ga-LMIS Sidewinder ion column at 5 keV. EOD simulated optics parameters and the calculated beam size contributions for the probe currents of 1 pA, 10 pA, and 100 pA are given in the tables.

Table 6-2. Ion source parameters assumed for the prototype ion column probe size-current calculations

	Ga LMIS-SW	Ar NAIS-SW
Reduced Brightness (A/m^2SrV)	1×10^6	1×10^6
Virtual source size (nm)	50	100
Energy spread FWHM (eV)	5	1
Probe current (pA)	Up to 65,000	Up to ~300

6.5 Conclusions

In this chapter, design details for integrating a prototype NAIS in a commercial FIB ion column (FEI Sidewinder) are presented. The main purpose of the integration is to continue to study and evaluate the new ion source properties and demonstrate ion imaging, milling, and deposition using a variety of ion species including the full range of noble gas ion species in a commercial FIB setup. In addition, it will provide an opportunity to directly compare the performance between the NAIS and the Ga LMIS, which is the dedicated ion source for Sidewinder. Although the general design goal is simply swapping the source, due to the large difference in size and mechanism of operation between the NAIS and the Ga LMIS, the integration project has presented many design challenges. First, a Schottky electron focusing column capable of providing > 50 nA in a 100 nm beam spot at 1 keV is designed and built. A custom vacuum chamber is designed and built to house the entire prototype NAIS (the electron gun plus a gas chamber) and integrate on the Sidewinder column. The prototype ion column also include a gas feed system capable operating up to 30 kV. The prototype NAIS is designed to provide a reduced source brightness comparable to that of the Ga-LMIS but due to much lower energy spread, the NAIS prototype ion column is expected to provide significantly better probe size-current performance compared to the Ga LMIS based Sidewinder ion column for the current range up to 300 pA. Our calculations have shown that we can expect about 2x improvement on the beam size for a given current or 10x more current for a given size for small currents up to ~ 10 pA in 5 and 30 keV operation.

Acknowledgement

The author gratefully acknowledges the support and expertise of Alix C. Wattjes, Ruud van Tol, Gerrit Schotte, and Cor Barends. They have been instrumental in designing and manufacturing custom components required for the integration project. He also acknowledges Jacques Nonhebel and Han van der Linden who developed a high voltage scanning system for this project. He also thanks Neal Landreville, Mike Lysaght, and Greg Schwind of FEI Company for their kind support and encouragement for this work. This research is supported by the “Stichting voor Fundamenteel Onderzoek der Materie (FOM)”, which is financially supported by the “Nederlandse Organisatie voor Wetenschappelijk Onderzoek” and FEI Company.

References

- [1] www.fei.com/products/dualbeams/quanta3d.aspx
- [2] Quanta3D FEG user manual
- [3] www.lencova.com
- [4] J. E. Barth and P. Kruit, Addition of different contributions to the charged particle probe size, *Optik*. **101(3)**. 101 (1996)
- [5] G. A. Schwind, G. Magera, and L. W. Swanson, Comparison of parameters for Schottky and cold field electron sources, *J. Vac. Sci. Technol. B* **24**, 2897 (2006)
- [6] H. S. Kim, M. L. Yu, M. G. R. Thomson, E. Kratschmer, and T. H. P. Change. Energy distributions of Zr/O/W Schottky electron emission. *J. Appl. Phys.*, **81(1)**: 461-465, 1997
- [7] M. J. Fransen, J. S. Faber, Th. L. van Rooy, P. C. Tiemeijer, and P. Kruit. Experimental evaluation of the extended Schottky model for ZrO/W electron emission, *J. Vac. Sci. Technol. B* **16**, 2063 (1998)
- [8] L. W. Swanson and G. A. Schwind, *Handbook of Charged Particle Optics*, 1st ed., edited by J. Orloff (CRC, New York, 1997), Chap. 2.
- [9] M. A. Lieberman and A. J. Lichtenberg, *Principles of plasma discharges and material processing*, 2nd edition, Wiley-Interscience (2005)
- [10] L. van Kouwen, High voltage testing of the NAIS gas feedthrough, CPO group internal report, Delft University of Technology, 2012
- [11] L. Wang, Design optimization for two lens focused ion beam columns, *J. Vac. Sci. Technol. B* **15(4)** (1997)

Summary

The goal of this PhD research was to develop a high performance ion source suitable for the next generation FIB tools. The new source, named Nano Aperture Ion Source (NAIS) after the unique physical feature incorporated in the gas ionization chamber design, aims to achieve high beam brightness and low energy spread suitable for sub-5 nm FIB processing. In addition, the source is quite versatile and different from the current state-of-the-art FIB sources in that it offers choices of a variety of ion species, including the full range of noble species. This is a very attractive source feature as it can extend the use of FIB tools in contamination sensitive applications and optimize all aspects of FIB functionality – ion imaging, material removal and deposition under a single tool. Key results and main conclusions drawn from the research work are highlighted below.

The NAIS concept (Chapter 2)

The core concept of the NAIS is a small volume based direct electron impact gas ionization. Electron impact gas ionization is a very convenient and reliable method to generate a variety of ion species by simply changing the source gas but in order to adopt this technique to create a high performance FIB source, the NAIS uniquely employs a novel gas chamber design and a Schottky electron column. The gas chamber, which is a MEMS fabricated structure consisting of two thin membranes (~100 nm) separated by a small spacing (~100-500 nm) and with two small concentric apertures (~100-500 nm in diameter) for electrons to enter and ions to exit, can trap a relatively dense gas in a small volume while a high current density beam from the Schottky electron column can maximize gas ionization. Because the gas ionization is mostly contained between the membranes, the ions can be simply accelerated out of the gas chamber by applying a small bias voltage between the membranes (<1 V). Also, because the ion source is operated at room temperature (or even lower temperature upon gas cooling) the extracted ions exhibit good beam parallelism and low energy spread (< 1 eV).

The total ion production inside the NAIS gas chamber depends on the amount of impact electron beam current, gas particle density (or pressure), gas ionization cross section, and the gas chamber spacing (the ionization path length). However, in limiting the gas chamber operation at the threshold of the molecular gas flow to maximize ion production while preventing any loss of ions from ion-neutral collisions, the ionization efficiency, the amount of ion current produced per incident electron beam current, is calculated to be about 0.6, 1.1, 1.3, 1.2, 1.2 % for helium, neon, argon, krypton, and xenon gas, respectively. The different ionization efficiencies reflect that each gas has a different ionization cross section and molecular diameter. Furthermore, from an analysis based on the Langmuir brightness model, we conclude that given a gas, the reduced brightness of the NAIS in this gas flow regime is fundamentally limited by the current density of the incident electron beam and the gas temperature. After considering the theoretical performance of the Schottky electron column and the electron beam energy dependence on the gas ionization cross section we estimate that the maximum reduced brightness of the NAIS using noble gases can reach $\sim 10^7$ A/m²srV for room temperature operation.

Simulated performance of the NAIS (Chapter 3)

Monte Carlo gas simulations and ion trajectory calculations were performed to understand the NAIS performance more in detail. The gas simulations based on the steady state free molecular flow have provided quantitative details on the gas particle density distribution throughout the miniaturized gas chamber and its dependence on the gas chamber dimensions. Not surprisingly, the gas particle loss through the double-aperture and the overall density distribution depend on the gas chamber spacing, membrane thickness, and particularly the aperture size. In general, it is found that by keeping the aperture size on the order of the spacing or smaller the particle distribution inside the gas chamber can be maintained almost uniform and the loss through the double-aperture rather insignificant.

The ion trajectory simulations, which incorporated the gas simulation results in defining the initial ion conditions, have shown that the gas chamber bias voltage, dimensions, and temperature are critical variables that influence the beam current output, ion energy distribution, and reduced brightness. However, the gas chamber bias voltage is particularly important as it can single-handedly influence all three source parameters at once and can be easily adjusted during source operation. Increasing the gas chamber bias voltage generally increases the current output, but also increases the energy spread. If the bias voltage is too high, it can also decrease the beam brightness and produce a bi-modal ion energy distribution due to the lens effect. Implementing a larger aperture size is another way to increase the current output, however this adversely reduces the beam brightness. The simulation results suggest that the best way to enhance both the current output and beam brightness is by lowering the gas temperature.

Given an incident electron beam having a diameter of 100 nm the optimum chamber dimensions that provide the best source performance for ion beam current, energy spread, and beam brightness are found to be 100-200 nm in aperture diameter, ~200 nm in spacing and ~100 nm in membrane thickness. Based on these gas chamber dimensions, argon gas at room temperature, and a 1 keV impact electron beam of 100 nA, the simulation results suggest that the NAIS is capable of providing an ion beam current up to 300 pA, an energy spread below 1 eV, and a reduced brightness above 1×10^6 A/m²srV which is comparable to our estimate based on the theoretical Langmuir brightness model. It should be mentioned that the electron current density ($J_e \sim 1.27 \times 10^7$ A/m²) assumed in this calculation is about a magnitude smaller than the theoretical limit that the Schottky electron focusing column can provide.

Design and fabrication of the miniaturized gas chamber (Chapter 4)

We have investigated two different approaches for fabricating the miniaturized gas chambers. The first approach, known as the double-chip design, is based on the MEMS bulk machining technology in which a thin metal membrane (100 nm) with a Si₃N₄ layer (100 nm) on top is fabricated on a single silicon chip through several lithographic etching and deposition steps. After etching a gas channel on the Si₃N₄ layer, two different chips are stacked with the etched gas channels facing and overlapping, and then glued to form a complete gas chamber. In contrast, the second approach is based on the MEMS surface micromachining technology in which all the gas chamber features are built on a single silicon chip, hence named the single-chip design. In this approach, a structure of two membranes sandwiching a TEOS layer (100-200 nm thick) is first fabricated on a silicon substrate and then a gas channel is formed by creating interconnected

cavities in the TEOS layer by BHF etching. In both designs, the double-aperture is simply fabricated at the end by FIB machining.

Presently, prototypes based on the double-chip design can be reliably produced and they have shown to be fully functioning as gas ionization chambers, however, the current assembly method using glue has presented difficulties in meeting our target gas chamber specification. Mechanical clamping and wafer bonding are being investigated to mitigate the issue. Although a reliable fabrication process based on the single-chip is still being actively developed, the design so far has shown to be very effective in controlling the gas chamber spacing by the thickness of the TEOS layer. Still further design optimization in membrane metallization and experimental validation are needed but the single-chip design appears to be very promising for the NAIS.

Proof-of-concept experiments (Chapter 5)

A commercial SEM was configured to demonstrate as an improvised NAIS prototype in order to perform several proof-of-concept experiments. The basic experimental work involved installing a prototype gas chamber inside the SEM specimen chamber, filling it with a gas, inducing gas ionization by simply focusing a SEM probe into it, and then characterizing the ion beam extracted from the gas chamber. Although our current gas chamber fabrication methods have not been fully optimized to produce gas chambers meeting our target spacing specification, the prototype gas chambers based on the double-chip design were found to be sufficient to demonstrate the concept of the NAIS. Notable experimental results are:

- Ion beam pattern observation: Several different gases (He, Ar, Xe, and air) were leaked into a gas chamber and the emission patterns of the extracted ions were captured using micro-channel plates and a phosphor screen. Although qualitative, the results clearly indicate that the NAIS can easily provide ions of different species by simply changing the source gas and the ions extracted from the miniaturized gas chamber indeed form a beam.
- Ion beam current measurement: We measured extracted ion beam currents using a Faraday cup system and experimentally verified that the ion production depends on the type of gas, gas pressure, incident electron current, beam energy, and the gas chamber bias voltage. The measurements were in good agreement with theoretical expectations.
- Short-term beam current stability: Typically we saw about 1%-3% change in ion beam current over an hour period, mostly affected by a gas pressure drift in our experimental setup. However, we also observed that a big electron beam spatial drift around the double-aperture can cause a significant ion current instability. It's speculated that the electron beam drift is attributed to charging of particle contaminants on the gas chamber surfaces.
- Angular intensity: An experiment in which a Faraday cup with a small aperture was scanned over an ion beam pattern showed that the current density distribution was Gaussian, consistent with what we expected from our simulation results. The measured angular current intensity at the center of the beam pattern was 1.25 $\mu\text{A}/\text{sr}$ at 2 keV.
- Energy spread: Ion energy distributions measured using a retarding field energy analyzer confirmed that the energy spread of the NAIS mainly depends on the applied gas chamber bias voltage. The development of a secondary peak from the lens effect of the gas chamber as predicted by the simulation study was also observed. The study confirmed that an energy spread < 1 eV is quite possible for the NAIS.

- Ion imaging and milling: A simple FIB system was built by adding ion probe forming optics and scan deflectors in the SEM experimental setup. Due to some unresolvable mechanical alignment problems in the test setup, the FIB imaging quality was poor, but for the first time ion imaging and milling using an argon ion beam arising from a miniaturized gas chamber were demonstrated.
- Reduced brightness: The reduced beam brightness of an ion probe focused by the experimental FIB setup using argon gas was estimated to be 3×10^3 A/m²srV. The result appears to be very reasonable considering that only ~8 nA of incident electron current at 1 keV was available for gas ionization and that the prototype gas chamber used for the experiment had sub-optimal dimensions (2 μm spacing and 1 μm diameter). With a 100 nA/100 nm electron beam at 1 keV and a gas chamber meeting our target specifications, $Br > 1 \times 10^6$ A/m²srV would be very possible.

Delft NAIS-FEI Sidewinder Integration: Concept and design (Chapter 6)

A full-scale prototype NAIS that can be integrated onto FEI's Sidewinder ion focusing column has been designed. The main purpose of the integration is to continue to study and evaluate the NAIS properties and to demonstrate nanometer resolution imaging and milling performance using a variety of ion species in a commercial FIB setup. In addition, it will provide an opportunity to directly compare the performance of the NAIS with the Ga LMIS, which is the dedicated ion source for the Sidewinder. The designed NAIS prototype includes a new Schottky electron focusing column based on FEI's CLM and mini-SEM optics and optimized for focusing >50 nA into a 100 nm beam spot at 1 keV. A special vacuum chamber has also been designed to provide gas and high voltage feedthrough connections to the prototype ion source and to interface with the existing Sidewinder chamber. The NAIS prototype is expected to provide a reduced brightness comparable to that of a typical Ga LMIS, but due to a much lower energy spread, the modified Sidewinder column is expected to provide significant performance improvement over the conventional Sidewinder. Based on a reduced brightness of 1×10^6 A/m²srV and an energy spread of 1 eV FWHM, we estimate that the NAIS equipped Sidewinder ion column can provide a minimum beam size of ~3 nm (FW50) for 1 pA at 30 keV, which is more than a 50% reduction in beam spot compared to what's possible with the Ga LMIS equipped Sidewinder ion column.

Project outlook

The work presented here sufficiently demonstrates the concept of the NAIS both numerically and experimentally and corroborates the realization of a complete source is very close. Going forward, the optimization in gas chamber fabrication and verifying the beam reduced brightness in the prototype ion column would be next critical steps. Additionally, long term stability and life test are needed to validate its commercial practicality. Up to now, our focus has been to generate noble gas ions for traditional FIB applications but it should be pointed out that developing the NAIS for reactive gases such as oxygen may open up new possibilities in ion beam chemistry and secondary ion mass spectrometry (SIMS). Developing a NAIS system as an inline dual beam tool would be another interesting idea.

Samenvatting

Het doel van dit PhD onderzoek was het ontwikkelen van een hoogwaardige ionenbron welke zal voldoen aan de volgende generatie FIB apparaten. Deze nieuwe bron, de Nano Aperture Ion Source (NAIS) welke genoemd is naar zijn unieke fysieke eigenschap namelijk het gas-ionisatiekamer ontwerp, streeft naar het behalen van een hoge bundel helderheid en lage energie spreiding wat deze bron geschikt maakt voor het sub-5nm FIB proces. Bovendien onderscheidt de bron zich ook van de huidige hoge kwaliteit bronnen door de beschikbare keuze aan edelgassen. Dit is een zeer aantrekkelijke bron eigenschap, omdat het de bruikbaarheid van FIB apparaten kan uitbreiden voor contaminatie gevoelige processen en het breidt de bruikbaarheid uit in zijn functionaliteit: beeldvorming, etsen en depositie allemaal in één tool. De hoofdresultaten en conclusies van dit onderzoek worden hieronder nader toegelicht.

Het concept van de NAIS (Hoofdstuk 2)

Het basis principe van de NAIS is gebaseerd op directe elektronimpact gas ionisatie in een klein volume. Dit type ionisatie is een heel gemakkelijke en betrouwbare methode om een verscheidenheid aan ion-types te creëren, simpelweg door de gasbron te veranderen. Maar om deze techniek zodanig toe te passen om zulk een hoogwaardige FIB bron te creëren, maakt de NAIS enkel gebruik van nieuw een gas-ionisatiekamer ontwerp en een Schottky elektronen kolom. De gas-ionisatiekamer, welke een MEMS gefabriceerde structuur is, bestaande uit twee dunne membranen (~100nm) met een kleine tussenafstand (~100-500nm) en twee kleine concentrische openingen (~100-500nm diameter) waar de elektronen binnenkomen en ionen de kamer verlaten, kan een relatief dichts gas in een klein volume vasthouden terwijl een elektronen bundel met hoge dichtheid vanuit de Schottky elektronen kolom de ionisatie van het gas maximaliseert. Omdat deze ionisatie grotendeels plaatsvindt tussen de membranen, kunnen de ionen vrij gemakkelijk uit de gas-ionisatiekamer versneld worden door een voltage in te stellen over de membranen (<1 V). Omdat de ionenbron functioneert op kamer temperatuur (en zelfs lager wanneer het gas wordt gekoeld), zullen de gecreëerde ionen goed parallel en met lage energie spreiding (<1 eV) de gaskamer verlaten.

De totale ionen productie binnen de NAIS gas-ionisatiekamer hangt af van de hoeveelheid invallende elektronen stroom, dichtheid van het gas (of druk), gas ionisatie cross sectie, en de tussenafstand van de membranen (de ionisatie weglengte). Door de gas-ionisatiekamer werking te limiteren tot de grens van de moleculaire gas stroom om de ionenproductie te maximaliseren terwijl verlies van ionen van ion-neutrale botsingen te voorkomen, kan de ionisatie efficiëntie berekend worden als zijnde ongeveer 0.6, 1.1, 1.3, 1.2, 1.2 % voor respectievelijk Helium, Neon, Argon, Krypton en Xenon gas. Het verschil in ionisatie efficiëntie weerspiegelt dat de gas types verschillen in ionisatie cross sectie en moleculaire diameter. Verder kunnen wij concluderen op basis van het Langmuir helderheid model dat bij een gegeven type gas, de gereduceerde helderheid van de NAIS in dit specifieke gas regime fundamenteel gelimiteerd is door de stroomdichtheid van de invallende elektronenbundel en de temperatuur van het gas. Wanneer men de theoretische prestatie van de

Schottky elektronen kolom en de afhankelijkheid van de elektronen bundel energie op de gas ionisatie cross sectie in beschouwing neemt, schatten wij dat de maximaal haalbare gereduceerde helderheid van de NAIS bij het gebruik van edelgassen op kamer temperatuur $\sim 10^7$ A/m²srV kan bereiken.

Gesimuleerde prestaties van de NAIS (Hoofdstuk 3)

Om de NAIS prestaties in meer detail beter te begrijpen, zijn Monte Carlo simulaties en ionen traject berekeningen uitgevoerd. Gas simulaties, welke gebaseerd zijn op gas dat zich begeeft in het moleculaire regime, hebben kwantitatieve details gegeven in de distributie van gasdeeltjes in en rondom de geminiaturiseerde gas-ionisatiekamer en hun afhankelijkheid van de gas-ionisatiekamer dimensies. Niet onverwacht blijkt dat het verlies van gasdeeltjes door de dubbele opening van de gaskamer en de distributie dichtheid van de gasdeeltjes afhangt van de ruimte tussen de membranen, de dikte van de membranen, en vooral de grootte van openingen. Over het algemeen is de bevinding dat wanneer de grootte van de opening gelijk of kleiner is dan de afstand tussen de membranen, dan zal distributie van de gasdeeltjes in de gas-ionisatiekamer bijna uniform blijven en zal het verlies van gasdeeltjes door de openingen eerder verwaarloosbaar zijn.

Intraject simulaties, welke de gas simulatie resultaten gebruikten bij het definiëren van de initiële ionen voorwaarden, tonen aan dat het gas-ionisatiekamer instelvoltage, de dimensies en de temperatuur kritische variabelen zijn welke een invloed hebben op de uitgaande ionen stroom, ionen energie distributie, en de gereduceerde helderheid. Echter is met name het gas-ionisatiekamer instelvoltage erg belangrijk, omdat deze eigenhandig alle drie de bron karakteristieken tegelijk kan beïnvloeden en hij gemakkelijk aan te passen is tijdens het opereren van de bron. Over het algemeen zal bij het verhogen van het instelvoltage ook de ionenstroom toenemen, maar ook de energiestreiding. Als het instelvoltage te hoog wordt, kan dit de gereduceerde helderheid verlagen en een bi-modale ionen energie distributie produceren door het lens effect. Het gebruik van grotere gas-ionisatiekamer openingen is een andere manier om de uitgaande ionenstroom te vergroten, maar hierdoor zal de gereduceerde helderheid van de bron afnemen. De simulatie suggereert dat de beste manier om zowel de uitgaande ionenstroom als de gereduceerde helderheid te verbeteren kan behaald worden door de gastemperatuur te verlagen.

Bij een invallende elektronen bundel met een diameter van 100 nm zijn de optimale kamer dimensies welke de beste bron prestaties leveren voor de ionenstroom, energiestreiding, en bronhelderheid, 100-200 nm voor de gas-ionisatiekamer opening, ~ 200 nm ruimte tussen de membranen en een dikte van het membraan van ~ 100 nm. Gebaseerd op deze dimensies en bij gebruik van Argon gas op kamer temperatuur en een 1 keV invallende elektronen bundel van 100 nA, suggereren de simulaties dat de NAIS in staat is een ionenstroom te leveren van 300 pA, met een energiestreiding onder de 1 eV en een gereduceerde helderheid boven de 1×10^6 A/m²srV, welke vergelijkbaar is met onze schatting met het Langmuir helderheid model. Het moet genoemd worden dat de aangenomen elektronen dichtheid ($J_e \sim 1.27 \times 10^7$ A/m²) in deze berekening ongeveer een orde kleiner is dan de theoretische limiet die een Schottky elektronen focusseer kolom kan leveren.

Ontwerp en de fabricage van de geminiaturiseerde gas-ionisatiekamer (Hoofdstuk 4)

Twee verschillende manieren werden onderzocht voor het fabriceren van de geminiaturiseerde gas-ionisatiekamer. De eerste methode, gekend als het dubbele chip ontwerp, is

gebaseerd op de 'MEMS bulk machining' technologie waarbij een dun metalen membraan (100 nm) met daarop een Si_3N_4 laag (100 nm) wordt gefabriceerd op een enkele silicium chip met verscheidene lithografische ets en depositie stappen. Na het etsen van het gaskanaal op de Si_3N_4 laag worden twee verschillende chips op elkaar geplaatst met de kanalen naar elkaar toe gericht en overlappend, waarna ze op elkaar gelijmd worden om zo een complete gas-ionisatiekamer te vormen. In tegenstelling hiermee is de tweede methode gebaseerd op de MEMS oppervlakte microfabricage technologie waarbij alle gas-ionisatiekamer onderdelen worden gebouwd op een enkele silicium chip, vandaar de benamings single-chip ontwerp. Bij deze benadering wordt een structuur van twee membranen met daartussen een TEOS laag (dikte 100-200 nm) eerst op een silicium substraat gefabriceerd, waarna het gaskanaal wordt gevormd door intern verbonden gaten te vormen in de TEOS laag door BHF etsen. Bij beide ontwerpen wordt de dubbele opening simpelweg op het einde gefabriceerd door FIB fabricage.

Momenteel kunnen prototypes gebaseerd op het dubbele-chip ontwerp betrouwbaar geproduceerd worden en ze hebben bewezen volledig functionerende gas-ionisatiekamers te zijn, hoewel het met de huidige assemblage methode met lijm lastig was om deze volledig aan onze specificaties te laten voldoen. Mechanisch vastklemmen en 'wafer bonding' worden onderzocht als verbeteringen voor deze problemen. Hoewel een betrouwbaar fabricage proces gebaseerd op het single-chip ontwerp nog steeds actief onderzocht wordt, heeft dit ontwerp tot nu toe bewezen effectieve gas-ionisatiekamer afmeting te controleren door de dikte van de TEOS laag. Er zijn nog optimalisaties voor membraan metallisatie en experimentele validatie nodig, maar het lijkt erop dat het 'single-chip' ontwerp een veelbelovende techniek is voor de NAIS.

Proof-of-concept experimenten (Hoofdstuk 5)

Een commerciële SEM werd ontwikkeld om dienst te doen als geïmproviseerd NAIS prototype voor het uitvoeren van verschillende 'proof-of-concept' experimenten. Als basis van het experimentele werk werden achtereenvolgens een prototype gas-ionisatiekamer geïnstalleerd in een SEM preparaat kamer, werd de gas-ionisatiekamer gevuld met gas waarna het gas geïoniseerd werd door een SEM probe erin te focuseren om tot slot de ionenbundels die uit de gas-ionisatiekamer onttrokken worden te karakteriseren. Hoewel onze huidige fabricage methoden voor de gas-ionisatiekamer niet optimaal zijn voor fabricage volgens onze doelspecificatie voor apertuur, voldoen de gas-ionisatiekamers gebaseerd op het dubbele chip ontwerp om het concept aan te tonen van de NAIS. Enkele opmerkelijke resultaten zijn:

- Ionenbundel patroon observatie: Meerdere verschillende gassen (He, Ar, Xe en lucht) werden in de gas-ionisatiekamer gelekt waarna de emissie patronen van de onttrokken ionen werden gedetecteerd met behulp van microkanaal platen en een fosfor scherm. Hoewel ze kwalitatief zijn, tonen de resultaten duidelijk dat de NAIS enkel door het veranderen van de gasbron gemakkelijk ionen van verschillende elementen kan voorzien en dat de ionen onttrokken aan de geminiaturiseerde gas-ionisatiekamer inderdaad een bundel vormen.
- Ionenbundel stroom meting: We hebben de onttrokken ionenbundelstroom gemeten met het Faraday cup systeem en experimenteel geverifieerd dat de ionenproductie inderdaad afhankelijk is van het type gas, de gasdruk, de inkomende elektronen stroom, de bundel energie, en de spanning van de gas-ionisatiekamer. De metingen waren in overeenstemming met de theoretische verwachtingen.

- Korte-termijn bundel stabiliteit: De karakteristieke verandering in ionenbundel stroom per uur was ongeveer 1% - 3%, welke het meest beïnvloed werd door een drift van de gasdruk in onze experimentele setup. Bovendien observeerden we ook dat een spatiale drift van de grote elektronenbundel rond de dubbele apertuur een significante ionenstroom instabiliteit kan veroorzaken. We veronderstellen dat de elektronenbundel drift veroorzaakt wordt door het laden van deeltjes verontreinigingen op de gas-ionisatiekamer oppervlakten.
- Angulaire intensiteit: Een experiment waarin een Faraday cup met een kleine apertuur werd gescand over een ionenbundel patroon toonde aan dat de stroomdensiteitsverdeling Gaussiaans was, overeenkomstig met wat we verwachtten van onze simulaties. De gemeten angulaire stroom intensiteit in het midden van de bundel was $1.25 \mu\text{A}/\text{sr}$ bij 2 keV.
- Energie spreiding: Ionen energie spreidingen gemeten met een vertragende veldenergie-analysator bevestigen dat de energie verspreid door de NAIS voornamelijk afhankelijk is van de gebruikte gas-ionisatiekamer instelspanning. De ontwikkeling van een secundaire piek door het lenseffect van de gas-ionisatiekamer werd, zoals verwacht na de simulaties, ook vastgesteld. De studie bevestigt dat een energie spreiding van $< 1 \text{ eV}$ mogelijk is voor de NAIS.
- Ionenbeeldvorming en –verduunningstechnieken: Een eenvoudig FIB systeem werd geconstrueerd door ionen probe vormende optica en scanning deflectoren toe te voegen in de SEM experimentele setup. Door enkele onoplosbare mechanische uitlijnproblemen in de test setup was de FIB beeldvorming kwaliteit laag, maar voor het eerst werden ionen beeldvorming en verduunningstechnieken aangetoond door gebruik te maken van een argon ionenbundel voortvloeiend uit de miniatuur gas-ionisatiekamer.
- Gereduceerde helderheid: De gereduceerde bundel helderheid van een ionen probe gefocusseerd door de experimentele FIB setup met argon gas werd geschat op $3 \times 10^3 \text{ A}/\text{m}^2\text{srV}$. Het resultaat lijkt zeer aannemelijk aangezien slechts $\sim 8 \text{ nA}$ van de inkomende elektronenstroom bij 1 keV beschikbaar is voor gas-ionisatie en dat de prototype gas-ionisatiekamer gebruikt voor dit experiment suboptimale dimensies had (2 μm tussenafstand en 1 μm diameter). Met een elektronenbundel van 100 nA/100 nm bij 1 keV en een gas-ionisatiekamer die aan onze specificaties voldoet, zou $\text{Br} > 1 \times 10^6 \text{ A}/\text{m}^2\text{srV}$ zeer goed mogelijk zijn.

Delft NAIS-FEI Sidewinder Integratie: Concept en ontwerp (Hoofdstuk 6)

Een prototype NAIS op normale schaal die geïntegreerd kan worden op de FEI Sidewinder ionenbundel focusseer kolom werd ontwikkeld. Het hoofddoel van de integratie is het verderzetten van de studie en het evalueren van de NAIS eigenschappen alsook om de nanometer resolutie beeldvorming en ets prestaties aan te tonen door gebruik te maken van verschillende ionenbronnen in een commerciële FIB setup. Bovendien zal het de kans bieden om direct de prestaties van de NAIS met de Ga LMIS, welke de aangeraden ionenbron is voor de Sidewinder te vergelijken. Het ontworpen NAIS prototype bevat een nieuwe Schottky elektronen focusseer kolom gebaseerd op FEI's CLM en mini-SEM optica en werd geoptimaliseerd voor focussering $> 50 \text{ nA}$ op een 100 nm bundelpunt bij 1 keV. Er werd ook een speciale vacuümkamer ontworpen om gas en hoge voltage voedingsconnecties te voorzien voor het prototype ionenbron en om als interface te dienen met de bestaande Sidewinder kamer. Het NAIS prototype wordt verondersteld om de helderheid te verminderen, vergelijkbaar met die van een typische Ga LMIS, maar door een veel lagere energie

spreiding, wordt een significante prestatie verbetering verwacht voor de aangepaste Sidewinder kolom vergeleken met de conventionele Sidewinder. Gebaseerd op de verminderde helderheid van 1×10^6 A/m²srV en een energiespreiding van 1 eV FWHM, verwachten we een minimale bundelgrootte van ~3 nm (FW50) voor 1 pA bij 30 keV voor de Sidewinder uitgerust met de NAIS ionenkolom, hetgeen een reductie betekent van bundelpunt van meer dan 50% vergeleken met wat mogelijk is voor de Sidewinder uitgerust met de Ga LMIS ionenkolom.

Project vooruitzichten

Het werk dat hier beschreven werd toont voldoende het concept van de NAIS aan, zowel numeriek als experimenteel, en bevestigt dat de realisatie van een complete bron nabij is. In de toekomst zullen de volgende kritische stappen de optimalisatie van de gas-ionisatiekamer fabricatie alsook het verifiëren van de gereduceerde helderheid in het prototypes ionenkolom zijn. Bijkomend zijn ook lange termijn stabiliteit en levensduur nodig om de commerciële toepasbaarheid te valideren. Tot heden lag de focus op het genereren van edelgasionen voor traditionele FIB toepassingen, maar het dient te worden opgemerkt dat het ontwikkelen van de NAIS voor reactieve gassen zoals zuurstof nieuwe mogelijkheden kan bieden in de ionenbundelchemie en secundaire ion massa spectrometrie (SIMS). Een ander interessant idee zou de ontwikkeling zijn van een NAIS systeem als inline dubbele bundel tool.

Acknowledgments

I had the enormous good fortune to surround myself over the years with a group of very talented and caring people in Delft. Truly, it was the basis for all the success and fun I had during my PhD and ultimately made this thesis possible.

I am immensely grateful to my thesis supervisor Prof. Pieter Kruit who invited me to come to the Netherlands in the first place and guided me through this research project with enduring patience and enthusiasm.

I would like to thank our group scientific staff members Dr. Kees Hagen and Dr. Jacob Hoogenboom for many fruitful project discussions and their mentorship.

I would also like to thank Dr. Vladimir Kutchoukov for teaching me various MEMS fabrication techniques and for taking the leading role in the development of the miniaturized gas chambers.

I gratefully acknowledge Jan de Looff, Carel Heerkens, Frans Berwald, Jacques Nonhebel, Han van der Linden, Alix Wattjes, Ruud van Tol, Gerrit Schotte, and the late Cor Barends for their technical assistance in designing and setting up many experiments. I also acknowledge Anjella van Vliet, Margaret van Fessem, and Elly van der Most for all their administrative help and organizing many memorable group events. The CPO group is truly blessed with capable and dedicated support members like you!

It was my great pleasure to get to know and work with fellow PhD researchers Vincenzo Castaldo, Anand Dokania, Yanxia Zhang, Merijn Bronsgeest, Willem van Dorp, Christiaan Zonneville, Ali M. Gheidari, Ben Cook, Nalan Liv, Angela Gonzalez, Ivan Lazic, Aurelien Botman, Yan Ren, Sangeeta Hari, Leon van Kouwen, Gerwald Weppelman, and Thomas Verduin. Thanks for all the fun memories and good luck in all your future endeavors!

And this list would not be complete without mentioning Marco van der Heijden who took a big part in developing a retarding field energy analyzer. It was a lot of fun sharing the office with you and thanks for introducing me to the music of Jimmy Rosenberg.

A very special heartfelt thanks goes out to my dearest friends Inez Finoulst and Eric Piel who I shared living spaces for many years. You guys made me feel at home and I will forever cherish the memories of our international dinner nights.

I am also deeply grateful for all the cheer and support I received from home across the big pond.

I would like to acknowledge Dr. Mike Lysaght and Greg Schwind of FEI Beam Tech R&D for their kind support on my project.

Many thanks to Neal Landreville who offered me a place to stay whenever I visited Hillsboro and gave many helpful advices on designing the NAIS-winder.

I would also like to thank my good friend Dr. Bud Magera for proofreading the manuscript.

Last but by no means least, I would like to express my deepest gratitude to Michelle, my parents, and my sisters for all their love and support in all my pursuits.

About the Author

David Jun was born in Seoul, South Korea in 1973. After receiving a Bachelor of Science degree in Physics in 1996 from Lewis and Clark College, Portland, Oregon, USA, he joined FEI Company, Hillsboro, Oregon where his interest and ambition in the field of charged particle optics began. While working as a R&D engineer at FEI, he successfully completed a Master of Science program in Electrical and Computer Engineering at Portland State University in 2005. In late 2007, he joined the Charged Particle Optics (CPO) group at Delft University of Technology where he took on a research project developing a novel gas ion source. He currently lives in Portland and provides contract services in electron/ion optics design and product development through his own venture Elion Optics LLC ^[*].

[*] For inquiries on services provided, please contact david.sb.jun@gmail.com